

UC San Diego

UC San Diego Electronic Theses and Dissertations

Title

Studies of co- and postseismic deformation of the lithosphere from numerical models and space geodetic data

Permalink

<https://escholarship.org/uc/item/1fw6n7st>

Author

Barbot, Sylvain

Publication Date

2009

Peer reviewed|Thesis/dissertation

UNIVERSITY OF CALIFORNIA, SAN DIEGO

**Studies of Co- and Postseismic Deformation of the Lithosphere from
Numerical Models and Space Geodetic Data**

A dissertation submitted in partial satisfaction of the
requirements for the degree
Doctor of Philosophy

in

Earth Sciences

by

Sylvain Barbot

Committee in charge:

Professor Yuri Fialko, Chair
Researcher Donna Blackman
Professor Xanthippi Markenscoff
Professor Guy Master
Professor David Sandwell
Professor Peter Shearer

2009

Copyright
Sylvain Barbot, 2009
All rights reserved.

The dissertation of Sylvain Barbot is approved, and it is acceptable in quality and form for publication on microfilm and electronically:

Chair

University of California, San Diego

2009

DEDICATION

To my sisters, Sarah and Aliénor, and my family, with love.

EPIGRAPH

His origins are become remote as is his destiny and not again in all the world's turning will there be terrains so wild and barbarous to try whether the stuff of creation may be shaped to man's will or whether his own heart is not another kind of clay.

— Cormac McCarthy

TABLE OF CONTENTS

	Signature Page	iii
	Dedication	iv
	Epigraph	v
	Table of Contents	vi
	List of Figures	ix
	List of Tables	xx
	Acknowledgements	xxi
	Vita and Publications	xxii
	Abstract of the Dissertation	xxiii
Chapter 1	Introduction	1
Chapter 2	Space geodetic investigation of the co- and post-seismic deformation due to the 2003 M_w 7.2 Altai earthquake: Implications for the local lithospheric rheology	5
	2.1 Introduction	6
	2.2 Co-seismic analysis	8
	2.2.1 Determination of the fault location	8
	2.2.2 Inversion for co-seismic model	11
	2.3 Post-seismic deformation	12
	2.3.1 Inversion for afterslip model	12
	2.3.2 Poro-elastic rebound	15
	2.3.3 Visco-elastic relaxation	17
	2.4 Discussion	18
	2.5 Conclusions	21
	2.6 Along-track Interferometry	22
	2.7 Full relaxation due to a screw dislocation	24
Chapter 3	Effect of a Compliant Fault Zone on the Inferred Earthquake Slip Distribution	30
	3.1 Introduction	31
	3.2 Semi-Analytic Model of Deformation in Heterogeneous and Anisotropic Media	32
	3.2.1 Theory	32
	3.2.2 Anti-Plane Deformation	34
	3.3 Co-seismic deformation in the presence of a compliant fault zone	39
	3.4 Conclusions	42
	3.5 Convergence Condition	42
	3.6 Anisotropy	44

Chapter 4	Three-dimensional models of elasto-static deformation in heterogeneous media, with applications to the Eastern California Shear Zone	46
	4.1 Introduction	47
	4.2 3-D Models of Deformation due to Faulting in Heterogeneous Media	48
	4.2.1 Governing equation and boundary conditions	48
	4.2.2 Decomposition of Elastic Moduli	51
	4.2.3 The Successive Approximation Method	54
	4.2.4 The Perturbation Method	55
	4.2.5 The Successive Over Relaxation Method	56
	4.2.6 Homogenization of Elastic Moduli	57
	4.2.7 Implementation	58
	4.3 Application to Compliant Fault Zones in the Mojave Desert	59
	4.4 Discussion	67
	4.5 Conclusions	69
	4.6 Benchmarks	72
	4.6.1 Antiplane strain	72
	4.6.2 Plane strain	74
	4.6.3 Three-dimensional deformation	76
Chapter 5	Postseismic Deformation due to the Mw 6.0 2004 Parkfield Earthquake: Stress-Driven Creep on a Fault with Spatially Variable Rate-and-State Friction Parameters	81
	5.1 Introduction	82
	5.2 Coseismic Slip Model	83
	5.3 Postseismic Transient Deformation	84
	5.4 Models of Time-Dependent Deformation	91
	5.5 Semi-Analytic Models of Afterslip	100
	5.6 Discussion	104
	5.7 Conclusions	107
	5.8 Impulse Response of a Point Source	109
	5.8.1 Power-Law Shear Bands	109
	5.8.2 Rate-and-State Creep	111
	5.9 Numerical Model of Time-Dependent Creep on Finite Faults in an Elastic Half-Space	111
	5.9.1 Continuum Representation of Dislocations	112
	5.9.2 Body Force Representation of Fault Creep	115
	5.9.3 Numerical Implementation	117
	5.10 Interseismic Slip Rates for a Slip Patch	120
Chapter 6	Fourier-Domain Green Function for an Elastic Semi-Infinite Solid with Gravity with Applications to Earthquake and Volcano Deformation	121
	6.1 Introduction	122
	6.2 Analytic solution to the traction boundary-value problem in a semi-infinite elastic solid with gravity	123
	6.2.1 The Galerkin vector potential	124
	6.2.2 The Boussinesq's problem with gravity	125
	6.2.3 The Cerruti's problem with gravity	128
	6.2.4 Arbitrary distribution of surface traction with gravity	130
	6.3 A semi-analytic Green function for the elastic half space with gravity	131
	6.3.1 A Fourier-domain elastic Green function	132
	6.4 Models of faulting and volcanic unrest	134
	6.5 Conclusions	139

6.6	Space-domain analytic Green function with buoyancy boundary condition	140
6.6.1	The Boussinesq-Papkovitch-Neuber potential	141
6.6.2	The Boussinesq problem with buoyancy surface boundary condition in the space domain	142
6.7	Static deformation in a half-space due to surface traction using the Boussinesq-Papkovitch-Neuber potential	147
6.7.1	The Boussinesq's problem	147
6.7.2	The Cerruti's problem	148
Chapter 7	Towards a Unified Representation of Postseismic Mechanisms: Semi-Analytic Models of Fault Creep, Poroelastic Rebound and Power-Law Flow	150
7.1	Introduction	151
7.2	A general viscoelastic model	152
7.3	Nonlinear viscoelastic flow	155
7.3.1	Numerical examples and benchmarks	156
7.3.2	Effect of gravity	163
7.4	Fault creep	164
7.4.1	Analytic benchmark	166
7.5	Poroelastic rebound	167
7.5.1	Methods and benchmarks	168
7.6	Conclusions	172
7.7	Continuum Theory of Poroelastic Compaction	173
7.7.1	The Classic Theory of Poroelasticity	174
7.7.2	A bulk-viscosity formulation for poroelasticity	175
Appendix A	Numerical models of static deformation: the semi-infinite solid elasto-static Green function	179
A.1	Model input	179
A.2	Fortran implementation	182
Appendix B	Numerical models of elastic deformation in heterogeneous media	186
B.1	User interface	186
B.2	Fortran implementation	189
Appendix C	Numerical models of time-dependent deformation	193
C.1	User Interface	193
C.2	Fortran implementation	197

LIST OF FIGURES

Figure 1.1:	Distribution of slip on a fault plane during the earthquake cycle. Earthquake nucleation takes place in areas with unstable friction in the seismogenic zone. The stable part of a fault slips aseismically during the inter- and postseismic phases of the earthquake cycle. The seismogenic zone is delimited by the transition from stable to unstable friction.	2
Figure 1.2:	Sketch of the partition of long-term surface displacement into parts of the earthquake cycle. Left panel: the spatial distribution of surface displacement as a function of distance from a fault. The interseismic period (green) is characterized by a regional length scale. The coseismic deformation (red) is highest near the fault and decays with across-fault distance. The postseismic transient (blue) occurs around the fault and its length scale depends on the particular source mechanism. Right panel: the time dependence of surface displacements as a function of position in the earthquake cycle. In the interseismic period, a point off the fault (black star) slowly moves in the direction of plate motion. As an earthquake happens, the point is suddenly displaced. A transient displacement occurs in the postseismic period.	3
Figure 2.1:	Location of the September 27th 2003, M_w 7.2 Altai earthquake, near the Russia-China-Mongolia border. a) Major geologic structures on the regional scale. b) Location of the epicenter (yellow star), with the following days $M_w \geq 6$ aftershocks (red stars). The black frames indicate the radar swath of ENVISAT tracks 434 and 391. Orange stars indicate aftershocks of M_w 5 and above after 2003/12/22.	6
Figure 2.2:	Co-seismic and post-seismic interferograms used in this study. The (grey) co-seismic interferograms were jointly used to invert for the co-seismic slip on the fault. The 3 year (blue) pairs were simultaneously inverted for afterslip. Other (black) pairs are used to verify the early stage of the post-seismic transient approximately 6 months, 2 years and 2.5 years after Altai earthquake. . . .	8
Figure 2.3:	Co-seismic data analysis and fault location. (a) The East component of the SPOT correlation reveals a clear right lateral motion across the fault. The SPOT optical data is overlaid on the topography. (b) The fine resolution of the along-track interferogram (2003/09/08-2003/10/13, track 391) shows where the fault ruptured. (c) The range offsets of pairs 2003/09/08-2003/10/13, track 391 and 2003/09/11-2004/07/22, track 434 reveal two apparently separated dextral ruptures. (d) Azimuthal offset of interferogram 2003/09/08-2003/10/13. The color scale has been saturated to highlight the fault location. The thick black line in each image is our estimate of the fault location. The thin red line is the survey of <i>Nissen et al.</i> [2007]. The AZI and LOS arrows indicate the satellite orbital direction (15°) and the look direction, with a 23° incidence. Positive LOS displacements are towards the satellite.	10
Figure 2.4:	Co-seismic slip Inversion. (a) Interferograms (2003/09/08-2003/10/13, track 391 and 2003/09/11-2004/07/22, track 434) used to invert for a co-seismic slip model. (b) Model co-seismic LOS displacements. (c) Co-seismic slip distribution obtained after inversion of LOS displacements of the 2 interferograms in (a). The black arrows indicate the direction and amplitude of slip for every patch. (d) LOS displacement residuals after inversion. (e) Range offsets residuals. (f) Azimuthal offsets residuals.	13

Figure 2.5:	Post-seismic interferograms and inversion for the afterslip model. (a) Interferogram 2003/10/13-2006/08/28, track 391 showing 3 years of post-seismic deformation, projected in the LOS direction. (b) Interferogram 2003/11/01-2006/09/16, track 162, showing also 3 years of post-seismic deformation. (c) Afterslip model showing a slip distribution confined in the seismogenic zone. (d) Forward model, fitting the two 3 year interferograms. (e-f) Residuals on interferograms (a) and (b) respectively.	14
Figure 2.6:	Predictions of the full poro-elastic rebound following Altai earthquake. The model is obtained by differentiating the two elastic responses of the crust with an undrained Poisson's ratio $\nu_u = 0.25$ and with a drained Poisson's ratio $\nu_d = 0.20$	16
Figure 2.7:	Simulated LOS displacement for 3 years of visco-elastic relaxation occurring between 2003/10/13 and 2006/08/28. (a) Weak lower crust or jelly-sandwich rheology. (b) Deformation due to a flow in a weak mantle. Note the larger wavelength of the deformation.	18
Figure 2.8:	Seismic moment release. Cumulative seismic moment after Oct. 13, 2003 and the LOS displacement of available InSAR data. The LOS displacements correlate with the seismic moment released in the corresponding time interval of each interferometric pair. The thin black line indicates the fault surface location. (a-d) LOS displacements in UTM coordinates relative to the origin ($87.74^\circ\text{E}, 50.30^\circ\text{N}$).	26
Figure 2.9:	Difference between the full relaxation of the co-seismic stresses on a vertical plane (afterslip) and on a horizontal plane (visco-elastic relaxation). In both cases, the seismogenic zone, of thickness H , is perfectly elastic and the fault extends from the surface to a depth L . The two-dimensional solution is self-similar and depends only on the dimensionless parameter $h = L/H$	27
Figure 2.10:	Doppler history f_D as a function of time, or equivalently, as a function of the look direction towards a scatterer P at the surface of the Earth. Positive and negative Doppler frequencies are associated with positive and negative look directions, respectively.	28
Figure 2.11:	Geometry and boundary conditions applied to the screw dislocation in an elastic half-space. The solutions represent the sum of the co-seismic and post-seismic contributions to the anti-plane displacement. Top: the free surface on a horizontal plane corresponds to the visco-elastic relaxation. Bottom: the free surface on a down-dip extension of the fault plane corresponds to the afterslip scenario.	29
Figure 3.1:	Dislocation in a half-space. A fault idealized by a plane of normal vector $\hat{\mathbf{n}}$ is sliding in a direction \mathbf{u} . In anti-plane deformation, strike-slip occurs along the x_1 -direction.	33
Figure 3.2:	Comparison between the analytic expressions and the numerical solutions for surface displacements due to a fault slip in heterogeneous media. a) Isotropic medium with a contrast of shear modulus across the transform fault zone. b) Isotropic medium after full relaxation of a visco-elastic substrate below the depth H . c) Isotropic medium with the compliant fault zone with total width $2W$. d) Contrast of anisotropy across the fault plane. The wavelength of deformation is larger in the softer anisotropic crust, to the left of the rupture.	37

Figure 3.3:	a) Synthetic co-seismic surface displacements in a homogeneous crust (solid line) and in a laterally heterogeneous crust with a compliant zone (dashed line). b) Slip inversions of surface displacements for the initial slip distribution shown by the continuous profile. c) Inversion of the algebraic difference between the homogeneous and the heterogeneous synthetics. d) Difference between the inversions of the homogeneous and heterogeneous synthetics. . .	41
Figure 3.4:	Convergence rate of the proposed algorithm as a function of the homogenization constant $\bar{\mu}$. The successive approximation works best for the value predicted by eq. (3.34) (as denoted by arrow). When using SOR, convergence is obtained for all range of $\bar{\mu}$ with an accelerated rate.	44
Figure 4.1:	The deformation of a heterogeneous elastic body Ω is driven by internal dislocations. A failure plane with normal $\hat{\mathbf{n}}^\alpha$ and slip \mathbf{s}^α cuts the volume with elastic tensors $\mathbf{C}_1 \neq \mathbf{C}_2$. The slip system α is associated with eigenstrain $\boldsymbol{\epsilon}^\alpha(\mathbf{x}) = \frac{1}{2}(\mathbf{s}^\alpha \otimes \hat{\mathbf{n}}^\alpha + \hat{\mathbf{n}}^\alpha \otimes \mathbf{s}^\alpha)$, moment density $\mathbf{m}^\alpha(\mathbf{x}) = \mathbf{C} : \mathbf{s}^\alpha \otimes \hat{\mathbf{n}}^\alpha$ and equivalent body force $\mathbf{f}^\alpha(\mathbf{x}) = -\nabla \cdot \mathbf{m}^\alpha$. The surface boundary $\partial\Omega$, with normal vector $\hat{\mathbf{n}}$, is traction free ($\boldsymbol{\sigma} \cdot \hat{\mathbf{n}} = 0$).	49
Figure 4.2:	An arbitrary slip system α for a point source dislocation (bottom sketch) can be decomposed into six linearly independent components. Eigenstrain $\boldsymbol{\epsilon}^\alpha$ is associated with an equivalent body force distribution $\mathbf{f}^\alpha(\mathbf{x})$ and equivalent surface traction \mathbf{t}^α . Equivalent surface traction occurs when fractures reach to the surface of the semi-infinite solid.	52
Figure 4.3:	Gradient of the LOS displacement residuals after the Hector Mine coseismic model was removed. Gradient emphasizes deformation around nearby faults and underlines possible creep events (dashed quadrants). Triangle indicates location of the seismic experiment of <i>Cochran et al.</i> [2008].	60
Figure 4.4:	A) Map view of surface displacement corresponding to full 3-D deformation in a heterogeneous crust due to the 1992 Landers, CA earthquake. Vectors and color scale indicate horizontal and vertical displacements, respectively and uplift is taken to be positive. B) Elastic structure contribution corresponding to the Landers model. C) Model of the total surface displacements due to the Hector Mine earthquake. D) Hector Mine elastic structure contribution. The deformation is localized around CZs: The Calico-Hidalgo (CH), the Rodman (RM) and the Pinto Mountain (PM) faults exhibit amplified strain. Profiles A-A', B-B' and C-C' are shown in subsequent figures. Origin corresponds to the epicenter of the Hector Mine earthquake (116.27W, 34.595N). Light gray lines correspond to identified faults in the ECSZ and darker gray lines indicate modeled compliant zones (CZ).	62
Figure 4.5:	Exploration of the CZ model space. Variance reduction of the Landers and Hector Mine LOS data for the (a) Calico/Rodman and (b) the Pinto Mountain profiles (transects A-A' and C-C', respectively, in Fig. 4.4) as a function of the CZ width, depth and rigidity reduction ΔG . All models assume a Poisson's solid ($\nu = 0.25$) in the ambient crust and in the CZ. The star symbol indicates the preferred model of <i>Cochran et al.</i> [2008] corresponding to a 36% reduction in P-wave velocity. The circle indicates our preferred model, based on fitting the Landers and Hector Mine LOS data simultaneously.	63

Figure 4.6:	Observed (diamond) and modeled (solid line) LOS displacements from profile A-A' corresponding to the Landers (bottom) and Hector Mine (top) coseismic interferograms North of Galway Dry Lake. The Calico model corresponds to a 4 km deep, 2.0 km wide structure with a 60% rigidity reduction, as indicated by a circle in Fig. 4.5a. The Rodman model is similar except for a shallow structure of 2 km. B) Observed and modeled LOS residual displacements across a southern segment of the Calico fault (profile B-B'). At this location, the Calico model implies a shallow (2-3 km) structure 1.8 km wide with 45-50% rigidity reduction. Topography (dashed line) does not correlate with InSAR phase delay, indicating a limited tropostatic noise contribution. The continuous profiles correspond to forward models from several closely spaced parallel profiles within boxes outlined in Fig. 4.4. The flip of polarity between the Landers and Hector Mine coseismic InSAR data is an expected signature of a compliant zone.	65
Figure 4.7:	Modeled (solid line) and observed (diamonds) LOS displacements across the Pinto Mountain fault, profile C-C'. The predictions correspond to a single compliant zone model with a 45% reduction in both shear and bulk moduli, indicated by a circle in Fig. 4.5b. The CZ structure is 1.75 km wide and at least 9 km deep. The continuous profiles correspond to several closely spaced parallel profiles from the forward model and indicate the variation of deformation within the C-C' box outlined in Fig. 4.4. Notice the separate scale for the Hector Mine data and forward model.	67
Figure 4.8:	Modeled (solid line) and observed (diamonds) LOS displacements across the Homestead fault. Forward model corresponds to a compliant zone with a 50% reduction in shear and bulk moduli in a block 4-5 km deep and 1.5 km wide. The continuous profiles correspond to forward models from several closely spaced parallel profiles within boxes outlined in Fig. 4.4.	68
Figure 4.9:	Three-dimensional calculation with axes of symmetry. Horizontal (u_1, u_2), and vertical u_3 surface displacements are represented by white arrows and the background color, respectively. A) An infinitely long strike-slip fault (dashed line) creates an antiplane symmetry (no vertical displacement). B) An infinitely long edge dislocation creates a plane-strain symmetry in the three-dimensional computational volume.	72
Figure 4.10:	Antiplane benchmarks along profile A-A' in fig. 4.9 in the case of a vertical left-lateral strike slip fault. A) The numerical and analytical solutions for a homogeneous half space are shown in left panel. The relative error is shown in the right panel and remains smaller than 0.5% 10 fault lengths away from the fault trace. B) Perturbation method. The difference between the surface displacements corresponding to a heterogeneous elastic structure and a homogeneous half space. The elastic structure consists in a plate of rigidity $G_1 = 1$, extending from the surface to the depth H , and the bottom half space of rigidity $G_2 = 1.5$. The strike slip fault extends from the surface to the locking depth $0.8 H$. Numerical solution is shown at 1 and 14 iterations of the perturbation method. C) Successive Over Relaxation method (SOR). Results similar to B) but with a higher elastic contrast $G_2/G_1 = 2.5$. Convergence is obtained after 20 iterations.	73

Figure 4.11:	Plane-strain benchmarks along profile B-B' in Fig. 4.9. A) Surface displacements corresponding to a unit slip occurring on a buried edge dislocation dipping 30°. Numerical error (right panel) does not exceed 3% compared to analytic solution. B) Perturbation method. An more compliant plate, with $\lambda_1 = G_1 = 0.7$ and extending from the surface to a depth H , overrides a half-space of Lamé parameters $\lambda_2 = G_2 = 1$. Left panel shows first iteration ($n = 1$) and converged ($n = 9$) solutions of the perturbation method. Norm of error corresponding to the converged solution remains smaller than 5% compared to results of the matrix propagator method. C) Same as A) but with a vertical dip slip fault. D) Successive Over Relaxation (SOR) method. Solution displacements and relative error compared to the matrix propagator method for the layered structure of B) with a greater elastic contrast $G_2/G_1 = 2.5$ and a constant $\lambda_1 = \lambda_2 = 1$	75
Figure 4.12:	Three-dimensional benchmark. A) A strike-slip fault fractures crustal areas with different elastic moduli. The rigidity in the bottom half space is 50% higher than in the top plate. B) The displacement field at the surface of the half space. C) Difference between the displacement field in B) and the corresponding homogeneous solution where $G_1 = G_2$. D) Residuals between our Fourier domain semi-analytic result and the result of <i>Wang et al.</i> [2003].	77
Figure 4.13:	Three-dimensional benchmark. A) A strike-slip fault breaks the upper crust. The rigidity in the bottom half space is 2.5 times higher than in the top plate. B) The displacement field at the surface of the half space. C) Elastic structure contribution. D) Residuals between our Fourier domain semi-analytic result and the result of <i>Wang et al.</i> [2003].	78
Figure 4.14:	A) Geometry. B) Displacement field at the surface. C) Elastic structure contribution for the case of uniform bulk modulus. D) Residuals between our result and a finite-element calculation for case C. E) Elastic structure contribution for the case of uniform Poisson's ratio. F) Residuals between our solution and finite-element calculations corresponding to case E.	80
Figure 5.1:	Coseismic slip model. A) amplitude of right-lateral strike slip inferred from the inversion of the 14 continuous GPS horizontal coseismic displacements. B) Map view of the coseismic displacement vectors. The blue arrows represent the GPS data with the two-sigma uncertainties; the black arrows correspond to our best forward model. The origin is located at (N35.8150, W120.3740).	85
Figure 5.2:	A) Effect of smoothing on the coseismic slip model. The smoothness of the slip model is controlled by the smoothness factor (SF) in the inversion. B) The smoothness/misfit curve. Our models use smoothness factor $SF=10^{-4}$ as indicated by the black cross.	86
Figure 5.3:	Resolution of the under-determined inverse problem. A) Diagonal of the resolution matrix R . Critical value $R = 0.1$ is reached at a depth of about 7 km. B) Correlation of inferred slip patches with their neighbors on the fault plane (off-diagonal terms of the resolution matrix). Position of central subpatches is indicated in white text (depth and distance along strike) and highlighted by black rectangle. Note the change of color scale in B. The fault segment that experienced the most afterslip is located at an along-strike distance of 24 km and a depth of 5 km; its location is robust in the strike direction.	87

Figure 5.4:	Kinematic inversions and seismicity. The right-lateral slip on the fault plane as a function of time after the coseismic rupture is constrained from the continuous GPS data. Upper-left model is the coseismic slip distribution along with the 1-day seismicity. The continuous profiles are the coseismic slip contour intervals. Next panels are the cumulative afterslip models at 0.05, 0.15, 0.30, 0.70, 1.10, 1.50 and 2.50 yr after the earthquake. Aftershocks -cumulative since the day following the earthquake- are superimposed to the afterslip models, colored from black to red for early to late occurrence time. The coseismic contour lines are superimposed to the afterslip models to facilitate comparison.	89
Figure 5.5:	Kinematic inversions (continued). GPS horizontal displacements (red arrows with two-sigma uncertainties) and corresponding forward models (black arrows). The GPS data in the 3yr postseismic transient can be explained by right-lateral afterslip on the coseismically ruptured fault segment. Origin is at the geographic coordinate (N35.8150, W120.3740).	90
Figure 5.6:	Creep tests for a simple crack frictional surface. The stress and strain impulse responses for (a) the linear and power-law creep and (b) the rate-strengthening (RS) friction laws. For a step-like increase in total strain, resulting from an instantaneous change in stress $\Delta\tau$, some inelastic deformation is triggered. The dotted profiles indicate the response of a linear rheology. The classic formulation of RS friction is ill-posed for a creep test whereas the generalized friction law remains bounded at small velocities. The detail of calculations can be found in Appendix 5.8.	94
Figure 5.7:	PCA decomposition of GPS time series. The first mode, with 95% of the total variance, corresponds to the postseismic signal. The associated GPS displacements exhibit the expected signature of right lateral slip on the fault and correspond to the cumulated surface displacement after three years. The second mode, which represents 1.7% of the total variance, is due to a common-mode seasonal signal, which is not removed from the SOPAC filtered time series [Langbein, 2008], and is about two orders of magnitude smaller. The associated surface displacements are generally aligned perpendicular to the fault.	96
Figure 5.8:	Functional fit to the dominant PCA mode of the postseismic component of the GPS time series. The impulse response of linear constitutive laws ($n = 1$ for power-law or $k \simeq 1$ for RS friction, shown by long-dashed profiles) only poorly simulate the observed time dependence of afterslip. Best fitting power-law (a) and RS models (b), corresponding to parameters $n = 6.9$ and $k = 7.0$, respectively, are represented by the thick solid lines. In other inversions, nonlinear coefficient n or k are imposed.	97
Figure 5.9:	Numerical simulation of afterslip with Rate-Strengthening (RS) friction. The simplified coseismic model (upper-left corner) is the initial condition for the postseismic fault creep. Time evolution of afterslip is described by the generalized RS friction law of eq. (5.11). Afterlip is not allowed to occur in areas that slipped coseismically and propagates on the fault plane away from the coseismic patch. The corresponding time series of surface displacements are shown in Fig. 5.10. Snapshots are separated by 20 time steps. The numerical method is described in Appendix 5.9.	101
Figure 5.10:	Postseismic GPS data (solid line), two-sigma uncertainties (gray shade) and best forward model (dashed lines) corresponding to the generalized rate-strengthening friction law for all the continuous GPS stations. Model prediction generally agrees with the data with the exception of station CARH and MIDA, in the very near field, which are affected by a fault migration.	102

Figure 5.11: Constraint on frictional parameters V_0 and $(a - b)$. The velocity best reducing the data for the 13 selected stations (CARH is removed) is inverted using only 1 year of data (dashed profiles) and 3 years of data (solid lines). Results are shown for a series of $(a - b)$ models, assuming an effective normal stress of $\sigma = 100$ MPa.	103
Figure 5.12: Aftershocks driven by aseismic creep. A) The equivalent seismic moment of our preferred RS creep model (solid line) compares well with the equivalent seismic moment inferred from kinematic inversions (circles). Aftershocks moment (dashed line) is two orders of magnitude lower and follows the creep evolution closely after 10^{-2} year (4 days). B) Linear correlation between the moment magnitudes of aftershocks and RS creep from two independent estimates of creep moment using geodetic inversion (circles) and forward modeling (crosses). The lines are a linear fit to the points. C) Depth distribution of aftershocks. Moments in A) and B) use the aftershocks that occurred in the top 9 km (shaded depths).	105
Figure 5.13: Schematic of the point-source approximation for a localized shear band of thickness T and linear dimension L . The cumulated displacement \mathbf{s} across the ductile zone relaxes the stress $\tau = G^*s$	110
Figure 5.14: A buried circular slip patch embedded in semi-infinite solid Ω with free surface $\partial\Omega$ at $x_3 = 0$. Slipping surface is defined by $n(\mathbf{x}) = 0$. Burgers' vector of dislocation is $\mathbf{s} = \mathbf{u}^i(0^+) - \mathbf{u}^i(0^-)$	113
Figure 5.15: Relative error of numerical models compared to the analytic solution of <i>Okada</i> [1992] for the Parkfield coseismic slip model. The displacement vector at the location of the 14 GPS stations is estimated numerically with the method of <i>Wang et al.</i> [2002] (triangles) and with the one developed in this study (circles). The percentage error is plotted as a function of the expected analytical solution for the 3 components of displacement. The red triangles correspond to a denser sampling of the <i>Wang et al.</i> [2002] Green function, which reduces the numerical error.	118
Figure 5.16: The time-dependent deformation due to frictional sliding on a surface of unit size. A) The stress on a fault is perturbed due to static slip on an upper segment leading to afterslip. B) The vector-valued displacement at a surface point driven by the deep afterslip is evaluated numerically using a second-order accurate Runge-Kutta method with adaptive time steps. The forward models compare well with the expected impulse response of linear ($\dot{s} = \Delta\tau/\eta$) and nonlinear ($\dot{s} = A (\Delta\tau/G)^n$, here $n = 2$) constitutive laws. The timescale of the synthetic signal is recovered within a 5% error. The adaptive time step is apparent only for the case of a nonlinear evolution law.	119
Figure 6.1: Geometry and boundary condition for the deformation due to an arbitrary distributions of surface traction. The surface traction $\mathbf{t}(\mathbf{x})$ is the sum of the applied load $\mathbf{p}(\mathbf{x})$ and the buoyancy restoring force $\mathbf{g} = \Delta\rho g u_3 \hat{\mathbf{n}}$. Displacement \mathbf{u} in the semi-infinite solid satisfies the homogeneous Navier's equation (6.4) with buoyancy boundary condition (6.3).	123
Figure 6.2: A) Fourier-domain solution for the Boussinesq's problem (eq. 6.20). The map view corresponds to displacements at a depth of 3 km. The arrows indicate the horizontal displacement; the vertical displacement is shown by the color. Vertical displacement is taken to be positive upward. A point-source moment \mathbf{m}_{23} is applied at the surface. A) Comparison between the analytic solution and the semi-analytic Fourier domain solution along profile A-A'. These results correspond to a Poisson's solid ($\lambda = \mu$) without buoyancy effects at the surface ($\Gamma = 0$).	126

Figure 6.3:	Benchmark of the Fourier-domain solution to the Cerruti's problem (Eqs. (6.26) and (6.27)). A) A point-source moment \mathbf{m}_{12} is applied at the surface of the half space. The map view corresponds to displacements at a depth of 3 km. The arrows indicate the horizontal displacement; the vertical displacement is shown in color. Vertical displacement is taken to be positive upward. B) Comparison between the analytic solution and the semi-analytic Fourier domain solution for the displacement along profile B-B'. In these calculations, we use a Poisson's solid ($\lambda = \mu$) and ignore the buoyancy effect ($\Gamma = 0$).	129
Figure 6.4:	A) Map view of surface displacement due to a dilatation source centered at $y_1 = y_2 = 0$ and buried at a depth of $y_3 = 0.5$ km. Horizontal and vertical components of displacement are represented by the vectors and the color, respectively. Uplift is taken to be positive. B) The norm of the residuals between the numerical solution and the formulation of Mindlin and Cheng [1950b] as a function of the number of nodes in the 3-D grid for a uniform isotropic sampling of $\Delta x_i = 0.05$ km. The error is normalized by the norm of the analytic solution. The dashed and solid-line profiles correspond to a dilatation source at depth of $y_3 = 0.5$ and $y_3 = 1.0$ km, respectively. The numerical error decreases as the boundaries of the computational domain increases and the non-desired effect of periodicity decreases.	135
Figure 6.5:	A) Map view of surface displacement due a vertical, 1 km long, strike-slip fault extending from the surface to a depth of 1 km with a 1 m slip (left) and residuals with the analytic solution of Okada [1992] (right). B) Surface displacements due to a 1 m slip on vertical dip-slip fault with same dimensions as in A). The fault trace is indicated by a solid black line. A dip-slip fault intersecting the surface is modeled with both internal body forces and surface traction. Residuals in A) are due to the tapering of the fault tip; residuals in B) come from the problem of sampling a displacement field that is not single-valued at the fault.	137
Figure 6.6:	A) Map view of surface displacement due a 45°-dip, 10 km long, 10 km wide (in down-dip direction) thrust fault buried at a depth of 5 km (dashed rectangle). B) Residuals with the analytic solution of Okada [1992]. C) The norm of the residuals as a function of the number of nodes in the 3-D grid.	138
Figure 6.7:	Benchmark of the Fourier-domain solution including a buoyancy boundary condition. A) A moment \mathbf{m}_{13} is applied at the surface of the half space. B) The full surface displacement. Horizontal and vertical components of displacement are represented with arrows and colors, respectively (positive for uplift). B) The surface displacement due to the surface buoyancy, corresponding to $\Gamma = 10^{-2} \text{ m}^{-1}$. Notice the reversal of the vertical displacements. C) The residuals between the Fourier-domain and the perturbation-method solutions, Eqs. (6.29) and (6.73), respectively.	145
Figure 7.1:	Sketch of inelastic properties of the lithosphere responsible for postseismic transients. Postseismic deformation may be due to a combination of poroelastic response, fault creep and viscous shear. The shear flow in the mantle and lower crust might be governed by a power-law viscosity for high stress and by a Newtonian viscosity at lower stress. Afterslip on fault roots is governed by a velocity-strengthening friction law. Poroelastic rebound can occur throughout the crust but likely decreases with increasing depth.	152

Figure 7.2:	Calculated time series of surface displacements due to a stress perturbation in an elastic plate over a nonlinear viscoelastic half space. A) A map view of postseismic surface displacements at the early stage of the transient. The right panel shows the difference between our solution and finite element solution computed using Abaqus. B) Time series of surface displacements for an array of points numbered from 1 to 9 in the corresponding map. Time is scaled by $t_m = \dot{\gamma}_0^{-1} s^{1-n} L^{n-1}$	157
Figure 7.3:	Calculated time series of surface displacements for a model shown in Figure 7.2, but for a linear viscoelastic layer (eq. (7.15) with $n = 1$). A) Left panel: A snapshot of postseismic surface displacements at time $t = 2t_m$. Right panel: difference between our solution and finite element benchmark. B) Time series of surface displacements for an array of points numbered from 1 to 9 in the corresponding map.	158
Figure 7.4:	Calculated time series of surface displacements due to a vertical dip-slip fault in an elastic plate overriding a nonlinear viscoelastic half space. The model geometry is the same as in Fig. 7.2. The postseismic flow is governed by a power-law rheology with stress exponent $n = 2$. A) Left panel: A map view of postseismic surface displacements after ten months. Right panel: difference between our solution and a finite element benchmark. B) Time series of surface displacements for an array of points numbered from 1 to 8 in the corresponding map.	161
Figure 7.5:	Calculated time series of surface displacement following the rupture of a vertical dip-slip fault in an elastic plate over a linear viscoelastic layer. The geometry is the same as in Fig. 7.2. The postseismic flow is governed by a linear viscoelastic rheology (eq. (7.15) with $n = 1$). A) Left panel: A snapshot of postseismic surface displacements at time $t = 0.5t_m$. Right panel: difference between our solution and a finite element benchmark. B) Time series of surface displacements for an array of points numbered from 1 to 9 in the corresponding map.	162
Figure 7.6:	Effect of gravity on the postseismic displacement due to a thrust fault. The brittle-ductile transition occurs at depth H . The fault is $20H/3$ long in the strike direction, H wide in the dip direction and U is the magnitude of dip-slip. A) Viscoelastic relaxation but no gravitational restoring force. The surface displacement after 5 and 45 relaxation times τ_a due to a linear viscous relaxation in the half space below depth H . B) The surface displacement after 5 and 45 relaxation times when the density contrast at the surface is accounted for.	163
Figure 7.7:	Benchmark for fault creep on a elementary fault segment (point source) governed by a rate-strengthening rheology. The Coulomb stress is perturbed homogeneously in the computational domain at time $t = 0$ with an amplitude τ_0 . The response of the fault as predicted by our numerical model and by the analytic solution to a spring-slider model are compared for various values of the initial stress perturbation.	166
Figure 7.8:	Benchmark for time series of surface displacement due to a stress perturbation in a homogeneous poroelastic half space. A strike-slip fault -with a uniform slip of 1 m along a vertical plane 1 km long extending from the surface to a depth of 1 km- changes the pressure in the surrounding rocks. A fraction β of the pressure change is relaxed by pore-fluid diffusion. The coseismic surface displacement due to the fault slip is shown in A (left panel). B) Comparison between fully time-dependent calculations and the analytic solution for the case of full relaxation (drained condition).	169

Figure 7.9:	Efficiency diagram of the Fourier/leapfrog (black profile) and the finite difference (gray profile) integration schemes. The $k = -1$ and $k = -2$ slopes indicate the expected error reduction of second and third-order integration methods, respectively. The span of possible time steps is limited for the finite difference method due to a conditional stability condition.	171
Figure A.1:	The discretized half space. The origin of the reference system is at the center of the surface. The modeled half space dimension is $-\Delta x_1 \times sx_1/2$ to $\Delta x_1 \times (sx_1 - 1)/2$ in the x_1 direction, $-\Delta x_2 \times sx_2/2$ to $\Delta x_2 \times (sx_2 - 1)/2$ in the x_2 direction and 0 to $\Delta x_3 \times (sx_3 - 1)/2$ in the x_3 (depth) direction.	180
Figure A.2:	Geologic model of slip on a fault. The fault is described by the position of its top tip, its length in the along-strike direction, width in the down-dip direction, its strike angle and its dip angle. The rake indicates the orientation of slip.	181
Figure A.3:	Example of three-dimensional output from the program STATICU. The slip model and the associated displacement field corresponding to the 1992 Landers, CA earthquake is automatically exported in the VTK format. Here the data is visualized with the free software Paraview.	182
Figure A.4:	Example of map-view output from the program STATICU. The surface displacement field corresponding to the 1992 Landers, CA earthquake can be automatically exported in the GRD format, allowing quick visualization with the GMT mapping tool.	183
Figure B.1:	Simulation of the deformation due to a strike-slip fault in a heterogeneous lithosphere. The elastic moduli are reduced around an infinitely long compliant zone in the near field of the fault. A) sketch of the geometry of the fault and the position of the compliant zone. B) Surface displacement corresponding to the elastic structure contribution showing additional strain in the vicinity of the compliant zone, compared to a model with a homogeneous lithosphere.	188

LIST OF TABLES

Table 2.1:	Visco-elastic coefficients (η - viscosity, μ - shear modulus, ν - Poisson's ratio and τ_m Maxwell relaxation time)	17
Table 5.1:	Inferred velocity of the SCIGN continuous GPS stations before the December 2003 San Simeon earthquake. Time t (a) refers to the duration of the interval used for the linear regression. Parameters V_N , V_E , σ_N and σ_E are the North and East components of the GPS velocity and corresponding standard deviation, respectively.	88
Table 5.2:	Best Fitting parameters to the first mode of the PCA decomposition. The time series is fitted with the functional describing the impulse response of power-law creep and rate-strengthening (RS) friction. Fit parameters C , t_0 and n or k are the amplitude, the timescale and the nonlinear exponent (n for power-law and k for RS), respectively, estimated from the inversion. Misfits χ_1 and χ_2 measure the residual variance for the first two months and for the three years time series, respectively.	98
Table 6.1:	Commonly used two-dimensional Fourier transforms of three-dimensional functions. We denote $ \mathbf{k} = (k_1^2 + k_2^2)^{1/2}$ and $r = (x_1^2 + x_2^2 + x_3^2)^{1/2}$	146

ACKNOWLEDGEMENTS

My thanks go first to my advisor for providing to me a constant and consistent support. Yuri was always available for discussion and guidance. He was an invaluable mentor and model, showing rigor, fairness and temper. Especially temper. I would also like to thank all the faculty members at IGPP who contributed to my scientific education. In particular, my graduate school experience would not have been the same without the mentoring of Dave Sandwell, who inspired numerous ideas and projects I worked on. Certainly, our surfing meetings will find no equivalent. I am also grateful to Glenn Ierley for inspiring me and stimulating me scientifically and intellectually. Glenn also supported my application to the Geophysical Fluids Dynamics summer school in Woods Hole which was a peak of my graduate school experience. I am immensely obliged to Steve Constable and Hubert Staudigel for inviting me, and other students, to cruises and hikes to Hawaii. This was an amazing and unforgettable experience. I am thankful to other faculty members who, by their lectures or in informal conversations, contributed to my broader scientific literacy. I think of Bruce Bills, Yehuda Bock, Xanthippi Markenscoff, Guy Master, Neal Driscoll, Jeff Gee, Sia Nemat-Nasser, Robert Parker, Peter Shearer, Lisa Tauxe and numerous others at Scripps and UCSD. I want to thank my fellow graduate students, Deborah, Diane, Karen, Leah, Lynn, Chris, Danny, Dave, German, Joseph, Robin, Xiaopeng (and others!) for making my graduate school life more tolerable. Finally, I want to thank my Leah for showing me that everything is possible.

Chapter 2, in full, is a reprint of the material as it appears in the *Journal of Geophysical Research* 2008. Barbot, Sylvain; Hamiel Y., Fialko Y., 2008. The dissertation author was the primary investigator and author of this paper. Chapters 3 and 4, in full, are reprints of the material as it appears in the *Journal of Geophysical Research*. Barbot, Sylvain; Fialko, Y.; Sandwell, D.. The dissertation author was the primary investigator and author of these papers. Chapter 5, in full, is a reprint of the material as it appears in the *Journal of Geophysical Research* 2009. Barbot, Sylvain; Fialko, Y.; Bock, Y., 2009. The dissertation author was the primary investigator and author of this paper. Chapters 6 and 7, in full, have been submitted for publication of the material as it may appear in *Geophysical Journal International*. Barbot, Sylvain; Fialko, Y.. The dissertation author was the primary investigator and author of these papers.

VITA

- 2009 Ph. D. in Earth Sciences, University of California, San Diego
- 2007 Master in Earth Sciences, Institute of Geophysics and Planetary Physics, University of California at San Diego
- 2005 Master in Geophysics, Institut de Physique du Globe, Paris

PUBLICATIONS

- S. Barbot and Fialko Y., “Towards a Unified Representation of Postseismic Mechanisms: Semi-Analytic Models of Fault Creep, Poroelastic Rebound and Power-Law Flow”, *Journal of Geophysical Research*, submitted, 2009
- S. Barbot and Fialko Y., “Towards of unified representation of postseismic mechanisms: Semi-analytic models of poroelastic rebound, fault creep and power-law shear flow”, *Journal of Geophysical Research*, submitted, 2009
- S. Barbot, Fialko Y., Sandwell D., “Three-dimensional models of elasto-static deformation in heterogeneous media: application to the East California Shear Zone”, *Geophysical Journal International*, doi:10.1111/j.1365-246X.2009.04194.x, 2009
- E. S. Cochran, Li Y.-G., Shearer P., Barbot S., Fialko Y., Vidale J. E., “Seismic and Geodetic Evidence For Extensive, Long-Lived Fault Damage Zones”, *Geology*, v. 37, no. 4, p. 315-318, doi: 10.1130/G25306A.1, 2009
- S. Barbot, Fialko Y., Bock Y., “Postseismic Deformation due to the Mw6.0 2004 Parkfield Earthquake: Stress-Driven Creep on a Fault with Spatially Variable Rate-and-State Friction Parameters”, *Journal of Geophysical Research*, vol. 114, B07405, doi:10.1029/2008JB005748, 2009
- S. Barbot, Fialko Y., Sandwell D., “Effect of a compliant fault zone on the inferred earthquake slip distribution”, *Journal of Geophysical Research*, 113, B06404, doi:10.1029/2007JB005256, 2008
- S. Barbot, Hamiel Y., Fialko Y., “Space geodetic investigation of the coseismic and postseismic deformation due to the 2003 Mw7.2 Altai earthquake: Implications for the local lithospheric rheology”, *Journal of Geophysical Research*, Volume 113, Issue B3, CiteID B03403, doi:10.1029/2007JB005063, 2008
- S. Leprince, Barbot S., Ayoub F., Avouac J.P., “Automatic and Precise Orthorectification, Coregistration, and Subpixel Correlation of Satellite Images, Application to Ground Deformation Measurements”, *IEEE Transactions on Geoscience and Remote Sensing*, vol. 45, issue 6, pp. 1529-1558, doi:10.1109/TGRS.2006.888937, 2007

ABSTRACT OF THE DISSERTATION

Studies of Co- and Postseismic Deformation of the Lithosphere from Numerical Models and Space Geodetic Data

by

Sylvain Barbot

Doctor of Philosophy in Earth Sciences

University of California, San Diego, 2009

Professor Yuri Fialko, Chair

In this dissertation, I study the co- and postseismic deformation of the lithosphere using numerical models of three-dimensional time-dependent deformation and space geodetic data. I derive an original approach to simulate the static deformation due to faulting and volcanic unrest in a heterogeneous half space with vertical and lateral variations in elastic moduli. The method is based on a semi-analytic elastic Green function in the Fourier domain. I extend the model to include time-dependent inelastic properties of the lithosphere. This approach can be used to model time series of poroelastic rebound, viscoelastic flow and fault creep, three important mechanisms thought to participate in postseismic transients. I use kinematic inversions and forward models of deformation to infer the postseismic mechanisms responsible for the transient that followed the 2003 Altai earthquake. I find that synthetic aperture radar (SAR) data are most compatible with afterslip. The absence of an observable viscoelastic relaxation in the three years following the earthquake can be explained by an effective viscosity of the ductile substrate greater than 10^{19} Pa.s. I use numerical models of coseismic deformation to explain anomalously strained areas in the East California Shear Zone imaged by SAR line-of-sight (LOS) data in the vicinity of the 1992 Landers and 1999 Hector Mine earthquakes. I find that the enhanced strain can be explained by compliant zones (CZs) surrounding long-lived faults in the Mojave desert. The LOS data is best explained by a 50% reduction of rigidity in volumes of the order of 1-2 km thick around historical faults that extend from 5 km depth for the Calico CZ to 9 km depth for the Pinto Mountain CZ. Finally, I use kinematic inversion of GPS data and forward models to identify the location and rheology of the afterslip that followed the 2004 Parkfield earthquake. The time dependence and amplitude of GPS time series can be explained by slip on an asperity centered at 5 km depth and governed by a rate-strengthening friction with parameter $(a - b) = 7 \times 10^{-3}$, compatible with values obtained from laboratory experiment. The GPS observations show evidence of lateral variations in the frictional properties on the Parkfield segment of the San Andreas fault.

Chapter 1

Introduction

In this thesis I contribute to our understanding of the physics that governs plate tectonics and the internal deformation of the continental lithosphere. Establishing a complete physical description of the deformation mechanisms in the crust and upper mantle is a formidable task because such a model involves time and length scales that vary over several orders of magnitude and that are associated with distinct dominant processes. A goal of tectonophysics is to provide physical laws and parameters that describe the behavior of the lithospheric deformation. Field observations and laboratory experiments provide some essential constraints on rock properties and fault rheology but this approach is limited by the required extrapolation of laboratory results to *in situ* conditions and the rare possibility of direct measurements. Earthquakes and other stress perturbations in the crust provide a natural laboratory to study the physical properties of the lithosphere. Crustal deformation may be imaged by geodetic instruments, including Global Positioning System (GPS) and Synthetic Aperture Radar (SAR) and these observations compared to models of deformation. In this thesis, I use the latter approach to improve our understanding of the physical properties of the lithosphere. In particular, I use space geodetic data of co- and postseismic deformation to constrain the elastic and ductile properties of the lithosphere. My contribution is twofold. First I present original mathematical and numerical methods to evaluate models of three-dimensional deformation, including static deformation in a heterogeneous crust and time-dependent deformation due to fault creep, viscoelastic flow and poroelastic rebound (three important source mechanisms in postseismic transients). Second, I use these models as well as other state-of-the-art modeling approaches to explain geodetic measurements around the 2003 Altai earthquake, around the Parkfield segment of the San Andreas fault and in the East California Shear Zone.

The movement of plates is accommodated at the plate boundary by slip on faults and shear flow in the lower crust and upper mantle. Once a fault has been formed in the schizosphere, the distribution of slip with depth and over time is controlled by friction. Below the brittle-ductile transition, the deformation is controlled by the ductile properties of rocks. The long-term motion on a fault is constrained by large-scale tectonics forces. As the plates migrate, faults accumulate stress which is released seismically with earthquakes and aseismically with fault creep. In general the earthquake cycle can be decomposed into three periods. The longest phase, which corresponds to the earthquake recurrence interval, is referred to as the interseismic period. In this period

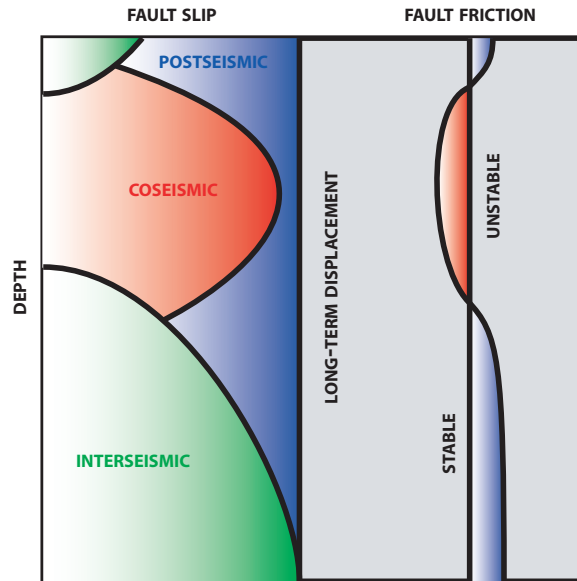


Figure 1.1: Distribution of slip on a fault plane during the earthquake cycle. Earthquake nucleation takes place in areas with unstable friction in the seismogenic zone. The stable part of a fault slips aseismically during the inter- and postseismic phases of the earthquake cycle. The seismogenic zone is delimited by the transition from stable to unstable friction.

of quiescence the unstable section of a fault is locked and is slowly loaded by regional shear and by motion on stable parts of the fault (see Figure 1.1). The coseismic period refers to the time interval required for an earthquake to nucleate, propagate and stop. The section of a fault that exhibits seismicity and where earthquakes nucleate is referred to as the seismogenic zone. The stress perturbation caused by sudden slip in the seismogenic zone can trigger an aseismic transient. In the postseismic interval, the so-called afterslip occurs on stable parts of the fault. Ideally, afterslip reduces stress asperities caused by the earthquake and restores a slip distribution compatible with long-term plate motion. The partition of fault slip into seismic and aseismic areas is controlled by the frictional properties of the fault. Unstable friction is associated with areas of seismicity and earthquake nucleation. Stable friction gives rise to (aseismic) fault creep both in the inter- and the postseismic part of the earthquake cycle. An earthquake can also be at the origin of time-dependent deformation away from the fault, triggering shear flow below the brittle-ductile transition or pore-fluid readjustments in the crust.

The co-, post- and interseismic phases of the earthquake cycle are characterized by a distinct signature in geodetic measurements of surface deformation (see Figure 1.2). On one hand, in the interseismic interval, the spatial distribution of strain has large wavelength corresponding to the plate margin. On the other hand, in the coseismic interval, the deformation only surrounds the near field of the fault. The wavelength of a postseismic transient depends on the source mechanism. In case of viscoelastic relaxation, it is controlled by the depths of the brittle-ductile

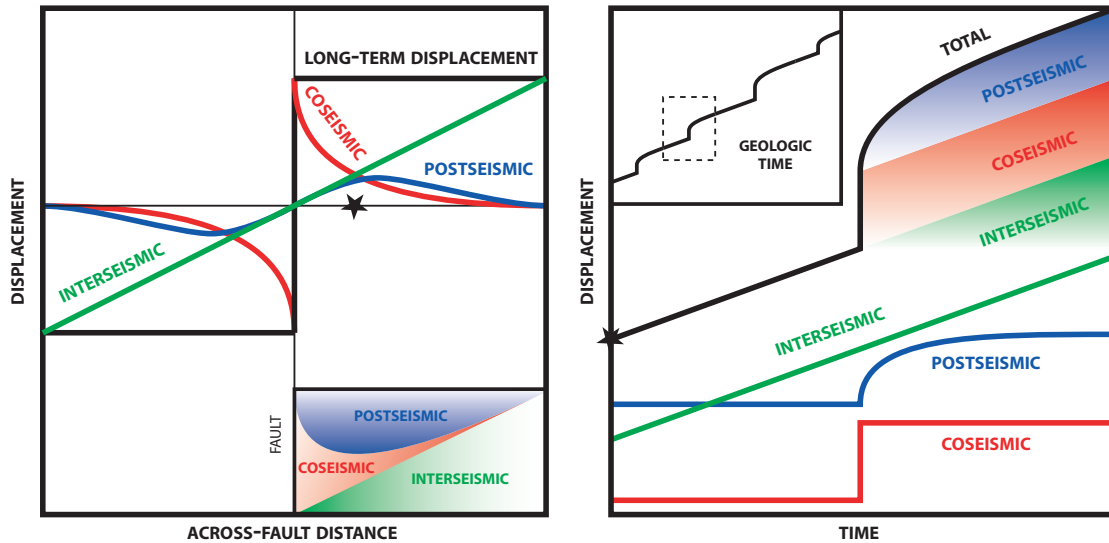


Figure 1.2: Sketch of the partition of long-term surface displacement into parts of the earthquake cycle. Left panel: the spatial distribution of surface displacement as a function of distance from a fault. The interseismic period (green) is characterized by a regional length scale. The coseismic deformation (red) is highest near the fault and decays with across-fault distance. The postseismic transient (blue) occurs around the fault and its length scale depends on the particular source mechanism. Right panel: the time dependence of surface displacements as a function of position in the earthquake cycle. In the interseismic period, a point off the fault (black star) slowly moves in the direction of plate motion. As an earthquake happens, the point is suddenly displaced. A transient displacement occurs in the postseismic period.

transition. Afterslip can occur at deep and shallow depth depending on the details of the coseismic rupture. The spatial extent of a poroelastic rebound is controlled by the linear dimension of the coseismic rupture. Observations of the spatial distribution and the temporal variations of surface displacements can be used to decipher the elastic and ductile properties of the lithosphere.

My dissertation is organized in the following way. Chapter 2 is a study of the coseismic and postseismic deformation due to the 2003 Mw 7.2 Altai earthquake. I use InSAR data to infer a coseismic slip distribution and to model three years of postseismic deformation. I compare the geodetic data to simulations of postseismic relaxation in the lower crust and upper mantle and to models of poroelastic rebound. I infer the spatial distribution of afterslip that can explain the radar observations. In Chapter 3, I describe the effect of compliant zones, finite crustal areas of reduced rigidity, on the inferred fault slip distribution. I present a method to simulate two-dimensional anti-plane deformation due to faulting in a heterogeneous crust. In Chapter 4, I extend the model to three-dimensional deformation due to finite faults in a semi-infinite half space in the presence of inclusions of finite size. Models can include lateral and vertical variations in elastic properties. I apply the method to explain observations of compliant zones in the East California Shear Zone in California: I compare deformation models to InSAR line-of-sight data to constrain the geometry and the elastic contrast that characterize the surroundings of

historical faults. In Chapter 5, I study the coseismic and postseismic deformation due to the 2004 Mw 6.0 Parkfield, CA earthquake. I use an array of 14 continuous GPS stations to constrain the kinematics of coseismic and postseismic slip on the Parkfield section of the San Andreas fault. I use stress-driven models of fault creep to infer the frictional properties of a stable asperity that is responsible for most afterslip. The postseismic relaxation that followed the 2004 Parkfield earthquake revealed a segment of the San Andreas fault with lateral and vertical variations in frictional properties. In Chapter 6, I present a semi-analytic method to simulate static deformation in a three-dimensional half space in the presence of a surface density contrast due to faulting or volcanic unrest. In Chapter 7, I develop an unified approach to simulate time-dependent deformation due to viscoelastic flow, aseismic fault creep and poroelasticity. The appendices describe the usage and the internal organization of three Fortran 90 programs that evaluate three-dimensional deformation in a half space with a free surface and a density contrast. In Appendix A, I explain how to use the Fortran program `STATICU` which evaluates the elastostatic deformation in a homogeneous elastic half space due to faults, dykes and Mogi sources of arbitrary orientation and position. The program `STATICU` implements the Fourier-domain elastic Green function which is at the root of other deformation calculations. In Appendix B, I describe the nuts and bolts of the Fortran 90 program `STATICI` which evaluates three-dimensional deformation in a heterogeneous elastic half space. Possible calculations with `STATICI` include models of deformation with vertical variations in elastic properties including the presence of finite inclusions. Finally, Appendix C describes the details of the Fortran 90 program `RELAX`, which performs simulations of the time-dependent relaxation that follows a stress perturbation due to fault creep and viscoelastic shear flow.

Chapter 2

Space geodetic investigation of the co- and post-seismic deformation due to the 2003 M_w 7.2 Altai earthquake: Implications for the local lithospheric rheology

Sylvain Barbot, Yariv Hamiel and Yuri Fialko

Abstract. We use ENVISAT Advanced Synthetic Aperture Radar data and SPOT optical imagery to investigate the co-seismic and post-seismic deformation due to the September 27th 2003, M_w 7.2 Altai earthquake, which occurred in the Chuya Basin near the Russia-China-Mongolia border. Based on the SAR and SPOT data, we determined the rupture location and developed a co-seismic slip model for the Altai earthquake. The inferred rupture location is in a good agreement with field observations, and the geodetic moment from our slip model is consistent with the seismic moment determined from the tele-seismic data. While the epicentral area of the Altai earthquake is not optimal for radar interferometry (in particular, due to temporal decorrelation), we were able to detect a transient signal over a time period of 3 years following the earthquake. The signal is robust in that it allows us to discriminate among several commonly assumed mechanisms of post-seismic relaxation. We find that the post-earthquake InSAR data do not warrant poro-elastic rebound in the upper crust. The observed deformation also disagrees with linear visco-elastic relaxation in the upper mantle or lower crust, giving rise to a lower bound on the dynamic viscosity of the lower crust of the order of 10^{19} Pa.s. The data can be explained in terms of fault slip within the seismogenic zone, on the periphery of areas with high co-seismic slip. Most of the post-seismic deformation can be explained in terms of seismic moment release in aftershocks; some shallow slip may have also occurred aseismically. Therefore, the observed post-seismic deformation due to the Altai earthquake is qualitatively different from deformation due to other similar-size earthquakes, in particular, the Landers and Hector Mine earthquakes in the Mojave desert, southern California. The observed variations in the deformation pattern may be indicative of different rheologic structure of the continental lithosphere in different tectonically active areas.

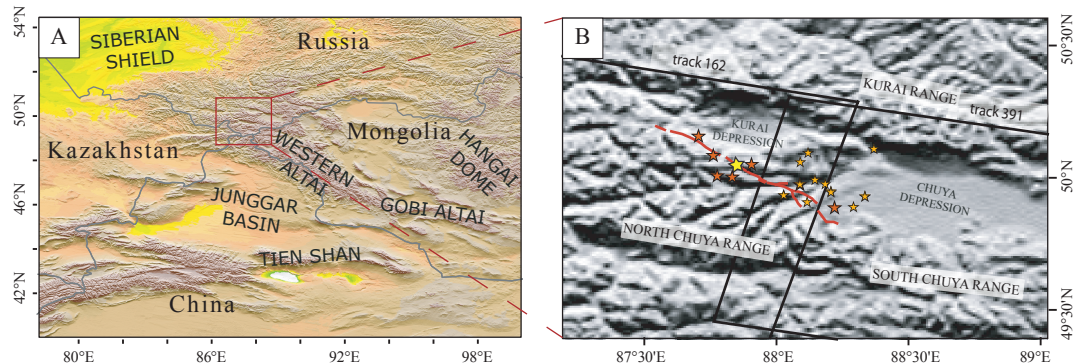


Figure 2.1: Location of the September 27th 2003, M_w 7.2 Altai earthquake, near the Russia-China-Mongolia border. a) Major geologic structures on the regional scale. b) Location of the epicenter (yellow star), with the following days $M_w \geq 6$ aftershocks (red stars). The black frames indicate the radar swath of ENVISAT tracks 434 and 391. Orange stars indicate aftershocks of M_w 5 and above after 2003/12/22.

2.1 Introduction

On September 27th 2003, a M_w 7.2 right-lateral strike-slip earthquake occurred in the Chuya Basin in the mountainous Altai region, near the Russia-China-Mongolia border (fig. 2.1). In the following few days, the Altai earthquake generated a robust sequence of aftershocks with moment magnitudes up to M_w 6.6 [Ekström et al., 2005, Nissen et al., 2007]. The M_w 7.2 mainshock is the largest earthquake in seventy years to occur in the Altai range, since the right lateral strike-slip M_w 7.9 Fu-Yun earthquake which struck the northeastern Junggar basin in 1931.

The Altai intraplate mountain ranges stretch from southwestern Siberia to the Gobi desert over a length of 1700 km. The tectonically active Altai ranges formed in the late Cenozoic in response to a northeast compression coming from the India-Eurasia collision 2000 km to the South [Tapponier and Molnar, 1979] and to a radial extension due to the warm, buoyant Hangay Dome area in central Mongolia to the East [Cunningham, 1998]. The Altai region is kinematically separate from the Hangay Dome, with a colder lithosphere and a greater elastic thickness [Windley and Allen, 1993, Bayasgalan et al., 2005]. The Altai orogen includes two distinct mountain belts: the right-lateral transpressive Western (or Mongolian) Altai and the left-lateral transpressive Gobi Altai. The Western Altai is dominated by a regional N-S shortening and N-NW trending right-lateral strike-slip faults that terminate in NW trending thrust faults [Cunningham, 2005]. In the Gobi Altai domain, these stresses are accommodated by transpressive, E-W, left-lateral strike-slip faults with inter-seismic slip rates of the order of 1 mm/yr, as constrained by GPS observations [Calais et al., 2003].

Large earthquakes are usually followed by transient surface deformation with velocities that exceed those for inter-seismic deformation. Such deformation transients present an opportunity to improve our understanding of the physical processes involved in crustal and upper mantle deformation. The instantaneous deformation field accompanying an earthquake can be explained assuming linear elastic deformation of the ambient rocks [Fialko, 2004a, Fialko et al., 2005]. Transient strains are systematically observed in years to decades following large earthquakes [Stein and Lisowski, 1983, Reilinger, 1986, Thatcher, 1983, Kenner and Segall, 2000], yet there is no consensus regarding constitutive laws that govern the mechanical time-dependent processes in the post-seismic epoch.

Several mechanisms have been proposed to explain the post-seismic transient deformation. One mechanism often invoked to explain post-seismic transients is afterslip on the ruptured fault or its extension. Evidence for afterslip is provided by kinematic inversions of geodetic data [Savage et al., 1994, Fialko, 2004b, Freed et al., 2006], although different physical explanations can be invoked to describe the process dynamics [Tse and Rice, 1986, Dieterich, 1987, Fialko, 2004b, Perfettini and Avouac, 2004]. Another commonly considered mechanism is the aseismic visco-elastic relaxation in the lower crust and upper mantle. The possibly ductile lower crust and upper mantle might not be able to sustain increases in deviatoric stresses due to the main shock. The co-seismically induced change in the deviatoric stress below the brittle-ductile transition might be relieved by viscous flow [Nur and Mavko, 1974, Pollitz, 1997, Deng et al., 1999]. If the viscous deformation is involved in post-seismic transients, observations indicate that simple linear visco-elastic models are inadequate. In particular, the latter fail to explain the temporal and spatial characteristics of deformation transients following the Mojave desert earthquakes, suggesting that multiple relaxation times and/or stress-dependent viscosities may be necessary [Pollitz, 2003b, Fialko, 2004b, Freed and Bürgmann, 2004]. Third suggested mechanism is the poro-elastic rebound of the upper crust [Reid, 1910]. For example, the post-seismic transient following the 1992 Landers earthquake has been explained by a combination of poro-elasticity above the brittle-ductile transition and a localized shear on the deep part of the fault [Peltzer et al., 1998, Fialko, 2004b]. Probably the best documented example of poro-elastic rebound is the one that occurred in the first few months following two June 2000 earthquakes in South Iceland: Jonsson et al. [2003] demonstrated that both surface deformation and water-level changes in geothermal wells are consistent with the pore pressure diffusion in response to the co-seismic stress changes.

In this study, we compare the predictions of each candidate mechanism to a set of interferometric data covering three years of post-seismic deformation following the 2003 Altai earthquake. In Section 2, we describe the co-seismic rupture, as constrained by SAR amplitude cross-correlation, azimuthal interferometry and SPOT optical image cross-correlation. In section 3, we present the interferometric data characterizing the post-seismic deformation and compare them to predictions of the afterslip, visco-elastic and poro-elastic models. Finally, we

discuss the implications from these results for the mechanical properties of the Altai lithosphere and variations in rheology among different tectonically active environments.

2.2 Co-seismic analysis

2.2.1 Determination of the fault location

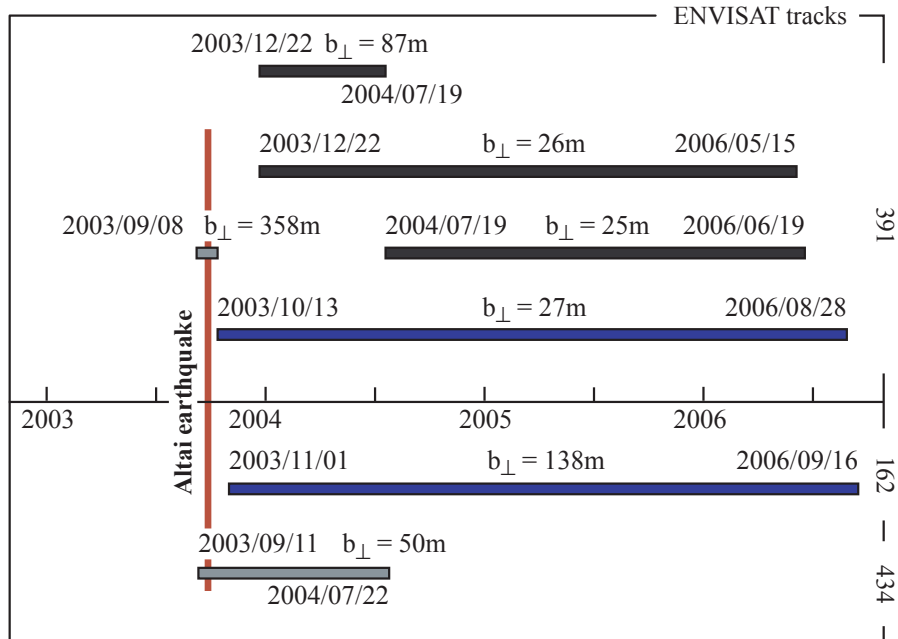


Figure 2.2: Co-seismic and post-seismic interferograms used in this study. The (grey) co-seismic interferograms were jointly used to invert for the co-seismic slip on the fault. The 3 year (blue) pairs were simultaneously inverted for afterslip. Other (black) pairs are used to verify the early stage of the post-seismic transient approximately 6 months, 2 years and 2.5 years after Altai earthquake.

The Altai earthquake struck the northern part of the Western Altai. The 70 km long rupture cut through the Chuya Range immediately SW of the Kurai and Chuya depressions [Nissen et al., 2007]. Due to the remote location of the earthquake, few ground-based observations are available. We investigated the earthquake rupture using space geodetic data. The co-seismic deformation was captured by several independent ENVISAT SAR pairs. Figure 2.2 shows interferograms from ENVISAT track 391, spanning a time interval between 2003/09/08 and 2003/10/13, and from track 434, spanning a time interval between 2003/09/11 and 2004/07/22. Unfortunately, the interferometric SAR (InSAR) coherence is poor in the near-field and to the South of the rup-

ture due to temporal decorrelation [Zebker and Villasenor, 1992] in the Chuya Range, so we could not use the radar line-of-sight phase information to determine the fault location. We found Along-track InSAR data [Bechor and Zebker, 2006] to be more useful for this purpose, the along-track interferometry being less sensitive to temporal decorrelation. The along-track interferogram exploits a parallax effect to detect the surface displacement in the azimuthal (along-track) direction. The along-track interferometry is a high-resolution phase measurement equivalent to the azimuthal offsets [Michel et al., 1999, Peltzer et al., 1999, Fialko et al., 2001b]. The details of our implementation of the along-track interferometry are given in Appendix 2.6. We processed the raw SAR data using the ROI-PAC software [Rosen et al., 2000] that was modified to compute the along-track interferograms. In our experience, successful along-track interferometry requires baselines that are a factor of two smaller than those required for the convention radar LOS interferometry. Given the relatively large baselines of the co-seismic SAR data for Altai, the along-track interferogram is affected by the baseline decorrelation. A displacement contrast is visible across the fault, but the measurement is complicated by the WNW-ESE fault orientation, almost normal to the satellite track. The range offset data are less sensitive to changes in the reflective properties of the ground compared to the radar phase (LOS) data, and therefore provide useful information on displacements near the fault trace, given the favorable fault orientation along the radar range. We also analyzed SPOT5 panchromatic optical images [Van Puymbroeck et al., 2000]. We used the cross-correlation software COSI-Corr [Leprince et al., 2007] to compute the deformation that occurred between two acquisitions bracketing the earthquake (2003/09/09-2004/01/17, frame K215-J249). This approach allows one to measure horizontal displacements with an accuracy up to 5 cm, in the E-W and N-S directions. The inferred signal in the E-W displacement component reveals a discontinuity consistent with the right-lateral strike-slip motion. The N-S component of the SPOT cross-correlation shows no significant displacement contrast across the fault and is not shown here. The SPOT data alone do not provide a precise fault location presumably due to temporal decorrelation and non-optimal orbital baseline.

Our simplified fault geometry (see thick black line in fig. 2.3) consists of six rectangular segments, rotating from an almost NE-SW strike in the westernmost section to a NNE-SSW strike in the middle section, west of the Chuya depression. We also identified a short SW-NE striking segment at the southern tip of the rupture based on the SAR offset data. The latter segment probably corresponds to a M_w 6.6 sub-event that occurred several hours after the main shock near the Chuya basin. Our estimation of the fault location, based on space geodetic data, agrees well with the field mapping of Nissen et al. [2007] (red profile in fig. 2.3).

2.2.2 Inversion for co-seismic model

To investigate the deformation due to the Altai earthquake, we begin by deriving the static rupture model. The co-seismic slip model plays an important role in studies of post-

seismic relaxation as it provides the initial condition exciting the time-dependent response of the lithosphere. Observed co-seismic deformation can often be explained by simple models based on solutions for dislocations in an elastic half-space [Massonnet et al., 1993, Fialko et al., 2001b, 2005, Hamiel and Fialko, 2007]. Solutions for surface displacements due to dislocations in elastic half-space are readily available for both homogeneous [Okada, 1985] and layered media [Wang et al., 2003]. As the velocity structure of the Earth’s crust in the Western Altai area is poorly known, we assume a homogeneous half-space with a Poisson’s ratio of $\nu = 0.25$. Previous work has shown that reasonable variations in the elastic moduli with depth have only moderate effect on the inferred slip models [Zhu and Rivera, 2002, Simons et al., 2002, Fialko, 2004a, Hamiel and Fialko, 2007].

Our slip model for the Altai earthquake was obtained from the inversion of SAR line-of-sight data, using a three-dimensional elastic half-space solution [Okada, 1985]. We extended the six segments down to a depth of 21 km and discretized each segment into 2×3 km patches in the strike and dip direction respectively. Each individual patch is allowed to slip in the strike and dip directions. The inversion for slip on the fault involves a regularized least-squares optimization. The residuals between the computed surface displacements, projected onto the LOS direction, and the measured SAR LOS displacements are minimized through an iterative procedure. The added regularization constraint is covariance between neighboring fault elements and no slip at the bottom and sides of the fault. Details on the data reduction and the inversion procedure can be found in Fialko [2004a]. We inverted simultaneously the ENVISAT pairs 2003/09/08-2003/10/13, track 391 and 2003/09/11-2004/07/22, track 434 (fig. 2.4) because the fault extends across multiple satellite tracks. The inclusion of track 434 data was needed to constrain slip on the western part of the fault. There are some discrepancies between the estimated focal mechanisms of the main shock and the first large aftershocks. The Sept. 27th, 2003 main shock was a sub-vertical right-lateral event which dip angle was estimated between 71° [Ekström et al., 2005] and 82° [Nissen et al., 2007]. We estimated the dip angle of each segment by performing a grid search between 60° and 120° and identifying the smallest misfit with the SAR LOS observations. We found that quite different dip angles along the fault gave rise to similar misfits. As the coherence is poor in the near field and south of the fault (fig. 2.4), the InSAR LOS data alone are not sufficient to constrain the fault dip angle. We performed a similar grid search for the best fitting dip angle for each segment, inverting pixel tracking data (range and azimuthal offsets), which are less affected by decorrelation near the fault trace. The best fitting model gave rise to segment orientation of less than 5° from the vertical. Inversions of InSAR phase and pixel offsets (both individually and jointly) gave rise to systematic residuals in the azimuthal offsets near the fault kink. We attempted to constrain the dip angles required by the azimuthal InSAR data. The required dip angles for each segment were also sub-vertical but oriented to the South, that is, opposite to those inferred from range offsets or phase change. As the vertical fault model was within the family of models giving the best variance reduction, we assumed that all fault

segments are vertical (fig. 2.4c). The residuals from range offsets (fig. 2.4e) reveal a zone of deformation to the South of the rupture that cannot be explained by slip on the fault plane as residuals appear on both sides of the fault. Azimuth offsets exhibit some asymmetry across the fault, which might be indicative of either dipping rupture, or deviations from the assumption of a laterally homogeneous elastic half-space.

The co-seismic slip model shows three patches of relatively high slip, which correspond to the main rupture and the immediate large aftershocks. The second segment from the eastern end of the rupture has a total seismic moment of $M_w = 6.7$, which agrees with the moment magnitude of a thrusting event that occurred several hours after the earthquake as estimated by Ekström et al. [2005]. This aftershock is located at the edge of the Chuya basin, in agreement with the relocation of Nissen et al. [2007]. According to our slip model, the maximum surface offsets are less than 4 m. Most of the slip occurs at relatively shallow depths, from the surface to about 9 km depth. The western section of the fault slip model shows about 1 m slip at greater depth, but is relatively poorly constrained by the SAR data. According to our slip model the total seismic moment is $M_0 = 4.8 \times 10^{19}$ N m (corresponding to a moment magnitude $M_w=7.1$), in fair agreement with the estimated moment derived from broadband tele-seismic data $M_w = 7.2$ [Ekström et al., 2005]. It should be noted that we invert for the total slip that occurred co-seismically and during the first 16 days following the mainshock. The corresponding forward model (fig. 2.4b), projected onto the LOS direction (positive towards the satellite), is qualitatively consistent with the co-seismic model of Nissen et al. [2007].

2.3 Post-seismic deformation

2.3.1 Inversion for afterslip model

We used SAR LOS interferometry to look at the post-seismic transients. We processed the available ENVISAT data from tracks 391 and 162 (fig. 2.2) and identified the LOS displacements common to all interferograms within the three year transient following the earthquake. The post-seismic interferograms clearly show strain accumulation at the southern tip of the fault, in the Chuya basin (fig. 2.5). The positive LOS displacements at the southern tip of the rupture are not due to tropospheric noise [Tarayre and Massonnet, 1996], as the signal appears in 4 independent interferograms. The observed post-seismic signal is localized close to the fault, with wavelengths much smaller than the fault length but of the order of the fault locking depth (5-10 km). Note that the near-field LOS post-seismic displacements have the same sign as the co-seismic ones.

The wavelength of the post-seismic transient and the polarity of the LOS displacements appear to favor a shallow slip on the earthquake rupture. We carried out a kinematic inversion for the post-seismic slip using two 3 year interferograms (2003/10/13-2006/08/28, track 391

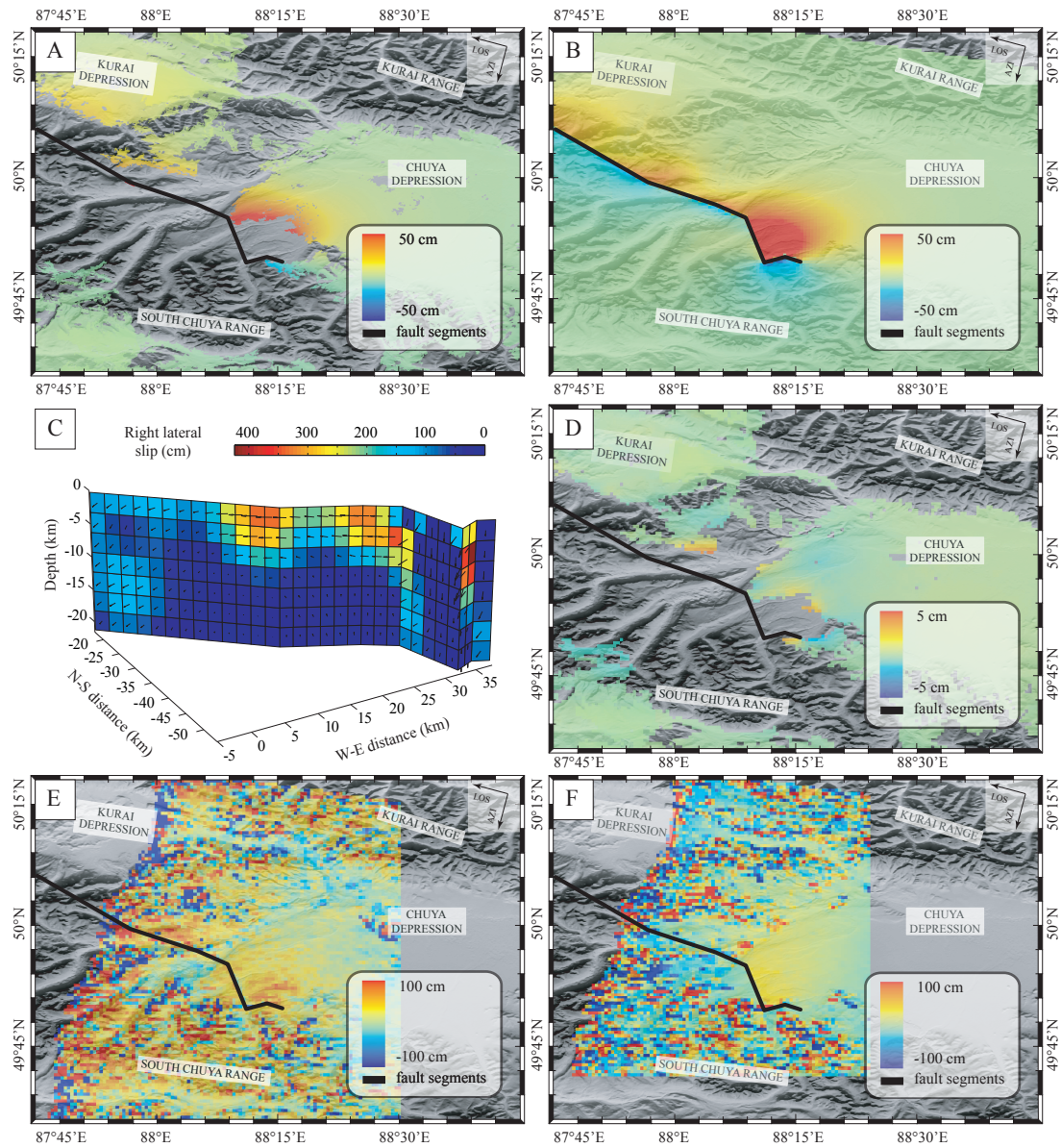


Figure 2.3: Co-seismic slip Inversion. (a) Interferograms (2003/09/08-2003/10/13, track 391 and 2003/09/11-2004/07/22, track 434) used to invert for a co-seismic slip model. (b) Model co-seismic LOS displacements. (c) Co-seismic slip distribution obtained after inversion of LOS displacements of the 2 interferograms in (a). The black arrows indicate the direction and amplitude of slip for every patch. (d) LOS displacement residuals after inversion. (e) Range offsets residuals. (f) Azimuthal offsets residuals.

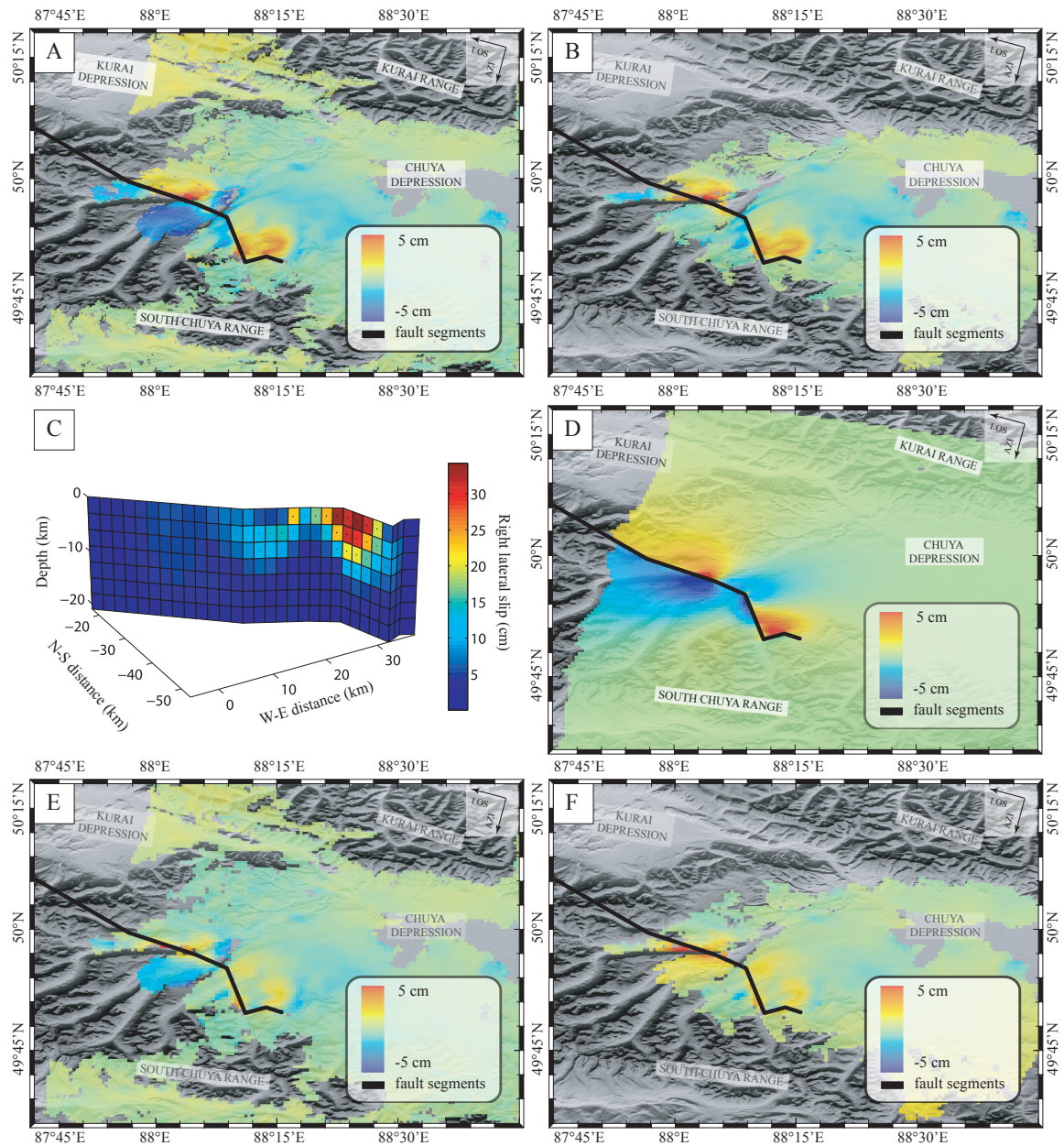


Figure 2.4: Post-seismic interferograms and inversion for the afterslip model. (a) Interferogram 2003/10/13-2006/08/28, track 391 showing 3 years of post-seismic deformation, projected in the LOS direction. (b) Interferogram 2003/11/01-2006/09/16, track 162, showing also 3 years of post-seismic deformation. (c) Afterslip model showing a slip distribution confined in the seismogenic zone. (d) Forward model, fitting the two 3 year interferograms. (e-f) Residuals on interferograms (a) and (b) respectively.

and 2003/11/01-2006/09/16, track 162). As the 3 year interferograms have a somewhat different spatial coverage, we performed a joint inversion, simultaneously minimizing the residuals between both interferograms and our model. The joint inversion allows us to reduce the tropospheric contribution of each interferogram. We used the same homogenous half-space model and fault model as in the co-seismic inversion. We initially performed the inversion allowing for slip on a deeper extension of the fault but such an inversion did not require any slip at depth greater than 21 km. Consequently, we chose a fault geometry that is the same as the co-seismic one in order to facilitate the model comparison (fig. 2.5c). In our best fitting model, most of the post-seismic slip occurs in the seismogenic zone, mainly above 6 km depth. The slip amplitude and depth of the inferred slip model are robust to perturbations in dip angles, as verified by inversions with variable dip angles on each segment, due to the short wavelength of the surface deformation. The maximum slip occurred on the third segment from the eastern end of the fault, in the middle of two relatively high co-seismic slip patches. The residuals of the inversion (fig. 2.5e-f) are concentrated in the North Chuya Range, in the middle section of the fault trace. Apart from these localized residuals, the bulk of the post-seismic SAR data is well explained by the afterslip model. This suggests that most of the post-seismic LOS displacements may represent slip (seismic or aseismic) on parts of the fault in the nominal seismogenic depth interval.

2.3.2 Poro-elastic rebound

The occurrence of a large earthquake alters the pore pressure in the crust close to the rupture. The induced volumetric strain can create significant pore pressure gradients that are relaxed by the movement of fluids following favorably the paths of maximum permeability in the host rocks. The coupling between the pore fluid diffusion and the effective elastic properties introduces a time-dependence into the response of the solid matrix [Reid, 1910, Biot, 1941, Coussy, 2004]. Fluids are usually assumed to be pervasive in the Earth's crust, so the poro-elastic rebound is a likely physical mechanism contributing to the post-seismic deformation. Based on theoretical arguments, pore fluid diffusion should occur at intermediate wavelengths from near-field to about 2.5 fault lengths from the fault [Piombo et al., 2005], and the co-seismic stress changes should be significantly altered on a timescale controlled by the hydraulic diffusion. The pore pressure readjustment was estimated to be several years long in case of the Landers earthquake [Peltzer et al., 1998, Fialko, 2004b], but only a few months long in case of the 2000 South Iceland earthquakes [Jonsson et al., 2003]. Radar interferometry is highly sensitive to the vertical component of the deformation field and is therefore well suited to detect poro-elastic rebound [e.g., Peltzer et al., 1998]. As the pore pressure dissipates, owing to the fluid diffusion, there is a gradual change of Poisson's ratio in the crustal rocks from the undrained conditions immediately after the earthquake to the lower, drained, values [Peltzer et al., 1998, Biot, 1941, Coussy, 2004]. We compute surface displacements corresponding to complete fluid diffusion by

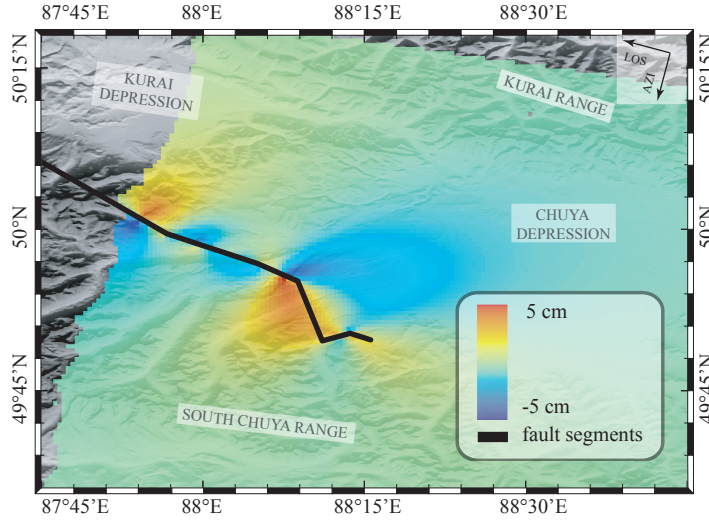


Figure 2.5: Predictions of the full poro-elastic rebound following Altai earthquake. The model is obtained by differentiating the two elastic responses of the crust with an undrained Poisson’s ratio $\nu_u = 0.25$ and with a drained Poisson’s ratio $\nu_d = 0.20$.

choosing the average value of the drained Poisson’s ratio $\nu_d = 0.20$. The prediction of the post-seismic transient (the difference between the drained and undrained states), projected in the LOS direction, is shown in fig. 2.6. The poro-elastic rebound model agrees relatively well with the 2003/10/13-2006/08/28 interferogram (fig. 2.5a) in the North Chuya Range, in the South side of the fault’s mid-section. At this location, however, the afterslip model and the poro-elastic model predict the same polarity of line-of-sight displacements. The LOS displacement in the South Chuya Range and the Chuya Basin, where both InSAR observations are consistent, is essentially opposite to the poro-elastic model (fig. 2.5a-b). The poro-elastic rebound of the upper crust therefore cannot explain the InSAR data. Analysis of interferograms spanning 1 yr of post-seismic deformation (see fig. 2.8) showed that the surface displacements had the same polarity during the observation period, suggesting that no significant poro-elastic rebound occurred in the three years following the Altai earthquake.

2.3.3 Visco-elastic relaxation

We also investigated a possibility of a visco-elastic response of the Altai lithosphere. The visco-elastic relaxation can explain a variety of observations from laboratory experiments [e.g., Karato and Wu, 1993] to large scale lithospheric rebounds [Thatcher and Rundle, 1979, Peltier, 1981]. High-temperature, high-pressure creep experiments suggest that the effective viscosity is controlled by the thermal properties of the lithosphere and the stress to which it is subjected [e.g.,

Table 2.1: Visco-elastic coefficients (η - viscosity, μ - shear modulus, ν - Poisson's ratio and τ_m Maxwell relaxation time)

	elastic moduli	weak mantle	weak lower-crust	jelly sandwich
UC	$\mu = 28 \text{ GPa}$ $\nu = 0.28$	elastic	elastic	elastic
LC	$\mu = 45 \text{ GPa}$ $\nu = 0.26$	$\eta = 10^{21} \text{ Pa s}$ $\tau_m = 350 \text{ yr}$	$\eta = 2 \cdot 10^{18} \text{ Pa s}$ $\tau_m = 0.7 \text{ yr}$	
UM	$\mu = 69 \text{ GPa}$ $\nu = 0.28$	$\eta = 2 \cdot 10^{18} \text{ Pa s}$ $\tau_m = 0.7 \text{ yr}$	$\eta = 10^{18} \text{ Pa s}$ $\tau_m = 0.3 \text{ yr}$	$\eta = 10^{25} \text{ Pa s}$ $\tau_m = 3 \text{ Myr}$

The upper crust (UC) extends from the surface to 15 km; the lower crust (LC) extends from 15 km to the upper mantle (UM) at 35 km.

Larsen et al., 1996, Gasperini et al., 2004]. A higher geotherm implies a weaker lower crust and a faster viscous relaxation. A direct way of characterizing properties of the ductile substrate is to infer its viscosity structure from the transient response to the co-seismic excitation. Little is known about the effective rheology of the lower crust and upper mantle in the Altai area. Previous studies in other tectonic environments have considered Maxwellian materials [Pollitz et al., 2000, Fialko, 2004b, Freed et al., 2006], standard linear solids [Pollitz et al., 2000], bilinear solids [Pollitz, 2003b] and nonlinear power-law rheologies [Freed and Bürgmann, 2004]. As we have little information on the structure of the lithosphere in the Mongolian Altai, we used a simplified, vertically stratified model with a Maxwellian visco-elastic body. We have tested three end-member rheologic models, having a different shear viscosity structure, all elastic parameters being otherwise the same (Table 2.1). All models have in common an elastic upper crust down to a depth of 15 km. Variations in the rheologic structure give rise to distinct wavelengths and timescales in the time-dependent response at the Earth's surface. We performed simulations of the visco-elastic relaxation due to the Altai earthquake using the approach developed by Wang et al. [2006] for a layered visco-elastic Earth model in the presence of gravity. In these simulations, we used our co-seismic slip model (fig. 2.4c) and the rheologic parameters shown in Table 2.1.

We computed the entire time series of the post-seismic transient and then simulated the SAR data (2003/10/13-2006/08/28) by computing the difference between the surface deformation corresponding to the SAR acquisition dates, projected onto the satellite LOS. The resulting surface displacements are shown in fig. 2.7. The jelly-sandwich model [Brace and Kohlstedt, 1980] and the weak lower-crust model produce very similar results for any value of the upper-mantle viscosity in the range $\eta = 10^{18} - 10^{25} \text{ Pa.s}$. This indicates that the post-seismic deformation we observe at the surface is not sensitive to variations in rheology at depths greater than 35 km (about 4 fault depths). The weak lower-crust rheology yields a deformation with wavelengths comparable to the thickness of the elastic upper crust, whereas the weak mantle rheology gives a

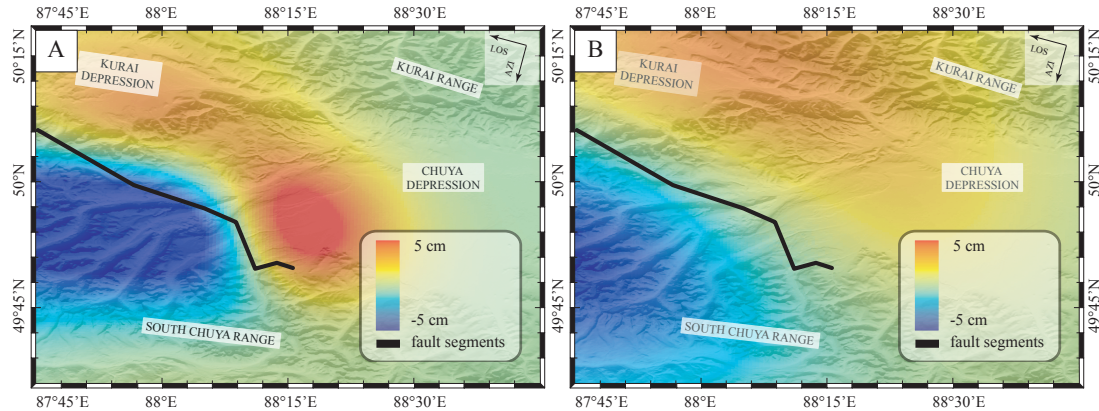


Figure 2.6: Simulated LOS displacement for 3 years of visco-elastic relaxation occurring between 2003/10/13 and 2006/08/28. (a) Weak lower crust or jelly-sandwich rheology. (b) Deformation due to a flow in a weak mantle. Note the larger wavelength of the deformation.

surface deformation with a larger wavelength, of the order of the Moho depth. This illustrates the self-similar behavior of the solution with a wavelength depending upon the relaxation depth and the deformation magnitude controlled by the length of the earthquake. None of the visco-elastic simulations show a strain accumulation as close to the fault as seen in the SAR data. The SAR observations therefore appear to rule out the viscous relaxation as a significant contributor to the post-seismic transient on the timescale of three years at depths shallower than 35 km.

2.4 Discussion

The 3-year post-seismic transient following Altai earthquake shows a localized deformation at the southernmost part of the fault, in the Chuya basin. This deformation is not consistent with the visco-elastic relaxation in the lower crust or upper mantle as the predicted deformation would have a larger wavelength (fig. 2.7). In the weak lower-crust model, the surface deformation is not sensitive to the value of the shear viscosity in the upper mantle, provided that the latter has a relaxation time greater than a few years. These results are consistent with our expectation that the bulk of the surface deformation is controlled by the most inviscid layer. The available data do not have the spatial and temporal coverage to constrain deep viscous flow that might occur in the upper mantle. However, any rapid viscous flow in the lower crust would yield a deformation field with a wavelength well within the detection limit of our SAR images. Therefore, we can put a lower bound on the effective shear viscosity of the lower crust in the Western Altai of $\eta \geq 10^{19}$ Pa.s. This result is consistent with other estimates of the thickness of the brittle layer. The strength of the lithosphere, as constrained by gravity measurements in the Western Altai, is believed to reside in the seismogenic layer, which spans the entire crust [Bayasgalan et al.,

2005]. Measurements of heat flux were interpreted as indicating that the effective thickness of the lithosphere in the Mongolian Altai is 55 km [Windley and Allen, 1993]. While the shallow location of the seismic rupture may not be able to excite significant visco-elastic response in the deep ductile substrate, a longer period of observations of the post-seismic deformation might nevertheless better constrain the visco-elastic properties of the lower crust.

The polarity of the LOS displacement shows that the poro-elastic rebound of the upper crust cannot explain the observed transient, as evidenced by the anti-correlation between the simulated poro-elastic interferogram and the InSAR data (fig. 2.6). The sense of motion in the LOS direction is essentially the same over 6 months and 3 years after the earthquake, as inferred from the corresponding InSAR data (pairs denoted by black lines in fig. 2.2 and shown in fig. 2.8). This is indicative of either very small effective fluid diffusivity, or absence of pore fluids in the upper crust in the Chuya Range and basin. This is somewhat surprising, given that poro-elastic rebound was previously inferred in quite diverse tectonic environments [Jonsson et al., 2003, Fialko, 2004b, Freed et al., 2006]. For example, in areas as arid as the Mojave Desert, the fluid diffusion was proposed to be a dominant contribution of the post-seismic transient imaged by InSAR during several years following the Landers earthquake [Peltzer et al., 1998, Fialko, 2004b].

The 3 years of post-seismic deformation following the Altai earthquake are best explained by shallow slip in the seismogenic zone. One possible interpretation of such slip is that the latter occurs in response to a stress concentration on the periphery of large co-seismic slip areas. Accelerated motion on a deep extension of the fault may occur aseismically, representing either velocity strengthening behavior or viscous-like deformation within a localized subvertical shear zone in the middle and lower crust [Fialko, 2004b]. Another possibility is that the observed deformation results from stick-slip motion in the brittle layer [Dieterich, 1994, Perfettini and Avouac, 2007]. Our inversions indicate that the geodetic moment released during three years of post-seismic transient was $M_0 = 2.32 \times 10^{18}$ N m (assuming a shear modulus of 33 GPa), which is comparable to a cumulative moment of aftershocks derived from long-period body wave and surface wave data, $M_0 = 1.51 \times 10^{18}$ N m [Ekström et al., 2005]. Some of the aftershocks may not have occurred on the 2003 Altai rupture, so the latter estimate should be considered an upper bound. Given the uncertainty ($\sim 0.1^\circ$) in the tele-seismically recorded event locations, there is permissive, but not conclusive evidence that most of the aftershock activity is concentrated on the fault that produced the mainshock. We minimized a potential bias by summing the seismic moment of aftershocks having magnitude 4 and above, 20 km from the epicenter, a distance corresponding to twice the location standard deviation, and verified that the temporal distribution of selected events follows Omori's law. The corresponding aftershocks of magnitude 5 and above are shown in fig 2.1. Note that the estimate of the epicenter location was bias by about 20 km so a similar error can be expected for aftershocks. Fig. 2.8 shows the cumulative seismic moment released from Oct. 13, 2003, date of the first available post-seismic InSAR data. Interferogram 2004/07/19-2003/12/22 spans a time interval about three times smaller than interferogram

2006/06/19-2004/07/19, yet exhibits comparable LOS displacements. Similarly, a comparable amount of seismic moment was released in the corresponding time intervals. Interferometric pairs 2006/08/28-2003/10/13 and 2006/09/16-2003/11/01 (fig. 2.8c and d, respectively) cover about the same time interval, but the former records the deformation a month earlier than the latter, and shows greater LOS displacements. The available InSAR data depict a deformation that correlates qualitatively with the time-dependent release of seismic energy of aftershocks. The inferred occurrence of post-seismic slip in the seismogenic zone between two areas of high co-seismic slip (2.5c and 2.4c), along with the general agreement between the tele-seismically-derived moment of aftershocks and the geodetic moment suggested by our inverse model (2.5c) indicate that most of the post-seismic deformation detected by InSAR may be explained in terms of continued seismic moment release. We cannot rule out a possibility that at least some slip on the fault might have occurred aseismically, but the available observations suggest that aseismic afterslip did not dominate the post-seismic relaxation contrary to inferences from other locations [Rymer, 1990, Savage and Svarc, 1997, Jacobs et al., 2002, Hearn et al., 2002, Fialko, 2004b]. Localized creep in the lower crust and upper mantle is a suggested mechanism for the loading on the fault in the inter-seismic period [Savage and Prescott, 1978], and it is reasonable to expect that co-seismic loading would result in an accelerated creep on a deep extension of the fault [Tse and Rice, 1986, Fialko, 2004b]. However, the deep afterslip is not evident in the three year post-seismic transient following the Altai earthquake. Our kinematic inversion did not require slip on a down-dip extension of the fault. In fact, a relatively short wavelength of the observed deformation transient precludes any contribution from possible relaxation phenomena below the brittle-ductile transition. To quantify this statement, we present analytical solutions for deep afterslip and visco-elastic response in the limit of complete relaxation in two dimensions (anti-plane strain). Consider a screw dislocation extending from the surface to a locking depth L . In the presence of a visco-elastic substrate below the depth H , the surface displacement after full relaxation of the co-seismic stress change is (see Appendix 2.7)

$$u(x) = \frac{s}{\pi} \tan^{-1} \left(\tan \frac{\pi L}{2H} \coth \frac{\pi x}{2H} \right) \quad (2.1)$$

where x is the horizontal distance from the fault and s is the total displacement occurring across the fault. In case of afterslip, the stress relaxation is believed to occur on a vertical plane below the seismogenic fault. As shown in Appendix 2.7, such relaxation gives rise to the following displacement at the surface,

$$u(x) = \frac{s}{\pi} \tan^{-1} \left(\frac{H}{x} \sqrt{1 + \frac{x^2}{H^2}} \tan \frac{\pi L}{2H} \right) \quad (2.2)$$

Figure 2.9 presents a comparison between the surface displacements due to visco-elastic relaxation and deep afterslip. For the same depth of the brittle-ductile transition H , and L/H ratio, the afterslip model produces a more localized deformation compared to the visco-elastic model.

However, the wavelength of surface displacements in both cases is of the order of H . This result also holds in three dimensions (the main difference being vanishing of surface displacements in the far field in case of 3-D deformation). InSAR observations of post-seismic deformation over three years following the Altai earthquake do not reveal lobes of LOS displacements with wavelengths greater than 20 km, indicating that the source is confined to the upper crust. The lack of long-wavelength deformation prevents us from considering more complicated (and presumably, more realistic) models of visco-elastic relaxation using non-linear rheologies. Therefore we conclude that the bulk of the observed post-seismic transient is due to additional slip on the fault plane at the periphery of areas with high co-seismic slip. The post-seismic fault adjustment is dominated by aftershocks but some aseismic creep in the upper crust cannot be ruled out.

2.5 Conclusions

The September 27th 2003, $M_w 7.2$ right-lateral strike-slip Altai earthquake ruptured a sub-vertical fault from the surface to a depth of ~ 12 km, as inferred from a kinematic inversion of SAR interferograms from the adjacent satellite tracks. Our InSAR observations do not have the spatial coverage to constrain the mantle viscosity at depths greater than about 40 km. We can, however, put a lower bound on the dynamic viscosity of the lower crust of 10^{19} Pa.s. A smaller viscosity would have caused a substantial surface deformation detectable by the InSAR data. The post-seismic deformation, as observed from all interferograms covering a time interval up to three years, cannot be explained by the viscous relaxation of any horizontal substrate above 35 km depth. The polarity of the post-seismic displacements around the fault do not warrant the poro-elastic rebound in the upper crust, suggesting a very low permeability or fluid saturation of the crustal rocks in the Chuya depression and Chuya Range. We cannot rule out, however, a possibility of a rapid pore fluid flow within the first 16 days following the earthquake, an interval for which we have no constraints from interferometry. According to our afterslip model obtained from a joint kinematic inversion of 2 independent interferograms, the total seismic moment release during the three years of the post-seismic transient was $M_0 = 2.32 \times 10^{18}$ N m. This estimate has the same order of magnitude as the cumulative aftershock moment of $M_0 = 1.51 \times 10^{18}$ N m derived from long period body wave and surface wave data over the corresponding time interval. Most of the 3 year line-of-sight displacements can be explained by the occurrence of aftershocks in the brittle upper crust next to areas of high co-seismic slip. Some slip may have occurred aseismically at depths less than 6 km. These results differ from those from other areas, and may be indicative of variations in rheology of the continental lithosphere in different tectonically active areas.

Acknowledgments

We thank Rowena Lohman, an anonymous reviewer, and the Associate Editor for their thorough and thoughtful reviews of this manuscript. We acknowledge E. Nissen for providing us with his mapping of the surface rupture in digital format. This work was supported by NSF (grant EAR-0450035) and SCEC. Original SAR data were provided by the European Space Agency. Numerical codes used in this study are available from the authors. This Chapter, in full, is a reprint of the material as it appears in the Journal of Geophysical Research 2008. Barbot, Sylvain; Hamiel Y., Fialko Y., 2008. The dissertation author was the primary investigator and author of this paper.

2.6 Along-track Interferometry

Conventional SAR interferometry allows one to measure surface displacements along the satellite line of sight (radar range). Any component of motion that is orthogonal to the LOS (for example, the along-track or azimuth displacements) cannot be detected with conventional interferometry. Other techniques utilizing radar amplitude information (e.g, pixel tracking) were proposed to measure azimuthal offsets [Michel et al., 1999, Van Puymbroeck et al., 2000, Leprince et al., 2007, Fialko et al., 2001b]. Such techniques involve subpixel correlation of the radar images, and are computationally expensive. Recently, Bechor and Zebker [2006] presented a new way to measure along-track displacements by forming forward-looking and backward-looking interferograms and computing their phase difference. The resulting image is a measure of the surface displacement projected in the azimuthal direction and the LOS plane. We propose a different way of generating the along-track interferogram by utilizing the already focused SAR images. Our method consists in filtering for positive and negative Doppler frequencies of the full-resolution complex SAR images. The proposed method is computationally efficient and can be easily implemented in existing SAR processors.

The high resolution of SAR imagery is obtained via bandwidth broadening. In the range direction, this is achieved by pulse compression. Along track, resolution is improved by making use of a Doppler synthesis or synthetic array approach [e.g., Elachi, 1987]. In the along-track, or azimuthal direction, the SAR geometry implies several relationships between time, frequency, velocity, look angle and satellite position. For instance, the instantaneous look angle θ , between the radar antenna and a scatterer, and the Doppler frequency f_D are related as follows,

$$f_D = \frac{2v}{\lambda} \sin \theta \quad (2.3)$$

where λ is the radar wavelength and v is the platform velocity (fig. 2.10). This relation allows one to select look angles by using the frequency content of the radar return. As the SAR image lines are recorded at the frequency f_{PRF} , the local look angle is also a function of time, and

equation (2.3) allows one to evaluate the radiation pattern of the SAR antenna as a function of time. In order to build forward-looking and backward-looking interferograms, we only need to separate the positive and negative Doppler returns. Because of the Earth's rotation and curvature and the platform's yaw, the zero Doppler f_0 does not exactly have a zero azimuth frequency, and is a function of range r . Energy distributed above the Doppler centroid corresponds to forward-looking angles and energy associated with frequencies lower than f_0 corresponds to the backward-looking part of the antenna beam. Our method thus consists in taking the one-dimensional Fourier transform in the azimuthal direction of each single look complex image and either tapering to zero unwanted frequencies or simply cropping the spectrum in order to select returns with a given Doppler sign. We do so for two SAR complex images, and we obtain 4 complex sub-images. We denote a_{11} , a_{12} the forward-looking and backward-looking parts of image 1, respectively; and a_{21} , a_{22} the corresponding parts of image 2. Thus,

$$\begin{aligned}\phi_1 &= \arg(a_{11} a_{21}^*) \\ \phi_2 &= \arg(a_{12} a_{22}^*)\end{aligned}\tag{2.4}$$

are the phase of the forward and backward interferograms, respectively. The along-track interferogram is the conjugate product $a_{11} a_{21}^* a_{12}^* a_{22}$. We now consider a scatterer in the LOS plane that moved $\Delta \mathbf{r}$ between the two acquisitions while staying in the LOS plane. The pulse energy is distributed along different angles so we call α the average look angle of half the beam aperture. Exploiting the parallax effect between the forward and backward look angles, and making use of simple trigonometric relations, the phase of the along-track interferogram is

$$\Delta\phi = \frac{8\pi}{\lambda} \sin \alpha \Delta \mathbf{r} \cdot \hat{\mathbf{a}}\tag{2.5}$$

where $\hat{\mathbf{a}}$ is a unit vector in the orbit direction and in the LOS plane. This is a measure of the azimuthal component of the displacement. The averaged look angle, assuming a non-tapered rectangular aperture, is

$$\alpha = \frac{\lambda}{L} \frac{\int_0^1 \theta \operatorname{sinc}^2 \theta d\theta}{\int_0^1 \operatorname{sinc}^2 \theta d\theta} \approx \frac{\lambda}{3.65 L}\tag{2.6}$$

where L is the antenna length and the sinc function is the theoretical angular distribution of the radar amplitude. In practice, the emitted pulse is tapered to avoid aliasing, which slightly changes the radiation pattern. (If the angular distribution were uniform, one would have $\alpha = \lambda/2L$.) In order to simplify the discussion, we make the conservative approximation $\alpha = \lambda/4L$. Noting that $\alpha \ll 1$, we can write

$$\Delta\phi = 2\pi \frac{\Delta \mathbf{r} \cdot \hat{\mathbf{a}}}{L}\tag{2.7}$$

The phase measurement is independent of the radar wavelength and is only a function of the radar antenna length and the horizontal component of the ground displacement. Furthermore, as L is about 10 m, relatively large displacements, of the order of 0.1-1 m, are needed to generate

acceptable signal-to-noise ratio. Due to the double phase difference, the along-track phase measurement is not relative, as opposed to conventional interferometry. A phase jump should occur at $\Delta \mathbf{r} \cdot \hat{\mathbf{a}} = L/2$ but the coherence is lost when displacements $\Delta \mathbf{r} \cdot \hat{\mathbf{a}}$ are greater than $L/4$, half the pixel size in the azimuth direction. Therefore, the obtained phase signal does not have the usual properties: it is not relative and phase jumps occur because of speckle only, not because of ground displacements. There is no need for phase unwrapping to uncover the azimuthal displacement field and the measured displacement lies in the range $[-L/4, L/4]$.

2.7 Full relaxation due to a screw dislocation

We consider a full relaxation at a depth H below an infinitely long screw dislocation extending from the surface to a depth L , with an anti-plane slip s (fig. 2.11). The displacement field is self-similar, so we introduce the dimensionless parameters $x_1 = x_1^*/H$, $x_3 = x_3^*/H$ and $h = L/H$, where the starred variables are the dimensional Cartesian coordinates. The corresponding surface displacements can be expressed using the general solution for an anti-plane dislocation in a layered half-plane of Weertman and Weertman [1964] and Rybicki and Kasahara [1977] by setting to zero the shear modulus of the underlying half-space (first line in eq. 2.8). This solution is in the form of an infinite series, and converges rather slowly. One way to improve convergence is to compute the series dual through Poisson's sum formula (second line in 2.8). The solution is still in the form of an infinite series. As the anti-plane screw dislocation problem consists essentially in solving Laplace's equation, a simplification comes from conformal mapping. Indeed, by the application of the mapping $w = \ln \frac{z-1}{z+1}$, we notice that the co-seismic screw dislocation in a plate, corresponding to the visco-elastic full relaxation, is the dual of the inter-seismic dislocation in a half-space. The equivalent solutions are

$$\begin{aligned} u_2(x_1) &= \frac{2}{\pi} \left[\tan^{-1} \frac{h}{x_1} + \sum_{k=1}^{\infty} \tan^{-1} \frac{h-2k}{x_1} + \tan^{-1} \frac{h+2k}{x_1} \right] \\ &= h + 2 \sum_{k=1}^{\infty} \frac{\sin k\pi h}{k\pi} e^{-k\pi x_1} \\ &= \frac{2}{\pi} \tan^{-1} \frac{\tan \pi h/2}{\tanh \pi x_1/2} \end{aligned} \quad (2.8)$$

The solution for afterslip, with a vertical stress-free surface extending from the dimensionless depth $x_3 = 1$ to infinity (bottom of fig. 2.11), can be also obtained with the help of conformal mapping: the afterslip and the plate solutions are dual through the mapping $w = \sin z$. It can be readily shown that the solution for afterslip in the limit of full relaxation is

$$\begin{aligned} u_2(x_1, 0) &= h + 2 \sum_{k=1}^{\infty} \frac{\sin k\pi h}{k\pi} e^{-2k \operatorname{asinh} x_1} \\ &= \frac{2}{\pi} \tan^{-1} \left(\frac{1}{x_1} \sqrt{1+x_1^2} \tan \frac{\pi}{2} h \right) \end{aligned} \quad (2.9)$$

The difference between the surface displacement due to the anti-plane dislocation in a plate and the dislocation underlain by a vertical stress-free surface shows how these end-member models result in different spatial wavelengths of post-seismic deformation at the surface.

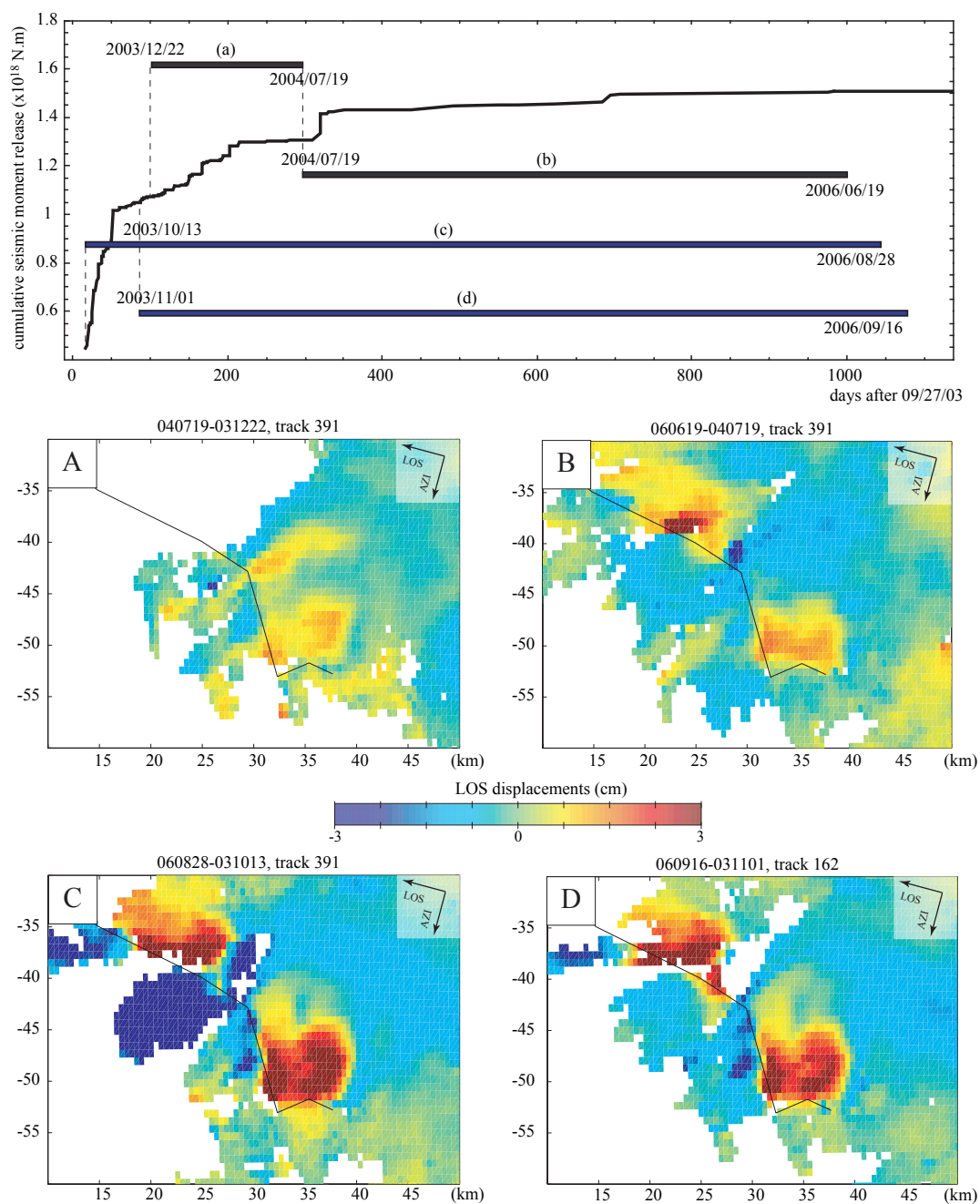


Figure 2.7: Seismic moment release. Cumulative seismic moment after Oct. 13, 2003 and the LOS displacement of available InSAR data. The LOS displacements correlate with the seismic moment released in the corresponding time interval of each interferometric pair. The thin black line indicates the fault surface location. (a-d) LOS displacements in UTM coordinates relative to the origin (87.74°E,50.30°N).

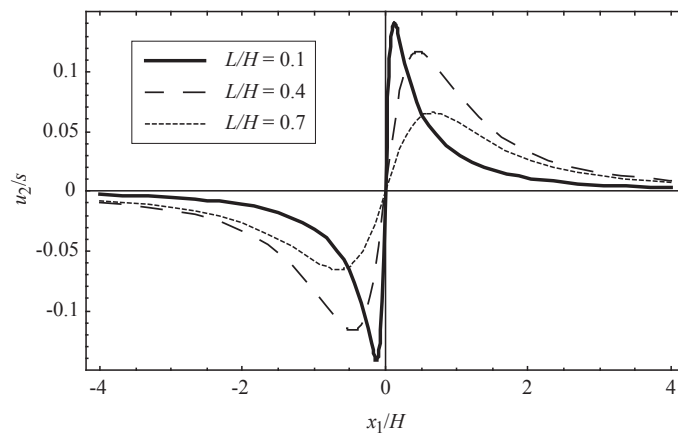


Figure 2.8: Difference between the full relaxation of the co-seismic stresses on a vertical plane (afterslip) and on a horizontal plane (visco-elastic relaxation). In both cases, the seismogenic zone, of thickness H , is perfectly elastic and the fault extends from the surface to a depth L . The two-dimensional solution is self-similar and depends only on the dimensionless parameter $h = L/H$.

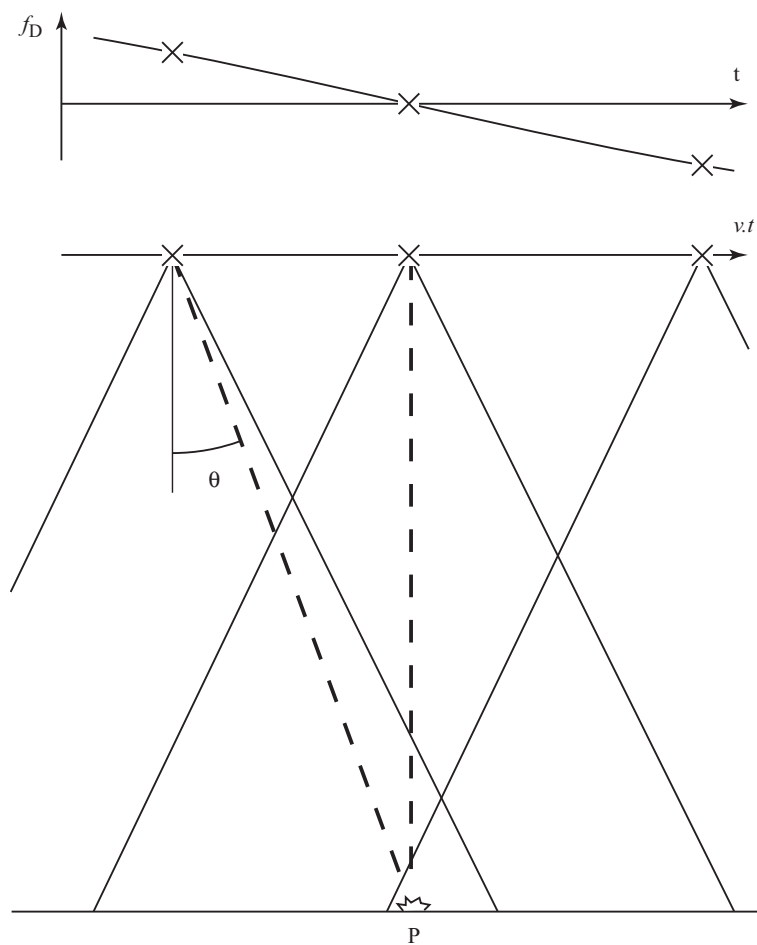


Figure 2.9: Doppler history f_D as a function of time, or equivalently, as a function of the look direction towards a scatterer P at the surface of the Earth. Positive and negative Doppler frequencies are associated with positive and negative look directions, respectively.

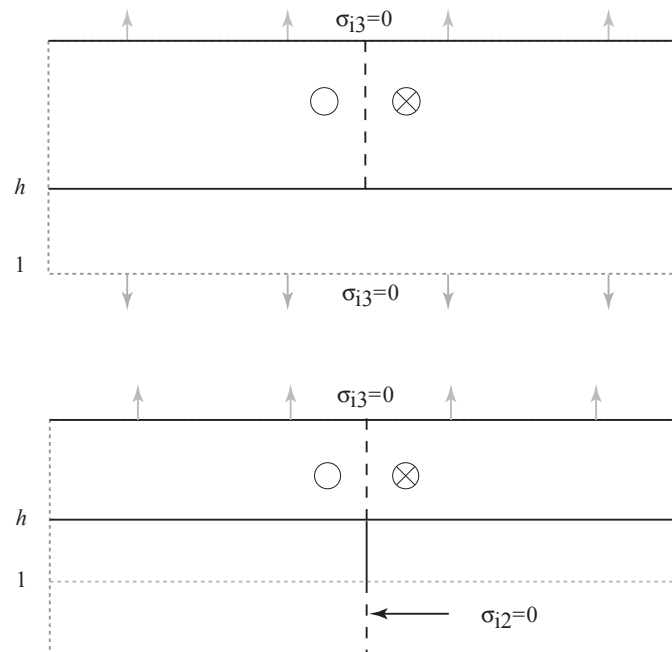


Figure 2.10: Geometry and boundary conditions applied to the screw dislocation in an elastic half-space. The solutions represent the sum of the co-seismic and post-seismic contributions to the anti-plane displacement. Top: the free surface on a horizontal plane corresponds to the visco-elastic relaxation. Bottom: the free surface on a down-dip extension of the fault plane corresponds to the afterslip scenario.

Chapter 3

Effect of a Compliant Fault Zone on the Inferred Earthquake Slip Distribution

Sylvain Barbot, Yuri Fialko and Dave Sandwell

Abstract. We present a new semi-analytic method to evaluate the deformation due to a screw dislocation in arbitrarily heterogeneous and/or anisotropic elastic half-plane. The method employs integral transformations to reduce the governing partial differential equations to the integral Fredholm equation of the second kind. Dislocation sources, as well as spatial perturbations in the elastic properties are modeled using equivalent body forces. The solution to the Fredholm equation is obtained in the Fourier domain using a method of successive over-relaxation, and is mapped into the spatial domain using the inverse Fast Fourier Transform. We apply this method to investigate the effect of a soft damage zone around an earthquake fault on the co-seismic displacement field, and on the earthquake slip distribution inferred from inversions of geodetic data. In the presence of a kilometer-wide damage zone with a reduction of the effective shear modulus of a factor of 2, inversions that assume a laterally homogeneous model tend to underestimate the amount of slip in the middle of the seismogenic layer by as much as 20%. This bias may accentuate the inferred maxima in the seismic moment release at depth between 3-6 km suggested by previous studies of large strike-slip earthquakes.

3.1 Introduction

Major crustal faults are often associated with zones of highly cracked and damaged rocks that can extend as far as 10^2 - 10^3 meters away from the slip interface [Ambraseys, 1970, Wilson et al., 2004, Chester et al., 2005]. Such zones may result from inelastic deformation associated with the fault growth [e.g., Vermilye and Scholz, 1998, Manighetti et al., 2001] or repeated seismic ruptures [Rice et al., 2005, Fialko, 2007]. Intense damage gives rise to a reduction in the effective elastic moduli of the fault zone material, as predicted by theoretical models [Rybicki, 1971, Kachanov, 1986, Lyakhovskiy et al., 2001, Turcotte et al., 2003], and evidenced by geodetic [Fialko et al., 2002, Fialko, 2004a, Hamiel and Fialko, 2007] and seismic [Li et al., 1994, Thurber et al., 2003, Cochran et al., 2006] observations. Macroscopic compliant fault zones result in significant lateral variations in the mechanical properties of the Earth’s crust, and may affect the pattern of surface deformation during the co-seismic, post-seismic, and inter-seismic phases of the earthquake cycle. In this paper we investigate the effect of a pre-existing damage zone on the co-seismic displacement field, and spatially variable fault slip inferred from inversions of geodetic data.

We develop a new computationally efficient semi-analytic model of the fault-induced deformation in an arbitrarily heterogeneous and anisotropic medium. We use integral transforms to reduce the problem to the Fredholm integral equation of the second kind which is solved by means of successive approximations [e.g., Delves and Mohamed, 1985, Fialko et al., 2001a]. The forcing terms are the equivalent body forces representing dislocations with prescribed slip [Eshelby, 1957, Burridge and Knopoff, 1964]. Our approach takes advantage of the convolution theorem and the fast Fourier transforms [e.g., Frigo and Johnson, 1998] and avoids the formation of a stiffness matrix, such that the overall computational burden scales only linearly with the model size. The method readily allows one to simulate deformation due to fault slip in the Earth’s crust or lithosphere with realistic variations in the elastic moduli (e.g., as inferred from seismic tomography data). It can be also extended to simulate the visco-elastic response by taking advantage of the correspondence principle, whereby the time-dependent response of a visco-elastic medium is determined by applying the Laplace transform and reducing a problem to a set of inhomogeneous static problems in the transformed domain [e.g., Pollitz, 1997, Smith and Sandwell, 2004, Wang et al., 2006].

In the next section, we present the elasto-static solution for heterogeneous media. The solution is implemented for a case of a two-dimensional anti-plane deformation, and verified against a number of available analytic solutions. In section 3, we apply our method to investigate the effects of a macroscopic compliant fault zone on co-seismic slip distributions inferred from inversions of geodetic data.

3.2 Semi-Analytic Model of Deformation in Heterogeneous and Anisotropic Media

3.2.1 Theory

Surface deformation due to slip on a fault can be well described using solutions for dislocations in an elastic half-space [Steketee, 1958a, Savage and Burford, 1973, Fialko, 2004a]. As demonstrated by Burridge and Knopoff [1964], one may transform the corresponding mixed boundary-value problem into a stress boundary-value problem using a body-force equivalent of the dislocation discontinuity in terms of double couples. Under this approach, the solution can simply be obtained from the integration of some forcing terms $\mathbf{f}(\mathbf{x})$. The equivalent body force for a total displacement \mathbf{u} on a fault located at position \mathbf{x} and oriented normal to $\hat{\mathbf{n}}(\mathbf{x})$ (see Fig. 3.1), in a linear elastic medium with an elasticity tensor $\mathbf{C}(\mathbf{x})$ is given by [e.g., Eshelby, 1957, Burridge and Knopoff, 1964, Aki and Richards, 1980, Alshits and Kirchner, 1995a,b, Nemat-Nasser and Hori, 1999]

$$\mathbf{f} = -\nabla \cdot (\mathbf{C} : \mathbf{u} \otimes \hat{\mathbf{n}}) \quad (3.1)$$

The static deformation resulting from fault slip satisfies the conservation of linear momentum [e.g., Malvern, 1969]

$$\nabla \cdot \boldsymbol{\sigma} + \mathbf{f} = 0 \quad (3.2)$$

subjected to the displacement-strain relation,

$$\boldsymbol{\varepsilon} = \frac{1}{2} [\nabla \otimes \mathbf{u} + (\nabla \otimes \mathbf{u})^t] \quad (3.3)$$

the stress-strain relation $\boldsymbol{\sigma} = \mathbf{C} : \boldsymbol{\varepsilon}$, and appropriate boundary conditions. For a finite deformation source in an elastic half-space, the relevant boundary conditions are zero tractions at the free surface and vanishing displacements at infinity.

We now introduce the following iterative approach to simulate a dislocation in a heterogeneous half-space. Consider the decomposition of the elastic moduli into a constant part $\bar{\mathbf{C}}$ and a heterogeneous part, $\mathbf{C}'(\mathbf{x})$ [e.g., Du et al., 1994],

$$\mathbf{C}(\mathbf{x}) = \bar{\mathbf{C}} + \mathbf{C}'(\mathbf{x}) \quad (3.4)$$

The choice of $\bar{\mathbf{C}}$ is discussed in Appendix 3.5. The conservation of linear momentum can then be written

$$\nabla \cdot (\bar{\mathbf{C}} : \boldsymbol{\varepsilon}) + \mathbf{f} + \nabla \cdot (\mathbf{C}' : \boldsymbol{\varepsilon}) = 0. \quad (3.5)$$

The contribution $\nabla \cdot (\mathbf{C}' : \boldsymbol{\varepsilon})$ can be interpreted as equivalent body forces mimicking the presence of heterogeneities. These fictitious forces are uniquely related to the elastic structure and can be distributed such that the resulting deformation in a homogeneous medium is equivalent to that in a heterogeneous medium. The proposed algorithm for solving the heterogeneous problem

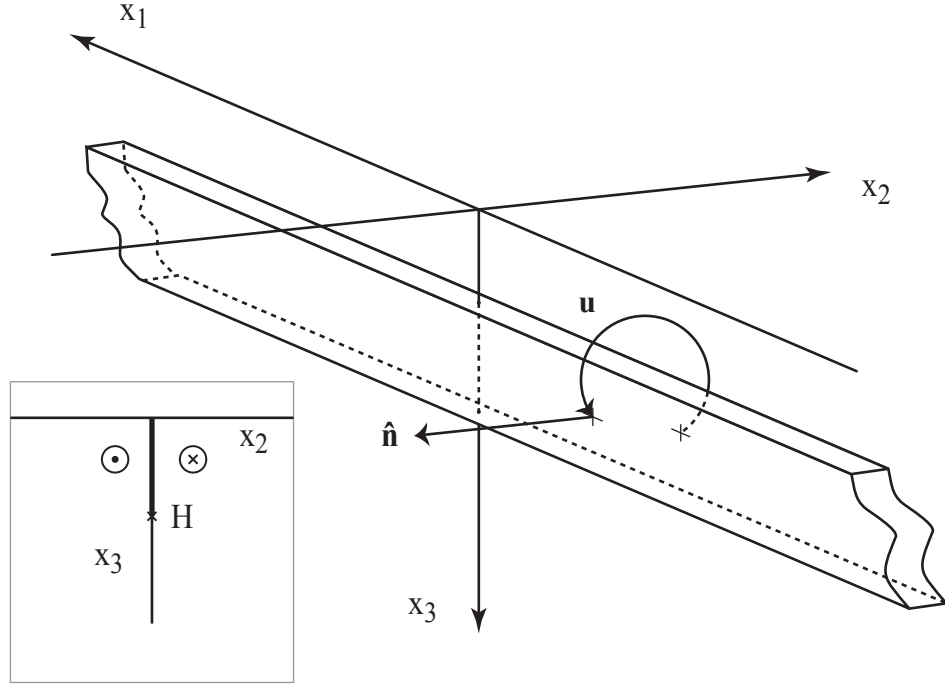


Figure 3.1: Dislocation in a half-space. A fault idealized by a plane of normal vector $\hat{\mathbf{n}}$ is sliding in a direction \mathbf{u} . In anti-plane deformation, strike-slip occurs along the x_1 -direction.

consists in the following steps: first, starting from the displacement field $\mathbf{u}_0 = 0$ (or some non-trivial guess), compute the equivalent body force at iteration $n = 1$,

$$\tilde{\mathbf{f}}_n = \mathbf{f} + \nabla \cdot (\mathbf{C}' : \boldsymbol{\varepsilon}_{n-1}) , \quad (3.6)$$

then solve the homogeneous problem

$$\nabla \cdot (\bar{\mathbf{C}} : \boldsymbol{\varepsilon}_n) + \tilde{\mathbf{f}}_n = 0 \quad (3.7)$$

for the entire displacement field with appropriate boundary conditions. Last, verify the convergence criterion

$$\frac{\langle \|\tilde{\mathbf{f}}_n - \tilde{\mathbf{f}}_{n-1}\|^2 \rangle}{\langle \|\mathbf{f}\|^2 \rangle} < \epsilon \quad (3.8)$$

where ϵ is the tolerance (hereafter, we use $\epsilon = 10^{-6}$), and the operator $\langle \cdot \rangle$ denotes integration over the entire domain. Steps (3.6) and (3.7) are repeated until condition (4.39) is satisfied. The convergence criterion is a necessary condition to ensure that the equivalent body forces adequately mimic heterogeneities in the elastic structure. The amplitude of stress and the equivalent body forces is governed by the forcing term \mathbf{f} , which depends upon the magnitude of slip on the dislocations and the local shear modulus, so the convergence criterion (4.39) is scaled accordingly.

The displacement field due to a dislocation in an arbitrarily heterogeneous material can be obtained by iteratively solving the corresponding homogeneous problems with the properly distributed body forces.

3.2.2 Anti-Plane Deformation

Implementation

Here we implement the described procedure for the case of an infinitely long screw dislocation in an elastic half-space, with two-dimensional variations in shear modulus [e.g., Barnett, 1972, Du et al., 1994]. The deformation is anti-plane strain, as $u_2 = u_3 = 0$, the only non-zero displacement component is $u_1 = u_1(x_2, x_3)$, and the only non-zero stress components are

$$\begin{aligned}\sigma_{12} &= 2\mu \varepsilon_{12} = \mu u_{1,2} \\ \sigma_{13} &= 2\mu \varepsilon_{13} = \mu u_{1,3}\end{aligned}\tag{3.9}$$

We now decompose the rigidity tensor into a constant part and a heterogeneous part as follows,

$$\mu(\mathbf{x}) = \bar{\mu} + \mu'(\mathbf{x})\tag{3.10}$$

We use the method of images to satisfy the free-surface boundary condition [Steketee, 1958a, Smith and Sandwell, 2004]. The equivalent body forces act in the x_1 -direction only, and we write $f_1(\mathbf{x})$ the sum of the equivalent body forces and their image. The conservation of linear momentum can now be written as

$$\bar{\mu}(u_{1,22} + u_{1,33}) = -f_1 - (\mu' u_{1,2})_{,2} - (\mu' u_{1,3})_{,3}\tag{3.11}$$

which simplifies to the Poisson's equation in case of a homogeneous medium. After Fourier transforming, eq. (3.11) is reduced to an algebraic expression representing the Fredholm integral equation of the second kind (see Appendix 3.5).

We solve equation (3.11) by using a method of successive approximations in the spectral domain. Convergence of the resulting series of iterated kernels is further discussed in the Appendix 3.5. A similar approach was previously used to study the cooling of the oceanic lithosphere [Sandwell, 1984], the mantle convection [Gable et al., 1991] and complex composites in mineral structures [Moulinec and Suquet, 1998, Lebensohn, 2001]. We employ the Successive Over-Relaxation (SOR) technique to accelerate convergence [e.g., Golub and Van Loan, 1996]. The iterative algorithm for solving equation (3.11) is as follows: starting from $\hat{u}_1^0(\mathbf{k}) = 0$ or some initial guess, compute the equivalent body forces in the spectral domain for iteration $n = 1$

$$\hat{g}^n(\mathbf{k}) = \hat{f}_1 - \omega_2 (\hat{\mu}' * \omega_2 \hat{u}_1^{n-1}) - \omega_3 (\hat{\mu}' * \omega_3 \hat{u}_1^{n-1})\tag{3.12}$$

where the hat denotes the relevant field in the transformed domain and we use $\omega = 2\pi \mathbf{k}$. The two-dimensional convolutions, denoted by the symbol $*$, are performed in the space domain,

taking advantage of the fast Fourier transform. Then, we update the displacement field using the SOR method

$$\hat{u}_1^n(\mathbf{k}) = \phi T(\mathbf{k}) \hat{g}^n(\mathbf{k}) + (1 - \phi) \hat{u}_1^{n-1}(\mathbf{k}) \quad (3.13)$$

where we have defined the transfer function

$$\hat{T}(\mathbf{k}) = \frac{1}{\bar{\mu}(\omega_2^2 + \omega_3^2)} \quad (3.14)$$

An optimal value for the SOR parameter ϕ for simple problems (single fault embedded in a subspace of uniform shear modulus) is $\phi = \bar{\mu}/\mu^*$ where μ^* is the shear modulus μ on the fault. This choice ensures the satisfaction of the boundary conditions on the fault at any iteration, so that the final solution is obtained with fewer iterations. If the geometry prohibits one from using this simple definition, the default value $\phi = 1$ should be preferred, which corresponds to the successive approximation approach. Finally, we evaluate the convergence criterion

$$\frac{\langle \|\hat{g}^n - \hat{g}^{n-1}\|^2 \rangle}{\langle \|\hat{f}_1\|^2 \rangle} < \epsilon \quad (3.15)$$

where the norm is $\|f\|^2 = f f^*$, and the functional $\langle \|\cdot\|^2 \rangle = \int_{-\infty}^{\infty} \|\cdot\|^2 d\mathbf{k}$ denotes the total error inferred from the Rayleigh's theorem. In order to satisfy the boundary condition of vanishing of displacement at infinity, we need to enforce $\hat{u}_1^n(0) = 0$. This is done by setting $\hat{T}(0) = 0$. Steps (3.12) and (3.13) are to be repeated until the convergence test (3.15) is satisfied. The suggested algorithm uses the direct and inverse two-dimensional Fourier transforms

$$\begin{aligned} \hat{f}(\mathbf{k}) &= \int_{-\infty}^{\infty} f(\mathbf{x}) e^{-i2\pi\mathbf{k}\cdot\mathbf{x}} d\mathbf{x} \\ f(\mathbf{x}) &= \int_{-\infty}^{\infty} \hat{f}(\mathbf{k}) e^{i2\pi\mathbf{k}\cdot\mathbf{x}} d\mathbf{k} \end{aligned} \quad (3.16)$$

The fault geometry is defined by the value of $f_1(\mathbf{x})$ and can be readily expressed in the Fourier domain in an analytic fashion. However, an accurate model depends upon the quality of the frequency sampling and the fault slip distribution should be tapered so that high frequencies vanish as one approaches the Nyquist frequency. We suggest two appropriate tapers which intensities are controlled by a roll-off parameter β . For any value of β in the range $0 < \beta < 1/2$, the tapers have a unit area and can be successively added so that only the tip of the fault or abrupt changes in slip are tapered. The first is a linear taper

$$\Pi_\beta(x) = \begin{cases} 1, & |x| < \frac{1}{2} - \beta \\ \frac{1}{2\beta} \left(\frac{1}{2} + \beta - |x| \right), & \frac{1}{2} - \beta < |x| < \frac{1}{2} + \beta \\ 0, & \text{otherwise} \end{cases} \quad (3.17)$$

$$\tilde{\Pi}_\beta(k) = \text{sinc}(k) \text{sinc}(2\beta k)$$

The second taper suppresses stress singularities at the tip of a fault and allows for a better frequency sampling,

$$\Omega_\beta(x) = \begin{cases} 1, & |x| < \frac{1-2\beta}{2(1-\beta)} \\ \cos\left(\pi \frac{(1-\beta)|x| - \frac{1}{2} + \beta}{2\beta}\right)^2, & \frac{1-2\beta}{2(1-\beta)} < |x| < \frac{1}{2(1-\beta)} \\ 0, & \text{otherwise} \end{cases}, \quad (3.18)$$

$$\tilde{\Omega}_\beta(k) = \frac{\text{sinc}\left(\frac{k}{1-\beta}\right) + (1-2\beta)\text{sinc}\left(k\frac{1-2\beta}{1-\beta}\right)}{2(1-\beta - 4k^2\frac{\beta^2}{1-\beta})}$$

For $\beta = 0$, both tapers reduce to a simple boxcar function. As an example, a vertical fault of unit length and slip, starting at depth d , has the equivalent body-force in the Fourier domain

$$\hat{f}_1(\mathbf{k}) = -\mu^* i 2\pi k_2 e^{-\pi^2 \Delta x_2^2 k_2^2} \times \tilde{\Omega}_\beta(k_3) 2 \cos(2\pi k_3(1/2 + d)) \quad (3.19)$$

where we make use of the Gaussian representation of a unit moment, Δx_2 being the horizontal sampling interval, and we utilize the shift property of the Fourier transform to add the source and its image.

Benchmarks

We test our semi-analytic solution against a number of available analytic solutions for an elastic half-space with the spatially variable elastic moduli. All benchmarks discussed below include a strike-slip fault extending from the surface to a depth L , and having the surface slip s . Our method allows one to treat dipping faults; for simplicity, here we restrict our attention to vertical faults only.

We begin with the case of an isotropic medium with a contrast in shear modulus across a transform fault (Fig. 3.2a). The analytic solution for the surface displacement is

$$u_1(x_2) = \begin{cases} \frac{2s}{\pi} \frac{\mu_2}{\mu_1 + \mu_2} \tan^{-1} \frac{L}{x_2}, & x_2 < 0 \\ \frac{2s}{\pi} \frac{\mu_1}{\mu_1 + \mu_2} \tan^{-1} \frac{L}{x_2}, & x_2 > 0 \end{cases} \quad (3.20)$$

where μ_1 and μ_2 are the value of the shear modulus at each side of the fault and s is the total slip across the dislocation. As expected, the deformation is enhanced in the softer region. Note an excellent agreement between the numerical and analytic solutions.

Next example illustrates the full post-seismic relaxation due to a visco-elastic substrate underlying the elastic-brittle layer (Fig. 3.2b). Viscous flow reduces the co-seismically induced shear stresses below the brittle-ductile transition. In the limit of full relaxation and no secular

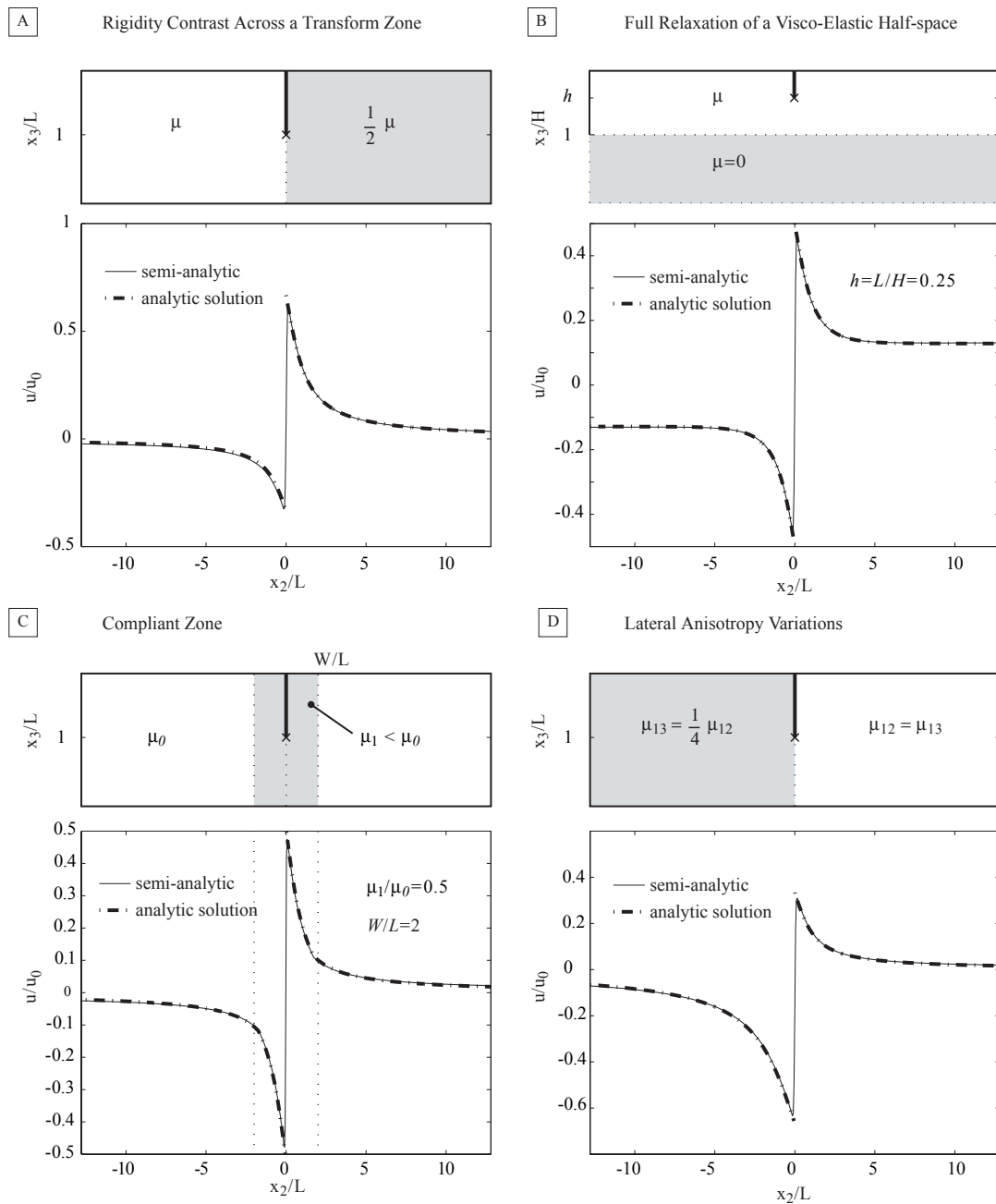


Figure 3.2: Comparison between the analytic expressions and the numerical solutions for surface displacements due to a fault slip in heterogeneous media. a) Isotropic medium with a contrast of shear modulus across the transform fault zone. b) Isotropic medium after full relaxation of a visco-elastic substrate below the depth H . c) Isotropic medium with the compliant fault zone with total width $2W$. d) Contrast of anisotropy across the fault plane. The wavelength of deformation is larger in the softer anisotropic crust, to the left of the rupture.

deformation, the latter effectively becomes a stress-free boundary [e.g., Fialko, 2004b]. The full visco-elastic deformation can be evaluated by subtracting the elastic half-space and the elastic plate solutions. The respective analytic solutions are available for the case of the antiplane strain [Weertman and Weertman, 1964, Rybicki, 1971, Nur and Mavko, 1974, Barbot et al., 2008b]. Due to the finite displacement at far field, a numerical cosine transform is more adequate to model the deformation. Our numerical solution is in an excellent agreement with the analytic expressions (see Fig. 3.2b). Note that the use of the SOR method allows one to treat such problems with arbitrarily large variations in elastic properties, as shown in this example.

We now consider deformation due to slip on a fault embedded in a relatively narrow zone of damaged material having a reduced effective shear modulus. An analytic solution is available in the form of an infinite series [e.g., Rybicki and Kasahara, 1977]. The corresponding surface deformation is shown in Fig. 3.2c. The semi-analytic solution well captures the localized deformation including a discontinuity in strain at the interface between the fault zone and the surrounding crust. The convergence is reached after 2 iterations, which takes only a few seconds for a 512×512 array on a low end laptop computer.

Finally, we consider the case of faulting in an anisotropic half-plane with heterogeneous shear moduli. The condition of anti-plane strain requires that the dislocation lines extend along an axis of two-fold symmetry in the elastic moduli tensor. A fault separating two media with anisotropic shear moduli μ_{12} and μ_{13} satisfies this condition. Any anti-plane isotropic solution can be generalized for the anisotropic case by scaling the horizontal coordinate by a factor

$$\alpha = \sqrt{\frac{\mu_{13}}{\mu_{12}}} \quad (3.21)$$

Deformation in the presence of anisotropic heterogeneity across a transform fault, as sketched in Fig. 3.2d, exhibits the following deformation profile at the surface:

$$u_1(x_2) = \begin{cases} \frac{2s}{\pi} \frac{1}{1+\alpha} \tan^{-1} \frac{L}{\alpha x_2}, & x_2 < 0 \\ \frac{2s}{\pi} \frac{\alpha}{1+\alpha} \tan^{-1} \frac{L}{x_2}, & x_2 > 0 \end{cases} \quad (3.22)$$

and is very well matched by the numerical solution (Fig. 3.2d). The wavelength of the deformation is larger on the left side of the fault where the medium is more compliant in the vertical direction. Solutions for dislocations in heterogeneous anisotropic media are further discussed in Appendix 3.6.

As one can see from Figure 3.2, there is a general agreement between our semi-analytic approach and closed form analytic solutions. We conclude that the proposed iterative scheme can be efficiently used to model crustal deformation in the presence of arbitrary variations in the effective elastic moduli in the Earth's crust.

3.3 Co-seismic deformation in the presence of a compliant fault zone

Major crustal faults are often surrounded by zones of highly cracked and damaged rocks, as evidenced by geologic [e.g., Wilson et al., 2004, Chester et al., 2005, Dor et al., 2006], seismic [Li et al., 1994, Thurber et al., 2003, Cochran et al., 2006] and geodetic [Fialko et al., 2002, Fialko, 2004a, Hamiel and Fialko, 2007] observations. Such zones introduce significant lateral variations in the crustal rigidity, and likely affect patterns of co-seismic deformation at the Earth’s surface (see Figure 3.2c). Consequently, inversions of geodetic data for the subsurface fault slip that are usually based on solutions for homogeneous or horizontally stratified Earth’s crust may be systematically biased.

We investigate this potential bias by modeling the co-seismic response of a heterogeneous brittle-elastic lithosphere in the presence of a damaged compliant fault zone. We approximate the damage zone by using a reduced shear modulus μ in a finite vertical strip centered on the fault plane and extending by the distance W in both directions away from the fault plane. Based on preliminary results from seismic tomography of the Calico fault zone in eastern California [Cochran et al., 2006], we assume that the effective shear modulus varies gradually from a background value μ to a minimum value $\mu/2$ at the center of the fault zone. We further assume that the fault zone width is six times smaller than the depth extent of the co-seismic slip, $W = L/6$, where L is the nominal locking depth. For a fault locking depth of 12 km typical of California, the assumed thickness of the compliant zone is 2 km, consistent with some geodetic and seismic observations [Fialko et al., 2002, Fialko, 2004a, Hamiel and Fialko, 2007, Cochran et al., 2006]. The fault slip is assumed to be constant in the uppermost crust, and gradually tapered to zero toward the bottom of the seismogenic zone according to the following expression,

$$s(x_3) = s_0 \left(\Pi_\beta \left[\frac{2x_3 - L}{2L} \right] + \Pi_\beta \left[\frac{2x_3 + L}{2L} \right] \right) \quad (3.23)$$

where s_0 is slip in the upper part of the fault. The assumed slip distribution is shown by the solid line in Fig. 3.3b for $\beta = 0.4$. The corresponding surface displacements are shown in Figure 3.3a for a homogeneous half-space (solid line) and a half-space with the compliant fault zone (dashed line). The difference between the two model predictions is maximum at a distance of $O(W)$ away from the fault, where it reaches $\sim 10\%$ of the local displacement amplitude.

We then invert the synthetic co-seismic surface displacements for the fault slip distribution at depth. Using the Green’s functions for a homogeneous elastic half-space, we perform two sets of inversions: one for the case of a heterogeneous half-space with a compliant zone, and another for the case of a homogeneous elastic half-space. The corresponding surface displacements are shown in Fig. 3.3a. As inversions of surface displacements are intrinsically non-unique [e.g., Parker, 1994, Mavko, 1981, Savage, 1990], we impose the non-negativity and smoothness constraints to regularize the problem (see [Fialko, 2004a] for details). The resulting slip distributions

are shown in Figure 3.3b for the homogeneous (long dashed line) and heterogeneous (short dashed line) models. Note that the use of the non-negativity constraint makes the inversion a non-linear one. One consequence of non-linearity is that the difference between the inverted slip models (e.g., corresponding to the homogeneous and heterogeneous forward models) is not equivalent to the inversion of the difference between the surface displacements (Figure 3.3a). Figures 3.3c and 3.3d illustrate results of the inversion of the difference between the synthetics for the homogeneous and heterogeneous half-space, and the difference between the slip distributions shown in Figure 3.3b, respectively. A comparison between the slip models inferred from inversions, and the assumed slip distribution (Figure 3.3b) shows that the neglect of a compliant fault zone gives rise to an underestimation of slip throughout much of the seismogenic layer. The largest discrepancy (as much as 20%) corresponds to a depth interval around $x_3 \sim 0.2L$. In addition, inversions neglecting a compliant zone tend to overestimate slip below the effective brittle-ductile transition (depths greater than L , see Figure 3.3b). The effect of a vertical compliant zone on the inferred slip distribution is opposite to the effect of horizontal layering. The latter tends to bias the moment centroid to shallower depths in slip inversions that assume a homogeneous elastic half-space [Simons et al., 2002, Fialko, 2004a, Hearn and Bürgmann, 2005].

These results bear on the interpretation of co-seismic deformation. In particular, inversions of high-quality geodetic data from several large strike-slip events including the Landers, Izmit, Hector Mine, and Bam earthquakes [Simons et al., 2002, Fialko, 2004a, Fialko et al., 2005] suggest that the maximum seismic moment release occurs in the middle of the seismogenic layer, with a peak in the interval between 3 and 6 km [Fialko et al., 2005]. Because co-seismic slip in the uppermost part of the brittle layer (shallower than ~ 3 km) appears to be systematically less than slip at greater depth, this pattern was referred to as the “shallow slip deficit” [Simons et al., 2002, Fialko et al., 2005]. It is of interest to establish whether the shallow slip deficit inferred from inversions of geodetic data represents actual variations in seismic slip with depth, or is an artifact of inversions (e.g., due to an oversimplified representation of the mechanical response of the Earth’s crust to fault slip). Results presented above suggest that previous inferences of the shallow slip deficit may be in fact conservative, as inversions based on homogeneous or horizontally stratified elastic half-space models likely underestimate the amount of slip in the depth interval between $\sim 3 - 6$ km if earthquake faults are embedded in large damage zones with reduced effective elastic moduli (Figure 3.3b).

The semi-analytic approach described in this paper allows one to accurately and efficiently calculate deformation due to fault slip in a heterogeneous elastic half-space under conditions of anti-plane strain. This approach can be readily extended for the general case of three-dimensional (3-D) deformation. The 3-D formulation will be presented in a separate paper.

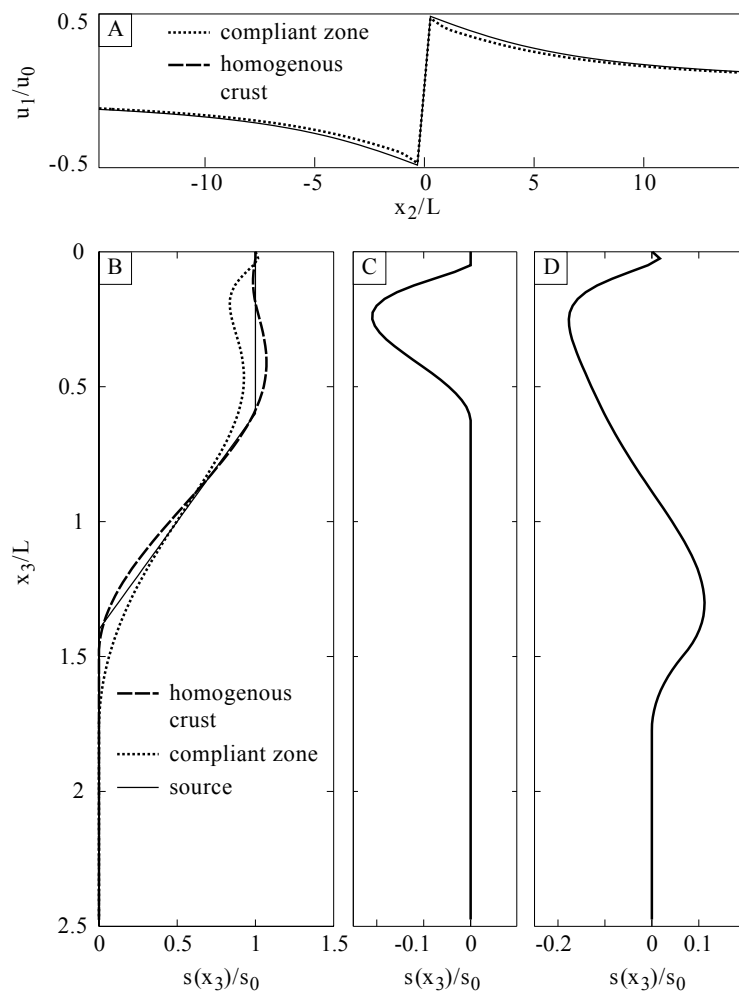


Figure 3.3: a) Synthetic co-seismic surface displacements in a homogeneous crust (solid line) and in a laterally heterogeneous crust with a compliant zone (dashed line). b) Slip inversions of surface displacements for the initial slip distribution shown by the continuous profile. c) Inversion of the algebraic difference between the homogeneous and the heterogeneous synthetics. d) Difference between the inversions of the homogeneous and heterogeneous synthetics.

3.4 Conclusions

We derived an iterative approach to model dislocations in heterogeneous and anisotropic media for the case of two-dimensional (anti-plane strain) deformation appropriate for infinitely long strike-slip faults. The method requires solving homogeneous problems with equivalent body forces that account for arbitrarily distributed elastic heterogeneities in the Earth’s crust. By making use of a series of integral transforms, the problem is reduced to the Fredholm integral equation of the second kind. The computational burden is alleviated by the application of the convolution theorem and the use of fast Fourier transforms. We have tested our numerical scheme against analytic solutions for surface displacements due to a finite dislocation with variable slip. The comparisons showed a very good agreement between the numerical and analytic solutions, indicating that the proposed method can be used to model deformation in heterogeneous and anisotropic media with essentially arbitrary distribution of elastic moduli.

We applied the Fredholm iterative scheme to model the co-seismic displacements in the presence of a narrow compliant zone with gradual variations in the shear modulus. Inversions of the corresponding surface displacements for subsurface fault slip show that models that neglect the presence of compliant damage zones around earthquake faults may underestimate fault slip by as much as 20% in the middle of the seismogenic layer. This bias implies more accentuated shallow slip deficit than suggested by previous studies of large strike-slip earthquakes, provided that the investigated earthquake ruptures are surrounded by wide damage zones.

Acknowledgments

We thank Associate Editor Johannes Weertman and two anonymous reviewers for their thorough and thoughtful reviews of this manuscript. We thank Glenn Ierley for sharing his insight on numerical methods and in particular for suggesting the use of the SOR approach. This work was supported by NSF (grant EAR-0450035) and SCEC. Numerical codes used in this study are available from the authors. This Chapters, in full, is a reprint of the material as it appears in the Journal of Geophysical Research. Barbot, Sylvain; Fialko, Y.; Sandwell, D.. The dissertation author was the primary investigator and author of this paper.

3.5 Convergence Condition

The displacement field due to a screw dislocation in a heterogeneous isotropic medium is, when expressed in the Fourier domain, the solution of the Fredholm integral of the second kind

$$\hat{u}(\mathbf{k}) = \frac{\hat{f}_2}{\bar{\mu} 4\pi^2 \mathbf{k} \cdot \mathbf{k}} + \int_{-\infty}^{\infty} K(\mathbf{k}, \mathbf{s}) \hat{u}(\mathbf{s}) d\mathbf{s} \quad (3.24)$$

where the kernel $K(\mathbf{k}, \mathbf{s})$ is

$$K(\mathbf{k}, \mathbf{s}) = \frac{\mathbf{k} \cdot \mathbf{s}}{\mathbf{k} \cdot \mathbf{k}} \frac{\hat{\mu}'(\mathbf{k} - \mathbf{s})}{\bar{\mu}}. \quad (3.25)$$

The estimation of $\hat{u}(\mathbf{k})$ can be performed by successive approximations

$$\hat{u}(\mathbf{k})^n = T[\hat{u}(\mathbf{k})^{n-1}]. \quad (3.26)$$

The corresponding series converges if

$$\|T[\hat{u}(\mathbf{k})^n] - T[\hat{u}(\mathbf{k})^{n+1}]\| < \|\hat{u}(\mathbf{k})^n - \hat{u}(\mathbf{k})^{n+1}\| \quad (3.27)$$

where we use the infinite norm

$$\|f\|^2 = \max_{\mathbb{R}^2} f(\mathbf{k}) f^*(\mathbf{k}) \quad (3.28)$$

As $T[\cdot]$ is a linear operator, we can write

$$\begin{aligned} T[\hat{u}^n] - T[\hat{u}^{n+1}] &= T[\hat{u}^n - \hat{u}^{n+1}] \\ &= \int_{-\infty}^{\infty} K(\mathbf{k}, \mathbf{s})(\hat{u}(\mathbf{s})^n - \hat{u}(\mathbf{s})^{n+1}) d\mathbf{s} \end{aligned} \quad (3.29)$$

Applying the Cauchy-Schwarz inequality, we have

$$\begin{aligned} &\left\| \int_{-\infty}^{\infty} K(\mathbf{k}, \mathbf{s})(\hat{u}(\mathbf{s})^n - \hat{u}(\mathbf{s})^{n+1}) d\mathbf{s} \right\| \\ &< \left\| \int_{-\infty}^{\infty} K(\mathbf{k}, \mathbf{s}) d\mathbf{s} \right\| \|\hat{u}(\mathbf{k})^n - \hat{u}(\mathbf{k})^{n+1}\| \end{aligned} \quad (3.30)$$

Combining eqs. (3.27) and (3.30), the convergence of the successive approximation method is obtained if

$$\left\| \int_{-\infty}^{\infty} K(\mathbf{k}, \mathbf{s}) d\mathbf{s} \right\| < 1 \quad (3.31)$$

Evaluation of the above integral gives

$$\begin{aligned} \int_{-\infty}^{\infty} K(\mathbf{k}, \mathbf{s}) d\mathbf{s} &= \int_{-\infty}^{\infty} \frac{\mathbf{k} \cdot \mathbf{s}}{\mathbf{k} \cdot \mathbf{k}} \frac{\hat{\mu}'(\mathbf{k} - \mathbf{s})}{\bar{\mu}} d\mathbf{s} \\ &= \int_{-\infty}^{\infty} \frac{\hat{\mu}'(\mathbf{s})}{\bar{\mu}} d\mathbf{s} - \int_{-\infty}^{\infty} \frac{\mathbf{k} \cdot \mathbf{s}}{\mathbf{k} \cdot \mathbf{k}} \frac{\hat{\mu}'(\mathbf{s})}{\bar{\mu}} d\mathbf{s} \\ &= \frac{\mu'(0)}{\bar{\mu}} + \frac{i2\pi\mathbf{k} \cdot \nabla\mu'(0)}{-4\pi^2\mathbf{k} \cdot \mathbf{k}\bar{\mu}} \end{aligned} \quad (3.32)$$

where the last step is obtained by application of the moment theorem [Bracewell, 2003]. We also require invariant convergence properties upon translation, so after Fourier transforming (3.32) to the space domain, one obtains the convergence criterion

$$\left| \frac{\mu'(\mathbf{x})}{\bar{\mu}} \right| < \frac{1}{2} \quad (3.33)$$

where $|\cdot|$ denotes the absolute value. The optimal choice for $\bar{\mu}$, that allows the maximum range of deviations, is

$$\bar{\mu} = \frac{1}{2} \left(\max_{\mathbb{R}^2} \mu(\mathbf{x}) + \min_{\mathbb{R}^2} \mu(\mathbf{x}) \right) \quad (3.34)$$

We have implemented the suggested algorithm for the case of the transform fault (Fig. 3.2a) and performed a series of calculations for various values of $\bar{\mu}$. Results shown in Fig. 3.4 indicate that convergence is obtained only for $\bar{\mu} > \min \mu(\mathbf{x})$ and that the optimal convergence rate is obtained for the value predicted by (3.34). When using SOR, there is much less sensitivity to the choice of $\bar{\mu}$, as convergence is always reached, and convergence rates are always faster compared to the successive approximation method.

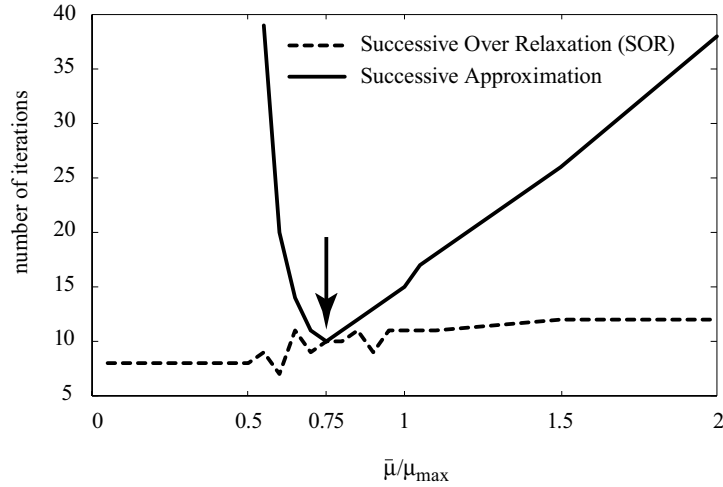


Figure 3.4: Convergence rate of the proposed algorithm as a function of the homogenization constant $\bar{\mu}$. The successive approximation works best for the value predicted by eq. (3.34) (as denoted by arrow). When using SOR, convergence is obtained for all range of $\bar{\mu}$ with an accelerated rate.

3.6 Anisotropy

Here we implement the suggested procedure for the case of anti-plane strain in the presence of arbitrary heterogeneity and anisotropy. The non-zero stress components are

$$\begin{aligned}\sigma_{12} &= 2C_{1212}\varepsilon_{12} = \mu_{12}u_{1,2} \\ \sigma_{13} &= 2C_{1313}\varepsilon_{13} = \mu_{13}u_{1,3}\end{aligned}\tag{3.35}$$

where we denote, for the sake of simplicity, the shear moduli as $\mu_{12} = C_{1212}$ and $\mu_{13} = C_{1313}$. Note that for an isotropic medium, $\mu = C_{1212} = C_{1313}$. The rigidity tensor is decomposed into a constant part and a heterogeneous part as follows,

$$\begin{aligned}\mu_{12}(\mathbf{x}) &= \bar{\mu}_{12} + \mu'_{12}(\mathbf{x}) \\ \mu_{13}(\mathbf{x}) &= \bar{\mu}_{13} + \mu'_{13}(\mathbf{x})\end{aligned}\tag{3.36}$$

and the conservation of linear momentum is written

$$\bar{\mu}_{12}u_{1,22} + \bar{\mu}_{13}u_{1,33} = -f_1 - (\mu'_{12}u_{1,2})_{,2} - (\mu'_{13}u_{1,3})_{,3} \quad (3.37)$$

The algorithm is essentially the same as in the isotropic case, but the equivalent body forces, corresponding to (3.12) in the isotropic case, become

$$\begin{aligned} \hat{g}^n(\mathbf{k}) = & \hat{f}_1 - \omega_2 (\hat{\mu}'_{12} * \omega_2 \hat{u}_1^{n-1}) \\ & - \omega_3 (\hat{\mu}'_{13} * \omega_3 \hat{u}_1^{n-1}) \end{aligned} \quad (3.38)$$

The transfer function is

$$\hat{T}(\mathbf{k}) = (\bar{\mu}_{12}\omega_2^2 + \bar{\mu}_{13}\omega_3^2)^{-1} \quad (3.39)$$

and an optimal value for the SOR parameter is now $\phi = \bar{\mu}_{12}/\mu_{12}^*$ where μ_{12}^* is the horizontal shear modulus μ_{12} on the fault. Similarly, the relevant elastic parameter for the body force representation in the presence of anisotropy is μ_{12} [Burridge and Knopoff, 1964]. As an example, a vertical fault of length L and slip s , starting at depth d , has the equivalent body-force

$$\begin{aligned} \hat{f}_1(\mathbf{k}) = & -s\mu_{12}^* i2\pi k_2 e^{-\pi^2 \Delta x_2^2 k_2^2} \\ & \times L\tilde{\Omega}_\beta(Lk_3) 2 \cos(2\pi k_3(L/2 + d)) \end{aligned} \quad (3.40)$$

Our solution for a dislocation in a heterogeneous and anisotropic half-plane favorably compares to the analytic one, as shown in Fig. 3.2d in the main text.

Chapter 4

Three-dimensional models of elasto-static deformation in heterogeneous media, with applications to the Eastern California Shear Zone

Sylvain Barbot, Yuri Fialko and David Sandwell

Abstract. We present a semi-analytic iterative procedure for evaluating the three-dimensional (3-D) deformation due to faults in an arbitrarily heterogeneous elastic half space. Spatially variable elastic properties are modeled with equivalent body forces and equivalent surface traction in a “homogenized” elastic medium. The displacement field is obtained in the Fourier domain using a semi-analytic Green function. We apply this model to investigate the response of 3-D compliant zones (CZ) around major crustal faults to coseismic stressing by nearby earthquakes. We constrain the two elastic moduli, as well as the geometry of the fault zones by comparing the model predictions to Synthetic Aperture Radar interferometric (InSAR) data. Our results confirm that the compliant zone models for the Rodman, Calico and Pinto Mountain faults in the Eastern California Shear Zone can explain the coseismic InSAR data from both the Landers and the Hector Mine earthquakes. For the Pinto Mountain fault zone, InSAR data suggest a 50% reduction in effective shear modulus and no significant change in Poisson’s ratio compared to the ambient crust. The large wavelength of coseismic line-of-sight displacements around the Pinto Mountain fault requires a fairly wide (~ 1.9 km) CZ extending to a depth of at least 9 km. Best fit for the Calico CZ, north of Galway Dry Lake, is obtained for a 4 km deep structure, with a 60% reduction in shear modulus, with no change in Poisson’s ratio. We find that the required effective rigidity of the Calico fault zone south of Galway Dry Lake is not as low as that of the northern segment, suggesting along-strike variations of effective elastic moduli within the same fault zone. The ECSZ InSAR data is best explained by CZ models with reduction in both shear and bulk moduli. These observations suggest pervasive and widespread damage around active crustal faults.

4.1 Introduction

Crustal faulting is often associated with development of highly fractured and damaged rocks around the primary slip surface [Ambraseys, 1970, Wilson et al., 2004, Chester et al., 2005]. Such damage zones may result from distributed inelastic deformation associated with the propagation and coalescence of cracks and joints during fault growth [Segall and Pollard, 1980, Vermilye and Scholz, 1998, Manighetti et al., 2001], relaxation of stresses at geometric irregularities [Dieterich and Smith, 2007, Liu et al., 2003] or dynamic loading at the propagating rupture front [Rice et al., 2005, Fialko, 2007]. Field observations suggest that the thickness of the cataclastic zones correlates with the cumulative fault slip [Scholz, 1987]. Intense damage gives rise to a reduction in the effective elastic shear modulus of the fault zone material, as predicted by theoretical models [Rybicki and Kasahara, 1977, Kachanov, 1986, Lyakhovskiy et al., 2001, Turcotte et al., 2003], and evidenced by geodetic [Fialko et al., 2002, Chen and Freymueller, 2002, Fialko, 2004a, Hamiel and Fialko, 2007] and seismic [Li et al., 1994, Thurber et al., 2003, Cochran et al., 2009, Ben-Zion et al., 2003] observations.

In a recent study, Cochran et al. [2009] showed that the geodetically inferred kilometer-wide compliant fault zones in the Mojave desert [Fialko et al., 2002, Fialko, 2004a] are also expressed in marked reductions in seismic velocities. The width of the tomographically imaged low velocity zones, as well as the magnitude of velocity reductions were found to be consistent with independent geodetic estimates. Seismic observations reveal the complex structure of the fault damage zones, with large gradients in the effective elastic moduli both laterally and as a function of depth. An accurate description of the deformation due to such fault zones requires models of fault slip in three-dimensional (3-D) heterogeneous media. In this study, we present an efficient algorithm for simulating the deformation due to faulting in the presence of arbitrary spatial variations in elastic properties. Several investigators have proposed ways to tackle this problem [e.g., Du et al., 1997, Moulinec and Suquet, 1998, Pollitz, 2003a]. The approach of Du et al. [1997] is limited to discrete variations in elastic properties. The method of Pollitz [2003a] is more general, allowing gradual variations in elastic -and viscous- parameters, but the normal-mode based solution makes it less practical for small-scale problems. Moulinec and Suquet [1998] and other investigators [Brown et al., 2003, Lebensohn, 2001, Yu et al., 2005] base their solution on a Fourier representation but do not include the free surface. All these semi-analytic techniques use essentially a perturbation approach and are limited to small variations in elastic properties. Our proposed method relaxes the constraint of weak inclusions and allows gradual variations in shear and bulk moduli. Our Fourier-domain semi-analytic solution is adequate for modeling intermediate-scale static deformation, such as fault slip in the presence of neighboring compliant zones.

In the Section 4.2, we present the governing equations and boundary conditions relevant to a three-dimensional heterogeneous problem. We generalize the description of dislocations in

terms of double-couple equivalent body forces by including equivalent surface traction in case of faults extending to the Earth’s surface. This generalized representation allows us to model normal, reverse and strike-slip faults of arbitrary geometry. We then present some iterative methods that evaluate the displacement field based on the homogenization of elastic properties. One such method is the successive approximation (SA) [Barbot et al., 2008a]; we show that it is in essence equivalent to the perturbation method [e.g., Du et al., 1994, 1997, Pollitz, 2003a, Yu et al., 2005]. The successive approximations and the perturbation methods are adequate for small variations in elastic properties [Moulinec and Suquet, 1998, Barbot et al., 2008a]. Another approach is the successive over-relaxation (SOR) method [Barbot et al., 2008a], which allows for larger contrasts in elastic properties. Comparisons with analytic solutions and some example calculations are presented in Appendix A. We apply our numerical method to model the static deformation in the Eastern California Shear Zone due to the 1992 Landers and 1999 Hector Mine earthquakes. We combine the model predictions with InSAR observations to refine inferences about the mechanical properties, geometry and structure of compliant zones associated with the Calico, Rodman and Pinto Mountain faults of the East California Shear Zone.

4.2 3-D Models of Deformation due to Faulting in Heterogeneous Media

In this section, we derive a 3-D model of elastostatic deformation in a semi-infinite solid with a free-surface boundary condition and 3-D variations in elastic properties. The formulation for 2-D antiplane deformation can be found in Barbot et al. [2008a]. We will first derive the forcing terms representing the effect of internal dislocations. Equivalent representations of dislocations include eigenstrain -Eq. (5.58)-, moment density -Eq. (4.6)- and equivalent body forces (including the equivalent surface traction) -Eqs. (4.9) and (4.13), respectively. We show that the governing equation is the inhomogeneous Navier’s equation with non-constant coefficients and Neumann-type boundary conditions. Next we discuss some iterative solution methods based on the decomposition of the elastic moduli. Finally, we present some details on the numerical implementation and discuss results from our numerical benchmarks of Appendix A.

4.2.1 Governing equation and boundary conditions

Consider a heterogeneous elastic body Ω comprised of two interfaced volumes with dissimilar elastic properties cut by a shear dislocation α (see Fig. 4.1). The surface of the elastic body $\partial\Omega$ is assumed to be traction free. A dislocation characterized by slip \mathbf{s}^α on a surface with normal vector $\hat{\mathbf{n}}^\alpha$ is associated with the eigenstrain tensor [Backus and Mulcahy, 1976b,

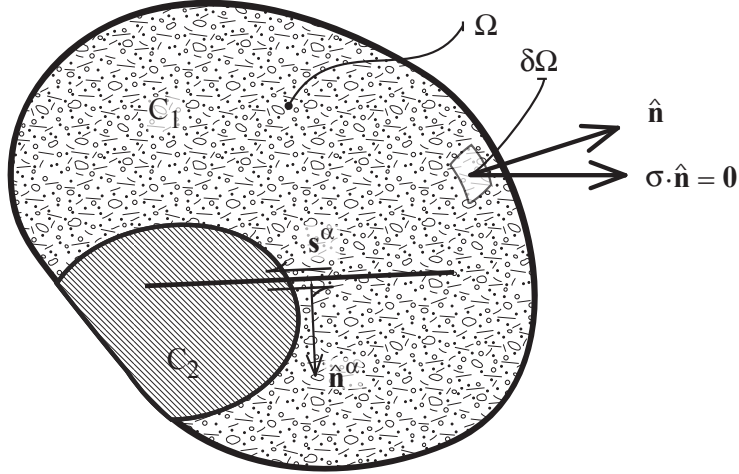


Figure 4.1: The deformation of a heterogeneous elastic body Ω is driven by internal dislocations. A failure plane with normal $\hat{\mathbf{n}}^\alpha$ and slip \mathbf{s}^α cuts the volume with elastic tensors $\mathbf{C}_1 \neq \mathbf{C}_2$. The slip system α is associated with eigenstrain $\boldsymbol{\epsilon}^\alpha(\mathbf{x}) = \frac{1}{2}(\mathbf{s}^\alpha \otimes \hat{\mathbf{n}}^\alpha + \hat{\mathbf{n}}^\alpha \otimes \mathbf{s}^\alpha)$, moment density $\mathbf{m}^\alpha(\mathbf{x}) = \mathbf{C} : \mathbf{s}^\alpha \otimes \hat{\mathbf{n}}^\alpha$ and equivalent body force $\mathbf{f}^\alpha(\mathbf{x}) = -\nabla \cdot \mathbf{m}^\alpha$. The surface boundary $\partial\Omega$, with normal vector $\hat{\mathbf{n}}$, is traction free ($\boldsymbol{\sigma} \cdot \hat{\mathbf{n}} = \mathbf{0}$).

Nemat-Nasser, 2004, Barbot et al., 2008a, 2009a]

$$\boldsymbol{\epsilon}^\alpha(\mathbf{x}) = \frac{1}{2}(\mathbf{s}^\alpha \otimes \hat{\mathbf{n}}^\alpha + \hat{\mathbf{n}}^\alpha \otimes \mathbf{s}^\alpha) \quad (4.1)$$

where operator \otimes is the dyadic product (for example if \mathbf{a} and \mathbf{b} are two vectors, then in index notation the product $\mathbf{a} \otimes \mathbf{b}$ is the second-order tensor $a_i b_j$). Both $\hat{\mathbf{n}}^\alpha$ and \mathbf{s}^α may in general vary along the dislocation surface. The eigenstrain depends on the geometry of a dislocation but is independent of elastic properties of the ambient solid. The static deformation undergone by body Ω compared to a reference state is characterized by the total strain $\boldsymbol{\epsilon}$, the sum of elastic and inelastic strains

$$\boldsymbol{\epsilon} = \boldsymbol{\epsilon}^e + \boldsymbol{\epsilon}^i \quad (4.2)$$

where $\boldsymbol{\epsilon}^i$ is the total inelastic eigenstrain due to internal dislocations

$$\boldsymbol{\epsilon}^i(\mathbf{x}) = \sum_{\alpha=1}^n \boldsymbol{\epsilon}^\alpha(\mathbf{x}), \quad (4.3)$$

where n is the total number of dislocations. The eigenstrain (4.3) is a tensor-valued forcing term and should not be confused with the elastic strain in the near field of the dislocation. Notice that the eigenstrain tensor is identically zero away from a dislocation. In general, any degree of localization of eigenstrain can be represented using generalized functions such as boxcar or Dirac-delta functions. For discussions and examples on the use of generalized functions for body-force

representation, see Backus and Mulcahy [1976b], Barbot et al. [2008a] and Barbot et al. [2009a]. In a heterogeneous body Ω with the tensor of elastic moduli $\mathbf{C} = \mathbf{C}(\mathbf{x})$, the Cauchy stress

$$\boldsymbol{\sigma} = \mathbf{C} : \boldsymbol{\epsilon}^e \quad (4.4)$$

where operation $:$ is the double scalar product (for instance if \mathbf{A} and \mathbf{B} are two second-order tensors, then in index notation the product $\mathbf{A} : \mathbf{B}$ is the scalar $A_{ij}B_{ij}$), can be written using Eq. (4.2) as follows,

$$\boldsymbol{\sigma} = \mathbf{C} : \boldsymbol{\epsilon} - \mathbf{C} : \boldsymbol{\epsilon}^i \quad (4.5)$$

where the second term can be recognized as the moment density [Aki and Richards, 1980, Shearer, 1999],

$$\mathbf{m}(\mathbf{x}) = \sum_{\alpha=1}^n \mathbf{C}(\mathbf{x}) : \boldsymbol{\epsilon}^\alpha. \quad (4.6)$$

As elastic properties are spatially variable, the moment density is not necessarily uniform along a dislocation surface. Using Eq. (5.49), the conservation of momentum for static equilibrium in Ω can be written [Malvern, 1969, Nemat-Nasser and Hori, 1999]

$$\nabla \cdot (\mathbf{C} : \boldsymbol{\epsilon}) - \nabla \cdot (\mathbf{C} : \boldsymbol{\epsilon}^i) = 0 \quad (4.7)$$

The second term in Eq. (4.7) depends upon the distribution and orientation of internal dislocations in Ω . The effect of all internal dislocations may be represented using equivalent body forces [Eshelby, 1957, Burridge and Knopoff, 1964, Nemat-Nasser, 2004]

$$\mathbf{f}(\mathbf{x}) = -\nabla \cdot (\mathbf{C} : \boldsymbol{\epsilon}^i) = \sum_{\alpha=1}^n \mathbf{f}^\alpha(\mathbf{x}) \quad (4.8)$$

where

$$\mathbf{f}^\alpha(\mathbf{x}) = -\nabla \cdot (\mathbf{C} : \mathbf{s}^\alpha \otimes \hat{\mathbf{n}}^\alpha) \quad (4.9)$$

is the equivalent body-force density due to an individual dislocation α , and \mathbf{s}^α and $\hat{\mathbf{n}}^\alpha$ refer to the Burger's vector and the normal direction of dislocation α , respectively. As dislocations may cut across heterogeneous regions, the equivalent body force (4.9) may not be readily reduced to a double couple. The conservation of momentum can now be written as

$$\nabla \cdot (\mathbf{C} : \boldsymbol{\epsilon}) + \mathbf{f} = 0, \quad (4.10)$$

where

$$\boldsymbol{\epsilon} = \frac{1}{2}(\nabla \otimes \mathbf{u} + (\nabla \otimes \mathbf{u})^t) \quad (4.11)$$

is the total strain and $\mathbf{u}(\mathbf{x})$ is the associated displacement. Governing Eq. (4.10) simplifies to the Navier's equation for a homogeneous isotropic elastic medium. The equivalent body force density $\mathbf{f}(\mathbf{x})$ depends upon the elastic structure $\mathbf{C}(\mathbf{x})$. The force distribution represents the effect of all internal dislocations and for now is supposed to be known.

We seek the displacement field $\mathbf{u}(\mathbf{x})$ within Ω that satisfies governing Eq. (4.10) subject to the free surface boundary condition. The surface traction can be expressed in terms of the total strain,

$$\begin{aligned}\boldsymbol{\sigma} \cdot \hat{\mathbf{n}} &= \hat{\mathbf{n}} \cdot (\mathbf{C} : \boldsymbol{\epsilon}^e) \\ &= \hat{\mathbf{n}} \cdot (\mathbf{C} : \boldsymbol{\epsilon}) - \hat{\mathbf{n}} \cdot (\mathbf{C} : \boldsymbol{\epsilon}^i)\end{aligned}\tag{4.12}$$

so that dislocations cutting through the boundary $\partial\Omega$ contribute to the equivalent surface traction as follows,

$$\begin{aligned}\mathbf{t} &= \hat{\mathbf{n}} \cdot (\mathbf{C} : \boldsymbol{\epsilon}^i) \\ &= \sum_{\alpha=1}^n \hat{\mathbf{n}} \cdot (\mathbf{C} : \mathbf{s}^\alpha \otimes \mathbf{n}^\alpha)\end{aligned}\tag{4.13}$$

where \mathbf{n}^α and \mathbf{s}^α are evaluated at the surface. The equivalent surface traction due to a dislocation α is therefore

$$\mathbf{t}^\alpha = \hat{\mathbf{n}} \cdot (\mathbf{C} : \mathbf{s}^\alpha \otimes \mathbf{n}^\alpha)\tag{4.14}$$

The presence of non-vanishing equivalent surface traction depends upon the relative orientation of the normal direction at the surface $\partial\Omega$ and the moment density $\mathbf{m}^\alpha = \mathbf{C} : (\mathbf{s}^\alpha \otimes \hat{\mathbf{n}}^\alpha)$ of dislocations that cut the surface [Backus and Mulcahy, 1976a]. A vertical strike-slip fault at the surface of a half-space, for example, is not associated with equivalent surface traction. Figure 4.2 shows the equivalent body-force distribution and the equivalent normal traction due to a given point dislocation intersecting the surface of a half-space in case of isotropic elasticity. The moment density of dislocation α with arbitrary direction is decomposed into six linearly independent directions in a symmetric tensor space. Whereas equivalent body forces for a point-source dislocation simplify to a double couple, the equivalent surface traction \mathbf{t}^α simplifies to a simple traction vector: purely tangential traction for off-diagonal moment density components and purely normal traction for diagonal components. Equivalent body forces and equivalent surface traction are dual through the application of the divergence theorem. Using Eq. (4.12), the free surface boundary condition in the presence of dislocations at the surface of Ω can be written as

$$\hat{\mathbf{n}} \cdot (\mathbf{C} : \boldsymbol{\epsilon}) = \mathbf{t} = \sum_{\alpha=1}^n \mathbf{t}^\alpha \quad \text{on } \partial\Omega.\tag{4.15}$$

Internal dislocations and associated boundary conditions can therefore be reduced to some equivalent body-force density $\mathbf{f}(\mathbf{x})$ in Ω and some equivalent normal traction \mathbf{t} on $\partial\Omega$. In the case of homogeneous and isotropic elasticity, the problem simplifies to Navier's equation with forcing terms and inhomogeneous boundary conditions.

4.2.2 Decomposition of Elastic Moduli

Our approach to solving the governing equation (4.10) subject to boundary condition (4.15) consists in using the elastic Green function for a homogeneous medium and in identi-

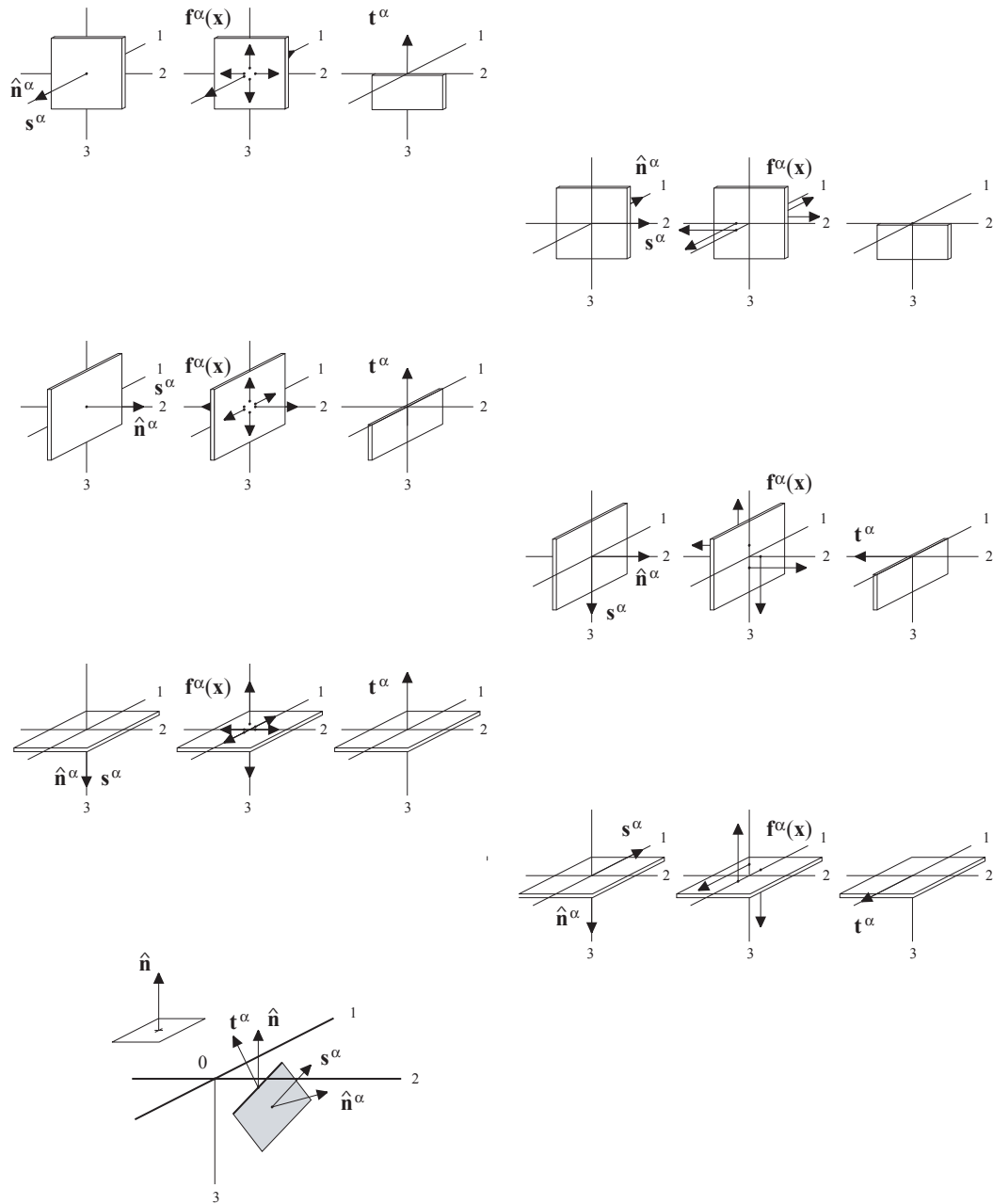


Figure 4.2: An arbitrary slip system α for a point source dislocation (bottom sketch) can be decomposed into six linearly independent components. Eigenstrain ϵ^α is associated with an equivalent body force distribution $\mathbf{f}^\alpha(\mathbf{x})$ and equivalent surface traction \mathbf{t}^α . Equivalent surface traction occurs when fractures reach to the surface of the semi-infinite solid.

ifying a set of equivalent body force and equivalent surface traction that represents the effect of spatial variations in elastic properties.

Consider the following decomposition of the elastic moduli tensor $\mathbf{C}(\mathbf{x})$ into a constant, homogeneous part \mathbf{C}_0 and a spatially variable part $\mathbf{C}'(\mathbf{x})$, such that

$$\mathbf{C}(\mathbf{x}) = \mathbf{C}_0 - \mathbf{C}'(\mathbf{x}). \quad (4.16)$$

We define

$$\boldsymbol{\sigma}' = \mathbf{C}' : \boldsymbol{\epsilon}, \quad (4.17)$$

the moment density corresponding to spatial variations in elastic properties. Using Eqs. (4.10) and (4.16), we now can write the governing equation as follows,

$$\nabla \cdot (\mathbf{C}_0 : \boldsymbol{\epsilon}) + \mathbf{f} - \nabla \cdot \boldsymbol{\sigma}' = 0. \quad (4.18)$$

The variations in elastic properties introduce the moment density $\mathbf{m}' = \mathbf{C}' : \nabla \otimes \mathbf{u}$ and the equivalent body-force representation of the effects of the inhomogeneous elastic properties in the “homogenized” medium is

$$\mathbf{f}'(\mathbf{x}) = -\nabla \cdot \boldsymbol{\sigma}' \quad (4.19)$$

Notice that the body force representation for dislocations is unaffected by the elastic moduli decomposition. The moment density introduced by internal dislocations is a function of the actual elastic properties $\mathbf{C}(\mathbf{x})$ of the body. Making use of Eq. (4.16), the surface traction becomes

$$\begin{aligned} \boldsymbol{\sigma} \cdot \hat{\mathbf{n}} &= \hat{\mathbf{n}} \cdot (\mathbf{C}_0 : \boldsymbol{\epsilon}) \\ &- \hat{\mathbf{n}} \cdot (\mathbf{C}' : \boldsymbol{\epsilon}) - \hat{\mathbf{n}} \cdot (\mathbf{C} : \boldsymbol{\epsilon}^i) = 0 \end{aligned} \quad (4.20)$$

Consequently, the free surface boundary condition in the homogenized body can be expressed as follows

$$\hat{\mathbf{n}} \cdot (\mathbf{C}_0 : \boldsymbol{\epsilon}) = \mathbf{t} + \mathbf{t}' \quad \text{on } \partial\Omega, \quad (4.21)$$

where

$$\mathbf{t}' = \boldsymbol{\sigma}' \cdot \hat{\mathbf{n}} \quad (4.22)$$

is the surface traction due to deviations from the homogenized elastic properties at the surface $\partial\Omega$. In case of a layered medium, if \mathbf{C}_0 is chosen to correspond to the value of $\mathbf{C}(\mathbf{x})$ in the top layer, the additional equivalent surface traction simply vanish as $\mathbf{C}'(\mathbf{x}) = 0$ on $\partial\Omega$. Similar to the equivalent body forces, the equivalent surface traction \mathbf{t} due to internal dislocations is unaffected by the decomposition of the elastic moduli tensor.

Decomposition (4.16) allows us to transform an equation with non-constant coefficients into a homogeneous equation with modified boundary conditions and additional internal forcing

terms. For known equivalent body forces and surface traction representing the elastic heterogeneity, the solution for a displacement field is [Aki and Richards, 1980]

$$\begin{aligned} \mathbf{u}(\mathbf{x}) &= \int_{\Omega} \mathbf{G}(\mathbf{x}, \mathbf{x}_0) \cdot [\mathbf{f}(\mathbf{x}_0) + \mathbf{f}'(\mathbf{x}_0)] d\mathbf{x}_0 \\ &+ \int_{\partial\Omega} \mathbf{G}(\mathbf{x}, \mathbf{x}_0) \cdot [\mathbf{t}(\mathbf{x}_0) + \mathbf{t}'(\mathbf{x}_0)] d\mathbf{x}_0 \end{aligned} \quad (4.23)$$

where $\mathbf{G}(\mathbf{x}, \mathbf{x}_0)$ is the Green function tensor (see [Love, 1927, Mindlin, 1936a] for the case of a semi-infinite solid) for an elastic body with a homogeneous elastic moduli tensor \mathbf{C}_0 . However, one cannot readily evaluate Eq. (4.23), as the distribution of body forces mimicking the presence of heterogeneities needs to be determined as part of the solution.

4.2.3 The Successive Approximation Method

One way to solve the heterogeneous problem (Eq. (4.23)) is to use the method of successive approximations [Bender and Orszag, 1978, Delves and Mohamed, 1985, Kato, 1980]. Extending the approach proposed by Barbot et al. [2008a] to the case of three-dimensional deformation, we adopt the following iterative procedure

$$\begin{aligned} \mathbf{u}_n(\mathbf{x}) &= \int_{\Omega} \mathbf{G} \cdot [\mathbf{f} - \nabla \cdot (\mathbf{C}' : \nabla \mathbf{u}_{n-1})] dV \\ &+ \int_{\partial\Omega} \mathbf{G} \cdot [\mathbf{t} + (\mathbf{C}' : \nabla \mathbf{u}_{n-1}) \cdot \hat{\mathbf{n}}] dA \end{aligned} \quad (4.24)$$

where index n denotes a level of approximation. Noticing integrals in Eq. (4.24) are linear with respect to \mathbf{u} , we define an operator

$$\begin{aligned} \mathcal{L}[\mathbf{v}] &= - \int_{\Omega} \mathbf{G} \cdot [\nabla \cdot (\mathbf{C}' : \nabla \mathbf{v})] dV \\ &+ \int_{\partial\Omega} \mathbf{G} \cdot [(\mathbf{C}' : \nabla \mathbf{v}) \cdot \hat{\mathbf{n}}] dA, \end{aligned} \quad (4.25)$$

where \mathbf{v} is a vector field in Ω . We then define the first non-zero term in series (4.24)

$$\begin{aligned} \mathbf{u}_0(\mathbf{x}) &= \int_{\Omega} \mathbf{G}(\mathbf{x}, \mathbf{x}_0) \cdot \mathbf{f}(\mathbf{x}_0) d\mathbf{x}_0 \\ &+ \int_{\partial\Omega} \mathbf{G}(\mathbf{x}, \mathbf{x}_0) \cdot \mathbf{t}(\mathbf{x}_0) dA. \end{aligned} \quad (4.26)$$

Using Eqs. (4.25) and (4.26), the proposed iterative procedure (4.24) can now be written as

$$\mathbf{u}_n(\mathbf{x}) = \mathbf{u}_0(\mathbf{x}) + \mathcal{L}[\mathbf{u}_{n-1}] \quad (4.27)$$

where $\mathbf{u}_0(\mathbf{x})$ is the first approximate solution, and the true solution to the heterogeneous problem is (assuming non-biased convergence),

$$\mathbf{u}(\mathbf{x}) = \lim_{n \rightarrow \infty} \mathbf{u}_n(\mathbf{x}) \quad (4.28)$$

We refer to formulation (4.24)-(4.27) as the Successive Approximation (SA) method to evaluate the solution of the heterogeneous elastic problem governed by Eq. (4.10) with boundary condition (4.15). The SA method is used in various geophysical contexts including flexure of the oceanic lithosphere [Sandwell, 1984], mantle convection [Gable et al., 1991], deformation of heterogeneous mineral composites [Moulinec and Suquet, 1998, Lebensohn, 2001, Brown et al., 2003] and volcano geodesy [Fialko et al., 2001a]. Iterative methods such as the SA allow one to handle complex media for which an exact Green function is not readily available.

4.2.4 The Perturbation Method

The successive approximation series (4.27) can be reorganized in a form of an infinite sum [Kato, 1980],

$$\mathbf{u}_n = \mathbf{u}^{(0)} + \sum_{k=1}^n \mathbf{u}^{(k)}, \quad n \in \mathbb{N}^* \quad (4.29)$$

with the recursive relation

$$\mathbf{u}^{(k)} = \mathcal{L}[\mathbf{u}^{(k-1)}] \quad (4.30)$$

and initial value

$$\mathbf{u}^{(0)} \equiv \mathbf{u}_0(\mathbf{x}) \quad (4.31)$$

The proof can be obtained by recurrence: consider the first iteration of the successive approximation solution

$$\begin{aligned} \mathbf{u}_1 &= \mathbf{u}_0 + \mathcal{L}[\mathbf{u}_0] = \mathbf{u}^{(0)} + \mathcal{L}[\mathbf{u}^{(0)}] \\ &= \mathbf{u}^{(0)} + \sum_{k=1}^1 \mathcal{L}[\mathbf{u}^{(k)}] \end{aligned} \quad (4.32)$$

Assuming that Eqs. (4.29) and (4.30) hold true for $n > 1$, we consider iteration $n + 1$

$$\begin{aligned} \mathbf{u}_{n+1} &= \mathbf{u}_0 + \mathcal{L}[\mathbf{u}_n] \\ &= \mathbf{u}^{(0)} + \mathcal{L} \left[\mathbf{u}^{(0)} + \sum_{k=1}^n \mathbf{u}^{(k)} \right] \\ &= \mathbf{u}^{(0)} + \mathcal{L}[\mathbf{u}^{(0)}] + \sum_{k=1}^n \mathcal{L}[\mathbf{u}^{(k)}] \\ &= \mathbf{u}^{(0)} + \mathbf{u}^{(1)} + \sum_{k=1}^n \mathbf{u}^{(k+1)} \\ &= \mathbf{u}^{(0)} + \sum_{k=1}^{n+1} \mathbf{u}^{(k)} \end{aligned} \quad (4.33)$$

where we took advantage of the fact that \mathcal{L} is a linear operator and thus can be moved inside the sum. As Eqs. (4.29) and (4.30) hold at iteration n , they must also hold at iteration $n + 1$. Therefore we have shown by recurrence that the successive approximation series (4.27) can be written

as the finite sum (4.29). The ultimate solution associated with the recurrence relation (4.30) is therefore

$$\mathbf{u}(\mathbf{x}) = \mathbf{u}^{(0)}(\mathbf{x}) + \sum_{n=1}^{\infty} \mathbf{u}^{(n)}(\mathbf{x}) \quad (4.34)$$

Formulation (4.34) is referred to as the perturbation method to solve Eq. (4.23). The perturbation method was used by Du et al. [1994, 1997] to model deformation due to faulting in heterogeneous media with some limiting assumptions about the spatial variations of elastic moduli. Our approach allows one to model gradual changes in elastic moduli as well as to evaluate numerically virtually any number of higher-order approximations of the true solution.

4.2.5 The Successive Over Relaxation Method

The Successive Over-Relaxation (SOR) technique [Press et al., 1992, Barbot et al., 2008a] is a minor modification of the successive approximation method. Defining a linear operator

$$\begin{aligned} T[\mathbf{v}] = & \int_{\Omega} \mathbf{G} \cdot [\mathbf{f} - \nabla \cdot (\mathbf{C}' : \nabla \mathbf{v})] dV \\ & + \int_{\partial\Omega} \mathbf{G} \cdot [\mathbf{t} + (\mathbf{C}' : \nabla \mathbf{v}) \cdot \hat{\mathbf{n}}] dA \end{aligned} \quad (4.35)$$

where \mathbf{v} is a vector field in Ω , the successive approximation method can be written

$$\mathbf{u}_n = T[\mathbf{u}_{n-1}] . \quad (4.36)$$

A natural way of regularizing the numerical evaluation of Eq. (4.36) is to use the successive over-relaxation method [Golub and Van Loan, 1996]: The iterative procedure becomes

$$\mathbf{u}_n = (1 - \phi) \mathbf{u}_{n-1} + \phi T[\mathbf{u}_{n-1}] \quad (4.37)$$

where $0 < \phi < 2$ is the SOR parameter. Obviously, the successive over relaxation method simplifies to the successive approximation or the perturbation method for $\phi = 1$. Solutions for cracked media with large variations in elastic properties can be obtained using $\phi \simeq 0.5$ when the homogenized elastic tensor satisfies certain conditions (e.g., see Eq. (4.43) in Section 2.5).

In practice, we use only a limited number of terms in the SOR series (4.37) or the perturbation method series (4.34). An estimate of the body force representing the presence of faults and variable elastic moduli is

$$\tilde{\mathbf{f}}_n = \mathbf{f} - \nabla \cdot (\mathbf{C}' : \nabla \mathbf{u}_n) , \quad (4.38)$$

and a common convergence criterion for the SA and SOR methods is

$$\frac{\langle \|\tilde{\mathbf{f}}_n\|^2 \rangle - \langle \|\tilde{\mathbf{f}}_{n-1}\|^2 \rangle}{\langle \|\mathbf{f}\|^2 \rangle} < \epsilon, \quad (4.39)$$

where ϵ is the tolerance (hereafter, we use $\epsilon = 10^{-6}$), and the angular bracket operator $\langle \cdot \rangle$ denotes integration over the domain Ω .

4.2.6 Homogenization of Elastic Moduli

The perturbation and the successive approximation methods are adequate only in case of small variations in elastic properties [Moulinec and Suquet, 1998, Barbot et al., 2008a]. For instance, in case of anti-plane deformation, a necessary convergence criterion is satisfied when rigidity contrasts are less than a factor of two of the homogenized value [Barbot et al., 2008a]. In the case of an isotropic heterogeneous body under condition of antiplane strain, the fastest convergence of the SA method is obtained for a homogenized rigidity that minimizes the maximum effective rigidity contrast in the body [Barbot et al., 2008a]. To generalize this result to three-dimensional deformation, we note that the isotropic elastic tensor can be decomposed into the pure volumetric and pure shear directions in tensor space, \mathbf{E}_1 and \mathbf{E}_2 , respectively [Hill, 1965, Nemat-Nasser and Hori, 1999]

$$\mathbf{E}_1 = \frac{1}{3}\mathbf{1}^{(2)} \otimes \mathbf{1}^{(2)}, \quad \mathbf{E}_2 = \mathbf{1}^{(4s)} - \frac{1}{3}\mathbf{1}^{(2)} \otimes \mathbf{1}^{(2)} \quad (4.40)$$

where $\mathbf{1}^{(4s)}$ is the symmetric and unitary fourth-order tensor and $\mathbf{1}^{(2)}$ is the second-order unitary tensor. Tensors \mathbf{E}_1 and \mathbf{E}_2 satisfy the orthonormality relations

$$\begin{aligned} \mathbf{E}_1 &= \mathbf{E}_1 : \mathbf{E}_1 \\ \mathbf{E}_2 &= \mathbf{E}_2 : \mathbf{E}_2 \\ \mathbf{E}_1 : \mathbf{E}_2 &= \mathbf{E}_2 : \mathbf{E}_1 = 0 \end{aligned} \quad (4.41)$$

and form a base for any isotropic fourth-order tensor. The isotropic elastic moduli tensor can therefore be written

$$\mathbf{C}(\mathbf{x}) = 3\kappa(\mathbf{x})\mathbf{E}_1 + 2G(\mathbf{x})\mathbf{E}_2 \quad (4.42)$$

where $\kappa = \lambda + 2G/3$ and G are the bulk and shear moduli that can vary spatially. As strain directions \mathbf{E}_1 and \mathbf{E}_2 are orthogonal, the constraints on the elastic moduli tensor reduce to independent constraints on scalars κ and G . Consequently, we choose the following values for the homogenized elastic parameters,

$$\begin{aligned} G_0 &= \frac{1}{2} \left(\max_{\Omega} G(\mathbf{x}) + \min_{\Omega} G(\mathbf{x}) \right), \\ \kappa_0 &= \frac{1}{2} \left(\max_{\Omega} \kappa(\mathbf{x}) + \min_{\Omega} \kappa(\mathbf{x}) \right). \end{aligned} \quad (4.43)$$

Given $\lambda_0 = \kappa_0 - 2G_0/3$, the homogenized isotropic tensor is therefore

$$\mathbf{C}_0 = \lambda_0 \mathbf{1}^{(2)} \otimes \mathbf{1}^{(2)} + 2G_0 \mathbf{1}^{(4s)}. \quad (4.44)$$

In Appendix A we demonstrate that the numerical constraint of small variations in elastic properties within volume Ω can indeed be relaxed by application of the successive over relaxation technique.

4.2.7 Implementation

We adopt a numerical approach presented by Barbot et al. [2008a] for 2-D antiplane strain and generalize it to the case of 3-D deformation. Sources of deformation include tensile cracks and strike-slip and dip-slip faults of arbitrary orientation and position in the half space. Notice that equivalent surface traction and the equivalent body forces appear in the representation of both the forcing terms due to internal dislocations and the effect of inclusions. Models of deformation in a homogeneous half space or in a 3-D heterogeneous half space can therefore be evaluated with the same elastic Green function, one which satisfies a prescribed traction boundary condition at the surface.

We perform the convolution between the equivalent body forces and the Green function for the homogeneous elastic half-space numerically in the Fourier domain. The expansion of the displacement field in a Fourier series introduces a periodicity in the solution that limits the solution accuracy near the edges of the computational grid. We mitigate this bias by using large computational domains, such that deformation sources are sufficiently far from the boundaries (except the free surface). We take advantage of the convolution theorem and the fast Fourier transforms to reduce the computational burden (compared, e.g., to convolutions in the space domain). We use the Boussinesq's [Steketee, 1958a,b] and Cerruti's [Love, 1927, Mindlin, 1936a] solutions for normal and tangential surface loading, respectively, to satisfy the free surface boundary condition.

We compute the gradient of the displacement field and the divergence of the moment density using finite impulse differentiator filters (FIR) [McClellan et al., 1973, Farid and Simoncelli, 2004] in the bulk of the half space, and simple finite difference schemes near the surface, in the vertical direction. The impulse response of finite difference filters has a narrow bandwidth so using FIR filters allows us to compute more precise and more localized derivatives. Numerical evaluation of derivatives is critical to preserve the accuracy throughout multiple iterations in both the perturbation and the SOR methods. We taper the dislocations using the Ω_β function (see Eq. (17) in [Barbot et al., 2008a]) to obtain band-limited sources and limit a potential Gibbs phenomenon [Bracewell, 2003] in the resulting displacement field near the faults. The tapering also suppresses the stress singularity at a fault tip.

The numerical technique was extensively validated against analytic solutions for antiplane-strain problems with lateral and vertical layering [Barbot et al., 2008a]. The accuracy of dislocation models that use the Fourier-domain Green function in a 3-D homogeneous half-space is discussed in [Barbot et al., 2009a, Appendix B3]. We performed some additional benchmarks for 3-D deformation in a 3-D heterogeneous half-space in Appendix A. These tests include cases of vertical and lateral variations in elastic properties, models of faults cutting through different elastic materials, large elasticity contrasts using the SOR method and forcing terms due to strike-slip and dip-slip faults. In general, the accuracy of the iterative solution away from the

(periodic) boundary is about 5 to 10% of the expected elastic structure contribution, the largest error arising from the strongest elastic contrast: If the expected signal due to the rigidity variation is 10% of the total displacement, then our numerical solution is associated with a 0.5% to 1% bias. The accuracy of our method as shown by comparisons with other analytic, semi-analytic or numerical solutions and our ability to include complex geometric structures makes this approach adequate to model deformation due to faulting in a heterogeneous crust.

4.3 Application to Compliant Fault Zones in the Mojave Desert

The Eastern California Shear Zone (ECSZ) is a region of active deformation that strikes northwest-southeast across the central Mojave desert [Dokka and Travis, 1990a,b, Savage et al., 1980, Sauber et al., 1994]. The ECSZ extends from the San Geronio bend of the San Andreas fault in the south to Owens Valley and the northern Basin and Range province. A system of young strike-slip faults comprising the ECSZ accommodates 8 to 14 mm/yr of motion between the North American and Pacific plates [Sauber et al., 1994, Miller et al., 2001, Oskin and Iriondo, 2004]. Active deformation within the ECSZ was highlighted by the occurrence of the 1992 Mw 7.3 Landers [Massonnet et al., 1993, Sieh et al., 1993] and the 1999 Mw 7.1 Hector Mine [Hauksson et al., 2002, Sandwell et al., 2000, Simons et al., 2002, Fialko et al., 2001b] earthquakes.

Early Interferometric Synthetic Aperture Radar (InSAR) observations of the Hector Mine earthquake revealed intriguing small-scale displacements along the satellite line-of-sight (LOS) on faults adjacent to the main rupture [Sandwell et al., 2000]. These anomalous LOS displacements were later interpreted to represent the response of compliant zones (tabular volumes of reduced rigidity), to the permanent co-seismic stress changes induced by the Hector Mine earthquake [Fialko et al., 2002]. Inspection of InSAR data from the 1992 Landers, CA earthquake also revealed small-scale deformation on pre-existing faults and confirmed that this deformation is consistent with the compliant zone response to coseismic loading [Fialko, 2004a]. Seismic probing of the Calico fault zone including trapped waves studies, and travelttime analysis of teleseismic and active source data discovered the existence of a low-velocity zone along the Calico fault coincident with the geodetically inferred compliant zone [Cochran et al., 2006, 2009]. Figure 4.3 shows the maximum gradients of the LOS displacement residuals (track 127, frame 2907, from January, 13th 1999 to October, 20th 1999) computed after removing the Hector Mine earthquake coseismic model of Simons et al. [2002]. Figure 4.3 illustrates amplified deformation around faults located near the Hector Mine rupture. In particular, the Calico-Hidalgo (CH), the Rodman (RM), the Pinto Mountain (PM), the Homestead-Johnson Valley and the Emerson faults all exhibit some anomalous strain. Location of the seismic experiment of Cochran et al. [2006] is indicated with the black triangle. Some of the localized strain seen in Fig. 4.3 may be

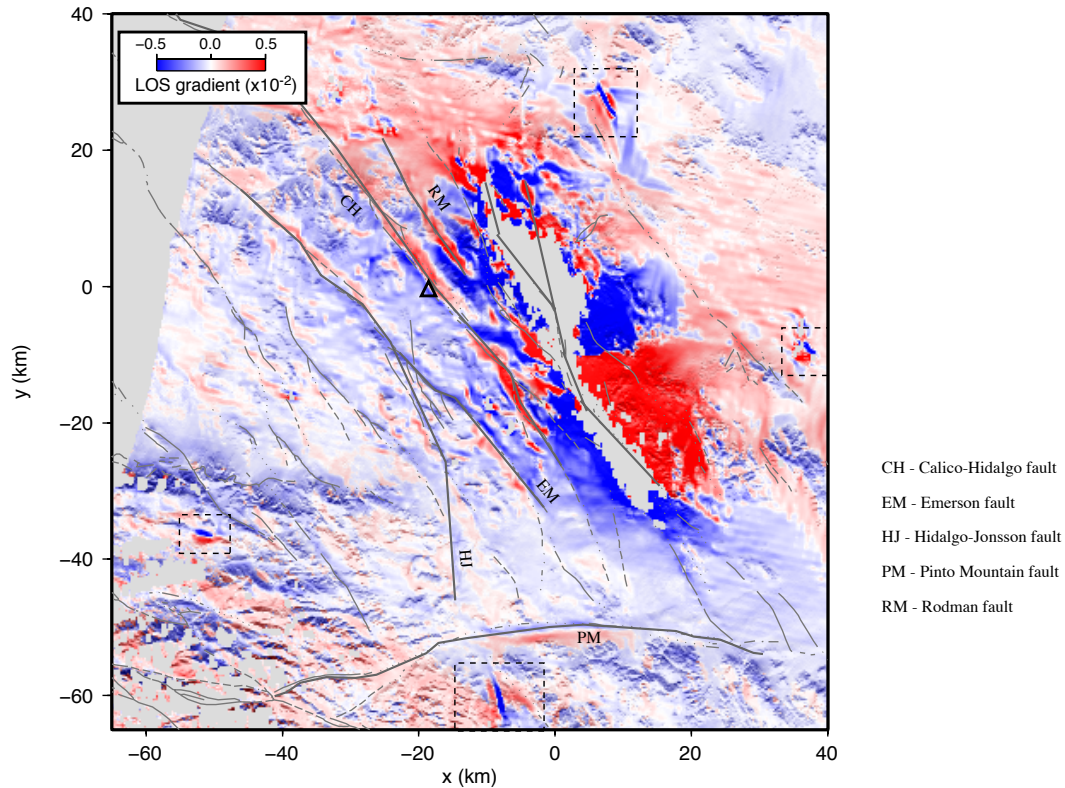


Figure 4.3: Gradient of the LOS displacement residuals after the Hector Mine coseismic model was removed. Gradient emphasizes deformation around nearby faults and underlines possible creep events (dashed quadrants). Triangle indicates location of the seismic experiment of *Cochran et al.* [2008].

due to shallow creep events (outlined by dashed rectangles). For example, the localized strain south of the Pinto Mountain fault in the Yucca Valley occurred prior to the Hector Mine earthquake, as it is absent in interferograms that bracket the Hector Mine earthquake more tightly. This localized strain is associated with a history of seismic swarms [Jones and Helmberger, 1998]. The other three anomalous strain areas appear to be aseismic.

Previous studies of small-scale deformation due to faults in the ECSZ used finite element models to evaluate the coseismic response of compliant fault zones assuming a constant drop in the shear modulus and no change in the Poisson ratio within the CZ compared to the host rocks [Fialko et al., 2002, Fialko, 2004a]. The fault zone response was modeled by applying coseismic stress changes inferred from the homogeneous elastic half-space solutions, and the interaction between neighboring fault zones (e.g., around the Calico and Rodman faults) was neglected. While in general it is possible to use more sophisticated finite element simulations including multiple fault zones and realistic earthquake rupture models, such simulations require elaborate and time-consuming meshing of a computational domain, especially for non-planar and branching faults. Also, assignment of spatially variable material properties to different

parts of a computational mesh is cumbersome. We use our iterative semi-analytic approach to evaluate three-dimensional deformation of the Earth’s crust with realistic variations in elastic properties due to the presence of fault zones. We use a Poisson’s solid for the “homogenized” starting model, corresponding to the value of Poisson’s ratio in the ambient crust assumed for the coseismic slip models. The modeled compliant zones (CZs) follow the geometry of the geologically mapped faults and are allowed to have across-strike, along-strike and down-dip variations in the effective elastic moduli. We assume a gradual decay in the rigidity contrast away from the fault trace. The spatial variation of elastic moduli, both lateral and vertical, is parameterized with the tapered boxcar function Ω_β of Barbot et al. [2008a], with a fixed taper coefficient of $\beta = 0.3$. Our model includes the inferred compliant zones associated with the Calico, Rodman, Pinto Mountain, Emerson, and Homestead-Johnson Valley faults in the central Mojave desert. Coseismic interferograms used to constrain the model include the April 24-August 7, 1992, ERS-1 acquisitions from the descending track 399 (Landers earthquake) and January 13-October 20, 1999, ERS-2 acquisitions from the descending track 127 (Hector Mine earthquake) [Fialko et al., 2002, Fialko, 2004a]. We assume that the fault-zone properties were not affected by nearby earthquakes (but see a discussion in Hearn and Fialko [2009]).

We use the respective earthquake slip models [Fialko, 2004a, Simons et al., 2002] to remove the LOS displacements predicted for a homogeneous half-space (referred to as the homogeneous model) from the interferograms. The residual LOS displacements represent propagation artifacts (e.g., atmospheric noise), as well as the small-scale deformation such as the amplified strain due to compliant zones. Similarly, we subtract the homogeneous model from the model accounting for the presence of CZs. The residual forward model is referred to as the heterogeneous contribution (deviation of the predicted displacement field from the homogeneous elastic half-space solution). The forward models are computed on a $512 \times 512 \times 512$ grid with a uniform node spacing of 350 m. The time involved in evaluating a single forward model is of order of five minutes on a 4-CPU shared-memory architecture computer. Figure 4.4 shows the total surface displacements and the heterogeneous contribution due to the Landers and Hector Mine earthquakes, modeled with our iterative semi-analytic approach. The origin corresponds to the epicenter of the Hector Mine earthquake (116.27W, 34.595N). Profiles A-A’ across the Calico and the Rodman faults, B-B’ across the Calico fault, and C-C’ across the Pinto Mountain fault are selected because LOS displacements from these profiles are available in both the Landers and Hector Mine coseismic interferograms. For a vertical strike-slip fault, the near-field uplift is due to compression and near-field subsidence is due to extension. As one can see from Fig. 4.4, profile A-A’ is located in the extensional quadrant of the Landers earthquake, and the compressional quadrant of the Hector Mine earthquake. Profiles B-B’ and C-C’ are in the compressional quadrant of the Landers earthquake, and the extensional quadrant of the Hector Mine earthquake. The fortuitous spatial configuration allows us to investigate the response of compliant fault zones to different loading conditions.

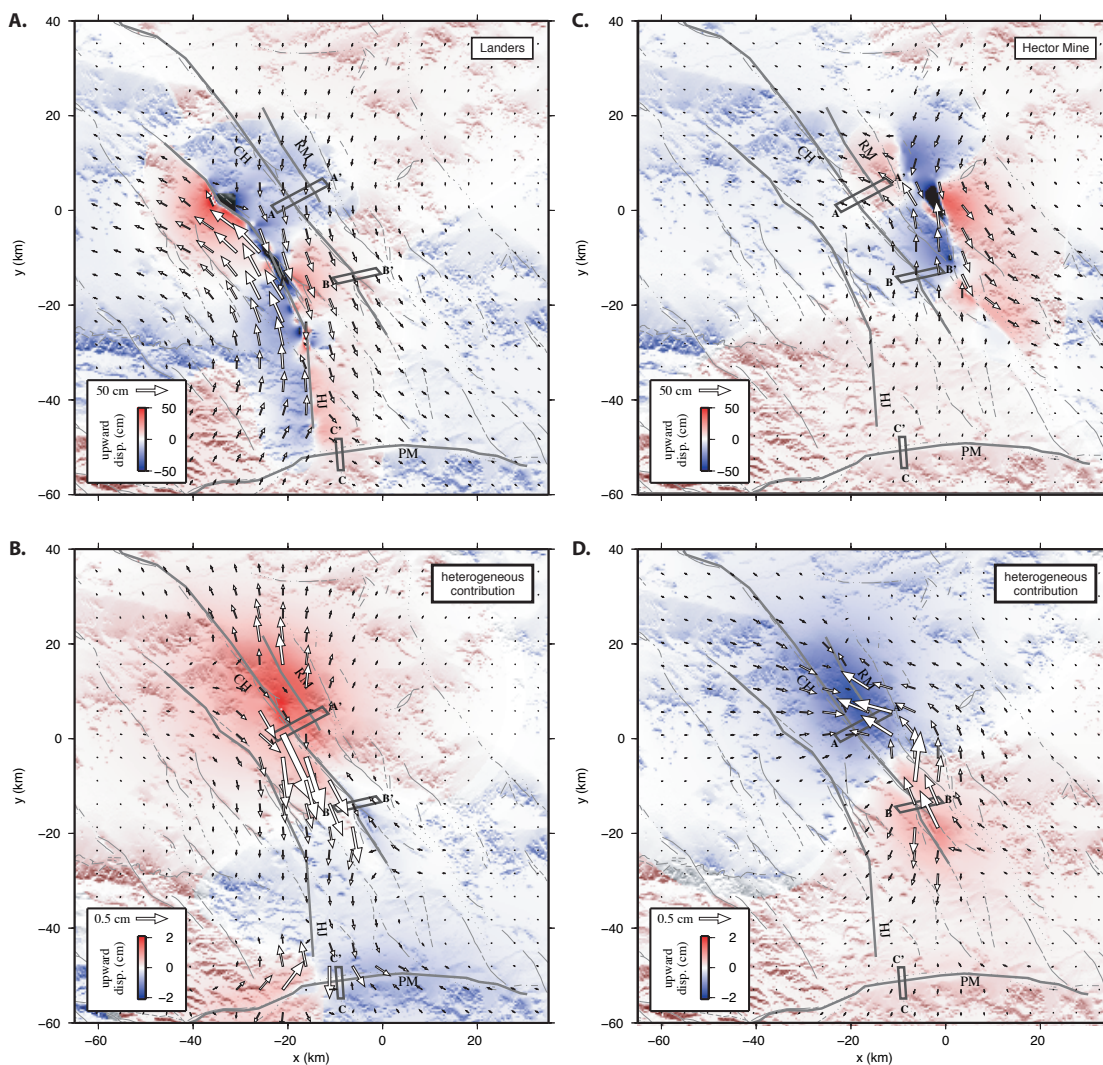


Figure 4.4: A) Map view of surface displacement corresponding to full 3-D deformation in a heterogeneous crust due to the 1992 Landers, CA earthquake. Vectors and color scale indicate horizontal and vertical displacements, respectively and uplift is taken to be positive. B) Elastic structure contribution corresponding to the Landers model. C) Model of the total surface displacements due to the Hector Mine earthquake. D) Hector Mine elastic structure contribution. The deformation is localized around CZs: The Calico-Hidalgo (CH), the Rodman (RM) and the Pinto Mountain (PM) faults exhibit amplified strain. Profiles A-A', B-B' and C-C' are shown in subsequent figures. Origin corresponds to the epicenter of the Hector Mine earthquake (116.27W, 34.595N). Light gray lines correspond to identified faults in the ECSZ and darker gray lines indicate modeled compliant zones (CZ).

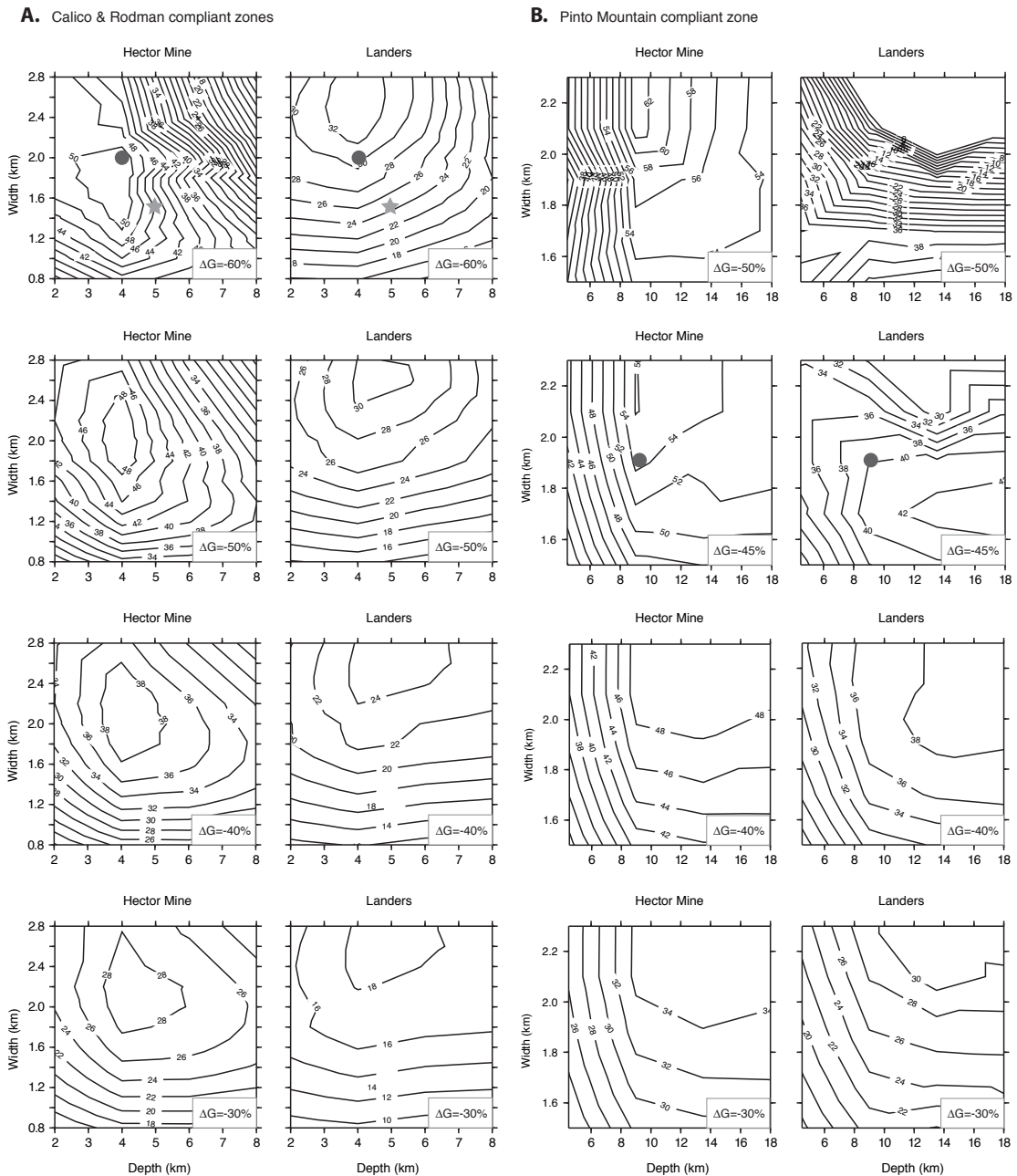


Figure 4.5: Exploration of the CZ model space. Variance reduction of the Landers and Hector Mine LOS data for the (a) Calico/Rodman and (b) the Pinto Mountain profiles (transects A-A' and C-C', respectively, in Fig. 4.4) as a function of the CZ width, depth and rigidity reduction ΔG . All models assume a Poisson's solid ($\nu = 0.25$) in the ambient crust and in the CZ. The star symbol indicates the preferred model of Cochran *et al.* [2008] corresponding to a 36% reduction in P-wave velocity. The circle indicates our preferred model, based on fitting the Landers and Hector Mine LOS data simultaneously.

We constrain the structural and elastic properties of a compliant zone by comparing the modeled elastic contribution to the LOS data from the Landers and Hector Mine earthquakes. The model parameters include the change in Lamé parameters $\Delta\lambda$ and ΔG , and the compliant zone width W (fault-normal dimension) and depth D (down-dip dimension). We assume that all CZs are extending vertically from the surface to a depth D and follow the strike of the corresponding fault trace at the surface. To identify the best fitting model, we explore a range of parameters with a grid search with depths going from 2 to 18 km, width varying from 0.8 to 2.8 km and rigidity reduction ranging from -30 to -60% compared to the ambient lithosphere. In all models, we assume a Poisson's solid for the ambient crust. The variance reduction of the Landers and Hector Mine LOS data for profiles A-A' and C-C' are shown in Fig. 4.5 for a range of model parameters. In these calculations, we assume that the rigidity reduction ΔG is accompanied with a similar reduction in the other Lamé parameter $\Delta\lambda$ or, equivalently, with a similar reduction in bulk modulus $\Delta\kappa$. Fig. 4.5a shows the variance reduction of profile A-A' corresponding to the Calico and Rodman CZs. Based on previous exploration, we assume that the thickness of the Rodman CZ is half that of the Calico CZ. The lesser depth extent of the Rodman CZ is required by the small wavelength of the corresponding LOS data, most visible in the Landers earthquake data (see Fig. 4.6a). The variance reduction is systematically better for the Hector Mine data, due to a better signal-to-noise ratio in the Hector Mine radar interferogram. Residuals are larger for CZs with a small rigidity contrast, the best variance reduction being obtained with the large reduction $\Delta G = -60\%$. For all the rigidity contrasts considered, the required width of the Calico CZ for both the Landers and the Hector Mine data lies in the range $W = 4 - 5$ km. The preferred thickness of the Calico CZ is slightly (about 20%) higher for the Landers than for the Hector Mine data. Our preferred model for the compliant zone surrounding the Calico fault, north of Galway Dry Lake, explaining both the Landers and Hector Mine data simultaneously, implies a 60% shear and bulk moduli reduction, a depth of 4 ± 0.5 km and a 2.0 ± 0.2 km width. Best model for the Rodman CZ is similar, except for a 2 km depth. We performed additional simulations, considering an increase in Poisson's ratio in the compliant zone. The best variance reduction was obtained for a shallower structure. However, all models with increased Poisson's ratio led to higher misfit with both Landers and Hector Mine LOS data. These results indicate that a change in the CZ bulk modulus accompanying the reduction in rigidity is a robust feature required by the radar data.

Fig. 4.5b shows the variance reduction of profile C-C' corresponding to the Pinto Mountain compliant zone. As in case of models shown in Fig. 4.5a, we assume that rocks in the fault zone behave as a Poisson's solid, so that Poisson's ratio is constant and equals 0.25. For small rigidity contrasts ($-\Delta G = 30 - 40\%$), the LOS data provide essentially a lower bound on the inferred width $W = 2.0 \pm 0.1$ km and depth $D = 9$ km of the Pinto Mountain CZ. There is an apparent trade-off between the required width and the rigidity reduction, most apparent for the Landers data. However, the best variance reduction is obtained for models with the

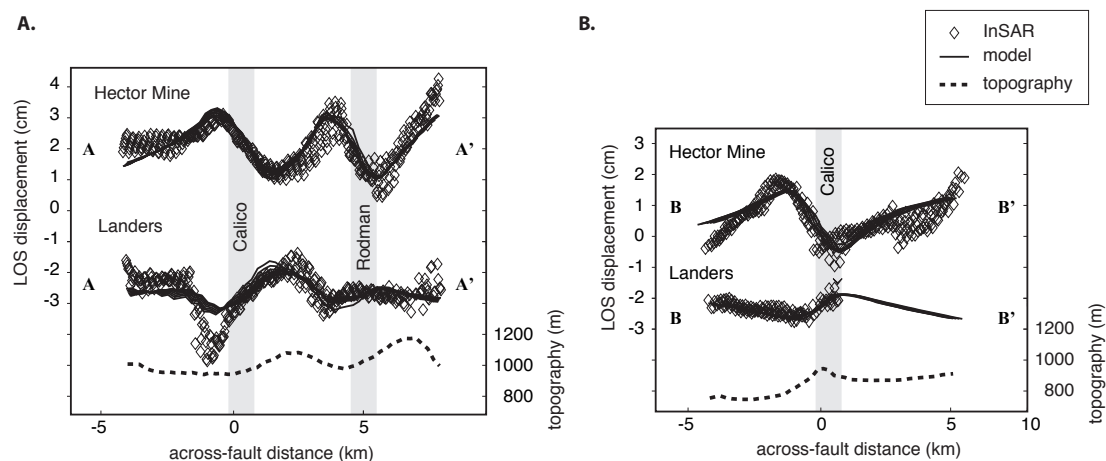


Figure 4.6: Observed (diamond) and modeled (solid line) LOS displacements from profile A-A' corresponding to the Landers (bottom) and Hector Mine (top) coseismic interferograms North of Galway Dry Lake. The Calico model corresponds to a 4 km deep, 2.0 km wide structure with a 60% rigidity reduction, as indicated by a circle in Fig. 4.5a. The Rodman model is similar except for a shallow structure of 2 km. B) Observed and modeled LOS residual displacements across a southern segment of the Calico fault (profile B-B'). At this location, the Calico model implies a shallow (2-3 km) structure 1.8 km wide with 45-50% rigidity reduction. Topography (dashed line) does not correlate with InSAR phase delay, indicating a limited topographic contribution. The continuous profiles correspond to forward models from several closely spaced parallel profiles within boxes outlined in Fig. 4.4. The flip of polarity between the Landers and Hector Mine coseismic InSAR data is an expected signature of a compliant zone.

largest rigidity reduction. For elastic contrasts larger than $\Delta G = -45\%$ the width required by the Landers and Hector Mine data differ by more than 15% and the models using the preferred width inferred from the Hector Mine data produce only a poor fit to the Landers LOS data. Our preferred model, which we indicate by a circle in Fig. 4.5, lies within 2% variance reduction of the independent best-fitting models for Landers and Hector Mine. Our preferred model, fitting both the Landers and Hector Mine data simultaneously, implies a 45% reduction in both shear and bulk moduli in a zone 1.75 km wide and at least 9 km deep surrounding the Pinto Mountain fault. The minimum depth of 9 km for the Pinto Mountain CZ is a robust feature that is required by both datasets.

Figure 4.6a shows the observed and modeled LOS displacements along profile A-A'. Profile A-A' crosses over the Calico and the Rodman faults, north of Galway Dry Lake, close to the seismic tomography experiment of Cochran et al. [2009] (see Fig. 4.3). There is little correlation between topography (dashed line) and the InSAR data, indicating that the observed variations in the LOS displacements do not result from atmospheric phase delays. We also note the change in polarity in the LOS displacements corresponding to the Hector Mine and Landers coseismic interferograms. This change in polarity is an expected signature of the vertical

displacement due to a compliant zone, given a reversal in sign of the fault-normal coseismic stress change. The assumed location and thickness of the Calico and Rodman compliant zones are indicated in Figure 4.6a by gray bands. Solid lines in Figure 4.6a represent deformation due to our preferred fault zone model, sampled along the respective profiles. The modeled LOS displacements account for range variations in the radar incidence angle. Results shown in Figure 4.6a accurately simulate the 3-D response of closely spaced compliant zones due to the Calico and Rodman faults to coseismic loading, and represent a substantial improvement over the previously published simplified models [e.g., Fialko et al., 2002]. Our preferred model for the compliant zone surrounding the Calico fault, north of Galway Dry Lake, implies a 60% reduction in shear modulus and no change in the Poisson's ratio (accompanied by a 60% reduction in the value of the bulk modulus) compared to ambient rocks, in a finite zone 4 km deep and 2.0 km wide. Our preferred model for the CZ due to the Rodman fault implies the same elastic moduli reduction, but to a shallower depth of $D = 2.0$ km.

Figure 4.6b shows the observed and modeled LOS displacements along profile B-B' in Fig. 4.4. InSAR data and models are shown for both the Landers and the Hector Mine earthquakes. Topography profile exhibits a ridge close to the location of the assumed compliant zone but LOS displacements corresponding to the two seismic events change polarity and are not well correlated with topography, suggesting that the observed LOS displacements are not an atmospheric artifact. Incomplete data for the Landers earthquake, east of the compliant zone is due to limited coverage of the available satellite track 399. InSAR data for the Landers earthquake are nevertheless sufficient to suggest a localized increase in LOS displacements centered on the Calico fault trace. Profile B-B' samples a segment of the Calico fault located to the South of Galway Dry Lake, about 35 km south of profile A-A'. This portion of the Calico fault was subjected to compression during the Landers earthquake and extension during the Hector Mine earthquake, coincident with the observed polarity of vertical displacement in Fig. 4.4. Our preferred CZ model indicates a reduction of 45-50% in shear and bulk moduli in a 1.8 km wide zone extending from the surface to a depth of 2-3 km. The CZ model can explain data from both the Hector Mine and Landers earthquakes. Reductions in the effective elastic moduli on the southern segment of the Calico fault are inferred to be somewhat smaller compared to those on the northern segment. This result highlights a possibility of substantial variations in effective elastic properties along the same fault zone. A 10% along-strike variation in elastic moduli compared to surrounding rocks was also inferred along the Johnson Valley and the Kickapoo faults, the southern segments of the Landers rupture [Li et al., 2000].

Fig. 4.7 shows the modeled and the observed LOS displacements across the Pinto Mountain fault due to the Landers and Hector Mine earthquakes (profile C-C' in Fig. 4.4). Profile C-C' is located to the east of the Landers rupture, in a compressional quadrant near the southern tip of the rupture. This proximity likely explains a relatively large (up to 30 mm) LOS displacement due to the compliant zone of the Pinto Mountain fault. The southern tip of the Hector Mine

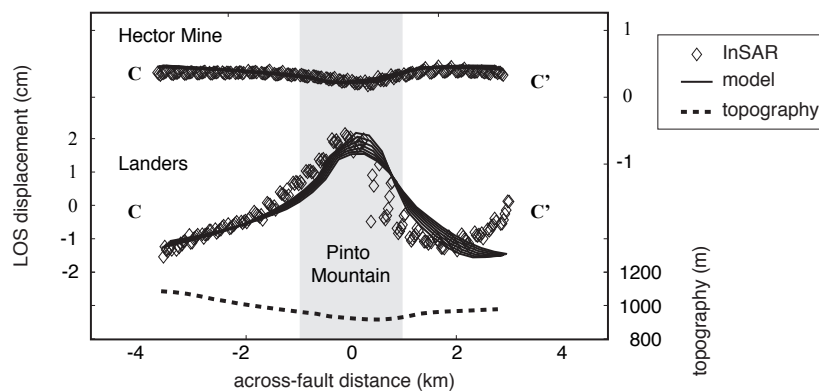


Figure 4.7: Modeled (solid line) and observed (diamonds) LOS displacements across the Pinto Mountain fault, profile C-C'. The predictions correspond to a single compliant zone model with a 45% reduction in both shear and bulk moduli, indicated by a circle in Fig. 4.5b. The CZ structure is 1.75 km wide and at least 9 km deep. The continuous profiles correspond to several closely spaced parallel profiles from the forward model and indicate the variation of deformation within the C-C' box outlined in Fig. 4.4. Notice the separate scale for the Hector Mine data and forward model.

rupture is located further away, about 80 km to the north-northeast. Both the larger distance to, and the smaller size of the Hector Mine earthquake imply smaller stress perturbation on the Pinto Mountain fault, and explain the reduced amplitude of the coseismic LOS displacements, compared to those from the Landers event. Similar to the observed deformation patterns on the Calico and Rodman faults, the polarity of LOS displacements on the Pinto Mountain fault is different for the Landers and Hector Mine events, consistent with coseismic stress changes. Our preferred model for the Pinto Mountain compliant zone, as indicated by a circle in Fig. 4.5, has width of 1.9 km, a depth of at least 9 km, a 50% reduction in shear modulus and no change in Poisson's ratio compared to ambient crust. The deeper compliant zone compared to neighboring Calico and Rodman is required by the large wavelength of the LOS displacements.

Fig. 4.8 shows the modeled and the observed LOS displacements across the Homestead fault due to the Hector Mine earthquake. The LOS displacements can be explained by the presence of a CZ about 1.5 km wide, extending from the surface to a depth of 4-5 km with 50% reduction in shear modulus, and the same Poisson's ratio as in ambient rocks. A model assuming a CZ around the Homestead fault shows a good agreement with the InSAR data. Unfortunately, no data exist for the 1992 Landers earthquake due to decorrelation in the near field of the rupture.

4.4 Discussion

Our analysis of space geodetic observations in the Eastern California Shear Zone using fully three-dimensional models lends support to previous inferences of long-lived compliant zones

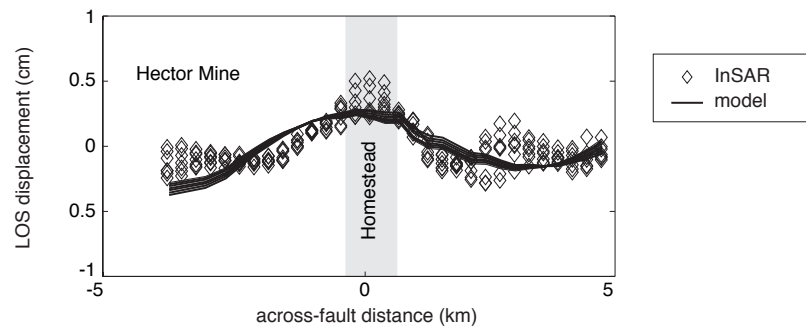


Figure 4.8: Modeled (solid line) and observed (diamonds) LOS displacements across the Homestead fault. Forward model corresponds to a compliant zone with a 50% reduction in shear and bulk moduli in a block 4-5 km deep and 1.5 km wide. The continuous profiles correspond to forward models from several closely spaced parallel profiles within boxes outlined in Fig. 4.4.

around major faults, with appreciable reductions in the effective shear and bulk moduli. Our inferred width of compliant zones is 2.0 km for the Calico and the Rodman process zones and 1.9 km for the Pinto Mountain fault. Over the past two decades, the structure of fault zones has been primarily investigated using fault zone trapped waves generated by earthquakes or explosions. For example, the Karadere-Duzce fault zone, a secondary branch of the North Anatolian Fault, is inferred to have a wave-trapping structure ~ 100 m wide, with a velocity decrease of about 50% compared to the surrounding rocks [Ben-Zion et al., 2003]. Trapped waves generated by aftershocks following the 1992 Landers earthquake are best explained by a 250 m-wide low velocity zone in the southern segment of the rupture, that tapers to 100-150 m at 8.2 km depth [Li et al., 2000]. Trapped-wave studies rely on seismic sources within compliant zones (most commonly, aftershocks) to detect and quantify the elastic contrasts [Li and Leary, 1990, Li et al., 1998a,b, 1999, 2000, Ben-Zion et al., 2003]. The strength of the low-velocity anomalies is believed to vary over the earthquake cycle [Marone et al., 1995, Li et al., 1998a, Vidale and Li, 2003], but it is still unclear if results from seismic studies are directly applicable to the longer geodetic time scale, due to the frequency dependence of elastic moduli. In this study, we investigated major faults that did not rupture in historic times and therefore are well within the interseismic phase of the earthquake cycle. Our preferred models suggest considerably (in case of the Pinto Mountain fault - an order of magnitude) larger fault zone width compared to most previous seismic studies of other faults. However, a recent seismic tomography and trapped wave experiment on the Calico fault [Cochran et al., 2009] confirms our interpretation and provides a direct independent evidence for the existence of a massive long-lived compliant fault zone along the Calico fault. Our preferred model of the Calico compliant zone, with a 4 km depth and 2.0 km width is very similar to the results of [Cochran et al., 2009] which imply a fault zone 1 – 2 km wide, ~ 5 km deep, with a rigidity reduction of 50 – 75%. Our interpretation of InSAR data from the Pinto Mountain fault suggests that a compliant zone extends from the surface to a depth of

at least 9 km, i.e., through much of the brittle seismogenic layer.

Our models of compliant zones along major strike-slip faults in the Eastern California Shear Zone require a significant reduction in the effective shear modulus. A robust feature of InSAR observations is the change in polarity of the LOS displacements within several fault zones due to the Landers and Hector Mine earthquakes. The observed change in polarity is primarily due to the vertical displacements within the compliant zone. The polarity of vertical motion is well constrained by InSAR observation and our results suggest that a reduction in both shear and bulk moduli better describes the variations in the effective elastic moduli within the compliant zones surrounding active faults in the ECSZ. These results contrast with the assumptions of theoretical models of fault damage in which the latter is related to changes in the shear modulus alone [Lyakhovsky et al., 2001, Hamiel et al., 2004]. Hearn and Fialko [2009] have investigated the response of compliant zones in the ECSZ due to both a permanent elastic moduli reduction in the fault process zones and a 2% coseismic change in rigidity in the same structure motivated by findings of Vidale and Li [2003]. The conclusion of Hearn and Fialko [2009] is that it is difficult to fit the data in the presence of coseismic softening of the fault zones, unless the fault zone material is nearly incompressible. This study suggests that the data can be well explained by permanent compliant zones with normal Poisson's ratios, this highlighting the need for accurate monitoring of changes in the fault-zone rigidity due to nearby earthquakes.

4.5 Conclusions

We have presented an iterative approach to model three-dimensional deformation due to faults in a heterogeneous elastic half-space. The decomposition of the elastic moduli into a constant part and a spatially varying part allows us to formulate an iterative solution that takes advantage of the Green function for a homogeneous medium. Spatial variations in elastic properties are accounted for by equivalent body forces and equivalent surface traction. This approach obviates the need for deriving or numerically calculating the specific Green function in case of heterogeneous elastic structures. It allows one to readily evaluate the effect of spatial variations in elastic properties on deformation in the surrounding medium.

A possible drawback of our iterative approach is a potentially large number of successive approximations (SA) required to accurately evaluate the heterogeneous elastic response. Likewise, the numerical estimation of the convolution between the homogeneous Green function and the equivalent body forces -typically scaling as N^2 , where N is the number of nodes- can be expensive as the equivalent body forces representing the effect of elastic variations in the homogenized medium can occupy large domains. Our approach consists in evaluating the deformation numerically in the Fourier domain. We use the semi-analytic Green function for a half-space to compute the displacement field due to the presence of arbitrarily distributed body forces in the computational domain. Free-surface boundary condition is enforced by counterbalancing the

stress field on the surface plane obtained first from the whole space solution. The halfspace solution is finally obtained by application of analytic solutions, in the Fourier domain, for some normal and tangential traction applied at the surface (the so-called Boussinesq's and Cerruti's problems). The computational burden associated with a Fourier domain solution is independent of the spatial extent or distribution of the body forces. The use of fast Fourier transforms allows us to compute multiple successive approximations efficiently. One iteration on a $512 \times 512 \times 512$ computation grid takes about a minute on a 4-CPU machine with a shared memory architecture. Typically, about 10 iterations are needed to reach convergence. In most cases, the proposed numerical method is a practical alternative to more advanced models like finite elements because it does not require elaborate and time-consuming meshing of a computational domain, especially for non-planar and branching faults. Also, the assignment of spatially variable material properties to different parts of a computational mesh is straightforward, due to the uniform sampling of the computation domain.

We compared our numerical results with analytic and semi-analytic solutions for antiplane, plane-strain and three-dimensional deformation problems. We find that our numerical solutions for antiplane problems fall within 5% of analytical solutions, even in the case of large contrasts in elastic properties. In the case of plane strain symmetry, we compared our solution to results of the propagator method [*P. Segall*, pers. comm., 2008]. We use the semi-analytic Green function approach of Wang et al. [2003] and finite element calculations to validate our approach in 3-D for vertical and lateral variations in elastic moduli. Accuracy is better than about 5% of the expected elastic structure contribution for elastic contrasts lower than 50% and better than about 10% for contrasts higher than 50% compared to homogenized values. We conclude that our semi-analytic method provides a sufficient accuracy to model realistic problems of three-dimensional deformation in a heterogeneous crust. We applied this method to investigate the structure and properties of compliant damage zones associated with young active faults in the Eastern California Shear Zone. We modeled the line-of-sight (LOS) displacements documented by radar interferometry during the 1992 Landers and the 1999 Hector Mine earthquakes [Fialko et al., 2002, Fialko, 2004a]. We model the inferred compliant zones by a gradual reduction in rigidity and bulk modulus around the geologically mapped fault trace. Using a grid search, we explored a range of parameters that can explain simultaneously LOS displacements from both the Landers and Hector Mine earthquakes.

The InSAR data near the Calico and the Rodman faults, respectively, are best explained by the presence of a compliant zone that extends from the surface to a depth of 4 and 2 km, respectively, with a rigidity reduction of 60% compared to ambient rocks. No contrast in the Poisson ratio is inferred between the host rocks and the Calico fault zone. The wavelength of LOS displacements around the Calico and the Rodman faults require an effective compliant zone width of about 2.0 km. One segment of the Calico fault, South of Galway Dry Lake is partially sampled by both Hector Mine and Landers interferograms. Data corresponding to this

southern segment is best modeled with a 45-50% reduction in shear and bulk moduli in a 2-3 km deep, 1.8 km wide structure. Our modeling results show substantial along-strike variations in the elastic properties and fault zone size for the Calico fault. InSAR data around the Pinto Mountain fault are best modeled with a compliant zone that extends from the surface to a least 9 km depth, in a 1.75 km wide zone with a 45% reduction in effective shear and bulk moduli. A single elastic model of a heterogeneous crust with lateral variations around the Calico, the Rodman and the Pinto Mountain faults can explain the InSAR data of both Landers and Hector Mine earthquakes. We conclude that the presence of compliant zones around the Calico, the Rodman and the Pinto Mountain faults in the East California Shear Zone is a robust feature of these InSAR observations. The anomalous LOS displacements observed in the Hector Mine and Landers interferograms correspond to the elastostatic response of a laterally heterogeneous crust in the east California shear zone. The residual LOS displacements in the Hector Mine InSAR data around the Homestead-Johnson Valley can be explained by the presence of a compliant zone with a 50% reduction in shear and bulk moduli in a block 4-5 km deep and 1.5 km wide. Inferred elastic properties in the Homestead Valley process zone indicates that the northernmost fault segments of the 1999 Landers earthquake ruptured in the middle of a compliant zone.

Our modeling results indicate that damage accumulation around active faults is accompanied by a reduction in both shear and bulk effective moduli with a relatively small increase in Poisson's ratio. The "conserved Poisson's ratio" end-member scenario seems to be more applicable to the ECSZ than the "conserved bulk-modulus" end-member. These observations suggest pervasive and widespread damage around active crustal faults. The inferred properties of compliant zones may be used to quantify the amount of damage experienced by the host rocks throughout the fault history.

Acknowledgments

We thank Jill Pearse for her help with finite element calculations. Finite element meshes were generated using the pre-processor APMODEL written by Shelly Kenner. The manuscript benefited from the comments of the Editor Thorsten Becker, and the thorough reviews of Kaj Johnson and an anonymous reviewer. A version of our code can be found at the address <http://sylvain.barbot.free.fr/crust/heterogeneous.html>. This work was supported by NSF (grant EAR-0450035) and SCEC. This Chapters, in full, is a reprint of the material as it appears in the Journal of Geophysical Research. Barbot, Sylvain; Fialko, Y.; Sandwell, D.. The dissertation author was the primary investigator and author of this paper.

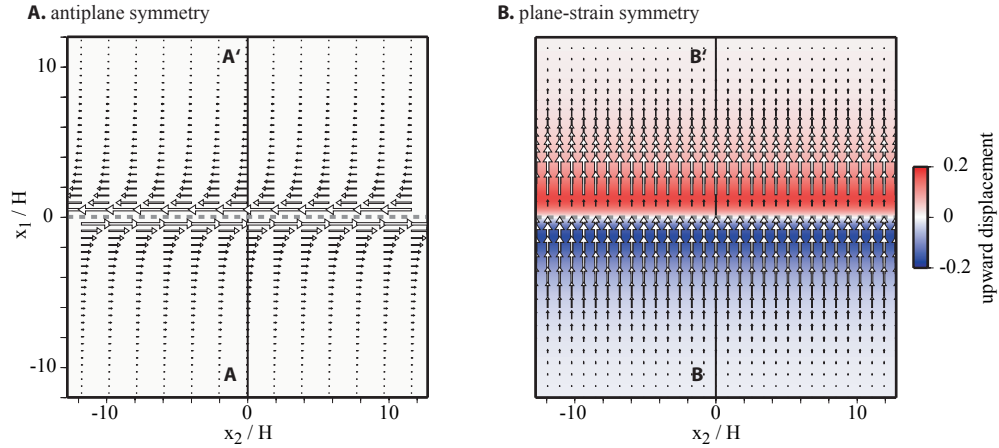


Figure 4.9: Three-dimensional calculation with axes of symmetry. Horizontal (u_1, u_2) , and vertical u_3 surface displacements are represented by white arrows and the background color, respectively. A) An infinitely long strike-slip fault (dashed line) creates an antiplane symmetry (no vertical displacement). B) An infinitely long edge dislocation creates a plane-strain symmetry in the three-dimensional computational volume.

4.6 Benchmarks

4.6.1 Antiplane strain

We compare our numerical solution to analytic and semi-analytic solutions for antiplane, plane-strain and three-dimensional deformation in a heterogeneous medium. In order to simulate two-dimensional deformation in our three-dimensional calculations, we introduce a dislocation extending across the computational grid. The periodicity of the solution, introduced by the Fourier expansion, makes the source effectively infinite in the along-strike direction. In Fig. 4.9a, a screw dislocation extends from both ends of the grid, and the resulting deformation is antiplane (the only non-zero component of displacement is along strike). Displacements across a fault exhibit a characteristic arctangent profile. In Fig. 4.9b, an infinitely long edge dislocation cuts the volume, representing plane strain (the only non-zero component of displacement orthogonal to the fault strike). Benchmarks for three-dimensional deformation are computed for finite faults.

First we consider cases of a screw dislocation in a vertically stratified elastic half plane. The modeled domain is composed of a strip of rigidity G_1 , extending from the surface to depth H , and a bottom half plane of rigidity G_2 . Figure 4.10a shows the surface displacement profile corresponding to profile A-A' in Fig. 4.9 (dashed line) along with the analytic solution for the case of a infinitely long vertical strike-slip fault extending from the surface to a depth of $0.8H$ in a homogeneous medium ($G_1 = G_2$). The numerical error, shown on the right panel of Fig. 4.10a, increases away from the source, due to the periodicity of the Fourier domain solution. Within an across-fault distance of ten fault lengths, error does not exceed 0.5% compared to the analytic

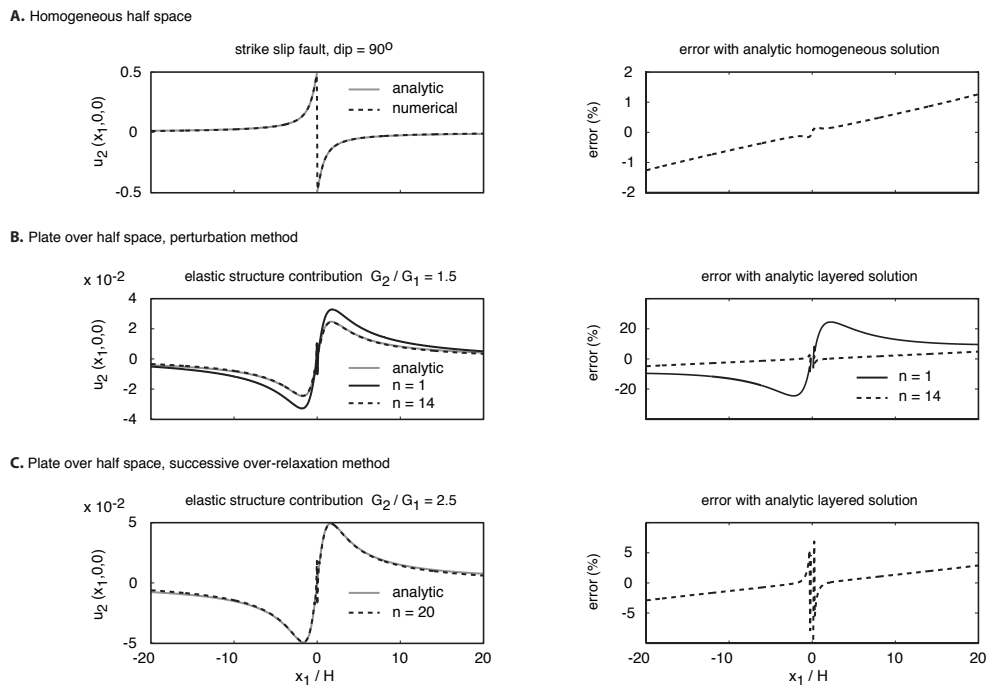


Figure 4.10: Antiplane benchmarks along profile A-A' in fig. 4.9 in the case of a vertical left-lateral strike slip fault. A) The numerical and analytical solutions for a homogeneous half space are shown in left panel. The relative error is shown in the right panel and remains smaller than 0.5% 10 fault lengths away from the fault trace. B) Perturbation method. The difference between the surface displacements corresponding to a heterogeneous elastic structure and a homogeneous half space. The elastic structure consists in a plate of rigidity $G_1 = 1$, extending from the surface to the depth H , and the bottom half space of rigidity $G_2 = 1.5$. The strike slip fault extends from the surface to the locking depth $0.8H$. Numerical solution is shown at 1 and 14 iterations of the perturbation method. C) Successive Over Relaxation method (SOR). Results similar to B) but with a higher elastic contrast $G_2/G_1 = 2.5$. Convergence is obtained after 20 iterations.

solution [Weertman and Weertman, 1964, Rybicki and Kasahara, 1977].

We use the perturbation method to compute the deformation in the case of the rigidity contrast $G_2/G_1 = 1.5$. Left panel of Fig. 4.10b shows the heterogeneous contribution (the difference between surface displacements in heterogeneous and homogeneous media). The first iteration of the perturbation method is shown in solid line and over-estimates the effect of the rigidity contrast. Corresponding error is about 20% compared to the analytic result. After 14 iterations, convergence criterion (equation 4.39 in the main text) is satisfied and error is comparable to the case of a homogeneous elastic structure.

We use the SOR method to compute the displacements in the case of the elastic contrast $G_2/G_1 = 2.5$. Convergence criterion is reached after 20 iterations. Numerical and analytic solutions for the heterogeneous structure and corresponding errors are shown in Fig. 4.10c. Error does not exceed 5% except in a small vicinity around the dislocation where it reaches a maximum of 10%. In case of a large elastic contrast, the homogenized elastic parameters must minimize the effective elastic contrast and does not correspond to a value of rigidity around the fault. The difference in effective stress is compensated at each iteration after estimating the amplitude of stress near the fault. Numerical evaluation of stress in the fault zone is complicated by the presence of the discontinuity and results in a greater final error at the fault location (see right panel in Fig. 4.10c.) Overall, our two-dimensional numerical solutions performed in a three-dimensional computational grid compare well to the analytic solutions for antiplane deformation. The use of the SOR method allows us to consider such crustal structures with large variations in rigidity.

4.6.2 Plane strain

Next, we consider the case of plane-strain deformation. Figure 4.11 shows the displacement field along profile B-B' in Fig. 4.9. The elastic structure consists of a strip of thickness H with Lamé parameters $\lambda_1 = G_1$ overlying a half-plane with elastic parameters $\lambda_2 = G_2$. An edge dislocation with unit slip, dipping 30° , starts in the bottom layer at depth $1.5H$ and extends to depth $3.5H$. Fig. 4.11a shows the surface displacement in the case of a homogeneous medium. Corresponding error compared to analytic solution [Savage, 1974, Niazzy, 1975] is shown on right panel and does not exceed 3%. The constant shift error is an artifact due to periodicity of the Fourier domain solutions.

We use the perturbation method to evaluate the surface displacement in the case of a more compliant top strip with $G_1/G_2 = 0.7$ (Poisson's ratio is the same for the two layers). We choose the homogenized elastic parameters corresponding to the bottom layer, where the fault is located. We compare our numerical solution with the displacement obtained using the matrix propagator method of *P. Segall* [personal communication, 2008]. Fig. 4.9b shows the elastic structure contribution, the difference between heterogeneous and homogeneous solutions. First

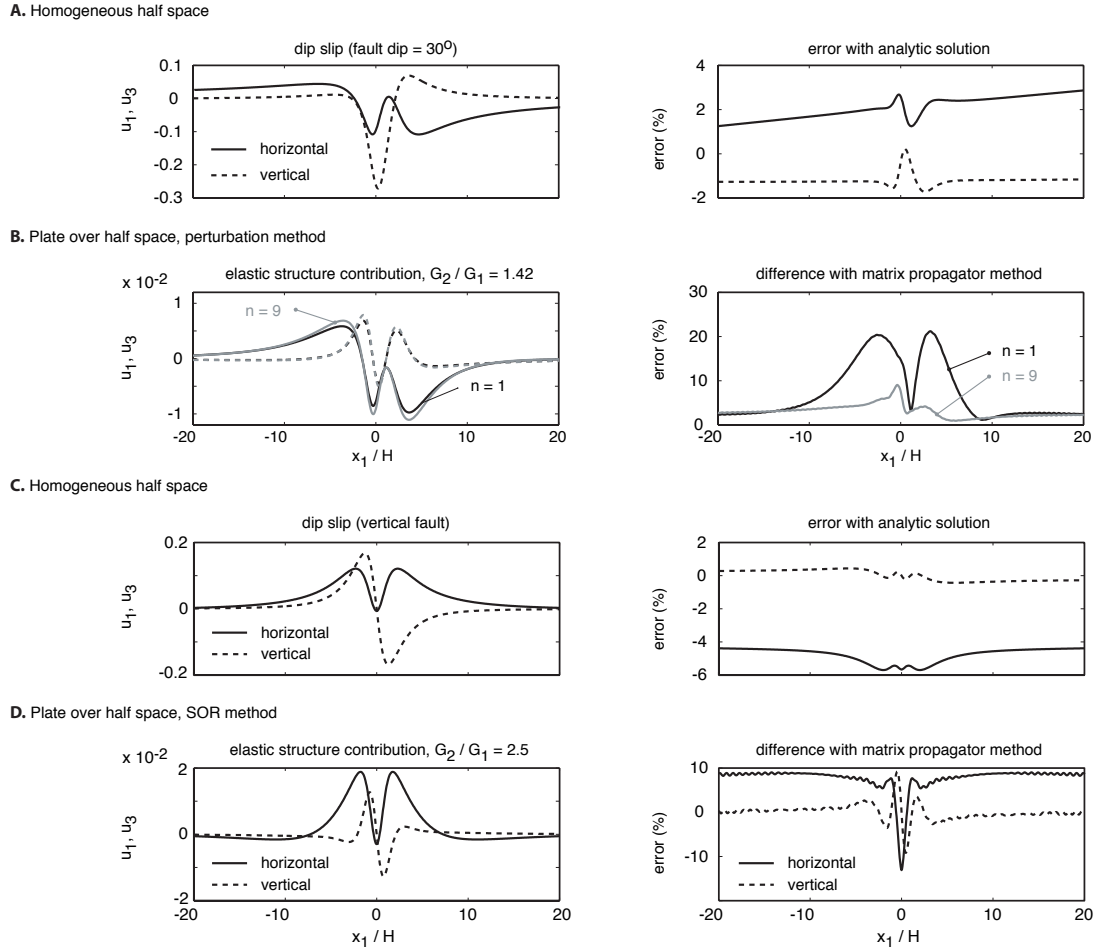


Figure 4.11: Plane-strain benchmarks along profile B-B' in Fig. 4.9. **A)** Surface displacements corresponding to a unit slip occurring on a buried edge dislocation dipping 30° . Numerical error (right panel) does not exceed 3% compared to analytic solution. **B)** Perturbation method. An more compliant plate, with $\lambda_1 = G_1 = 0.7$ and extending from the surface to a depth H , overrides a half-space of Lamé parameters $\lambda_2 = G_2 = 1$. Left panel shows first iteration ($n = 1$) and converged ($n = 9$) solutions of the perturbation method. Norm of error corresponding to the converged solution remains smaller than 5% compared to results of the matrix propagator method. **C)** Same as A) but with a vertical dip slip fault. **D)** Successive Over Relaxation (SOR) method. Solution displacements and relative error compared to the matrix propagator method for the layered structure of B) with a greater elastic contrast $G_2/G_1 = 2.5$ and a constant $\lambda_1 = \lambda_2 = 1$.

approximate solution, at first iteration of the perturbation method, is an under-estimate the final solution. Convergence criterion is reached after 9 iterations with a final error smaller than about 5% of the expected elastic contribution signal. Notice that the elastic contribution is one order of magnitude smaller than the total displacement. The difference between the total displacements obtained using the propagator-matrix method or our approach is therefore barely distinguishable. The surface displacement due to a vertical edge dislocation extending from depth $1.5H$ to $3.5H$ is shown in figure 4.9c. Horizontal displacement error is characterized by a constant bias of about 5% of the expected signal. Vertical displacement is anti-symmetric and does not display such constant bias. Error in the vertical direction is limited to about 0.5%.

We use the SOR method to compute the displacement in the presence of a large elastic contrast between the horizontal layers. We use $\lambda_1 = G_1 = 1$ in the top layer and $\lambda_2 = 1$ and $G_2 = 2.5$ in the bottom layer. Convergence is reached after 18 iterations. We compare our solutions with results from the matrix propagator technique. Horizontal displacements exhibit a bias close to 10% of the expected signal. Error in the vertical direction is limited to about 2% except close to the fault for reasons discussed above in the case of antiplane strain. We conclude that our two-dimensional simulations for plane strain and antiplane problems compare well with available analytic or semi-analytic solutions.

4.6.3 Three-dimensional deformation

We compare our 3-D numerical models to the Green function approach of Wang et al. [2003] for three dimensional deformation in a vertically stratified elastic half space. We introduce a finite strike-slip fault in a semi-infinite solid where the elastic moduli increase at the transition depth H . Poisson's ratio ($\nu = 0.25$) is identical in each layer but the shear modulus is increased by 50% in the bottom half space compared to its value in the overlying plate. The left-lateral strike-slip fault extends vertically from the surface to a depth of $1.5H$ and is $L = 2W$ long in the along-strike direction. This geometric configuration allows us to evaluate our modeling of dislocations intersecting materials with dissimilar elastic moduli. Figure 4.12a shows the horizontal (black arrows) and vertical (background color) displacements that represent the difference between the displacement field obtained with a heterogeneous medium and with a homogeneous medium, respectively. The fault trace is indicated by the black line in the x_1 -direction (North). The final solution is obtained with the perturbation method after 14 iterations. Figure 4.12b shows the comparison with the solution of Wang et al. [2003], using the same scaling for arrows and same color scale as in Fig. 4.12a. Some large residuals in the horizontal direction appear only on the fault trace and are due to the fact that slip is not single-valued at the fault interface. Residuals in the vertical direction occur near the quadrants of the computational grid due to the effect of periodicity of the Fourier domain solution. Despite some small differences inherent to the method, our Fourier domain perturbation approach compares very well with the Green

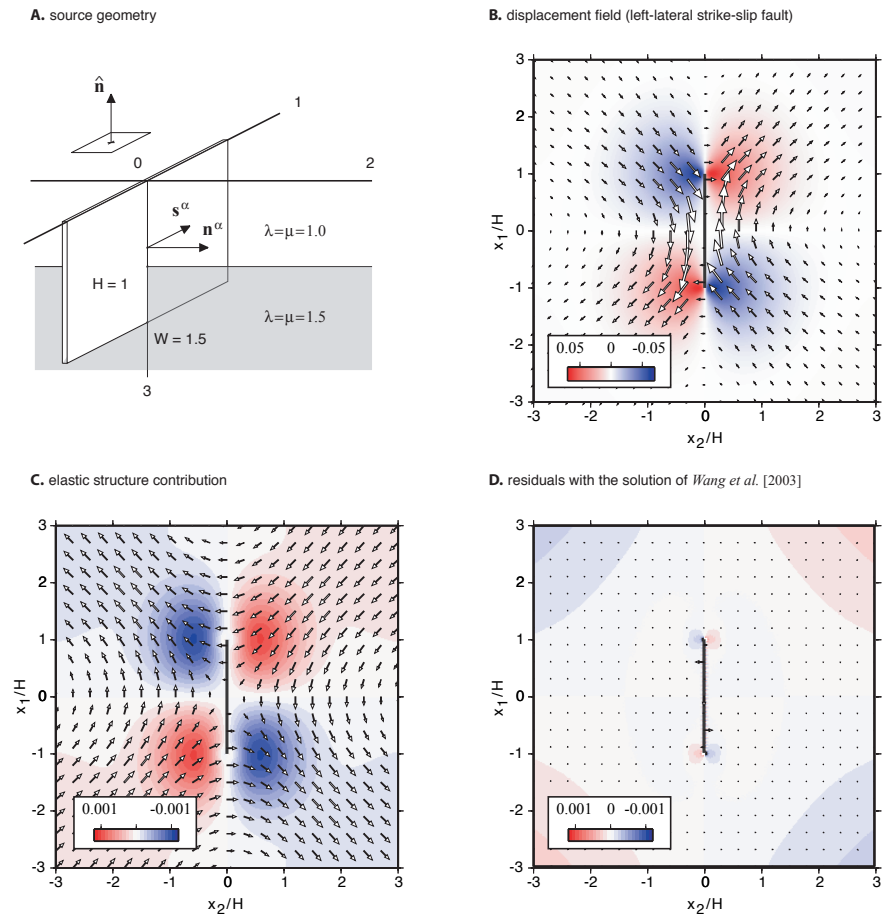


Figure 4.12: Three-dimensional benchmark. A) A strike-slip fault fractures crustal areas with different elastic moduli. The rigidity in the bottom half space is 50% higher than in the top plate. B) The displacement field at the surface of the half space. C) Difference between the displacement field in B) and the corresponding homogeneous solution where $G_1 = G_2$. D) Residuals between our Fourier domain semi-analytic result and the result of Wang et al. [2003].

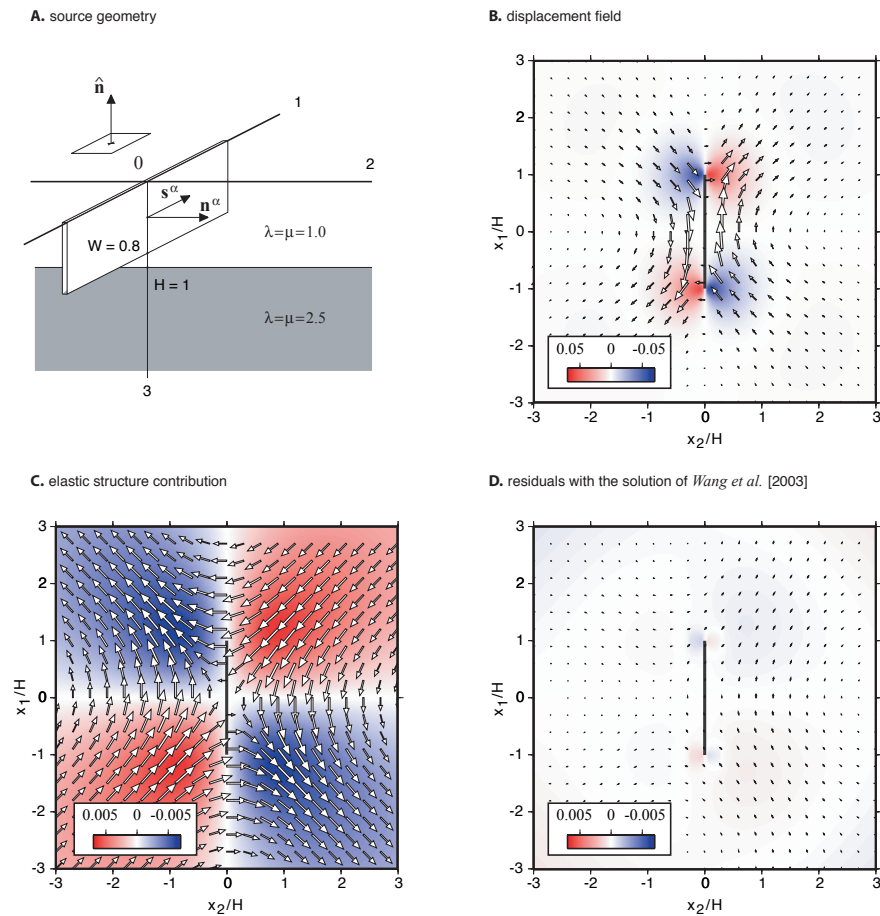


Figure 4.13: Three-dimensional benchmark. A) A strike-slip fault breaks the upper crust. The rigidity in the bottom half space is 2.5 times higher than in the top plate. B) The displacement field at the surface of the half space. C) Elastic structure contribution. D) Residuals between our Fourier domain semi-analytic result and the result of *Wang et al.* [2003].

function method of Wang et al. [2003]. In a test with a large increase of elastic moduli with depth, we introduce a finite strike-slip fault extending from the surface to a depth of $0.8 H$ (see Fig. 4.13). We use the SOR method to evaluate the deformation in the computational volume. Our numerical estimate of three-dimensional elastostatic deformation in a heterogeneous half space with large variations in elastic moduli also favorably compares to results obtained with the Green function approach of Wang et al. [2003].

Finally, we test the proposed method for a case of lateral variations in elastic moduli. We compare the predictions of our model with finite-element calculations using the Abaqus software. We introduce a right-lateral strike-slip fault of length L striking North-South along the x_1 -axis from the surface to a depth W . An infinitely long compliant zone runs parallel to the fault. The fault and the center of the compliant zone are separated by a distance $W/2$. The geometry and resulting calculations are shown in Fig. 4.14. We create a mesh with increasing node density closer to the fault and the compliant zone. The minimum distance separating the nodes is $W/30$. For the Fourier-domain solution, we use a uniform sampling of $W/30$ and a computation grid of $256 \times 256 \times 256$ nodes. We consider two cases. In a first simulation, the shear modulus in the compliant zone is reduced by a factor of 10% and the Poisson's ratio $\nu = 1/4$ is uniform in the half space. In a second simulation, the shear modulus is reduced by 10% compared to surrounding solid, but the bulk modulus is uniform in the half space. In this second case, Poisson's ratio is $\nu = 0.26$ in the compliant zone. Using the perturbation approach, we obtain convergence in both cases after 4 iterations. The perturbation due to the presence of the compliant zone in both cases represents about 5% of the maximum signal in a uniform half space. The corresponding surface displacement is shown in Fig. 4.14a. The elastic contribution is shown in Fig. 4.14c and 4.14e for the uniform bulk modulus and uniform Poisson's ratio, respectively. The pattern of horizontal displacements, shown by the arrows in Fig. 4.14, is comparable in both cases, with additional displacements to the East of the fault. We observe more vertical displacement to the West of the fault in the case where Poisson's ratio is conserved. The difference between predictions of our approach and the finite-element solution is shown in Fig. 4.14d and 4.14f, for the uniform bulk modulus and the uniform Poisson's ratio, respectively. In the course of our numerical validation, we have noticed that the benchmark corresponding to the conserved bulk modulus (Fig. 4.14c and 4.14d) could be only be matched with the inclusion of equivalent surface traction, as indicated by Eq. (4.21). The residuals represent about 10% of the corresponding elastic contribution signal and about 1% of the cumulative displacement. There is an overall excellent fit between our Fourier domain solutions and the finite-element calculations. We conclude that our semi-analytic iterative approach can be successfully used to model crustal deformation due to faulting in the Earth with realistic spatial distribution of elastic moduli.

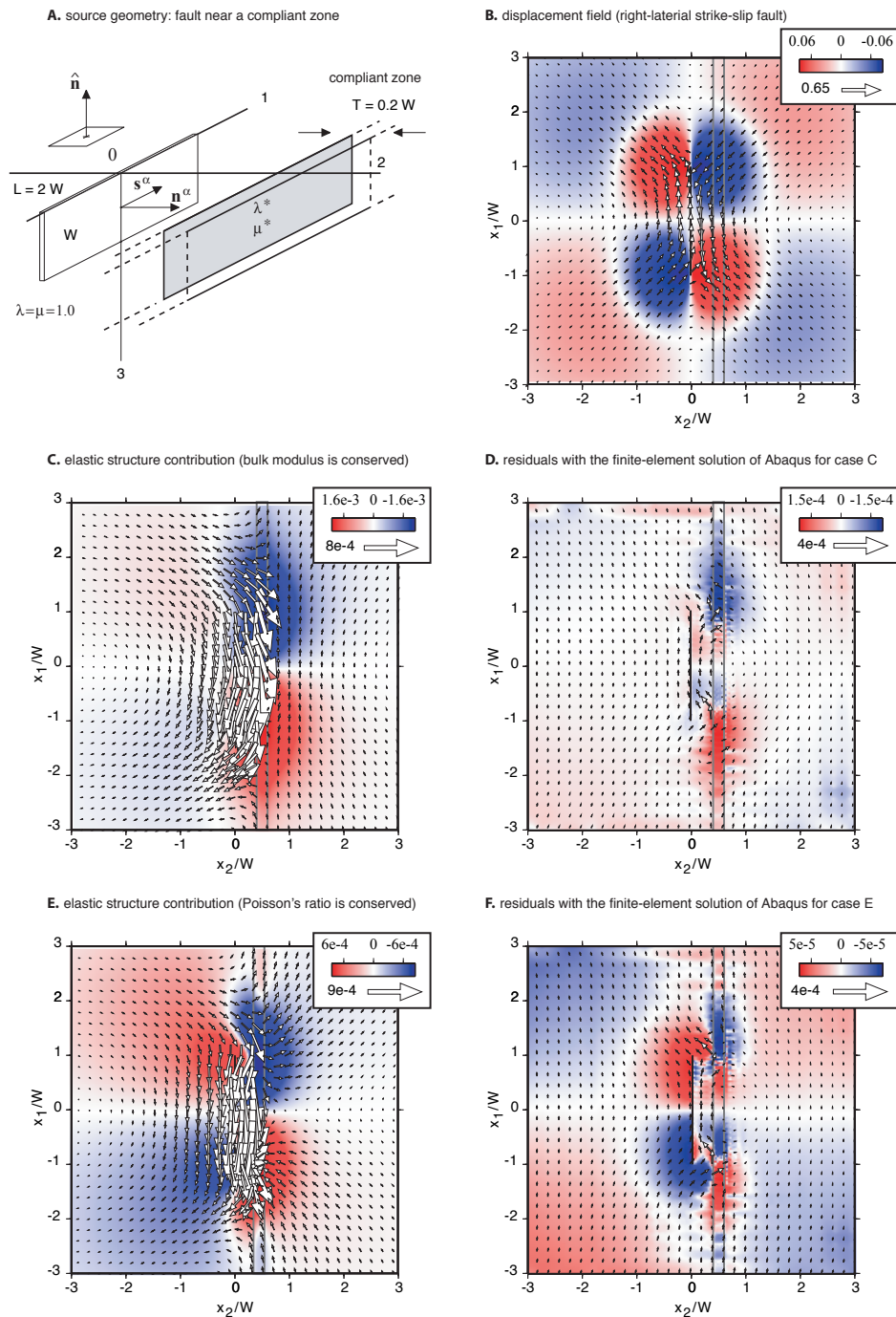


Figure 4.14: A) Geometry. B) Displacement field at the surface. C) Elastic structure contribution for the case of uniform bulk modulus. D) Residuals between our result and a finite-element calculation for case C. E) Elastic structure contribution for the case of uniform Poisson's ratio. F) Residuals between our solution and finite-element calculations corresponding to case E.

Chapter 5

Postseismic Deformation due to the Mw 6.0 2004 Parkfield Earthquake: Stress-Driven Creep on a Fault with Spatially Variable Rate-and-State Friction Parameters

Sylvain Barbot, Yuri Fialko and Yehuda Bock

Abstract. We investigate the co- and postseismic deformation due to the Mw 6.0 2004 Parkfield, CA earthquake. We produce co- and postseismic slip models by inverting data from an array of 14 continuous GPS stations from the SCIGN network. Kinematic inversions of postseismic GPS data over a time period of three years show that afterslip occurred in areas of low seismicity and low coseismic slip, predominantly at a depth of ~ 5 km. Inversions suggest that coseismic stress increases were relaxed by predominantly aseismic afterslip on a fault plane. The kinetics of afterslip is consistent with a velocity-strengthening friction generalized to include the case of infinitesimal velocities. We performed simulations of stress-driven creep using a numerical model that evaluates the time-dependent deformation due to coseismic stress changes in an visco-elastoplastic half-space. Starting with a coseismic slip distribution, we compute the time-dependent evolution of afterslip on a fault plane and the associated displacements at the GPS stations. Data are best explained by a rate-strengthening model with frictional parameter $(a - b) = 7 \times 10^{-3}$, at a high end of values observed in laboratory experiments. We also find that the geodetic moment due to creep is a factor of 100 greater than the cumulative seismic moment of aftershocks. The rate of aftershocks in the top 10 km of the seismogenic zone mirrors the kinetics of afterslip, suggesting that post-earthquake seismicity is governed by loading from the nearby aseismic creep. The San Andreas fault around Parkfield is deduced to have large along-strike variations in rate-and-state frictional properties. Velocity strengthening areas may be responsible for the separation of the coseismic slip in two distinct asperities and for the ongoing aseismic creep occurring between the velocity-weakening patches after the 2004 rupture.

5.1 Introduction

The San Andreas fault around Parkfield, California, exhibits a transition from a creeping segment to the northwest to a locked segment to the southeast. The creeping section experiences a quasi-steady sliding at a rate of 33 mm/yr [Murray et al., 2001], close to the estimated 35 mm/yr long-term rate of the San Andreas fault at that latitude [Lisowski et al., 1991]. Moderate magnitude 6 earthquakes repeatedly occur in this transition zone. The 2004 Mw 6.0 Parkfield earthquake is the most recent in a series of events including a least five historical earthquakes in 1881, 1901, 1922, 1934, and 1966 rupturing approximately the same area on the fault [Bakun and McEvilly, 1984, Bakun et al., 2005]. The Earthquake Prediction Experiment [Bakun and Lindh, 1985], motivated by the small recurrence time of the Parkfield sequence, sought to monitor the anticipated earthquake and reveal the earthquake process in unprecedented detail. The event of September 28, 2004 was the subject of numerous studies that exploited a large variety of available geophysical data [e.g., Harris and Arrowsmith, 2006].

The coseismic rupture was imaged using various geodetic [e.g., Johanson et al., 2006, Johnson et al., 2006, Langbein et al., 2006] and seismic [e.g., Liu et al., 2006, Allmann and Shearer, 2007] observations. A common feature of these studies is the partition of the earthquake slip distribution in two distinct areas of high slip: a first patch located close to the epicenter, and a second, larger amplitude patch, further to the northwest. Previous studies showed that the postseismic transient is likely dominated by afterslip [e.g., Johanson et al., 2006, Johnson et al., 2006, Freed, 2007]. Johanson et al. [2006] inferred the details of the early afterslip distribution from GPS and interferometric synthetic aperture radar (InSAR) measurements. Somewhat surprisingly, more fault-averaged slip was found to have occurred during the postseismic period than during the coseismic rupture. The inferred geodetic moment due to afterslip was equivalent to a magnitude Mw 6.1 earthquake over four months following the rupture [Johanson et al., 2006], and Mw 6.3 two years after the event [Freed, 2007] (i.e., about three times the coseismic moment release.) The moment release during co- and postseismic slip differs from that observed in other instrumented areas and might be peculiar because of the transition between the creeping and locked segments of the San Andreas fault.

In this study, we take advantage of the continuous GPS array of the SCIGN network [Langbein and Bock, 2004], which covers the Parkfield segment during the inter-, co- and postseismic intervals, to constrain the dominant mechanisms driving the postseismic deformation over three years following the 2004 earthquake. In the next section, we begin by deriving a coseismic slip model and estimating the resolving power of the GPS array. In section 3, we perform a series of kinematic inversions to track the evolution of slip on the fault plane over three years following the earthquake. In section 4, we describe stress-driven creep models incorporating power-law and velocity-strengthening friction laws. We perform a principal component analysis of the GPS time series. We fit the dominant mode to analytic solutions for the postseismic

relaxation of a simple creeping patch. In section 5, we use stress-driven creep models to constrain constitutive properties of the fault interface [Stuart and Tullis, 1995, Johnson et al., 2006, Perfettini and Avouac, 2004, 2007]. We explore predictions of the rate- and state-dependent friction [Dieterich, 1992, 1994] using a new semi-analytic model of nonlinear fault creep. Using our kinematically inferred coseismic slip distribution as an initial condition, we compute forward models of fault brittle creep and discuss implications for *in situ* constitutive frictional properties of rocks in the San Andreas fault zone. In Appendix 5.8, we derive the analytic impulse response of a power-law shear zone and of a Rate-Strengthening (RS) crack due to coseismic stress change. In Appendix 5.9 we describe our mathematical approach to model three-dimensional deformation due to nonlinear creep and present our numerical implementation. The rate of creep of the RS crack in the interseismic period is discussed in Appendix 5.10.

5.2 Coseismic Slip Model

We use the September 28th 2004 one-day static offsets in the SCIGN continuous GPS time series computed at the Scripps Orbit and Permanent Array Center (<http://sopac.ucsd.edu/>) to invert for a coseismic slip distribution. We approximate the fault zone with a single fault segment and allow for right-lateral strike slip only. We discretize a 40 km long, 15 km deep plane with 2×1 km patches in the strike and dip directions, respectively. As inversions of surface displacements are intrinsically non-unique [e.g., Parker, 1994, Mavko, 1981, Savage, 1990], we impose slip non-negativity, a smoothness constraint and zero slip at the bottom of the fault to regularize the problem (see [Fialko, 2004a] for details). In particular, we use the homogeneous elastic Green function [Okada, 1992] for a Poisson solid and the finite difference approximation of the gradient operator to smooth the slip model.

We determine our preferred source geometry by performing a grid search for the strike, dip and position of the fault that best fit the GPS offsets. Fig. 5.1 shows our best model, corresponding to a vertical fault striking N136°. Effects of the smoothness factor (SF) on the inferred geometry are illustrated in Fig. 5.2. For high values of SF, the inferred slip distribution on the fault is smooth (see upper-left slip model in Fig. 5.2a). At intermediate values of SF, the slip distribution becomes bimodal, with two distinct slip patches appearing along strike. For smaller values of SF, the two slip patches persist, and become more localized with a smaller slip area and a higher slip amplitude. We choose our smoothing factor $SF=10^{-4}$ to be at the position where misfit is weakly dependent upon the degree of smoothing, as illustrated by the smoothness/misfit curve of Fig. 5.2b. Using a uniform shear modulus of $G = 30$ GPa, our best-fitting coseismic model has a geodetic moment of $m = 1.98 \cdot 10^{18}$ N equivalent to moment magnitude Mw 6.16, somewhat higher than the seismic moment of Mw 6.0. Inversions using a high-rate GPS data and a smaller coseismic interval gave rise to a geodetic moment of Mw 6.0, in a better agreement with estimates from seismic data [Murray and Langbein, 2006]. Our use of daily GPS solutions

may include some early afterslip in the coseismic model. Fig. 5.1b shows the modeled surface displacements at the 14 GPS stations, along with the GPS measurements and their two-sigma uncertainty. Most of the GPS displacements can be explained by right-lateral strike slip on the fault plane.

The station distribution in the GPS array and the geometry of the fault limit our ability to infer slip equally well everywhere on the fault plane. Following the approach of Backus [1970] and Tarantola [2004], the resolution kernel of the under-determined inverse problem is

$$\mathbf{R} = \mathbf{G}^t (\mathbf{G} \mathbf{G}^t)^{-1} \mathbf{G} \quad (5.1)$$

where \mathbf{G} is the matrix of the elastic Green function [Okada, 1992] used in the slip distribution inversion. Fig. 5.3a shows the diagonal of matrix \mathbf{R} , which represents the sensitivity of the GPS array to variations in slip at each patch on the fault. The resolution, a dimensionless quantity, varies from 1 in well-resolved areas to 0 in essentially unresolved areas. Inspection of the resolution matrix shows that the available GPS data constrain mostly the upper part of the fault. A critical value of resolution $R = 0.1$ is reached at a depth of about 7 km. Fig. 5.3b shows off-diagonal components of the resolution matrix of eq. (5.1) for slip patches down to 8 km depth. Resolution on deeper patches is degraded, as expected. Off-diagonal terms indicate the correlation between inferred slip on a fault patch and neighboring patches. For example, inference of slip on a fault patch intersecting the Earth's surface at along-strike position $x = 24$ km is unbiased. However, inferred slip at the ends of the fault, away from most GPS stations, is less resolved. For the slip patch at depth of 5 km and along-strike position of $x = 24$ km, the inferred slip location is more robust along the strike than along the dip direction. At the same position in azimuth but greater depth, the inferred slip is more diffuse and azimuthal position is less robust. We conclude that inversion for slip using the current distribution of GPS stations is robust down to a depth of about 7 km immediately below the center of the GPS array at along-strike range $x = 18 - 30$ km. We note however that the inferred slip at about 5 km depth might appear distributed along a greater depth range of about 2-3 km.

Our coseismic slip model exhibits two zones of relatively high slip (see Fig. 5.1a). The area to the northwest, characterized by the highest slip, is directly below the GPS array, above the 7 km resolution limit of the array aperture, and is therefore a well constrained feature. The second area, to the southeast and closer to the epicenter, is further away from the GPS network and extends to a depth of 10 km. The corresponding slip is more poorly constrained, and might be over-smoothed.

5.3 Postseismic Transient Deformation

Large earthquakes are usually followed by episodes of gradually decaying deformation. Various mechanisms proposed to explain the postseismic transients include poroelastic rebound [Peltzer

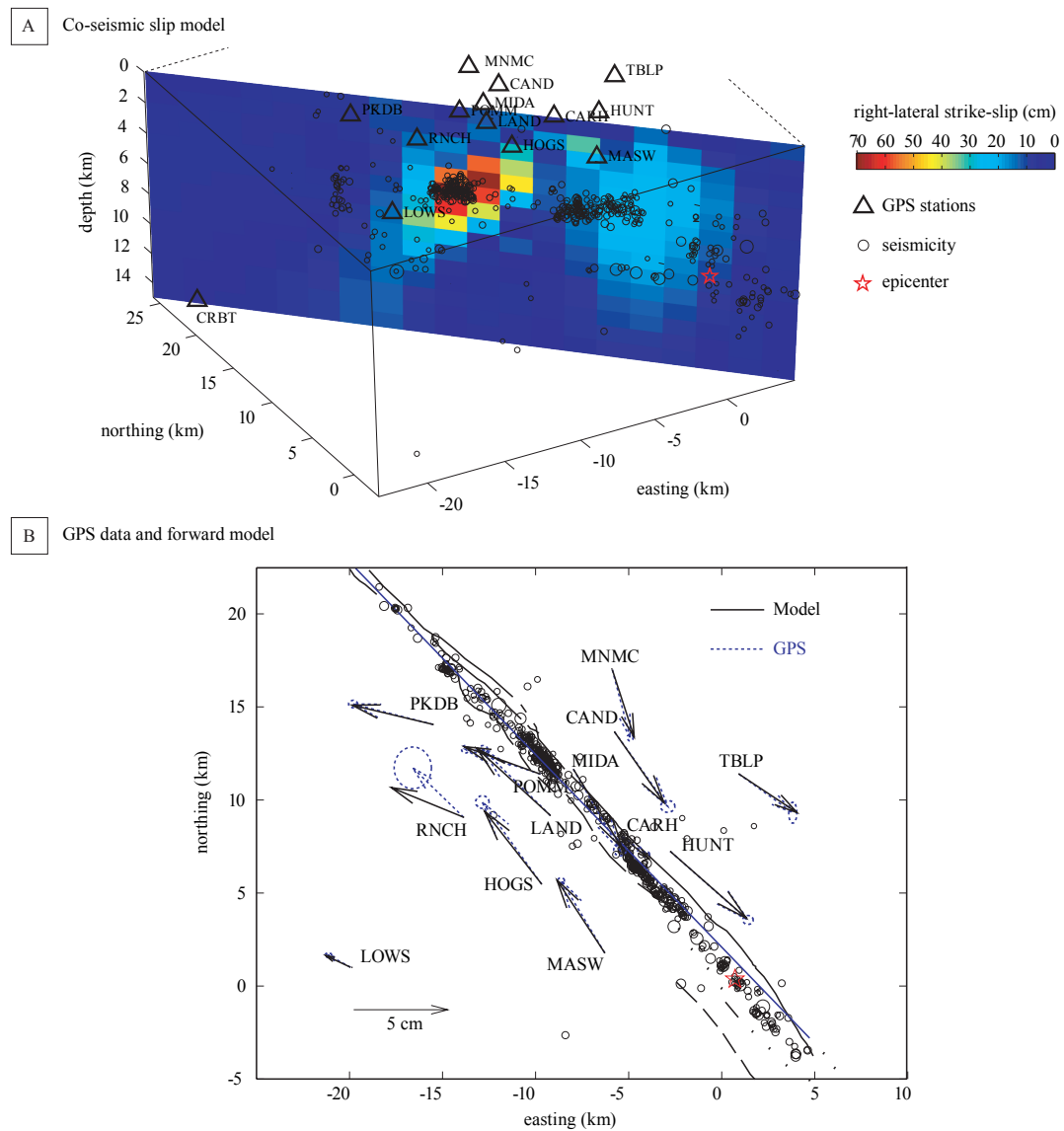


Figure 5.1: Coseismic slip model. A) amplitude of right-lateral strike slip inferred from the inversion of the 14 continuous GPS horizontal coseismic displacements. B) Map view of the coseismic displacement vectors. The blue arrows represent the GPS data with the two-sigma uncertainties; the black arrows correspond to our best forward model. The origin is located at (N35.8150, W120.3740).

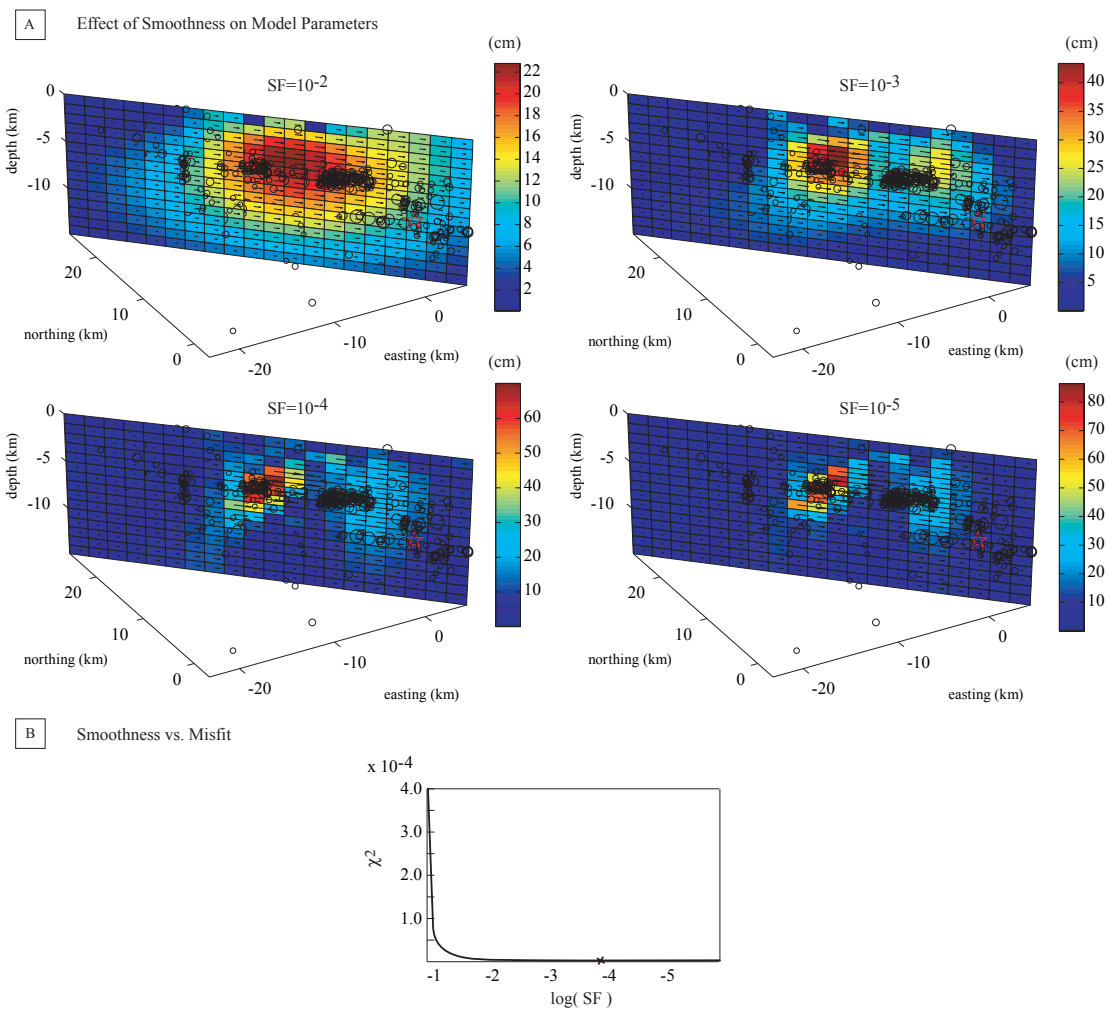


Figure 5.2: A) Effect of smoothing on the coseismic slip model. The smoothness of the slip model is controlled by the smoothness factor (SF) in the inversion. B) The smoothness/misfit curve. Our models use smoothness factor $SF=10^{-4}$ as indicated by the black cross.

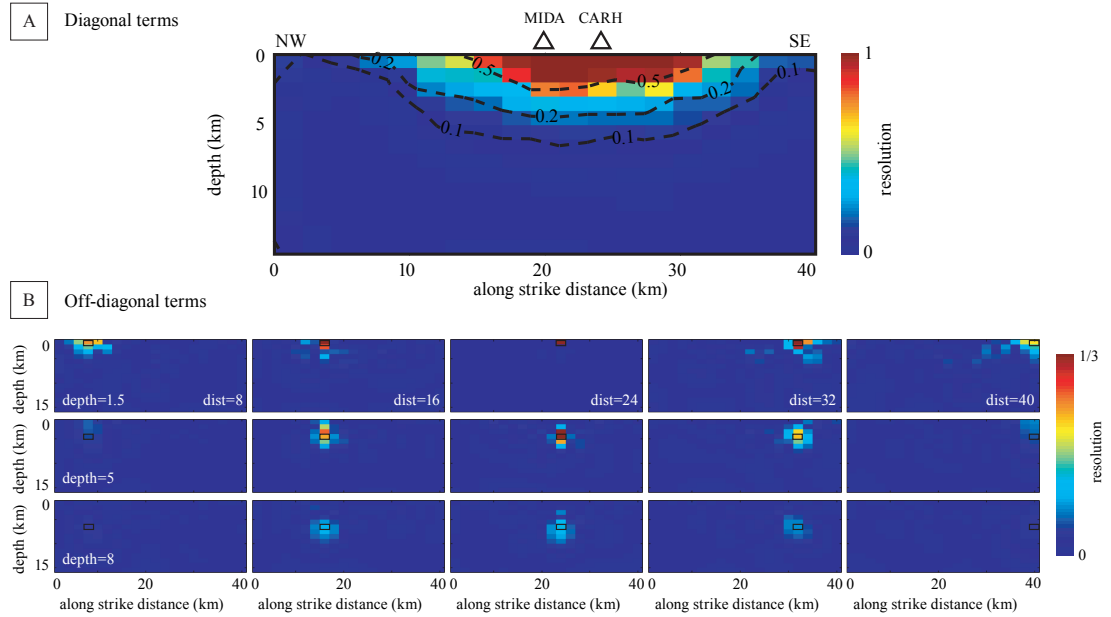


Figure 5.3: Resolution of the under-determined inverse problem. A) Diagonal of the resolution matrix \mathbf{R} . Critical value $R = 0.1$ is reached at a depth of about 7 km. B) Correlation of inferred slip patches with their neighbors on the fault plane (off-diagonal terms of the resolution matrix). Position of central subpatches is indicated in white text (depth and distance along strike) and highlighted by black rectangle. Note the change of color scale in B. The fault segment that experienced the most afterslip is located at an along-strike distance of 24 km and a depth of 5 km; its location is robust in the strike direction.

et al., 1998, Jonsson et al., 2003, Fialko, 2004a], afterslip on the ruptured fault or its extension [Marone et al., 1991, Savage et al., 1994, Fialko, 2004b, Freed et al., 2006, Barbot et al., 2008b], and viscoelastic relaxation in the lower crust or upper mantle [Nur and Mavko, 1974, Pollitz et al., 2000, Freed and Bürgmann, 2004]. Several authors have shown that the postseismic transient following the 2004 Parkfield earthquake is dominated by afterslip [e.g., Johnson et al., 2006, Johanson et al., 2006, Freed, 2007]. The focus of this study is the physical mechanisms of afterslip caused by the 2004 event. We utilize the network of 14 continuous GPS stations [Langbein and Bock, 2004] to infer a time-dependent postseismic slip on the fault plane. We use SOPAC’s filtered daily position time series where a common mode noise has been removed. The methodology for noise reduction is standard and details can be found in Wdowinski et al. [1997]. We isolate the postseismic signal from the filtered GPS time series by removing a linear trend corresponding to the interseismic displacements. The time window used in the regression for interseismic velocities corresponds to the interval from first availability of data to December 2003, before the occurrence of neighboring San Simeon earthquake. The duration of the time series used in the inversion at each GPS station varies from 2.2 to 7.2 a and is listed in Table 5.1. Inferred interseismic GPS velocities and uncertainties are shown in Table 5.1. We also remove

Table 5.1: Inferred velocity of the SCIGN continuous GPS stations before the December 2003 San Simeon earthquake. Time t (a) refers to the duration of the interval used for the linear regression. Parameters V_N , V_E , σ_N and σ_E are the North and East components of the GPS velocity and corresponding standard deviation, respectively.

Name	lon	lat	t (a)	V_N (m/a)	V_E (m/a)	σ_N (mm/yr)	σ_E (mm/yr)
CAND	-120.433	35.939	4.3	-0.0242	0.0070	0.1	0.1
CARH	-120.430	35.888	2.3	-0.0353	0.0159	0.2	0.2
CRBT	-120.750	35.791	2.2	-0.0380	0.0211	0.3	0.3
HOGS	-120.479	35.866	2.3	-0.0348	0.0175	0.2	0.2
HUNT	-120.402	35.880	2.3	-0.0274	0.0082	0.1	0.1
LAND	-120.473	35.899	4.3	-0.0346	0.0173	0.2	0.1
LOWS	-120.594	35.828	2.3	-0.0365	0.0200	0.2	0.1
MASW	-120.443	35.832	2.3	-0.0348	0.0168	0.2	0.1
MIDA	-120.458	35.921	4.3	-0.0236	0.0085	0.2	0.2
MNMC	-120.434	35.969	2.3	-0.0239	0.0055	0.2	0.2
PKDB	-120.541	35.945	7.2	-0.0351	0.0188	0.1	0.1
POMM	-120.478	35.919	4.3	-0.0343	0.0161	0.2	0.2
TBLP	-120.360	35.917	2.3	-0.0255	0.0039	0.2	0.5
RNCH	-120.524	35.899	2.2	-0.0375	0.0167	0.7	0.8

the coseismic displacements due to the December 2003 Mw 6.6 San Simeon and the 2004 Parkfield earthquakes, along with other spurious static offsets. (Some static offsets appear in GPS time series after antenna updates.) Postseismic data clearly show that the transient deformation triggered by the coseismic stress change is still occurring three years after the earthquake (see Figs. 5.7 and 5.10).

We invert the postseismic signal for cumulative afterslip as a function of time. Formalism of the inversion is the same as the one used for the coseismic model discussed above (including the smoothing constraint and the resolution, as shown in Fig. 5.3.) Most of the surface displacements occur during the first year following the earthquake. Fig. 5.4 shows snapshots of the inferred afterslip evolution at 0.05, 0.15, 0.30, 0.70, 1.10, 1.50 and 2.50 years after the main event. We did not regularize the afterslip evolution in the time domain which may result in spurious variations in slip velocity (e.g., see a patch of high slip at along-strike distance of 30 km at time 0.7 years that disappears at later times, Fig. 5.4.) Such second-order variations in the inferred cumulative afterslip are likely due to unmodeled periodic signals and the presence of noise in the postseismic time series [Williams et al., 2004, Langbein, 2008]. GPS horizontal displacements and fit to the data are shown in Fig. 5.5. Most stations are very well fitted by our afterslip models throughout the 3 year interval. Given that the 2004 Parkfield earthquake induced little if any viscous relaxation in the lower crust or upper mantle [Johnson et al., 2006, Freed, 2007], our

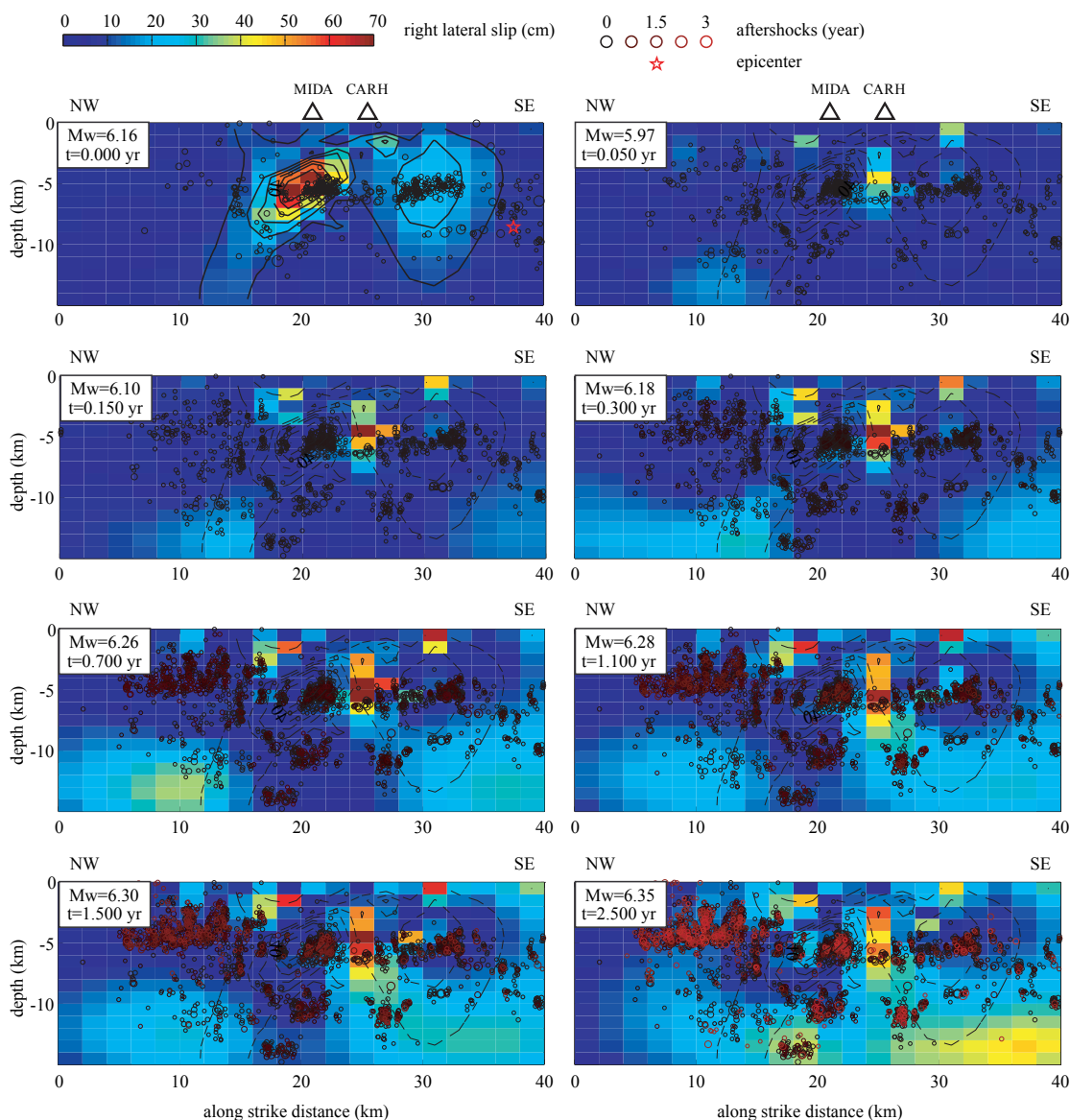


Figure 5.4: Kinematic inversions and seismicity. The right-lateral slip on the fault plane as a function of time after the coseismic rupture is constrained from the continuous GPS data. Upper-left model is the coseismic slip distribution along with the 1-day seismicity. The continuous profiles are the coseismic slip contour intervals. Next panels are the cumulative afterslip models at 0.05, 0.15, 0.30, 0.70, 1.10, 1.50 and 2.50 yr after the earthquake. Aftershocks -cumulative since the day following the earthquake- are superimposed to the afterslip models, colored from black to red for early to late occurrence time. The coseismic contour lines are superimposed to the afterslip models to facilitate comparison.

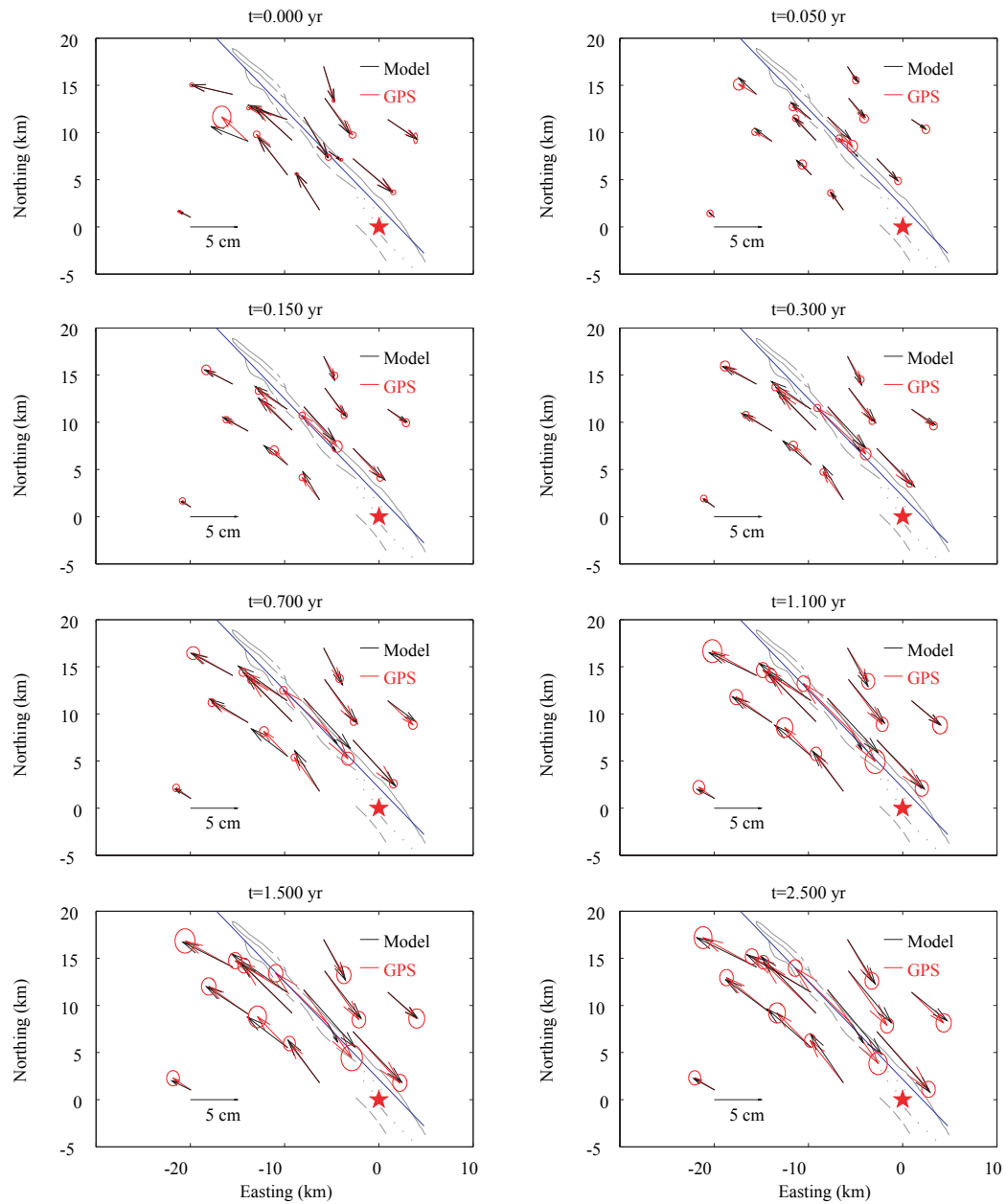


Figure 5.5: Kinematic inversions (continued). GPS horizontal displacements (red arrows with two-sigma uncertainties) and corresponding forward models (black arrows). The GPS data in the 3 yr postseismic transient can be explained by right-lateral afterslip on the coseismically ruptured fault segment. Origin is at the geographic coordinate (N35.8150, W120.3740).

results confirm that the postseismic deformation is primarily driven by right-lateral afterslip on the fault plane. Station CARH, located inside the fault zone, exhibits a reversal in the direction of motion. This behavior is likely due to slip migration to a nearby parallel fault strand [Murray and Langbein, 2006].

Also shown in Fig. 5.4 is our coseismic slip model (top-left panel) and the cumulative seismicity. The coseismic slip contour lines are superimposed on all kinematic inversions to facilitate comparison between co- and postseismic slip distributions. At early stages of deformation, afterslip occurs principally around a depth of 5 km, between two areas of high coseismic slip. In the time interval of about 3 months, afterslip reaches an equivalent geodetic moment greater than the seismic moment of the Parkfield earthquake, in agreement with earlier results by Johanson et al. [2006]. After 2.5 years, afterslip reaches a cumulative geodetic moment of Mw 6.35 (c.f. our inferred coseismic moment of Mw 6.16). The shallow location (depth smaller than 7 km) of early afterslip is robust, given the sensitivity of the GPS array (Fig. 5.3). We performed two other series of inversions of coseismic and postseismic GPS data varying the discretization of the fault plane as a function of depth [Fialko, 2004a, Fialko et al., 2005]. In these inversions we increased the along-strike and the down-dip dimensions of sub-fault rectangles by 25% and 50%, respectively, resulting in a sampling of the deepest part of the fault by 5 to 4 slip patches, respectively. We find that, similar to what appears in Fig. 5.4, coseismic slip and afterslip occupy a remarkably complementary area on the fault plane. There is no resolvable overlap between afterslip and coseismic slip. At later times, some afterslip occurs also at greater depth, but the location cannot be precisely inferred from the available data. Our estimate of the postseismic geodetic moment includes the poorly resolved deep slip (Fig. 5.3) that occurs in the last two years and may be biased towards higher values in this period. Earthquake locations correlate with areas of coseismic slip and seem not to evolve spatially throughout the postseismic epoch. Afterslip is confined to areas of low seismicity and does not represent deformation due to aftershocks.

Time-dependent kinematic inversions of GPS data suggest that afterslip occurs at the periphery of the coseismic rupture, in areas characterized by low aftershock activity. Such aseismic creep is suggestive of spatial variations in frictional properties on the San Andreas fault near Parkfield. In particular, velocity-weakening areas appear to correspond to zones of high seismicity and coseismic slip; velocity-strengthening areas appear to pose an obstacle to rupture propagation and to the occurrence of aftershocks, but favor postseismic creep.

5.4 Models of Time-Dependent Deformation

We investigate several mechanisms that might contribute to the observed deformation pattern. The deformation may be localized on a frictional surface [Marone et al., 1991, Marone, 1998, Scholz, 2002] or in a ductile shear zone [Evans and Kohlstedt, 1995, Roberts and Turcotte, 2000, Montesi, 2004]. In the latter case, the so-called plastic instabilities can spread over a narrow,

yet finite, volume encompassing the fault zone. In case of a frictional interface, all deformation is accommodated by slip on a narrow fault. These two hypotheses give rise to specific constitutive laws relating the effective stress to the slip rate.

Shear failure and slip at seismogenic depth are controlled by the Coulomb stress [Byerlee, 1978], which is to the first order given by

$$\tau - \mu \sigma = 0 \quad (5.2)$$

where τ is the amplitude of shear stress in the direction of sliding, σ is the effective normal stress accounting for the pore pressure contribution (positive for compression) and μ is the coefficient of friction. We decompose shear and effective normal stresses resolved on a fault into a background (e.g., tectonic) level and a coseismic change, respectively,

$$\begin{aligned} \tau &= \tau_b + \Delta\tau \\ \sigma &= \sigma_b + \Delta\sigma \end{aligned} \quad (5.3)$$

In the context of strike-slip faulting, we further assume that the change in the normal stress is negligible compared to the tectonic and lithostatic contributions

$$\Delta\sigma \ll \sigma_b, \quad (5.4)$$

and that the pre-earthquake Coulomb stress is negligible compared to the coseismic stress change,

$$\Delta\tau \gg \tau_b - \mu_0 \sigma_b \quad (5.5)$$

Under these assumptions, the effective stress driving afterslip on the fault plane is the shear component of coseismic loading $\Delta\tau$. Subsequent evolution of stress changes depends upon a particular mechanism of shear.

Plastic instabilities can be modeled with linear or power-law creep rheologies [Weertman and Weertman, 1964, 1975, Evans and Kohlstedt, 1995],

$$\dot{\gamma} = A \left(\frac{\Delta\tau}{G} \right)^n \quad (5.6)$$

where $\dot{\gamma}$ is the rate of plastic strain, n is a power exponent between 1 and 5 indicating the degree of stress sensitivity, G is the shear modulus, and A is the reference strain rate controlling the timescale of deformation. For $n = 1$, the creep rheology is linear and $\eta = G/A$ is the viscosity. Equation (5.6) may be coupled to thermal softening, which implies depth-dependent parameters [Kohlstedt et al., 1995]. Dependence on thermal or other specific state parameters can simply be included by allowing parameter A to vary spatially.

Localized slip on frictional interfaces can be described by rate- and state-dependent friction laws [Ruina, 1983, Dieterich, 1992]

$$\mu = \mu_0 + a \ln \left(\frac{\dot{s}}{\dot{s}_0} \right) + b \ln \theta, \quad (5.7)$$

where \dot{s} is the slip rate on the fault, μ_0 is the coefficient of friction at a reference slip rate \dot{s}_0 , a and b are the frictional parameters and θ is a state variable subjected to an evolution law. Under the consistency condition (5.2) and the assumptions (5.4) and (5.5), the friction law can be written

$$\dot{s} = \dot{s}_0 \theta^{-\frac{b}{a}} e^{\frac{\tau}{a\sigma}} \quad (5.8)$$

where the ratio b/a is a work-hardening parameter, weakening for $b/a > 1$ and strengthening for $b/a < 1$. An unphysical feature of the original rate-and-state formulation (5.7) is an asymptotic divergence of friction at small velocities $\dot{s} < \dot{s}_0$. We adopt a generalized version of eq. (5.7),

$$\mu = \mu_0 + a \sinh^{-1} \left[\frac{\dot{s}}{2\dot{s}_0} \theta^{\frac{b}{a}} \right] \quad (5.9)$$

motivated by thermo-dynamic considerations [Lapusta et al., 2000, Rice et al., 2001]. Under the same assumptions the corresponding slip rate is

$$\dot{s} = 2 \dot{s}_0 \theta^{-\frac{b}{a}} \sinh \frac{\tau}{a\sigma} \quad (5.10)$$

Note that formulations (5.7) and (7.25), or equivalently formulations (5.8) and (5.10), are asymptotically equivalent at high velocities, but eqs. (7.25) and (5.10) remain bounded at small slip rates. We assume that most of the postseismic creep occurs at steady state ($\dot{\theta} = 0$) and we ignore the healing and slip-weakening effects. The steady-state assumption is valid only if the cumulative afterslip largely exceeds the strengthening or weakening distance D_c of the state variable. The magnitude of afterslip at Parkfield reaches about half a meter (see Fig. 5.4), which is several orders of magnitude larger than values of D_c inferred from laboratory experiments [Marone, 1998]. The steady-state assumption gives rise to a purely rate-strengthening constitutive law

$$\dot{s} = 2 \dot{s}_0 \sinh \left[\frac{\Delta\tau}{a\sigma} \right] \quad (5.11)$$

which represents the direct effect between slip rate and stress change. Note that formulation (5.11) resembles the empirical relationship of Garofalo [1975] for power-law breakdown [Tsen and Carter, 1987]. Velocity-strengthening friction models are an approximation to the full rate-and state-dependent friction model for a positive parameter ($a - b$) and negligible evolution of the state variable, $\dot{\theta} = 0$ [e.g., Marone et al., 1991, Marone, 1998, Perfettini and Avouac, 2007]. We note that the Rate-Strengthening (RS) friction parameter \dot{s}_0 does not correspond to the so-called "interseismic" velocity of the friction interface (see discussion in Appendix 5.10.) Eq. (5.11) relates the rate of steady afterslip to coseismic stress change, and RS parameter \dot{s}_0 is a rock property that controls the timescale of transient slip episodes similar to parameter A in power-law models.

To test the predictive power of RS friction and power-law creep in explaining the GPS time series, we consider the impulse response of a simple shear zone. For a planar shear crack, afterslip is controlled by the effective stiffness of the slip patch

$$G^* = \frac{C G}{L} \quad (5.12)$$

where scalar C is a dimensionless constant close to 1 that depends on the geometry [Eshelby, 1957, Kanamori and Anderson, 1975, Shearer, 1999, Fialko, 2007] and L is the linear dimension of the crack. The strain accumulated across a ductile shear band of linear dimension L and thickness T depends upon its aspect ratio $\alpha = CT/L$. Fig. 5.6 illustrates the impulse response

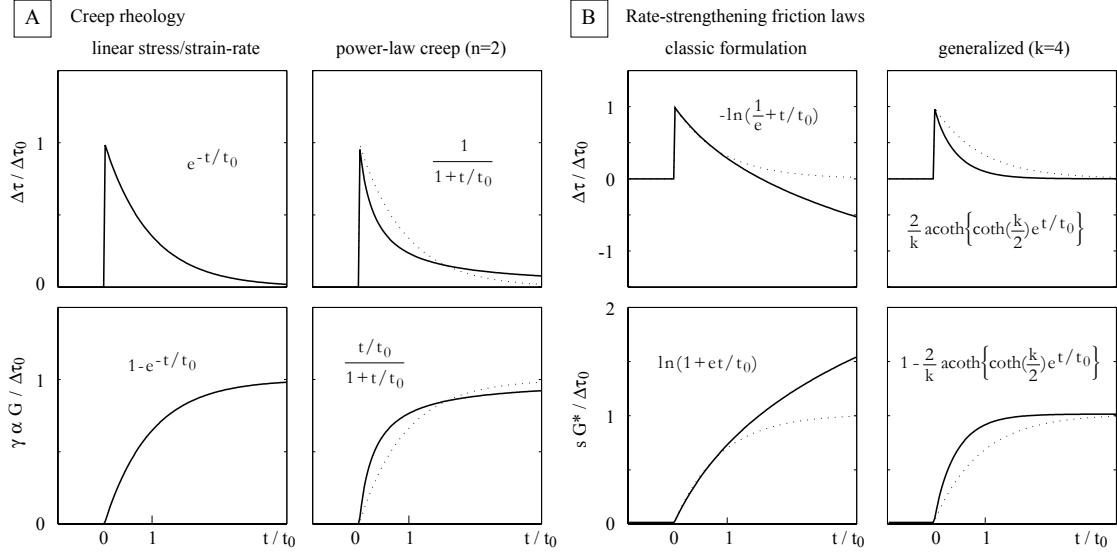


Figure 5.6: Creep tests for a simple crack frictional surface. The stress and strain impulse responses for (a) the linear and power-law creep and (b) the rate-strengthening (RS) friction laws. For a step-like increase in total strain, resulting from an instantaneous change in stress $\Delta\tau$, some inelastic deformation is triggered. The dotted profiles indicate the response of a linear rheology. The classic formulation of RS friction is ill-posed for a creep test whereas the generalized friction law remains bounded at small velocities. The detail of calculations can be found in Appendix 5.8.

to an instantaneous stress change for the linear and power-law creep rheologies, as well as for the classic and generalized rate-strengthening laws. Details of calculations are given in Appendix 5.8. The impulse response for a linear rheology is

$$\gamma(t) = \frac{\Delta\tau_0}{\alpha G} \left(1 - e^{-t/t_0}\right) \quad (5.13)$$

where γ is the strain across the ductile shear zone, $\Delta\tau_0$ is the initial shear traction, t_0 is the relaxation time scale. A schematic of the creep evolution described by eq. (5.13) is shown in the first column of Fig. 5.6 and superimposed on other profiles as a dashed line. Linear creep is a particular case of power-law creep for the case $n = 1$ (see eq. (5.6)), and of the generalized rate-strengthening friction for large $a\sigma/\Delta\tau_0$. The power-law response

$$\gamma(t) = \frac{\Delta\tau_0}{\alpha G} \left(1 - \left[1 + \frac{t}{t_0}\right]^{\frac{-1}{n-1}}\right), \quad n > 1 \quad (5.14)$$

associated with the timescale

$$t_0 = \frac{1}{A(n-1)} \left(\frac{G}{\Delta\tau_0} \right)^{n-1} \quad (5.15)$$

is illustrated in Fig. 5.6 for a power exponent $n = 2$. Compared to the linear case most of the deformation happens at an early time but complete relaxation, however, takes a much longer time. In case of rate-strengthening friction, the dimensionless ratio

$$k = \frac{\Delta\tau_0}{a\sigma} \quad (5.16)$$

controls the degree of nonlinearity during slip evolution, similar to the exponent n for power-law creep. The impulse response of strain for RS friction is

$$s(t) = \frac{\Delta\tau_0}{G^*} \left(1 - \frac{2}{k} \coth^{-1} \left(e^{t/t_0} \coth \frac{k}{2} \right) \right), \quad (5.17)$$

where we defined the reference time

$$t_0 = \frac{1}{2} \frac{a\sigma}{\dot{s}_0 G^*} \quad (5.18)$$

Deformation is also characterized by high velocities at early times, but reaches complete relaxation more rapidly, compared to linear or power-law models. Note that strain rates predicted by eq. (7.31) eventually vanish, as stress is relaxed, in contrast to the prediction of the original form of rate-dependent friction, shown in the third column of Fig. 5.6.

We test whether the impulse response of power-law creep and the generalized rate-strengthening friction law are able to explain the observed GPS time series. We use solutions (5.13), (5.14) and (7.31) for the deformation of a simple crack to fit the GPS time series. We optimize the timescale t_0 , an amplitude and a nonlinear coefficient (parameters n or k for power-law and RS friction, respectively) to reduce a misfit between the data, with associated uncertainties, and the forward models. Inversions are performed with a random walk and simulated annealing with a positivity constraint on model parameters [e.g., Tarantola, 2004]. We first performed a series of inversion of individual time series. We found that, regardless of the rheology considered, inferred model parameters were remarkably consistent among GPS stations and components. The uniformity of inferred timescale t_0 and nonlinear coefficient is indicative of a time-space separable source mechanism.

Motivated by this finding, we perform a Principal Component Analysis (PCA) of the GPS time series [Dong et al., 2006]. Considering that individual time series are ordered as lines in matrix \mathbf{X} , we define the projection $\mathbf{Y} = \mathbf{P}^T \mathbf{X}$, with $\mathbf{P}^{-1} = \mathbf{P}^T$, such that

$$\begin{aligned} \mathbf{\Lambda} &= \text{Cov}(\mathbf{Y}) \\ &= \mathbf{P}^T \text{Cov}(\mathbf{X}) \mathbf{P} \end{aligned} \quad (5.19)$$

where $\mathbf{\Lambda}$ is the diagonal covariance matrix of the PCA modes. As one has

$$\mathbf{X} = \mathbf{P}\mathbf{Y} \quad (5.20)$$

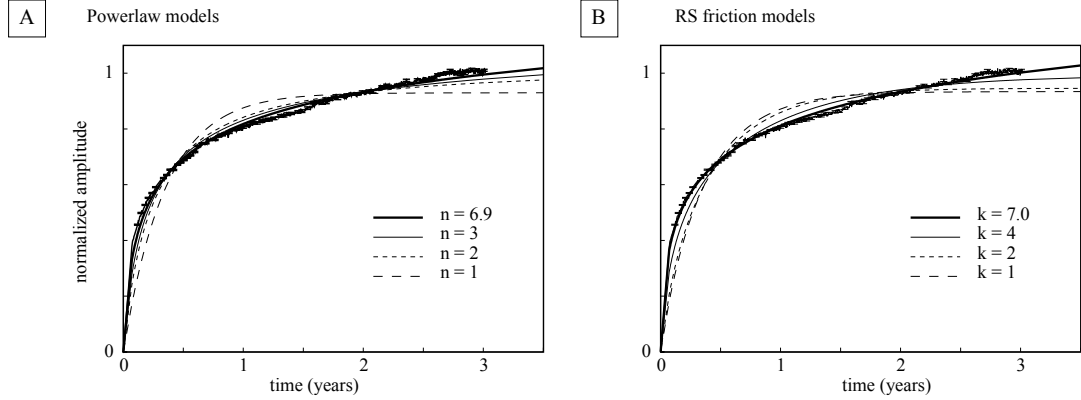


Figure 5.8: Functional fit to the dominant PCA mode of the postseismic component of the GPS time series. The impulse response of linear constitutive laws ($n = 1$ for power-law or $k \simeq 1$ for RS friction, shown by long-dashed profiles) only poorly simulate the observed time dependence of afterslip. Best fitting power-law (a) and RS models (b), corresponding to parameters $n = 6.9$ and $k = 7.0$, respectively, are represented by the thick solid lines. In other inversions, nonlinear coefficient n or k are imposed.

depth similar to the last slip distribution in Fig. 5.4. The second mode is due to a common-mode seasonal signal, which is not removed from the SOPAC filtered time series [Langbein, 2008], and is about two orders of magnitude smaller. The associated GPS displacements appear to be generally perpendicular to the fault. We consider the first mode to be representative of the postseismic response.

We test the possibility of the impulse response of different rheologies to explain the dominant PCA mode. We use a random walk with simulated annealing to find the amplitude C , timescale t_0 and nonlinear coefficient (n or k) required by the data. In a series of inversions we impose the degree of nonlinearity to illustrate its role in reducing the data. Results are shown in Table 5.2. We compute the square root of the weighted sum of the square of the residuals for the first two months and for the entire duration of the time series. These are reported in Table 5.2 as χ_1 and χ_2 , respectively. As we normalized the first PCA mode to reach the value of 1 after three years, the inferred amplitude C of fit functions is an indicator of the degree of completion predicted by the different models. For example, values of $C \simeq 1$ indicate a postseismic transient close to termination whereas higher values indicate an ongoing transient. For both power-law and RS friction rheologies, the residuals are reduced by increasing the degree of nonlinearity. The best model for power-law corresponds to $n = 6.9$, associated with an amplitude of $C = 2.03$. The best power-law model predicts that the post-Parkfield transient is only half complete. The best RS-friction fit to the PCA mode is superior to those of power-law models, as shown by the short term and the long term residual norms. The best fit is obtained for $k = 7.0$ and $C = 1.25$, indicating that the afterslip is only 75 % complete three years after the earthquake. The better fit

Table 5.2: Best Fitting parameters to the first mode of the PCA decomposition. The time series is fitted with the functional describing the impulse response of power-law creep and rate-strengthening (RS) friction. Fit parameters C , t_0 and n or k are the amplitude, the timescale and the nonlinear exponent (n for power-law and k for RS), respectively, estimated from the inversion. Misfits χ_1 and χ_2 measure the residual variance for the first two months and for the three years time series, respectively.

rheology	C	t_0	n or k	χ_1	χ_2
power-law	0.93	2.8	1	$4.1 \cdot 10^{-1}$	$7.6 \cdot 10^{-2}$
	1.04	0.23	2	$2.4 \cdot 10^{-1}$	$4.2 \cdot 10^{-2}$
	1.19	0.10	3	$1.7 \cdot 10^{-1}$	$3.0 \cdot 10^{-2}$
	2.03	0.03	6.9	$8.1 \cdot 10^{-2}$	$1.6 \cdot 10^{-2}$
RS	0.93	0.38	1	$3.9 \cdot 10^{-1}$	$7.2 \cdot 10^{-2}$
	0.94	0.47	2	$3.4 \cdot 10^{-1}$	$6.2 \cdot 10^{-2}$
	0.99	0.9	4	$1.7 \cdot 10^{-1}$	$3.2 \cdot 10^{-2}$
	1.25	4.8	7.0	$3.2 \cdot 10^{-2}$	$1.0 \cdot 10^{-2}$

of the RS model favors the rate-strengthening creep model over the power-law shear zone model.

The excellent fit of the RS friction model to the observed time series lends support to our assumptions (5.4) and (5.5). The best power-law creep model gives rise to an inferior fit with a power exponent outside of the experimentally measured range [Weertman and Weertman, 1964, 1975, Tsenn and Carter, 1987, Kohlstedt et al., 1995, Montési and Hirth, 2003], and we conclude that the bulk of postseismic relaxation is due to afterslip governed by a generalized rate-strengthening friction model. All original time series are well explained by eq. (7.31) for values of k ranging from $k = 5$ to $k = 8$. Best fit for the first PCA mode is obtained, as shown in Fig. 5.8 and Table 5.2, for $k = 7$. Inferred magnitude of the corresponding timescale is subject to greater uncertainty, with $t_0 = 4.8 \pm 2.4$ years.

As evidenced by our geodetic inversions (Fig. 5.4), the afterslip occurring in the first 4 months following the Parkfield earthquake is located between two patches of high coseismic slip, at about 5 km depth, in an area having a characteristic radius $l = 2$ km. In the first 4 month period, the equivalent geodetic moment due to afterslip, assuming $G = 30$ GPa, reaches $2.1 \cdot 10^{18}$ N (equivalent Mw 6.18), compared to a cumulative seismic moment of aftershocks of $8.2 \cdot 10^{14}$ N (Mw 3.9) over the same time period in the top 10 km. The lack of coseismic slip and the occurrence of essentially aseismic afterslip are interpreted as indicating the presence of a velocity-strengthening area in the middle of a nominally velocity-weakening layer at depth of 5 km.

As postseismic creep gives rise to a total slip of $s \simeq 0.5$ m, an estimate of the effective stress drop is [e.g., Eshelby, 1957, Kanamori and Anderson, 1975, Shearer, 1999, Fialko, 2007]

$$\Delta\tau_0 = C \frac{s}{l} G \simeq 2.5 \cdot 10^{-4} G \quad (5.21)$$

where G is the shear modulus of the upper crust and C is a constant, of order of unity, that depends upon the geometry of the slip patch. Static values of the shear modulus are not well constrained, but likely vary between 3 and 30 GPa, leading to estimates of the stress drop between $\Delta\tau_0 = 0.75$ MPa and $\Delta\tau_0 = 7.5$ MPa. For a uniform rock density of $\rho = 2700$ kg/m³, the lithostatic pressure at 5 km depth is $p = 135$ MPa. Using our inference of $k = 7$, a low-end shear modulus, and assuming an effective normal stress of $\sigma = 100$ MPa, our low-end estimate of the frictional parameter is

$$a = \frac{\Delta\tau_0}{k\sigma} \simeq 10^{-3} \quad (5.22)$$

Considering the range of possible values of the shear modulus, estimate of the friction parameter can vary between $a \simeq 10^{-3}$ and $a \simeq 10^{-2}$. Noting that parameter a is a proxy for $(a - b)$ in the context of full rate- and state-dependent friction, our inferred value falls in the range of frictional parameters observed in laboratory experiments, with values for $(a - b)$ lower than 10^{-2} at temperatures corresponding to the middle of the seismogenic zone [Scholz, 1990, 1998, Marone, 1998]. Using the same assumptions, the timescale inferred from fitting the GPS data gives rise to

$$\dot{s}_0 = \frac{\Delta\tau_0}{2G^*t_0} \simeq 5 \cdot 10^{-5} \text{ m a}^{-1} \quad (5.23)$$

The Maxwell relaxation time t_m associated with afterslip on a simple crack depends upon the effective crack stiffness,

$$t_m = \frac{\Delta\tau}{G^*\dot{s}} \quad (5.24)$$

The inferred value for the RS parameter \dot{s}_0 corresponds to linear relaxation timescales growing from $t_m = 0.45$ a, at onset of transient deformation, to $t_m \simeq 200$ a at later times. Estimates of the velocity parameter based on GPS time series and analytic solutions for a point source might be biased by a spatially variable afterslip on the fault. The effective timescale of deformation might be longer than that for a point source, and therefore eq. (5.23) should be considered a lower bound. We conclude that the parameters obtained from fitting eq. (7.31) to the postseismic GPS signal are consistent with a physical model of stress relaxation. The better fit of the RS model within a reasonable range of parameters contrasts with the inferior fit obtained with a power-law model that requires an exponent inconsistent with the laboratory data. Notice that the 28 three-year time series corresponding to the 14 GPS stations can be explained with a model having only 3 degrees of freedom. Another approach to explain the data, relating surface displacements to rate of aftershocks [e.g., Savage et al., 2007], requires many more degrees of freedom.

The inferred rate-strengthening segment of the fault experiencing an accelerated creep after the 2004 Parkfield earthquake is estimated to be slipping at rates of 1.1 mm/yr in the interseismic period in response to slip at 33 mm/yr below the seismogenic zone [Murray et al., 2001], on the down-dip extension of the San Andreas fault (see Appendix 5.10.) However, a shallow rate-strengthening patch was not apparent in inferred slip distributions corresponding to the interseismic period [Murray et al., 2001, Murray and Langbein, 2006]. The surface velocities

in GPS network corresponding to this shallow creep patch alone vary between 0.01 mm/yr at the closest station and 0.001 mm/yr at the furthest station. Such small surface velocity contributions are below the detection limit, given GPS uncertainties and the rate of interseismic loading of 33 mm/yr at the bottom of the seismogenic layer.

5.5 Semi-Analytic Models of Afterslip

As our analysis of the GPS data using solutions for a simple crack impulse response (Section 5.4) favored the generalized friction model, we further explore the latter using full 4-D simulations with a finite source. We model the aseismic creep occurring after the Parkfield event using a semi-analytical model of deformation in an visco-elastoplastic half-space. Our approach allows one to evaluate a time-dependent deformation due to a quasi-static fault slip in response to the driving coseismic stress changes. Our model includes the linear and power-law creep as well as the generalized velocity-strengthening friction law but, based on results in Section 5.4, we focus on RS models. We compute deformation due to fault creep using integral transforms [Barbot et al., 2008a]. The time-dependent fault creep is modeled by integrating the constitutive laws with a second-order accurate Runge-Kutta method with adaptive time steps. Details of our modeling approach and example calculations are discussed in Appendix 5.9.

We evaluate the velocity-strengthening parameters using our coseismic slip model as the initial condition driving the afterslip sequence. Guided by results of kinematic inversions (Fig. 5.4), we assume that areas of high coseismic slip are velocity-weakening, and do not participate in postseismic creep. We also assume that areas on the periphery of high-slip asperities are predominantly velocity-strengthening. Because seismic slip may have propagated into a transition between the velocity-weakening and velocity-strengthening areas, we include this zone in our model by limiting the coseismic slip distribution to areas where coseismic slip was greater than 0.2 m (about 30% of maximum coseismic slip.) We compensate the reduction in geodetic moment by rescaling the amplitude of the coseismic slip model. The result is a more compact slip distribution where the two main coseismic slip patches are separated by a RS patch that did not slip during the 2004 earthquake. The coseismic slip model is shown in Fig. 5.4 by the contours. The rest of the fault is allowed to participate in afterslip driven by the coseismic stress changes. We do not constrain the rake of afterslip. The slip direction is dictated by the instantaneous stress field (and may in general have a dip-slip component.)

We compute displacements resulting from time-dependent creep on a fault plane at the location of the 14 GPS stations. To evaluate how well the generalized rate-strengthening model is able to explain the GPS data, we perform a grid search to find the coefficient k that best explains the postseismic time series. In each numerical solution, we fit the GPS signals to find the reference strain rate \dot{s}_0 that gives rise to the largest misfit reduction at all stations.

Fig. 5.9 shows snapshots of the simulated RS creep evolution on the fault plane. Afterslip

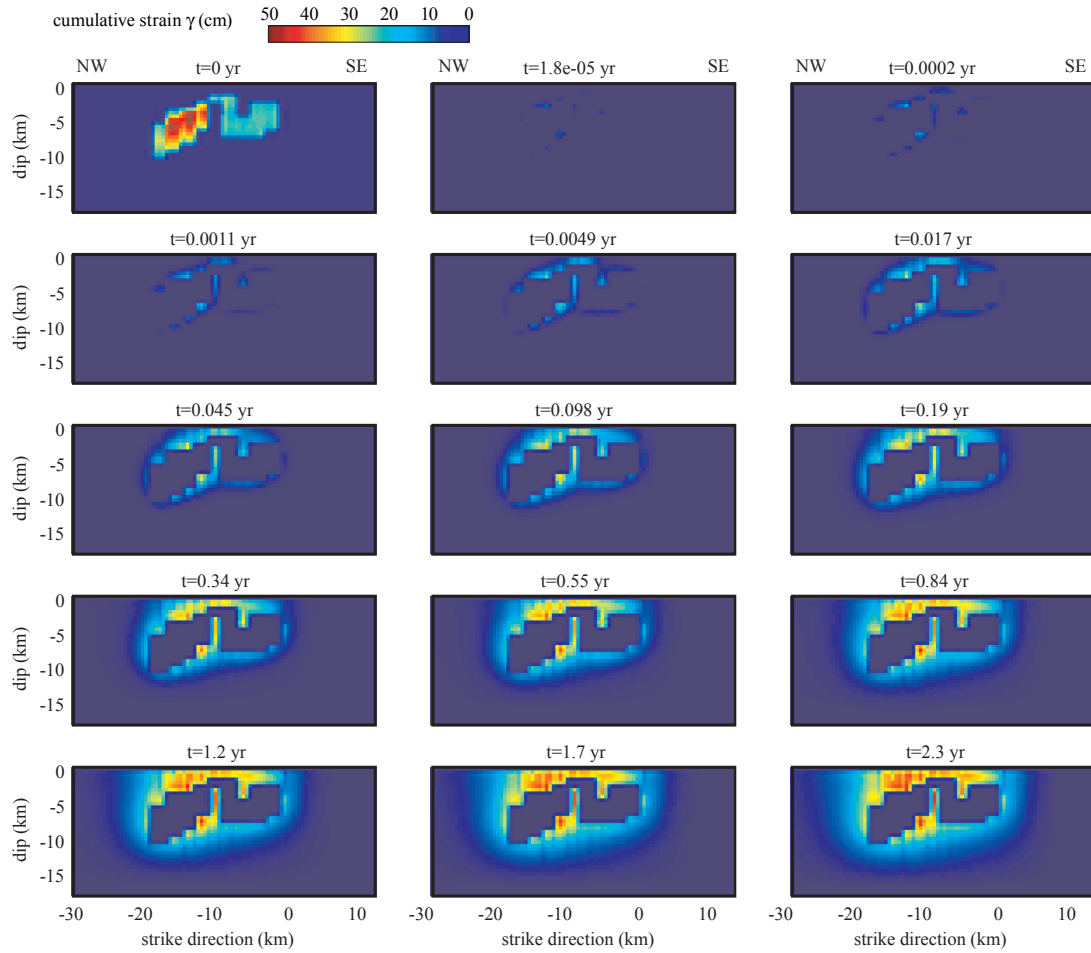


Figure 5.9: Numerical simulation of afterslip with Rate-Strengthening (RS) friction. The simplified coseismic model (upper-left corner) is the initial condition for the postseismic fault creep. Time evolution of afterslip is described by the generalized RS friction law of eq. (5.11). Afterslip is not allowed to occur in areas that slipped coseismically and propagates on the fault plane away from the coseismic patch. The corresponding time series of surface displacements are shown in Fig. 5.10. Snapshots are separated by 20 time steps. The numerical method is described in Appendix 5.9.

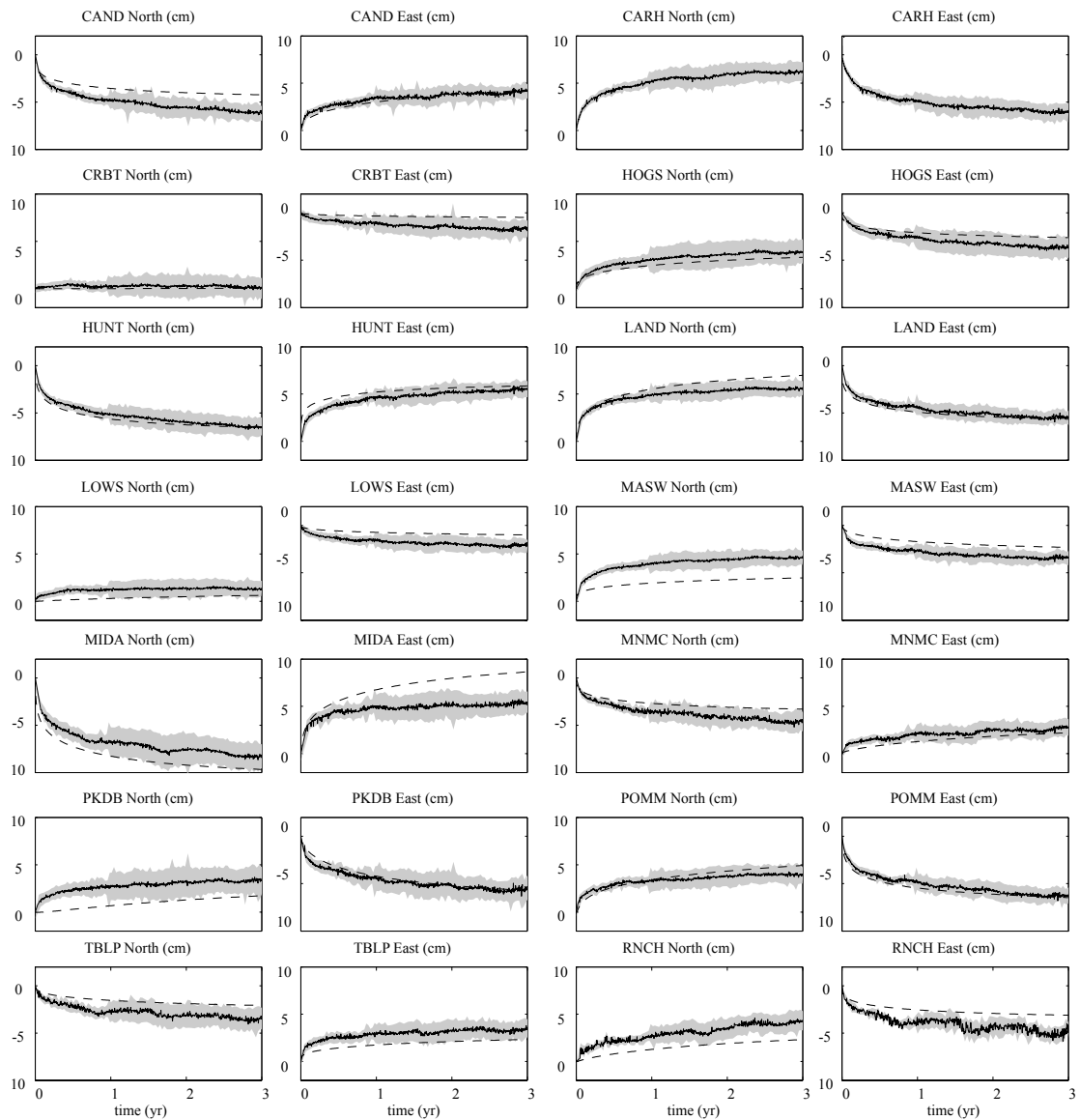


Figure 5.10: Postseismic GPS data (solid line), two-sigma uncertainties (gray shade) and best forward model (dashed lines) corresponding to the generalized rate-strengthening friction law for all the continuous GPS stations. Model prediction generally agrees with the data with the exception of station CARH and MIDA, in the very near field, which are affected by a fault migration.

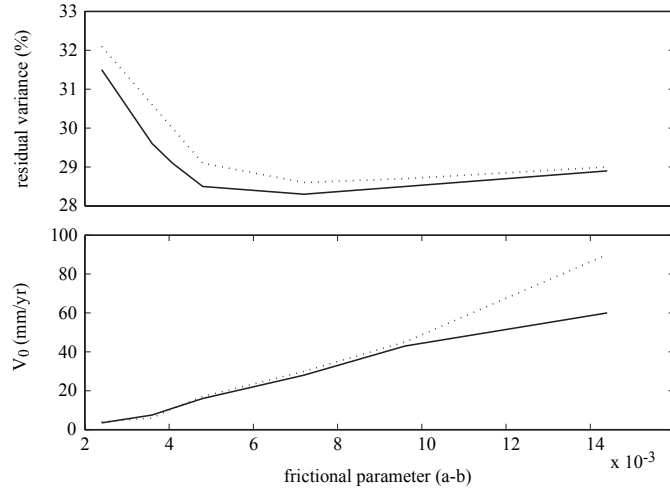


Figure 5.11: Constraint on frictional parameters V_0 and $(a - b)$. The velocity best reducing the data for the 13 selected stations (CARH is removed) is inverted using only 1 year of data (dashed profiles) and 3 years of data (solid lines). Results are shown for a series of $(a - b)$ models, assuming an effective normal stress of $\sigma = 100$ MPa.

takes place in the middle of the two patches of high coseismic slip and propagates preferentially towards the free surface. At later times our model predicts more shallow afterslip than is actually deduced in kinematic inversions. We suggest that this difference may result from the assumption of uniform frictional parameters on the fault plane. A higher value of \dot{s}_0 near the surface would delay the occurrence of shallow afterslip. Investigations of the depth dependence of frictional properties is beyond the scope of the study. Fig. 5.10 shows the GPS displacements and our best fitting model. For each forward model associated with a value of k , one parameter, \dot{s}_0 , controlling the timescale of deformation, is optimized through a grid search. Amplitude of displacements at each station is determined from the elastic Green function. Stations CARH and MIDA, in the very near field, are the only GPS stations showing a large misfit. This misfit may be due to our assumption of afterslip occurring on a geometrically simple fault plane. At the rest of the stations, our model predicts the correct sense of horizontal displacements, and most forward models are within the uncertainties of GPS measurements (95% confidence interval). Despite the approximations introduced in the initial condition, the forward model results in more than 70% variance reduction.

We computed a series of solutions for different values of $a\sigma$ ranging from 0.2 MPa to 1.4 MPa, assuming a shear modulus of $G = 30$ GPa, and inverted GPS data for the reference slip rate \dot{s}_0 . Variables \dot{s}_0 and a in our formulation correspond to the parameter V_0 and the steady-state friction parameter $(a - b)$, respectively, in spring-slider analogs of rate- and state-dependent friction [e.g., Dieterich, 1994, Marone et al., 1991, Marone, 1998, Perfettini and Avouac, 2007]. Fig. 5.11 shows the misfit and inferred velocity V_0 as a function of the velocity-strengthening

parameter $(a - b)$, assuming an effective normal stress $\sigma = 100$ MPa. We evaluated the misfit between data and model during the first year of deformation (dashed profiles) and the entire 3 years of data. Variance reduction is slightly better for the shorter interval, but in general is quite consistent. For both periods, we obtain the best fit for $(a - b) = 7 \times 10^{-3}$ and $\dot{s}_0 = 20$ mm/yr. Smaller values of $(a - b)$ give rise to a higher misfit, but the variance reduction remains sufficiently low for higher values of $(a - b)$. Our finite-size source modeling essentially provides a lower bound on the frictional parameter $(a - b)$.

Inferences of RS parameter $(a - b)$ in our full 3-D calculation are not biased by a particular choice of the shear modulus in the homogeneous elastic half-space. Some bias in estimating steady state friction parameters may arise due to the presence of a compliant fault zone [Fialko et al., 2002, Fialko, 2004b, Hamiel and Fialko, 2007, Barbot et al., 2008a, 2009b]. As we model the Parkfield coseismic rupture and the subsequent creep using the same value for the rigidity, corresponding to the compliant zone, this potential bias is limited. Another bias may come from using daily GPS solutions to derive the coseismic model, which might map some early afterslip into the coseismic model. We ignore the evolution of the state parameter. For this reason, we expect our forward models to be less accurate in the first few days following the rupture and to capture accurately the longer timescale deformation. Parameters inferred from 3-D calculations are consistent with our impulse response estimates in the previous section and our preferred value of $(a - b) = 7 \times 10^{-3}$, corresponding to the largest misfit reduction, is at the high end of inferences from laboratory experiments [Marone, 1998].

5.6 Discussion

The 2004 Mw 6.0 Parkfield earthquake triggered a transient deformation that was responsible for larger cumulative surface displacements compared to those from the main event. Velocities that are higher than the interseismic ones are still observed at near-field GPS stations three years after the event. Our inversions of the continuous GPS postseismic time series reveal that afterslip occurred conspicuously between two areas of high coseismic slip at depth of about 5 km, in the middle of the seismogenic zone. Numerous aftershocks following the earthquake are located mostly in areas that participated in seismic slip, and not in areas that hosted postseismic creep. We conclude that the post-Parkfield transient deformation is due to aseismic slip that relaxed the stress increase caused by the main shock. Furthermore, observations of microseismicity and aftershocks of previous Parkfield earthquakes have shown that earthquakes occur repeatedly on the same asperities, suggestive of variations in effective frictional properties on the fault plane [Waldhauser et al., 2004]. Our time series analysis and finite-source modeling of the GPS data indicate that afterslip occurred on a periphery of patches of high seismic slip, and is likely governed by a rate-strengthening friction law.

Results of our modeling bear on the extrapolation of laboratory measurements to natu-

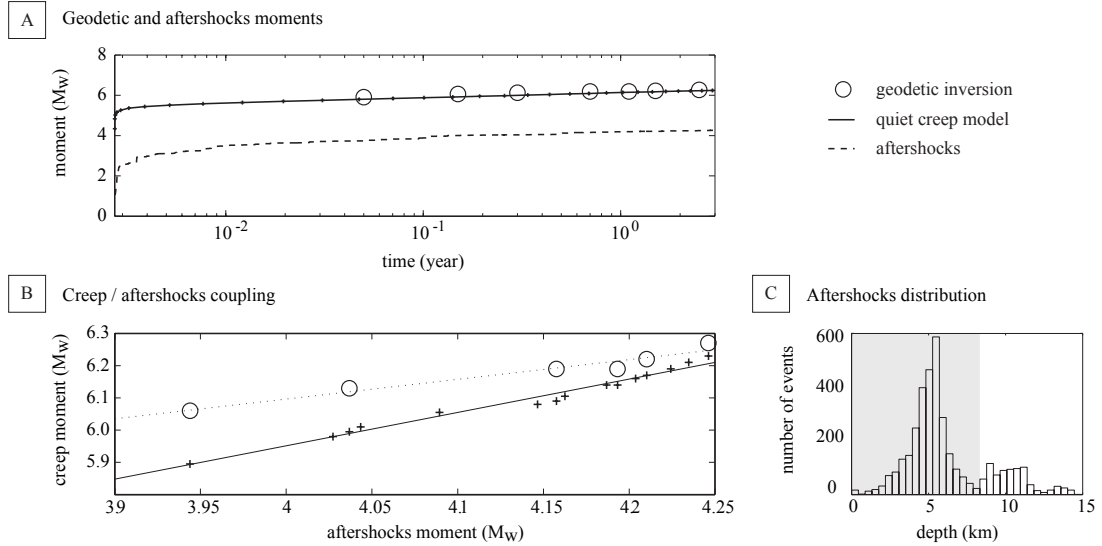


Figure 5.12: Aftershocks driven by aseismic creep. A) The equivalent seismic moment of our preferred RS creep model (solid line) compares well with the equivalent seismic moment inferred from kinematic inversions (circles). Aftershocks moment (dashed line) is two orders of magnitude lower and follows the creep evolution closely after 10^{-2} year (4 days). B) Linear correlation between the moment magnitudes of aftershocks and RS creep from two independent estimates of creep moment using geodetic inversion (circles) and forward modeling (crosses). The lines are a linear fit to the points. C) Depth distribution of aftershocks. Moments in A) and B) use the aftershocks that occurred in the top 9 km (shaded depths).

ral faults. Our inferred value of the steady rate-strengthening frictional parameter is of order of $(a - b) = 7 \times 10^{-3}$. Typical laboratory measurements at temperatures representative of the seismogenic zone suggest values of the friction rate parameter in the range from 0 to 0.006, depending on the cumulative shear displacement experienced by the samples [Marone, 1998, Scholz, 2002]. Morrow and Lockner [2001] found the velocity dependence of friction $(a - b) = 0.005 - 0.007$ for samples of the Hayward fault for a variety of rocks in effective pressure conditions simulating depths of burial up to 12 km. Experiments with clay minerals in pressure conditions relevant to the top 15 km revealed a rate-strengthening friction with parameter $a - b = 0.007$ [Morrow et al., 1992]. Experiments on thick gouge layers sheared between rough surfaces at high normal stress [Marone et al., 1990] predict higher friction rate parameters, and seem to be most consistent with our inferences of $(a - b)$ on a mature fault such as the San Andreas fault in the Parkfield area.

Johnson et al. [2006] modeled the afterslip evolution following the 2004 Parkfield event using a full rate-and-state dependent friction formulation. In their approach afterslip is controlled by the pre-earthquake stress level on the fault, the stress change due to the earthquake and frictional properties on the fault (a , b , critical slip distance D_c and V_0), some of which are

allowed to vary laterally and with depth. They invert for a range of parameters that reproduces the GPS 9 month time series. They find a rate-strengthening coefficient of $(a - b) = 10^{-4} - 10^{-3}$, an order magnitude lower than values inferred from laboratory experiments. In our study, we use longer (3 years) time series and constrain the fault frictional properties with 1) time series analysis and 2) a pure rate-strengthening model with lateral variations in frictional properties. Our kinematic inversions of afterslip show that much of postseismic slip occurs on a patch between seismic asperities so we model a fault with uniform frictional properties that we attribute to this slipping patch. Our best afterslip model explains 70% of the 3 year GPS signal and produces fit to the data that is comparable to that of [Johnson et al., 2006, see Fig. 11] over the first 9 months. A reasonably good performance of our simpler model compared to the approach of Johnson et al. [2006] can be explained by the fact that most of afterslip occurs in a limited area and samples the frictional properties of the fault at this location.

The aftershock sequence following the 2004 Parkfield earthquake has a cumulative moment much lower than the geodetic moment due to postseismic creep. The equivalent geodetic moment for afterslip, assuming a shear modulus of $G = 30$ GPa, exceeds $3.23 \cdot 10^{18}$ N (Mw 6.3) three years after the earthquake whereas aftershocks account for a moment of $5.96 \cdot 10^{16}$ N (Mw 5.15) in the same period. The higher moment of afterslip compared to cumulative moment of aftershocks disfavors the assumption that postseismic creep is driven by the occurrence of aftershocks [Savage and Yu, 2007]. The depth distribution of aftershocks is tri-modal, as shown in Fig. 5.12c (also, see Fig. 5.4.) Most earthquakes occur between 3 and 9 km depth, with cumulative magnitude of Mw 4.26. The rest of the moment release is due to three large aftershocks that occurred at greater depth (> 10 km.) The moment release due to shallow (depth < 10 km) aftershocks is found to be strongly correlated with aseismic slip. Fig. 5.12a shows the cumulative moment of aftershocks occurring above 9 km depth and the equivalent geodetic moment of creep estimated from our finite-source modeling and the geodetic inversions. The geodetic moment corresponding to our best forward model is represented with the black solid line, assuming a shear modulus of $G = 30$ GPa. The geodetic moment inferred from afterslip kinematic inversions is plotted as circles. Finally, cumulative aftershock moment is shown by the dashed line. We did not remove a seismic moment rate corresponding to background seismicity from the cumulative aftershock moment. The moment of seismic noise in interseismic times is immediately overshadowed by the occurrence of larger magnitude aftershocks. Correlation between creep and seismicity seems to start 4 days (10^{-2} a) after the main shock. However, precise evaluation of the kinetics of early creep in our model is limited by our assumption of a pure rate-strengthening friction. In a rate- and state-dependent friction model, the state variable accounts for the effect of fault contact aging on the effective friction. For the same stress initial condition, the initial velocity is reduced compared to a pure rate-strengthening model. As a result, the onset of excitation of aftershocks by creep could happen earlier than our model predicts. Fig. 5.12b illustrates the relationship between the cumulative aftershock moment and estimates of the equivalent geodetic

moment for the aseismic slip based on geodetic inversions and finite-source forward modeling. As creep accounts for a moment release that is two orders of magnitude greater than that due to aftershocks, data suggest that stressing from aseismic slip in velocity-strengthening areas governs the seismicity rates in neighboring velocity-weakening areas.

Similar inferences were made in previous studies of postseismic deformation in other locations, including the 1992 Landers, California [Perfettini and Avouac, 2007] and the 2005 Nias-Simeulue, Sumatra [Hsu et al., 2006] earthquakes. Savage and Yu [2007] also showed that the rate of aftershocks and surface velocities were linearly related during the first year of the postseismic transient. At Parkfield, aftershocks and afterslip occur principally at depth of about 5 km, in areas well resolved by the GPS network. The aftershocks hypocenters do not overlap with inferred areas of postseismic creep. An integrated view on seismic and aseismic transients following the Parkfield earthquake (Fig. 5.4) suggests the presence of along-strike variations in frictional properties of the fault in the middle of the seismogenic zone. Such variations are likely due to proximity of the Parkfield segment of the San Andreas fault to the creeping section, and might be rare in other locations, where the transition from velocity-weakening to velocity-strengthening behavior occurs primarily as a function of depth.

5.7 Conclusions

We investigated the co- and postseismic deformation due to the Mw 6.0 2004 Parkfield, CA earthquake. We used daily position time series from the SCIGN network to derive our coseismic slip model. Inferred strike-slip distribution exhibits two areas of high slip, consistent with results of previous investigations. We find a geodetic coseismic moment of Mw 6.16, somewhat higher than the seismic moment of Mw 6.0. We next inverted the horizontal components of the postseismic time series for evolution of afterslip. Most of the postseismic data can be explained by right-lateral afterslip on the fault plane that ruptured coseismically. After two years, the cumulative postseismic geodetic moment reaches an equivalent magnitude Mw 6.35, higher than our coseismic geodetic estimate of Mw 6.16. During the first year following the earthquake, afterslip is confined to the upper half of the seismogenic zone, occurring principally around 5 km depth, and between two areas of large coseismic slip. There is no resolvable overlap between coseismic slip and afterslip. The aftershock sequence took place in areas devoid of afterslip, with most of the earthquakes occurring in areas that ruptured coseismically. The seismicity in the top 10 km has a cumulative moment about two orders of magnitude smaller than the equivalent geodetic moment of afterslip. We conclude that the postseismic transient is dominated by aseismic slip driven by coseismic stress changes and we interpret the occurrence of afterslip and aftershocks in separate locations as being due to along-strike variations in effective frictional properties.

Modeling of GPS time series using solutions for shear cracks suggests that afterslip is more likely localized on discrete planes rather than distributed over finite-width plastic zones with

power-law rheology. A rate-strengthening friction law generalized for small velocities [Rice et al., 2001] can explain the surface displacements at all stages of the postseismic period. A distinction between candidate mechanisms has been possible due to availability of temporally dense GPS solutions. Power-law models were found to provide an inferior fit to GPS time series. To investigate the rate-strengthening creep hypothesis further, we developed a new semi-analytic method to evaluate the time-dependent deformation due to coseismic loading in an visco-elastoplastic half-space. The method uses integral transforms to compute the three-dimensional static deformation. The time integration for a given constitutive law is performed using a second-order accurate Runge-Kutta method with adaptive time steps. We modeled the postseismic transient using the generalized rate-strengthening friction law and our coseismic slip model as initial condition. The best-fitting model can explain 72% of all GPS data, except at station CARH in the very near field, which suffered a velocity reversal due to migration of the creep interface. Finite-source modeling of the creep evolution puts a lower bound on the rate-strengthening frictional parameter, $a\sigma > 0.5 \text{ MPa}$, in agreement with inferences from the simple crack approximation. The same rate-strengthening forward model can explain both the time dependence of GPS data and the spatio-temporal evolution of creep on the fault plane inferred from kinematic inversions.

Assuming an effective normal stress of $\sigma = 100 \text{ MPa}$, appropriate for 5 km depth, we infer a steady-state rate-strengthening friction parameter of $(a - b) = 7 \times 10^{-3}$, which is on a high end of values measured in laboratory experiments [Scholz, 1990, 1998, Marone, 1998]. Our result suggests that laboratory data corresponding to high normal stresses and thick gauge layers are most consistent with our *in situ* inferences of frictional properties of mature faults such as the San Andreas fault near Parkfield. Our modeling results indicate that areas that ruptured during the 2004 Parkfield event continued to experience seismicity in the postseismic period. The occurrence of unstable sliding (stick-slip behavior), suggests that the respective areas are characterized by a negative frictional parameter $(a - b)$. The strong correlation between creep and aftershock moments, as well as the spatial anti-correlation between creep and seismicity suggest that creep is governing the rate and magnitude of aftershocks in the top 10 km of the seismogenic zone. This scenario of reloading of the velocity weakening surfaces by afterslip on nearby velocity-strengthening patches is suggestive of strong lateral variations in frictional properties along the Parkfield segment of the San Andreas fault. Velocity-strengthening areas represent an obstacle to the propagation of the main rupture and are responsible for the aseismic relaxation of coseismic stress by creep, thereafter governing the rate of seismicity in velocity-weakening areas. These results emphasize the effect of aseismic deformation on the rate of aftershocks and the spatio-temporal distribution of slip throughout the seismic cycle.

Acknowledgments

We thank Associate Editor John Townend, as well as Allan Rubin and an anonymous reviewer for their thorough and thoughtful reviews of this manuscript. Our work benefited from discussions with Olivier Castelnau, Eric Dunham and Nadia Lapusta. This work was supported by NSF through grant EAR-0450035. The SCEC contribution number for this paper is 1270. Numerical codes used in this study are available from the authors. Chapter 5, in full, is a reprint of the material as it appears in the Journal of Geophysical Research 2009. Barbot, Sylvain; Fialko, Y.; Bock, Y., 2009. The dissertation author was the primary investigator and author of this paper.

5.8 Impulse Response of a Point Source

A finite area of localized shear with linear dimension L embedded in a elastic medium Ω with shear modulus G can be idealized with a time-space separable spring-slider model with the effective spring constant per unit area

$$G^* = \frac{CG}{L} \quad (5.25)$$

where scalar C is a constant close to 1 that depends on the geometry [Eshelby, 1957, Kanamori and Anderson, 1975, Shearer, 1999, Fialko, 2007]. We treat this idealization as "point source" because it ignores details of displacements within the slipped area and provides an accurate approximation in the far field. The point-source approximation also assumes that stress resolved on the slip area is uniform.

The inelastic response of a medium to coseismic stress change is, in general, the solution for a constant total strain $\dot{\epsilon} = 0$ subjected to some initial conditions or, using eqs. (5.61) and (5.62), in terms of stress

$$\mathbf{D}:\dot{\boldsymbol{\sigma}} + \mathbf{F}:\boldsymbol{\sigma} = 0 \quad (5.26)$$

where \mathbf{D} and \mathbf{F} are the elastic compliance and fluidity tensors, respectively and $\boldsymbol{\sigma}$ is the Cauchy stress. Projecting eq. (5.26) in the -constant- strain direction \mathbf{R} and using the point-source approximation, we develop the associated governing ordinary differential equations for localized shear bands with power-law creep and afterslip with rate-strengthening friction.

5.8.1 Power-Law Shear Bands

In a simple shear zone model $s(t)$ is the displacement across the finite shear band which relaxes the stress $\tau = G^*s$. A schematic of the geometry is shown in Fig. 5.13. The rheology of fault creep is described by eq. (5.6) where the plastic strain rate can be approximated by $\dot{\gamma} = \dot{s}/T$, where T is the thickness of the shear zone (see Fig. 5.13). In the case of linear creep

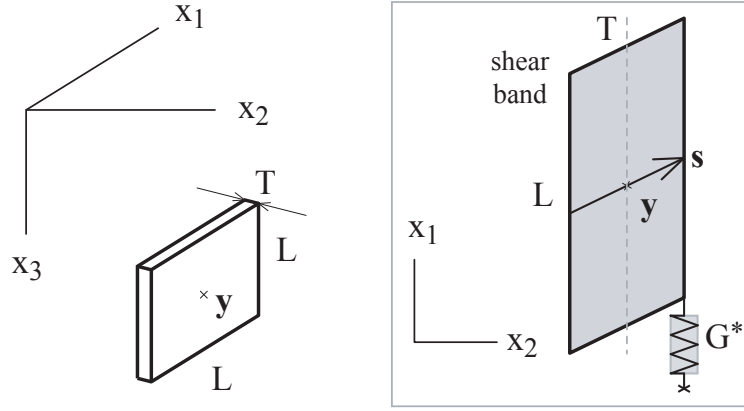


Figure 5.13: Schematic of the point-source approximation for a localized shear band of thickness T and linear dimension L . The cumulated displacement s across the ductile zone relaxes the stress $\tau = G^* s$.

of eq. (5.6) with $n = 1$, the evolution of shear stress across the ductile zone is governed by the differential equation

$$\dot{\tau} + \alpha A \tau = 0 \quad (5.27)$$

where $\alpha = CT/L$ is the aspect ratio of the ductile zone. The solution is given by

$$\tau(t) = \tau_0 e^{-t/t_0} \quad (5.28)$$

where τ_0 is the initial (coseismic) loading and the time scale

$$t_0 = \frac{1}{\alpha A} \quad (5.29)$$

is independent of the initial stress condition and controlled by the aspect ratio of the ductile zone and the effective rheology of rocks within the shear zone. As stress is relaxed, cumulative displacement across the ductile volume is

$$s(t) = \frac{\tau_0}{G^*} (1 - e^{-\alpha A t}) . \quad (5.30)$$

Displacement in the elastic medium exhibits similar time dependence, but amplitudes decay away from the shear zone. Similarly, for nonlinear creep, the governing equation for stress on the fault plane is

$$\frac{\dot{\tau}}{G} + \alpha A \left(\frac{\tau}{G} \right)^n = 0 \quad (5.31)$$

and the decay of shear stress is

$$\tau(t) = \tau_0 \left[1 + \alpha A (n-1) \left(\frac{\tau_0}{G} \right)^{n-1} t \right]^{\frac{-1}{n-1}} \quad (5.32)$$

where the timescale of deformation t_0 scales with the reference strain rate A , the aspect ratio α and the initial stress τ_0

$$t_0 = \frac{1}{\alpha A (n-1)} \left(\frac{G}{\tau_0} \right)^{n-1} \quad (5.33)$$

Integrating eqs. (5.6) and (5.32), we obtain the displacement evolution across the ductile zone

$$s(t) = \frac{\tau_0}{G^*} \left(1 - \left[1 + \frac{t}{t_0} \right]^{\frac{-1}{n-1}} \right) \quad (5.34)$$

or, in terms of strain,

$$\gamma(t) = \frac{\tau_0}{\alpha G} \left(1 - \left[1 + \frac{t}{t_0} \right]^{\frac{-1}{n-1}} \right) \quad (5.35)$$

5.8.2 Rate-and-State Creep

For the generalized rate-strengthening friction, with a constitutive relationship represented by eq. (5.11), the scalar ordinary differential equation for stress is

$$\frac{\dot{\tau}}{G^*} + 2 \dot{s}_0 \sinh\left(\frac{\tau}{a\sigma}\right) = 0 \quad (5.36)$$

where a and \dot{s}_0 are the frictional parameters and scalar σ is the fault normal stress (compression is assumed positive). The degree of nonlinearity in the transient sliding depends upon the dimensionless ratio

$$k = \frac{\tau_0}{a\sigma} \quad (5.37)$$

and the resulting stress evolution on the slip patch is

$$\tau(t) = \tau_0 \frac{2}{k} \coth^{-1} \left(e^{2\dot{s}_0 \frac{G^*}{a\sigma} t} \coth \frac{k}{2} \right) \quad (5.38)$$

Introducing the timescale

$$t_0 = \frac{a\sigma}{2\dot{s}_0 G^*} \quad (5.39)$$

we obtain the slip evolution

$$s(t) = \frac{\tau_0}{G^*} \left(1 - \frac{2}{k} \coth^{-1} \left(e^{t/t_0} \coth \frac{k}{2} \right) \right) \quad (5.40)$$

The generalized friction model is highly nonlinear for $k \gg 1$, but is quasi-linear for $k \leq 1$. We note that the timescale t_0 depends upon the size of the slipping patch.

Time series of postseismic deformation can be compared to predictions of eqs. (5.30), (5.35) or (5.40). Inferred timescale t_0 and degree of nonlinearity (n or k in case of power law and generalized rate-strengthening friction, respectively) can be used to constrain initial effective stress and frictional parameters.

5.9 Numerical Model of Time-Dependent Creep on Finite Faults in an Elastic Half-Space

We present a novel approach to evaluate the three-dimensional time-dependent deformation due to a localized creep in an otherwise elastic half-space. The method is based on a

continuum representation of fault slip. In particular, our treatment extends the usual double-couple representation of static faults and derive an expression for the equivalent body force rate that reproduces the required slip velocity on the fault. In a first subsection, we introduce a formulation for slip systems that describes static slip and creeping dislocations. In a second subsection, we derive a continuum formulation of the constitutive and governing equations that describe afterslip of a fault plane and associated elastic deformation in a half space. In a final subsection, we present details of our numerical implementation.

5.9.1 Continuum Representation of Dislocations

Faults can be viewed as dislocations that introduce an irreversible displacement discontinuity in an otherwise elastic domain. These dislocations cannot simply be treated using Dirichlet boundary conditions on each side of the interface because only the relative displacement between the two sides are formally known, as opposed to the absolute position of the particles that lie across the contact. Boundary conditions might be sensibly prescribed in terms of strain (Neumann-type boundary conditions), but a difficulty arises because of the discontinuous nature of the interface.

Consider semi-infinite solid Ω with a traction-free surface $\partial\Omega$. We use a Cartesian coordinate system where position in a half space is denoted by $\mathbf{x} = (x_1, x_2, x_3)$ with x_3 positive downward and $x_3 = 0$ at the surface $\partial\Omega$. We adopt the infinitesimal strain approximation of linear elasticity. A fault \mathcal{S} is defined by a surface

$$n(\mathbf{x}) = 0 . \quad (5.41)$$

The normal unit vector on \mathcal{S} is the unit vector

$$\hat{\mathbf{n}} = \frac{\partial n}{\partial \mathbf{x}} \quad (5.42)$$

Hereafter, we denote \mathcal{S}^+ one side on the fault and \mathcal{S}^- the other, such as $n = 0^+$ on \mathcal{S}^+ and $n = 0^-$ on \mathcal{S}^- . After some slip occurred on the fault surface, the previously adjacent points across \mathcal{S} are separated by \mathbf{s} , which is the Burgers' vector associated with the dislocation. We define the plastic displacement $\mathbf{u}^i(n)$, where superscript i stands for irreversible or inelastic, due to slip on the fault as follows

$$\mathbf{u}^i(0^+) - \mathbf{u}^i(0^-) = \mathbf{s} \quad (5.43)$$

A schematic of the geometry is shown in Fig. 5.14. The gradient of the inelastic deformation is the tensor

$$\nabla \mathbf{u}^i = \frac{\partial \mathbf{u}^i}{\partial \mathbf{x}} = \hat{\mathbf{n}} \otimes \frac{\partial \mathbf{u}^i}{\partial n} \quad (5.44)$$

Defining the gradient

$$\frac{\partial \mathbf{u}^i}{\partial n} = \delta(n) \mathbf{s} , \quad (5.45)$$

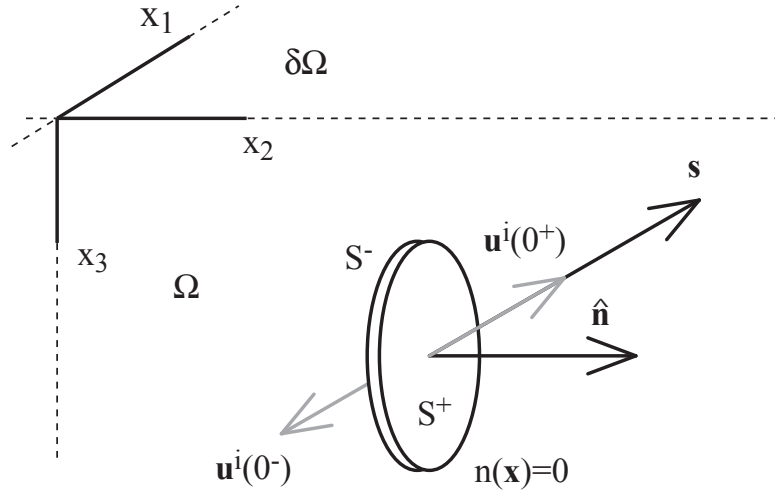


Figure 5.14: A buried circular slip patch embedded in semi-infinite solid Ω with free surface $\partial\Omega$ at $x_3 = 0$. Slipping surface is defined by $n(\mathbf{x}) = 0$. Burgers' vector of dislocation is $\mathbf{s} = \mathbf{u}^i(0^+) - \mathbf{u}^i(0^-)$.

where $\delta(x)$ is the Dirac delta function, and integrating, we find a continuum description of plastic deformation that satisfies condition of eq. (5.43). Decomposing the gradient into the canonical symmetric and skew-symmetric parts, respectively

$$\nabla \mathbf{u}^i = \boldsymbol{\epsilon}^i + \boldsymbol{\Omega}^i \quad (5.46)$$

we obtain the eigenstrain associated with the dislocation

$$\boldsymbol{\epsilon}^i(\mathbf{x}) = \frac{1}{2} (\hat{\mathbf{n}} \otimes \mathbf{s} + \mathbf{s} \otimes \hat{\mathbf{n}}) \delta(n(\mathbf{x})) \quad (5.47)$$

The delta function of eq. (5.47) is a continuous representation of the fault discontinuity at $n = 0$ and also prescribes the location of the dislocation in the medium. Notice that no intrinsic fault thickness is associated with eigenstrain. In particular, eigenstrain is not defined as the ratio of some cumulative displacement over some small, yet finite, distance. The use of generalized functions to describe seismic sources has been discussed by Backus and Mulcahy [1976b].

Before completing the continuum representation of a dislocation, we consider a purely static deformation. We decompose the total strain $\boldsymbol{\epsilon}$ in the semi-infinite solid into elastic and inelastic parts, respectively

$$\boldsymbol{\epsilon} = \boldsymbol{\epsilon}^e + \boldsymbol{\epsilon}^i \quad (5.48)$$

where the inelastic strain, only occurring on the dislocation, is formally valid everywhere in the solid due to the use of the Dirac delta function (eq. (5.47)). (In most of the domain Ω , we have $\boldsymbol{\epsilon} = \boldsymbol{\epsilon}^e$.) Using decomposition of eq. (5.48) the Cauchy stress becomes

$$\boldsymbol{\sigma} = \mathbf{C} : \boldsymbol{\epsilon}^e = \mathbf{C} : \boldsymbol{\epsilon} - \mathbf{C} : \boldsymbol{\epsilon}^i \quad (5.49)$$

where \mathbf{C} is the fourth-order elastic moduli tensor in Ω and operator $:$ is the double scalar product. The distinction between elastic and plastic strains in the stress-strain relationship of eq. (5.49) makes apparent the moment density of the dislocations

$$\mathbf{m}(\mathbf{x}) = \mathbf{C} : \boldsymbol{\epsilon}^i(\mathbf{x}) \quad (5.50)$$

Whereas the moment density of dislocations can be obtained by other means [e.g., Aki and Richards, 1980, Shearer, 1999], our formulation is advantageous because it includes the location, size and magnitude of the dislocations. Furthermore, using the Cauchy stress definition of eq. (5.49) and conservation of momentum $\nabla \cdot \boldsymbol{\sigma} = 0$, we find the inhomogeneous Navier's equation

$$\nabla \cdot (\mathbf{C} : \boldsymbol{\epsilon}) + \mathbf{f} = 0 \quad (5.51)$$

where $\boldsymbol{\epsilon}$ is unknown and the body-force density term is

$$\mathbf{f}(\mathbf{x}) = -\nabla \cdot (\mathbf{C} : \boldsymbol{\epsilon}^i(\mathbf{x})) \quad (5.52)$$

As in the case of the moment density, the equivalent body forces for dislocations can be obtained using different approaches [e.g., Eshelby, 1957, Burridge and Knopoff, 1964]. Note that expression (5.52) contains information about the double couple representation of dislocations as well as their location and size in the half space. For example, the elastic potential energy of the dislocation is simply

$$E = \int_{\Omega} \boldsymbol{\sigma} : \boldsymbol{\epsilon}^i(\mathbf{x}) dV = \int_S \boldsymbol{\sigma} : \mathbf{s} \otimes \hat{\mathbf{n}} dA \quad (5.53)$$

which comes from the continuum representation of eigenstrain of eq. (5.47), the symmetry of the stress tensor and the definition of the Dirac delta function. The solution displacement in Ω due to static slip described by eq. (5.47) and (5.52) is

$$\begin{aligned} \mathbf{u}(\mathbf{x}) &= \int_{\Omega} \mathbf{G}(\mathbf{x}, \mathbf{x}_0) \cdot \mathbf{f}(\mathbf{x}_0) dV \\ &= \int_S \nabla \mathbf{G} : \mathbf{C} : \mathbf{s} \otimes \hat{\mathbf{n}} dA \end{aligned} \quad (5.54)$$

where \mathbf{G} is the elastic Green function tensor, and last term is obtained by integration by part and using the definition of the Dirac delta function.

The continuum representation of static dislocations in terms of eigenstrain accurately captures the discontinuous nature of displacement fields due to fault slip. The eigenstrain is a forcing term in the strain domain which should not be confused with the elastic strain in the near field of the dislocation. Using the tensor inner product $\langle \mathbf{A}, \mathbf{B} \rangle = \sqrt{2} \mathbf{A} : \mathbf{B}$ and assuming purely tangential fault slip (no opening or interpenetration), one can write [e.g., Nemat-Nasser, 2004]

$$\boldsymbol{\epsilon}^i(\mathbf{x}) = \gamma(\mathbf{x}) \mathbf{R} \quad (5.55)$$

where \mathbf{R} is a unitary, symmetric and deviatoric, second-order tensor and γ , the norm of $\boldsymbol{\epsilon}^i(\mathbf{x})$, is the total slip across the dislocation. In particular, noting $\mathbf{s} = s \hat{\mathbf{s}}$, one has

$$\gamma(\mathbf{x}) = s \delta(n(\mathbf{x})) \quad (5.56)$$

The eigenstrain describes the slip on a fault patch. This definition can be readily extended to represent slip velocities across the dislocation. To do so, we define the eigenstrain rate

$$\dot{\boldsymbol{\epsilon}}^i(\mathbf{x}) = \dot{\gamma}(\mathbf{x}) \mathbf{R} \quad (5.57)$$

As shown for the case of static dislocations, the plastic deformation rate $\dot{\gamma} = \dot{s}$ nominally applies to the fault interface only, but is formally valid in the entire domain Ω by use of the Dirac delta function. We use this continuum representation to formulate the constitutive equations in the solid and at the contact interface in a uniform, consistent manner. Various degrees of strain localization on a fault can be readily modeled using Dirac's delta, boxcar, Gaussian, etc. functions.

5.9.2 Body Force Representation of Fault Creep

In a general case, a static dislocation with slip vector \mathbf{s} along a surface of normal $\hat{\mathbf{n}}(\mathbf{x})$ is associated with the eigenstrain

$$\boldsymbol{\epsilon}^i = \frac{1}{2} (\mathbf{s} \otimes \hat{\mathbf{n}} + \hat{\mathbf{n}} \otimes \mathbf{s}) \quad (5.58)$$

and, in a linear elastic medium Ω with elastic tensor \mathbf{C} , with the moment density $\mathbf{m} = \mathbf{C} : \boldsymbol{\epsilon}^i$. The equivalent body force (formally a body-force density) for such a dislocation is [e.g., Eshelby, 1957, Burridge and Knopoff, 1964, Nemat-Nasser, 2004]

$$\mathbf{f}(\mathbf{x}) = -\nabla \cdot (\mathbf{C} : \mathbf{s} \otimes \hat{\mathbf{n}}) \quad (5.59)$$

and the resulting displacement \mathbf{u} in the elastic half-space is obtained with application of the elastic Green function [Love, 1927, Nemat-Nasser and Hori, 1999]

$$\mathbf{u}(\mathbf{x}) = \int_{\Omega} \mathbf{G}(\mathbf{x}, \mathbf{x}_0) \cdot \mathbf{f}(\mathbf{x}_0) d\mathbf{x}_0 \quad (5.60)$$

In an visco-elastoplastic material, with elastic compliance tensor \mathbf{D} and fluidity tensor $\mathbf{F}(\mathbf{x})$, the elastic strain-rate tensor is

$$\dot{\boldsymbol{\epsilon}}^e = \mathbf{D} : \dot{\boldsymbol{\sigma}} \quad (5.61)$$

and the irreversible plastic strain rate occurring on the fault is

$$\dot{\boldsymbol{\epsilon}}^i = \mathbf{F} : \boldsymbol{\sigma} \quad (5.62)$$

where $\boldsymbol{\sigma} = \mathbf{C} : \boldsymbol{\epsilon}^e$ is the Cauchy stress [Malvern, 1969], and the amplitude of \mathbf{F} is stress and space dependent. Note that the fluidity tensor \mathbf{F} has a non-vanishing value only on the fault surface,

even though it can be defined everywhere in Ω by use of generalized functions. The total strain rate is the sum of elastic and inelastic contributions

$$\dot{\boldsymbol{\epsilon}} = \dot{\boldsymbol{\epsilon}}^e + \dot{\boldsymbol{\epsilon}}^i \quad (5.63)$$

Assuming infinitesimal strain, combining eq. (5.61), (5.62) and (5.63) and integrating, we obtain

$$\boldsymbol{\sigma}(t) = \mathbf{C}:\boldsymbol{\epsilon}(t) - \int_0^t \mathbf{C}:\dot{\boldsymbol{\epsilon}}^i(s) ds \quad (5.64)$$

where the integrand

$$\dot{\mathbf{m}}(\mathbf{x}, t) = \mathbf{C}:\dot{\boldsymbol{\epsilon}}^i(\mathbf{x}, t) \quad (5.65)$$

is the internal torque density applied in the solid to gradually relax stress. The total strain $\boldsymbol{\epsilon}$ can simply be evaluated from the state of current deformation

$$\boldsymbol{\epsilon}(t) = \frac{1}{2} [\nabla \otimes \mathbf{u} + (\nabla \otimes \mathbf{u})^T] \quad (5.66)$$

We derive the solution velocities from the integration of forcing terms

$$\dot{\mathbf{f}}(\mathbf{x}) = -\nabla \cdot (\mathbf{C}:\dot{\boldsymbol{\epsilon}}^i) \quad (5.67)$$

using the elastic Green function

$$\dot{\mathbf{u}}(\mathbf{x}) = \int_{\Omega} \mathbf{G}(\mathbf{x}, \mathbf{x}_0) \cdot \dot{\mathbf{f}}(\mathbf{x}_0) d\mathbf{x}_0 \quad (5.68)$$

We compute the time-dependent deformation by integrating simultaneously eq. (5.64) and eq. (5.68).

The inelastic strain-rate tensor $\dot{\boldsymbol{\epsilon}}^i$ is usually decomposed into a direction \mathbf{R} and a scalar strain rate $\dot{\gamma}$ [Nemat-Nasser, 2004]

$$\dot{\boldsymbol{\epsilon}}^i = \mathbf{F}:\boldsymbol{\sigma} = \dot{\gamma} \mathbf{R} \quad (5.69)$$

While the decomposition (5.69) is general, in the case of the extreme localization of a discontinuous fault interface the eigenstrain rate $\dot{\gamma}$ corresponds to the slip rate on the fault \dot{s} . The strain direction \mathbf{R} for strike-slip and dip-slip faults is a deviatoric, symmetric and unitary second-order tensor that describes the geometry of the slip system. The traction $\mathbf{t}(\mathbf{x})$ resolved on a fault surface can be decomposed into normal and shear components,

$$\mathbf{t} = \boldsymbol{\sigma} \cdot \hat{\mathbf{n}} = (\mathbf{t} \cdot \hat{\mathbf{n}}) \hat{\mathbf{n}} + \boldsymbol{\tau} \quad (5.70)$$

Noting $\mathbf{s} = s \hat{\mathbf{s}}$, we assume that the slip-rate vector is collinear with the direction of shear traction evaluated on the fault patch,

$$\dot{\mathbf{s}} = \dot{s} \hat{\boldsymbol{\tau}} \quad (5.71)$$

Extending the static case of eq. (5.58) to time-dependent slip, the plastic strain-rate direction becomes

$$\mathbf{R} = \frac{1}{2} (\hat{\boldsymbol{\tau}} \otimes \hat{\mathbf{n}} + \hat{\mathbf{n}} \otimes \hat{\boldsymbol{\tau}}) \quad (5.72)$$

and the corresponding equivalent body-force rate, from eqs. (5.67), (5.69) and (7.28), simplifies to

$$\dot{\mathbf{f}}(\mathbf{x}) = -\nabla \cdot (\dot{\gamma} \mathbf{C} : \mathbf{R}) \quad (5.73)$$

A dislocation slips only when a yield condition $g(\boldsymbol{\sigma}) = 0$ is satisfied, such that

$$\dot{\gamma} = \begin{cases} 0, & \text{if } g(\boldsymbol{\sigma}) < 0 \\ f(\boldsymbol{\sigma}, \gamma, t), & \text{if } g(\boldsymbol{\sigma}) = 0 \end{cases} \quad (5.74)$$

where in general the formulation $\dot{\gamma} = f(\boldsymbol{\sigma}, \gamma, t)$ allows for a direct effect, some work hardening and a possible healing. We use the Coulomb yield surface given by eq. (5.2). Coseismic static displacements $\mathbf{u}(\mathbf{x}, t=0)$ and stress change $\boldsymbol{\sigma}(\mathbf{x}, t=0)$ define a set of initial conditions that govern the subsequent inelastic deformation. Constitutive relationships for plastic flow or generalized rate-strengthening friction, eqs. (5.6) and (5.11) respectively, complete the description of our model.

5.9.3 Numerical Implementation

We extend the approach of Barbot et al. [2008a] to three-dimensional deformation, and use integral transforms to evaluate the elastic response of a half space, i.e. to solve eq. (5.60) and (5.68) numerically. We perform the convolution between the equivalent body forces and the elastic Green function in the Fourier domain, taking advantage of the convolution theorem and the fast Fourier transform. The method is computationally efficient: the evaluation of the instantaneous velocity field in a 512^3 node grid with uniform sampling is obtained in a few seconds on a parallel computer with shared-memory architecture. One possible drawback of Fourier methods is the periodicity of the numerical solution. We mitigate undesirable effects of periodic boundary conditions using sufficiently large computational grids. We taper the fault segments to reduce aliasing and temper stress singularities [Barbot et al., 2008a]. Our approach allows one to compute deformation due to the presence of buried faults of arbitrary orientation.

We benchmarked our numerical code against the analytic solution of Okada [1992] for strike-slip and dip-slip faults. Fig. 5.15 shows the relative error between analytic and numerical solutions at the location of the GPS stations at Parkfield, for our inferred coseismic model. Numerical error is usually smaller than 5%, and exceeds 10% in the far field where absolute displacements are vanishingly small and at the precise location of the fault where the displacement discontinuity is represented by a continuous field. We also compared our solution to another numerical approach. Fig. 5.15 shows the relative error introduced by the numerical Green function of Wang et al. [2003] for a spatial sampling of $\Delta = 0.5$ km and $\Delta = 0.2$ km. As one can see from Fig. 5.15, our model, with a uniform sampling of $\Delta = 0.25$ km performs well compared to the method of Wang et al. [2003].

We evaluate the integrals in eq. (5.68) and (5.64) using a second-order accurate Runge-Kutta scheme with adaptive time steps [Abramowitz and Stegun, 1972]. From the instantaneous

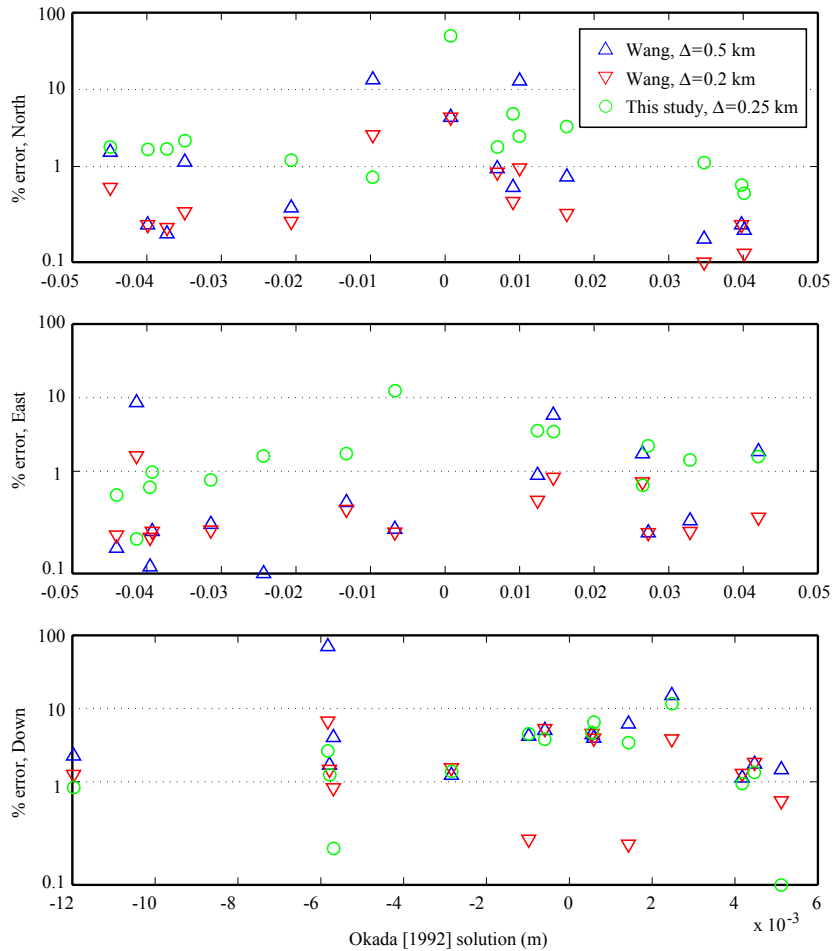


Figure 5.15: Relative error of numerical models compared to the analytic solution of *Okada* [1992] for the Parkfield coseismic slip model. The displacement vector at the location of the 14 GPS stations is estimated numerically with the method of *Wang et al.* [2002] (triangles) and with the one developed in this study (circles). The percentage error is plotted as a function of the expected analytical solution for the 3 components of displacement. The red triangles correspond to a denser sampling of the *Wang et al.* [2002] Green function, which reduces the numerical error.

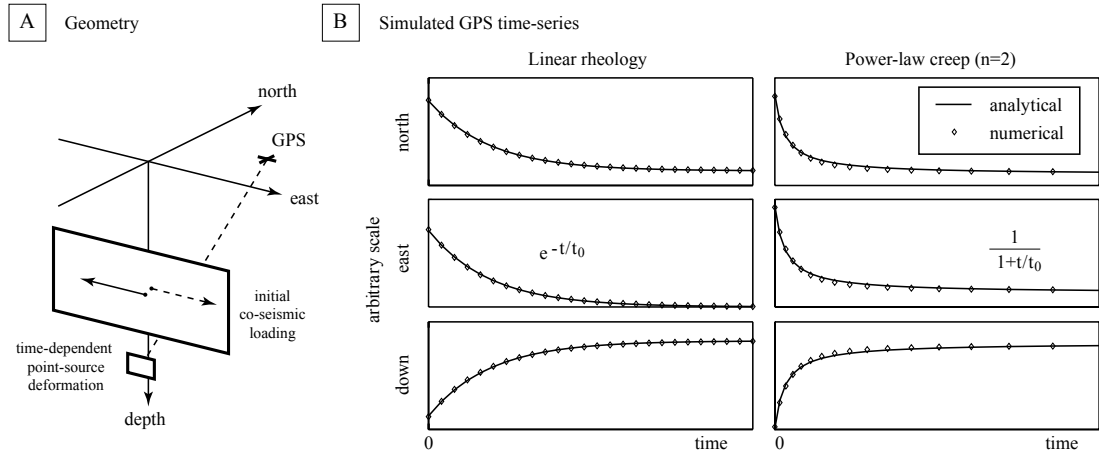


Figure 5.16: The time-dependent deformation due to frictional sliding on a surface of unit size. A) The stress on a fault is perturbed due to static slip on an upper segment leading to afterslip. B) The vector-valued displacement at a surface point driven by the deep afterslip is evaluated numerically using a second-order accurate Runge-Kutta method with adaptive time steps. The forward models compare well with the expected impulse response of linear ($\dot{s} = \Delta\tau/\eta$) and nonlinear ($\dot{s} = A (\Delta\tau/G)^n$, here $n = 2$) constitutive laws. The timescale of the synthetic signal is recovered within a 5% error. The adaptive time step is apparent only for the case of a nonlinear evolution law.

effective linear viscosity,

$$\eta(t) = \frac{\tau}{\dot{\gamma}} \quad (5.75)$$

we determine the characteristic relaxation timescale

$$t_m = \frac{\eta}{G} \quad (5.76)$$

where G is the shear modulus. We use a fraction of t_m , also referred to as the Maxwell relaxation time, for time increments. Finally, we estimate the spatial gradients in eq. (7.6) using a finite impulse response differentiator filter [McClellan et al., 1973]. Filters are much better estimates of localized deformation than simple finite difference schemes because the latter smooth the derivative estimates near discontinuities such as slip on a fault.

Fig. 5.16 shows a benchmark of our approach for a simple geometry. We place a small slip patch in a coseismic stress field with a choice of parameters constrained to satisfy $t_0 = 1$ a in eqs. (5.29) and (5.33). We compare the time series of surface displacement at an arbitrary location at the surface of the half-space to the impulse response of linear and nonlinear rheologies (Fig. 5.16b). Our adaptive time steps are apparent for the nonlinear power-law creep, with shorter time increments at early time of deformation and longer ones at later times, when most stress has already been relaxed. The numerical solution is very well fit by the expected impulse response of linear or nonlinear rheologies and the theoretical timescale of deformation is recovered within

a 5% error. We conclude that our modeling approach and its numerical implementation are sufficiently robust for modeling stress-driven afterslip with linear as well as nonlinear rheologies.

5.10 Interseismic Slip Rates for a Slip Patch

The response of a rate-strengthening (RS) friction patch to a constant interseismic strain rate obeys

$$\dot{\epsilon}^e + \dot{\epsilon}^i = \dot{\Gamma} \mathbf{R} \quad (5.77)$$

where $\dot{\epsilon}^e$ and $\dot{\epsilon}^i$ are the elastic and inelastic strain rates, respectively, and $\dot{\Gamma}$ and \mathbf{R} are the amplitude and direction, respectively, of the interseismic strain rate evaluated on the fault patch. After the initial period of transient deformation, the steady-state response is inelastic only ($\dot{\epsilon}^e = 0$) and the rate of strain release due to the RS friction patch equals to the strain rate imposed by interseismic loading

$$\dot{\gamma} = \dot{\Gamma} \quad (5.78)$$

The strain rate of the slipping patch, $\dot{\gamma}$, is given by

$$\dot{\gamma} = \frac{\dot{s}}{CL} \quad (5.79)$$

where C is a dimensionless parameter depending upon the geometry of the patch and L is the linear dimension of the patch. The RS friction parameter \dot{s}_0 is equivalent to parameter V_0 of classic rate-and-state friction for large velocity, but does not represent the “interseismic” velocity. Friction parameter \dot{s}_0 controls the timescale of deformation transients and the effective “viscosity” of the shear zone (see eq. (5.75) and (5.76).)

In case of strike-slip faults, interseismic deformation may be idealized by slip below the seismogenic zone at rates corresponding to the long-term (averaged over multiple earthquake cycles) plate motion [Savage, 1990]. The velocity field for a long vertical strike-slip fault locked from the surface to the depth H is

$$\dot{u}_1 = \frac{v}{2\pi} \left[\tan^{-1} \frac{x_2}{H - x_3} + \tan^{-1} \frac{x_2}{H + x_3} \right] \quad (5.80)$$

where $\dot{u}_1(x_2, x_3)$ is the along-strike velocity, x_2 is the across-fault distance, x_3 is depth and v is the long-term slip rate. Consider a creeping patch in the locked zone at depth $x_3 < H$. The strain rate imposed on the creeping patch by interseismic loading is

$$\dot{\Gamma} = \frac{v}{2\pi} \frac{H}{H^2 - x_3^2} \cdot \quad (5.81)$$

Assuming a circular patch of radius L , the creep rate is [Eshelby, 1957]

$$\dot{s} = \dot{\Gamma} \frac{16}{7\pi} L \quad (5.82)$$

In the case of a fault slipping at the rate of 33 mm/yr with a locking depth of 15 km and a creeping circular patch of radius $L = 2$ km buried at a depth of 5 km, the average creep velocity is $\dot{u}_1 = 1.1$ mm/yr.

Chapter 6

Fourier-Domain Green Function for an Elastic Semi-Infinite Solid with Gravity with Applications to Earthquake and Volcano Deformation

Sylvain Barbot and Yuri Fialko

Abstract. We present an analytic solution in the Fourier domain for an elastic deformation in a semi-infinite solid due to an arbitrary surface traction. We generalize the so-called Boussinesq's and Cerruti's problems to include a restoring buoyancy boundary condition at the surface. Buoyancy due to a large density contrast at the Earth's surface is an approximation to the full effect of gravity that neglects the perturbation of the gravitational potential. Using the perturbation method, and assuming that the effect of gravity is small compared to the elastic deformation, we derive an approximation to the space-domain Boussinesq's problem that accounts for a buoyancy boundary condition at the surface. The Fourier- and space-domain solutions are shown to be in good agreement. Numerous problems of elasto-static or quasi-static time-dependent deformation relevant to faulting in the Earth's lithosphere (including inelastic deformation) can be modeled using equivalent body forces and surface traction. Solving the governing equations with the elastic Green function in the space domain can be impractical as the body force can be distributed over a large volume. We present a computationally efficient method to evaluate the elastic deformation in a three-dimensional half space due to the presence of an arbitrary distribution of internal forces and traction at the half-space surface. We first evaluate the elastic deformation in a periodic Cartesian volume in the Fourier domain, then use the analytic solutions to the generalized Boussinesq's and Cerruti's problems to satisfy the prescribed mixed boundary condition at the surface of the half space. We show some applications for magmatic intrusions and faulting. This approach can be used to solve elasto-static problems involving spatially heterogeneous elastic properties (by employing a homogenization method) and time-dependent problems such as nonlinear viscoelastic relaxation, poroelastic rebound, and non-steady fault creep under the assumption of spatially homogeneous elastic properties.

6.1 Introduction

An instantaneous deformation field accompanying an earthquake can be well explained assuming linear elastic deformation of the ambient rocks [Reid, 1910, Fialko et al., 2001b, Simons et al., 2002, Fialko, 2004a]. Postseismic and interseismic phases of the earthquake cycle are also commonly modeled using solutions for an elastic half space [Savage, 1974, McGuire and Segall, 2003, Miyazaki et al., 2003, Hsu et al., 2006, Fialko, 2006, Barbot et al., 2009a]. Elastic solutions are also widely used to model volcanic unrest [e.g., Mogi, 1958, Yang et al., 1988, Fialko et al., 2001a]. Some types of time-dependent inelastic deformation can also be simulated using an elastostatic Green function by virtue of the Laplace transform whereby the time series of deformation are obtained from a series of static deformation fields evaluated given the effective elastic moduli [Rundle, 1982, Pollitz, 1997, Wang et al., 2003, 2006, Smith and Sandwell, 2004]. Recent geodetic observations suggest that the time-dependent response of the crust to stress change is in fact non linear [Freed and Bürgmann, 2004]. If so, models used to interpret observations of postseismic deformation need to account for nonlinear rheologies of the lower crust or upper mantle. Barbot and Fialko [submitted, 2009a] proposed a method to evaluate mechanisms thought to be common in a postseismic relaxation (e.g., afterslip, viscoelasticity, and poroelasticity), based on a fundamental solution for a body force in a homogeneous elastic half space. In this paper we present such a solution in the Fourier domain, to allow an efficient evaluation of the time-dependent displacement field by taking advantage of the fast Fourier transforms and the convolution theorem. The proposed semi-analytic method involves two steps: first we evaluate a displacement field in a full space, then apply a correction to satisfy the boundary condition (also, see Nguyen et al. [2008]). Our model includes a mixed boundary condition with a gravitational restoring force that results from displacements across the density contrast interface. The method can be used to model postseismic deformation involving nonlinear rheologies [Barbot and Fialko, submitted, 2009a], and static deformation in a heterogeneous elastic half space [Barbot et al., 2009b].

This article is organized as follows. First, we describe a Fourier-domain analytic solution to the displacement field in an elastic half space under a prescribed traction boundary condition. The solution is obtained using the Galerkin vector potential. We consider cases of tangential traction and normal load then describe a solution that accounts for an arbitrary spatial distribution of traction in all directions. Our solution generalizes the so-called Cerruti's and Boussinesq's problems to incorporate the buoyancy effect due to a density contrast at the surface. In Section 6.3 we derive a semi-analytic Green function for the elastic half space in the Fourier domain. Our formulation allows one to evaluate the displacement field due to an arbitrary distribution of internal forces and surface traction accounting for a buoyancy effect at the surface. In Section 6.4, we discuss applications relevant to crustal deformation and compare calculations using our method to known analytic solutions. In Appendix 6.6 we use a perturbation method

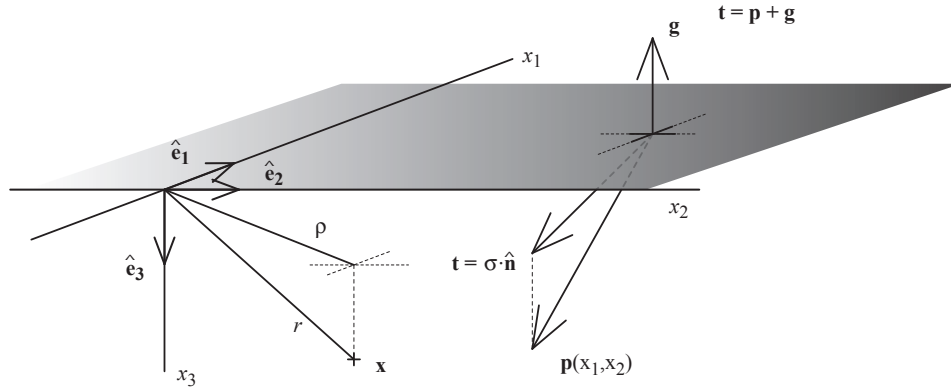


Figure 6.1: Geometry and boundary condition for the deformation due to an arbitrary distribution of surface traction. The surface traction $\mathbf{t}(\mathbf{x})$ is the sum of the applied load $\mathbf{p}(\mathbf{x})$ and the buoyancy restoring force $\mathbf{g} = \Delta\rho g u_3 \hat{\mathbf{n}}$. Displacement \mathbf{u} in the semi-infinite solid satisfies the homogeneous Navier's equation (6.4) with buoyancy boundary condition (6.3).

to derive an approximation to the solution to the generalized Boussinesq's problem in the space domain. We use this analytic solution to validate our Fourier-domain formulation. Finally, in Appendix 6.7, we validate the results presented in Section 6.2 using an alternate derivation based on the Boussinesq-Papkovich potential.

6.2 Analytic solution to the traction boundary-value problem in a semi-infinite elastic solid with gravity

We wish to obtain an expression for the static deformation of a homogeneous elastic half space Ω subject to a distribution of traction $p_i(x_1, x_2)$ at its surface $x_3 = 0$. The surface $\partial\Omega$ is associated with the normal vector $n_i = -\delta_{i3}$, where δ_{ij} is the Kronecker's delta. The vertical displacement at the surface gives rise to a buoyancy restoring force so that the equilibrium holds [Wolf, 1991, Johnston et al., 1998],

$$t_i = p_i + g_i , \quad (6.1)$$

where p_i is the applied surface load,

$$g_i = \Delta\rho g u_3 n_i . \quad (6.2)$$

is the pressure due to the assumed density contrast $\Delta\rho$ at the surface and $t_i = \sigma_{ij}n_j$ is the resulting traction at the surface (see Fig. 6.1). In terms of stress components we obtain the

surface boundary condition

$$\begin{aligned}\sigma_{13}(x_1, x_2) &= -p_1(x_1, x_2) \\ \sigma_{23}(x_1, x_2) &= -p_2(x_1, x_2) \\ \sigma_{33}(x_1, x_2) &= -p_3(x_1, x_2) + \Delta\rho g u_3\end{aligned}\tag{6.3}$$

where σ_{ij} is the Cauchy stress tensor [Malvern, 1969, Nemat-Nasser and Hori, 1999]. In the homogeneous elastic half-space the conservation of linear momentum and Hooke's law give rise to the homogeneous Navier's equation

$$(\lambda + \mu)u_{j,ij} + \mu u_{i,jj} = 0\tag{6.4}$$

where u_i is the vector-valued displacement field and λ and μ are the Lamé parameters. We look for a displacement field that satisfies the governing equation (6.4) with boundary condition (6.1) at the surface and vanishing displacement at infinity.

Next we introduce the Galerkin vector potential and use it to solve for two related subproblems: the Boussinesq's problem for the deformation due to normal loads at the surface, and the Cerruti's problem for the deformation due to the application of tangential traction at the surface. We consider a generalization of the classic formulation of the Cerruti's and Boussinesq's problems that includes a buoyancy restoring force at the surface. By applying the superposition theorem, we derive a general solution for the deformation in a half-space due to the application of some arbitrary traction at the surface.

6.2.1 The Galerkin vector potential

The Galerkin vector potential G_i [Westergaard, 1935, Mindlin, 1936b, Mindlin and Cheng, 1950a, Steketee, 1958a] is defined by the change of variable

$$u_i = G_{i,jj} - \alpha G_{j,ij}\tag{6.5}$$

where the dimensionless constant α can be expressed in terms of Lamé's parameters or Poisson's ratio

$$\alpha = \frac{\lambda + \mu}{\lambda + 2\mu} = \frac{1}{2(1 - \nu)}\tag{6.6}$$

Inserting the Galerkin potential in the homogeneous Navier's equation (6.4) gives rise to

$$G_{i,jjkk} = 0.\tag{6.7}$$

In the absence of internal forces the three Cartesian components of G_i are biharmonic. By applying the two-dimensional horizontal (x_1, x_2) Fourier transforms

$$\begin{aligned}\hat{f}(k_1, k_2, x_3) &= \int_{-\infty}^{\infty} \int_{-\infty}^{\infty} f e^{-i2\pi(k_1x_1 + k_2x_2)} dx_1 dx_2 \\ f &= \int_{-\infty}^{\infty} \int_{-\infty}^{\infty} \hat{f}(k_1, k_2, x_3) e^{-i2\pi(k_1x_1 + k_2x_2)} dk_1 dk_2\end{aligned}\tag{6.8}$$

where f is a scalar field and defining the angular velocities $\omega_i = 2\pi k_i$ the biharmonic equation (6.7) simplifies to the fourth-order ordinary differential equation

$$\left(\frac{\partial^2}{\partial x_3^2} - \beta^2\right)^2 G_i = 0 \quad (6.9)$$

where we have defined the radial angular velocity

$$\beta = (\omega_1^2 + \omega_2^2)^{1/2} \quad (6.10)$$

A general solution for the components of the Galerkin vector is

$$\hat{G}_i = (A_i + B_i \beta x_3) e^{-\beta x_3} + (C_i + D_i \beta x_3) e^{+\beta x_3} \quad (6.11)$$

Vanishing displacements at infinity ($x_3 \rightarrow \infty$) require $C_i = D_i = 0$, so that the general solution and its successive derivatives are,

$$\begin{aligned} \hat{G}_i &= (A_i + B_i \beta x_3) e^{-\beta x_3} \\ \hat{G}_{i,3} &= \beta (B_i - A_i - B_i \beta x_3) e^{-\beta x_3} \\ \hat{G}_{i,33} &= \beta^2 (-2B_i + A_i + B_i \beta x_3) e^{-\beta x_3} \\ \hat{G}_{i,333} &= \beta^3 (3B_i - A_i - B_i \beta x_3) e^{-\beta x_3} \end{aligned} \quad (6.12)$$

The components of the stress tensor are, without loss of generality,

$$\begin{aligned} \sigma_{ij} &= \mu \left[(2\alpha - 1) \delta_{ij} G_{k,kl} \right. \\ &\quad \left. + G_{i,jkk} + G_{j,ikk} - 2\alpha G_{k,ijk} \right] \end{aligned} \quad (6.13)$$

The semi-analytic solution in the Fourier domain for the deformation in a half-space subject to surface traction consists in finding the values of the A_i and the B_i from the Fourier transform of the surface stresses, i.e., removing the six degrees of freedom in the Galerkin vector of eq. (6.12). Such a solution might be obtained directly by inverting a 6×6 square matrix, but this approach is not generally tractable. Instead, we solve independently the so-called Boussinesq's and Cerruti's problems, corresponding to the application of normal and tangential loads, respectively, at the surface of the half space, and obtain the full solution by linear superposition.

6.2.2 The Boussinesq's problem with gravity

The Boussinesq's problem consists in the application of a concentrated normal load $\mathbf{p} = p_3 \mathbf{e}_3$ at the surface of the half-space. We consider an extended problem of an arbitrary distribution of normal traction with buoyancy effects. The solution to this problem in the Fourier domain with no gravity was presented by Steketee [1958a]. Assuming that the first two components of the Galerkin vector potential can be set to zero, $G_1 = G_2 = 0$, we obtain the shear stress components

$$\begin{aligned} \hat{\sigma}_{13} &= -2\mu i\omega_1 \beta^2 [(1 - 2\alpha)B_3 + \alpha(A_3 + B_3 \beta x_3)] e^{-\beta x_3} \\ \hat{\sigma}_{23} &= -2\mu i\omega_2 \beta^2 [(1 - 2\alpha)B_3 + \alpha(A_3 + B_3 \beta x_3)] e^{-\beta x_3} \end{aligned} \quad (6.14)$$

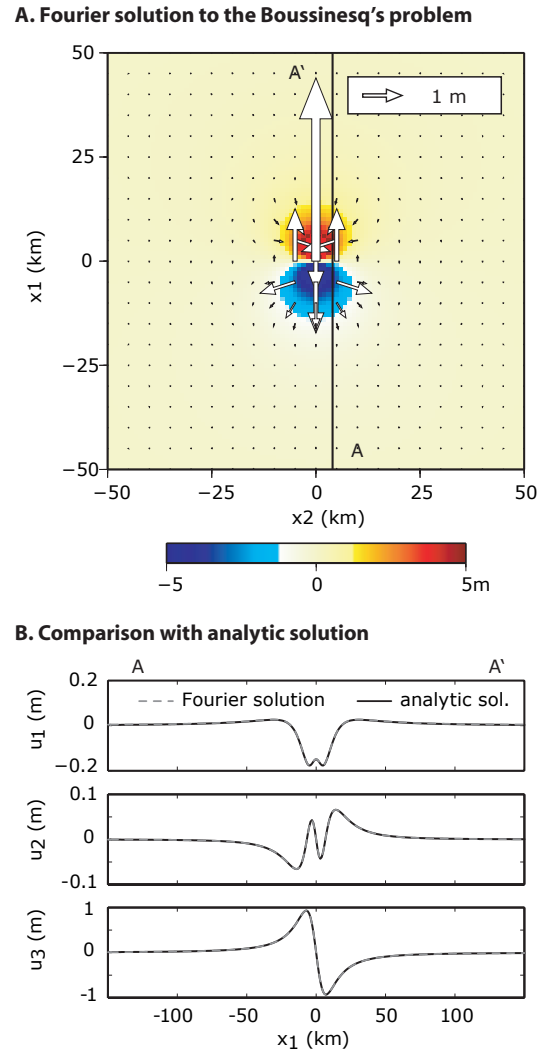


Figure 6.2: A) Fourier-domain solution for the Boussinesq's problem (eq. 6.20). The map view corresponds to displacements at a depth of 3 km. The arrows indicate the horizontal displacement; the vertical displacement is shown by the color. Vertical displacement is taken to be positive upward. A point-source moment \mathbf{m}_{23} is applied at the surface. A) Comparison between the analytic solution and the semi-analytic Fourier domain solution along profile A-A'. These results correspond to a Poisson's solid ($\lambda = \mu$) without buoyancy effects at the surface ($\Gamma = 0$).

that both vanish identically at the surface if

$$A_3 = (2 - \alpha^{-1})B_3 \quad (6.15)$$

Combining the surface normal stress

$$\hat{\sigma}_{33} = 2\mu\alpha B_3\beta^3 \quad (6.16)$$

and the vertical displacement at the surface

$$\hat{u}_3 = -\beta^2 B_3 \quad (6.17)$$

and using the boundary condition $\hat{\sigma}_{33} = -\hat{p}_3 + \Delta\rho g \hat{u}_3$ of eq. (6.1), one finds

$$B_3 = \frac{-\hat{p}_3}{2\mu\alpha\beta^2(\beta + \Gamma)} \quad (6.18)$$

where we have introduced the critical wavenumber

$$\Gamma = \frac{\Delta\rho g}{2\mu\alpha} = (1 - \nu)\frac{\Delta\rho g}{\mu} \quad (6.19)$$

that represents the relative effect of gravity compared to the elastic rigidity. For a typical density contrast at the Earth's surface $\Delta\rho = 2.8 \cdot 10^3 \text{ kg/m}^3$ and shear modulus $G = 30 \text{ GPa}$, the associated critical wavelength is $\Gamma^{-1} = 10^3 \text{ km}$. The solution for the displacement field for the Boussinesq's problem with the buoyancy effect is

$$\begin{aligned} \hat{u}_1(k_1, k_2, x_3) &= i\alpha\omega_1\beta B_3 [1 - \alpha^{-1} + \beta x_3] e^{-\beta x_3} \\ \hat{u}_2(k_1, k_2, x_3) &= i\alpha\omega_2\beta B_3 [1 - \alpha^{-1} + \beta x_3] e^{-\beta x_3} \\ \hat{u}_3(k_1, k_2, x_3) &= -\alpha\beta^2 B_3 [\alpha^{-1} + \beta x_3] e^{-\beta x_3} \end{aligned} \quad (6.20)$$

A comparison between the Fourier domain solution (6.20) and the corresponding analytic solution using the space-domain Green function (eq. 6.74 in Appendix 6.6) is shown in Fig. 6.2. We compute the response of a moment load \mathbf{m}_{23} applied at the surface $x_3 = 0$ and compute the displacements at a depth of 3 km ignoring the role of gravity ($\Gamma = 0$). The difference between the two fields is within a few percents of the maximum value. The effect of gravity on the displacement field (6.20) is to damp long-wavelength displacement components with the high-pass filter $1/(1 + \Gamma x)$, where $x = 1/\beta$ is the two-dimensional radial wavelength. Displacement wavelengths greater than the critical wavelength Γ^{-1} are strongly attenuated whereas wavelengths much shorter than Γ^{-1} are little affected by the buoyancy boundary condition. An elastic Green function in the space domain that incorporates the effect of buoyancy is developed in Appendix 6.6 and compares well with the Fourier-domain formulation. The effect of gravity on viscoelastic relaxation following slip on a thrust fault is illustrated by Barbot and Fialko [submitted, 2009a].

6.2.3 The Cerruti's problem with gravity

The Cerruti's problem corresponds to the deformation in a half-space due to the application of some tangential forces at the surface. As there is no fundamental difference between applying forces in the x_1 or the x_2 direction, we simplify the problem and solve for surface stress in the x_1 direction only. The solution corresponding to the tangential forces oriented in the x_2 direction can be obtained by rotation about the x_3 axis. We therefore solve the homogeneous Navier's equation (6.4) considering the following boundary conditions: a prescribed surface stress σ_{13} , vanishing surface stress σ_{23} , equilibrium between the restoring buoyancy force and the normal stress σ_{33} and vanishing of displacements at infinity.

We start by using only one component of the Galerkin vector potential, such that $G_2 = G_3 = 0$. In the Fourier domain we obtain the stress components at the surface,

$$\begin{aligned}\hat{\sigma}_{13} &= 2\mu\beta [\alpha\omega_1^2 A_1 + (\beta^2 - \alpha\omega_1^2)B_1] \\ \hat{\sigma}_{23} &= 2\mu\alpha\omega_1\omega_2\beta[A_1 - B_1]\end{aligned}\tag{6.21}$$

From the surface boundary condition $\sigma_{23} = 0$, we obtain

$$A_1 = B_1\tag{6.22}$$

and from the prescribed shear stress in the x_1 -direction we find

$$B_1 = \frac{-\hat{p}_1}{2\mu\beta^3}\tag{6.23}$$

At this point, however, we have no vertical displacement at the surface and the condition of vanishing of normal stress at the surface is not satisfied. The Galerkin potential G_1 contributes to the surface normal stress

$$\hat{\sigma}_{33} = (\alpha - 1)\frac{i\omega_1\hat{p}_1}{\beta}\tag{6.24}$$

This normal stress can be readily cancelled by application of the solution (6.20) to the Boussinesq's problem with the constant

$$B_3 = -i\omega_1\frac{1 - \alpha}{\alpha}\frac{B_1}{\beta + \Gamma}\tag{6.25}$$

The solution to the Cerruti's problem requires two components of the Galerkin vector potential. Using eqs. (6.22), (6.23) and (6.25) the solution displacement can be written

$$\begin{aligned}\hat{u}_1 &= B_1 \left\{ -2\beta^2 \right. \\ &\quad \left. + \frac{\omega_1^2}{1+h} \left[2 - \alpha^{-1} + \alpha h + (1 + \alpha h)\beta x_3 \right] \right\} e^{-\beta x_3} \\ \hat{u}_2 &= \omega_1\omega_2 \frac{B_1}{1+h} \left\{ 2 - \alpha^{-1} + \alpha h + (1 + \alpha h)\beta x_3 \right\} e^{-\beta x_3} \\ \hat{u}_3 &= i\omega_1\beta \frac{B_1}{1+h} \left\{ \alpha^{-1} - 1 + (1 + \alpha h)\beta x_3 \right\} e^{-\beta x_3}\end{aligned}\tag{6.26}$$

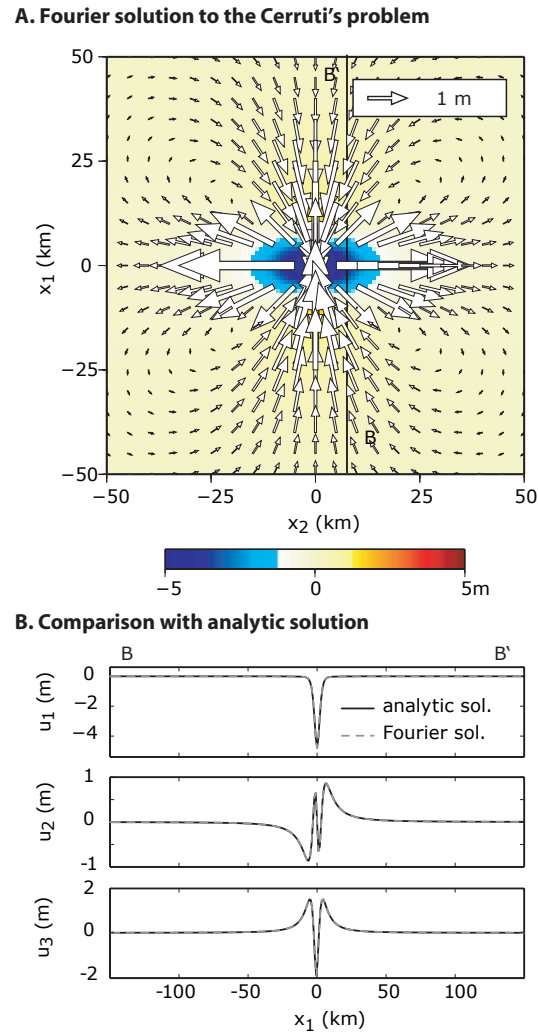


Figure 6.3: Benchmark of the Fourier-domain solution to the Cerruti's problem (Eqs. (6.26) and (6.27)). A) A point-source moment \mathbf{m}_{12} is applied at the surface of the half space. The map view corresponds to displacements at a depth of 3 km. The arrows indicate the horizontal displacement; the vertical displacement is shown in color. Vertical displacement is taken to be positive upward. B) Comparison between the analytic solution and the semi-analytic Fourier domain solution for the displacement along profile B-B'. In these calculations, we use a Poisson's solid ($\lambda = \mu$) and ignore the buoyancy effect ($\Gamma = 0$).

where, for convenience, we have introduced the dimensionless parameter $h = \Gamma/\beta$. The solution to the Boussinesq's and Cerruti's problems can also be obtained analytically in the Fourier domain using the Boussinesq-Neuber-Papkovitch potential, as shown in Appendix 6.7.

In case when the tangential traction is exerted in the x_2 direction, we have $\mathbf{p} = p_2 \hat{\mathbf{e}}_2$, $B_1 = 0$, $B_2 = -\hat{p}_2/2\mu\beta^3$ and the displacement field is

$$\begin{aligned}\hat{u}_1 &= \omega_1\omega_2 \frac{B_2}{1+h} \left\{ 2 - \alpha^{-1} + \alpha h + (1 + \alpha h)\beta x_3 \right\} e^{-\beta x_3} \\ \hat{u}_2 &= B_2 \left\{ -2\beta^2 \right. \\ &\quad \left. + \frac{\omega_2^2}{1+h} \left[2 - \alpha^{-1} + \alpha h + (1 + \alpha h)\beta x_3 \right] \right\} e^{-\beta x_3} \\ \hat{u}_3 &= i\omega_2\beta \frac{B_2}{1+h} \left\{ \alpha^{-1} - 1 + (1 + \alpha h)\beta x_3 \right\} e^{-\beta x_3}\end{aligned}\tag{6.27}$$

The space-domain solution for the case of a concentrated load acting normal to the surface of a half-space [Love, 1927, Nemat-Nasser and Hori, 1999, Soutas-Little, 1999] is given by

$$\begin{aligned}u_1 &= \frac{1}{4\pi\mu r} \left[1 + \frac{x_1^2}{r^2} + (1 - 2\nu) \left(\frac{r}{r + x_3} - \frac{x_1^2}{(r + x_3)^2} \right) \right] \\ u_2 &= \frac{x_1 x_2}{4\pi\mu r} \left[\frac{1}{r^2} - \frac{1 - 2\nu}{(r + x_3)^2} \right] \\ u_3 &= \frac{x_1}{4\pi\mu r} \left[\frac{x_3}{r^2} + \frac{1 - 2\nu}{r + x_3} \right]\end{aligned}\tag{6.28}$$

where $r = (x_1^2 + x_2^2 + x_3^2)^{1/2}$. We note a discrepancy in sign between the solutions given by Nemat-Nasser and Hori [1999] and Soutas-Little [1999] for the vertical component of displacement. Our results (eq. 6.28) agree with those of Soutas-Little [1999] and Okumura [1995]. A comparison between the analytic solution (6.28) and the Fourier-domain formulation (6.26) is shown in Fig. 6.3. We apply a moment \mathbf{m}_{12} at the surface of the half space and compute the solution on a horizontal plane at a depth of 3 km. In this calculation, the buoyancy is ignored ($\Gamma = 0$). Fig. 6.3b compares the analytic and numerical solutions along the horizontal profile B-B'. The error is less than 1% of the maximum value of either displacement component.

6.2.4 Arbitrary distribution of surface traction with gravity

The general solution corresponding to the application of an arbitrary traction p_i at the surface of the half space is provided by the superposition of solutions to the Boussinesq's and Cerruti's problems. It makes use of the three components of the Galerkin vector potential.

Combining results (6.20), (6.26) and (6.27) we obtain the complete displacement solution

$$\begin{aligned}
\hat{u}_1 &= \left[-2B_1\beta^2 + \alpha\omega_1(B_1\omega_1 + B_2\omega_2)(1 + \beta x_3) \right. \\
&\quad \left. + \alpha i\omega_1\beta B_3(1 - \alpha^{-1} + \beta x_3) \right] e^{-\beta x_3} \\
\hat{u}_2 &= \left[-2B_2\beta^2 + \alpha\omega_2(B_1\omega_1 + B_2\omega_2)(1 + \beta x_3) \right. \\
&\quad \left. + \alpha i\omega_2\beta B_3(1 - \alpha^{-1} + \beta x_3) \right] e^{-\beta x_3} \\
\hat{u}_3 &= \alpha\beta^2 \left[i(\omega_1 B_1 + \omega_2 B_2)x_3 \right. \\
&\quad \left. - B_3(\alpha^{-1} + \beta x_3) \right] e^{-\beta x_3}
\end{aligned} \tag{6.29}$$

where the constants B_i depend upon the applied traction

$$\begin{aligned}
B_1 &= \frac{-\hat{p}_1}{2\mu\beta^3} \\
B_2 &= \frac{-\hat{p}_2}{2\mu\beta^3} \\
B_3 &= \frac{-\beta\hat{p}_3 + i(1 - \alpha)(\omega_1\hat{p}_1 + \omega_2\hat{p}_2)}{2\mu\alpha\beta^3(\beta + \Gamma)}
\end{aligned} \tag{6.30}$$

Our formulation (6.29) is a closed-form solution in the Fourier domain to the traction boundary-value problem in a half space including a buoyancy restoring force at the surface.

6.3 A semi-analytic Green function for the elastic half space with gravity

The elastic Green function for a semi-infinite elastic solid with a free-surface boundary condition [Love, 1927, Mindlin, 1936a] provides the elementary solution that can be used to evaluate the three-dimensional deformation due to a distribution of point forces. As body force representations can be used to imitate dislocations [Burridge and Knopoff, 1964, Steketee, 1958a], an elastic response of the crust due to slip on buried faults can be evaluated using the elastic Green function [Okada, 1992, Meade, 2007]. Both internal forces and surface traction are required to represent slip on a fault if the latter intersects the surface [Backus and Mulcahy, 1976a,b, Barbot et al., 2009b]. An inhomogeneous traction boundary condition is also used in models of a heterogeneous crust [Barbot et al., 2009b]. Finally, it can be required in models of time-dependent poroelastic relaxation [Barbot and Fialko, submitted, 2009a].

Theoretically, the three-dimensional displacement field can be obtained with the convolution between the equivalent body force and the elastic Green function [Love, 1927, Mindlin, 1936a]. However, the forcing terms might occupy a large volume and the convolution in the space domain might not be computationally tractable. Our approach is to evaluate the elastic deformation numerically using a semi-analytic Green function in the Fourier domain [Barbot et al., 2008a, 2009a,b]. This approach takes advantage of the convolution theorem of the Fourier transform

whereby the convolution becomes a product in the Fourier domain. The surface traction boundary condition is enforced using superposition. The Fourier-domain semi-analytic Green function satisfying arbitrary surface traction boundary conditions can be used in multiple applications including elasto-static deformation in homogeneous and heterogeneous materials [Moulinec and Suquet, 1998, Barbot et al., 2009b], models of fault creep [Barbot et al., 2009a] and other post-seismic phenomena [Barbot and Fialko, submitted, 2009a].

6.3.1 A Fourier-domain elastic Green function

Our approach to evaluate the three-dimensional displacement in a half space due to an arbitrary distribution of body forces f_i subject to an inhomogeneous traction and buoyancy boundary condition is as follows. Consider the inhomogeneous Navier's equation

$$\mu \left(\frac{\alpha}{1-\alpha} u_{j,ij} + u_{i,jj} \right) + f_i = 0 \quad (6.31)$$

subject to the surface boundary condition

$$\sigma_{ij} n_j = q_i + \Delta \rho g u_3 n_i, \quad x_3 = 0 \quad (6.32)$$

where u_i is the vector-valued displacement field, σ_{ij} is the Cauchy stress tensor, $n_i = (0, 0, -1)$ is the surface normal vector and $q_i(x_1, x_2)$ is the prescribed load. The displacement that satisfies eq. (6.31) and (6.32) can be decomposed into a homogeneous and a particular contribution

$$u_i = u_i^h + u_i^p \quad (6.33)$$

where the displacement field u_i^h is a solution to the homogeneous Navier's equation

$$\alpha u_{j,ij}^h + (1-\alpha) u_{i,jj}^h = 0 \quad (6.34)$$

with inhomogeneous surface boundary conditions and the particular solution u^p satisfies eq. (6.31) regardless of the surface boundary condition. The particular solution can be obtained in a straight-forward manner in the Fourier domain. Upon Fourier transforming in the three directions eq. (6.31) becomes algebraic

$$\mu \left(\frac{\alpha}{1-\alpha} k_i k_j + k_l k_l \delta_{ij} \right) \hat{u}_j^p = \frac{1}{4\pi^2} \hat{f}_i \quad (6.35)$$

where k_i are the wavenumbers and the displacement field can be directly inverted to obtain

$$\hat{u}_i^p = \frac{1}{\mu} \frac{(1-\alpha) k_l k_l \delta_{ij} - \alpha k_i k_j}{4\pi^2 (k_l k_l)^2} \hat{f}_j \quad (6.36)$$

where hats denote the Fourier transform of the corresponding variables. We note that eq. (6.36) is ill-posed for $k_1 = k_2 = k_3 = 0$. The zero wavenumber component of the Fourier solution corresponds to a rigid-body displacement and does not involve elastic deformation. We do not

allow for a net displacement of the half space and we simply set $\hat{u}_i(0,0,0) = 0$. The particular solution to eq. (6.31) is provided by eq. (6.36) for any distribution of internal forces.

We now seek a homogeneous solution u^h such that the sum (6.33) satisfies the boundary condition (6.32). For convenience, as eq. (6.29) is already a Fourier-domain solution, we evaluate the surface traction and the surface vertical displacements in the Fourier domain. A displacement field is associated with the stress

$$\sigma_{ij} = \mu \left(u_{i,j} + u_{j,i} - \frac{1-2\alpha}{1-\alpha} u_{k,k} \delta_{ij} \right) \quad (6.37)$$

and we define the surface traction due to the homogeneous and particular displacement fields by $t_i^h = \sigma_{ij}^h n_j$ and $t_i^p = \sigma_{ij}^p n_j$, respectively. In the Fourier domain the stress can be written

$$\hat{\sigma}_{ij} = \mu \left(k_j \delta_{il} + k_i \delta_{jl} - \frac{1-2\alpha}{1-\alpha} k_l \delta_{ij} \right) \hat{u}_l \quad (6.38)$$

The contributions of vertical displacement \hat{u}_3^p and traction \hat{t}_i^p from the particular solution at the surface are, respectively,

$$\hat{u}_3^p(k_1, k_2) = \int_{-\infty}^{\infty} \hat{u}_3^p(k_1, k_2, k_3) dk_3 \quad (6.39)$$

and

$$\begin{aligned} \hat{t}_i^p(k_1, k_2) = \\ \mu \int_{-\infty}^{\infty} \left(k_j \hat{u}_i^p + k_i \hat{u}_j^p - \frac{1-2\alpha}{1-\alpha} k_l \hat{u}_l^p \delta_{ij} \right) n_j dk_3 \end{aligned} \quad (6.40)$$

The solution to the homogeneous Navier's equation (6.34) was discussed in Section 6.2 and given by eq. (6.29). By definition of eq. (6.1), the traction and the surface vertical displacement of the homogeneous solution satisfy

$$t_i^h = p_i + \Delta \rho g u_3^h n_i \quad (6.41)$$

where the traction $p_i(x_1, x_2)$ is a degree of freedom required to satisfy eq. (6.32). We use linear superposition to cancel the contribution from the particular solution and satisfy (6.32). The displacements in the semi-infinite solid can be evaluated for a given applied traction $p_i(x_1, x_2)$ at the surface and the buoyancy boundary condition is automatically satisfied. We write

$$u^h = u^h(; p_i) \quad (6.42)$$

where we use the semi colon to denote the dependence of the homogeneous solution upon the prescribed boundary condition p_i at the surface. Using the decomposition of eq. (6.33) the boundary condition (6.32) can be written

$$t_i^h + t_i^p = q_i + \Delta \rho g (u_3^h + u_3^p) n_i \quad (6.43)$$

Using eq. (6.41) we constrain the last degree of freedom

$$p_i = -t_i^p + \Delta \rho g u_3^p n_i + q_i \quad (6.44)$$

In the Fourier domain, the required homogeneous contribution is

$$\hat{u}_g = \hat{u}_g(; -\hat{t}_i^p + \Delta\rho g \hat{u}_3^p n_i + \hat{q}_i) \quad (6.45)$$

The displacement field due to a distribution of internal body forces and surface traction is ultimately evaluated using the following steps. First, we apply a three-dimensional Fourier transform to the body-force field. Second, we apply the Fourier-domain Green function of eq. (6.36). We obtain a displacement field that satisfies periodic boundary conditions. The intermediate solution requires a correction to satisfy the traction boundary condition. We evaluate the two-dimensional traction field (6.44) in the Fourier domain by calculating the integrals (6.39) and (6.40) numerically. We then evaluate a homogeneous solution that satisfies eq. (6.44) using the analytic solution (6.29). Summing the two displacement fields results in a solution that satisfies the inhomogeneous Navier's equation (6.31) and the prescribed traction boundary condition (6.32). Finally, we perform a three-dimensional inverse Fourier transform to obtain a displacement field in the space domain.

6.4 Models of faulting and volcanic unrest

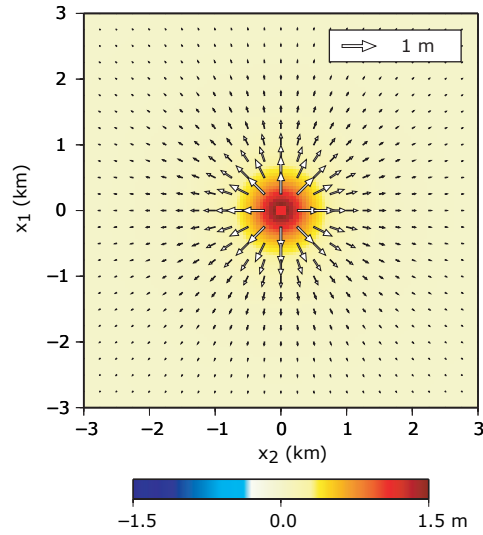
We test the semi-analytic Green function described in Section 6.3 against analytic solutions for the three-dimensional displacements due to fault slip and magmatic intrusions. Some benchmarks for strike-slip faults and a comparison with the numerical approach of Wang et al. [2003] are presented in Barbot et al. [2009a]. Benchmarks for dip-slip faults in plane strain problems can be found in Barbot et al. [2009b]. We start by comparing models of deformation for a point source using the solution of Mindlin and Cheng [1950a] for a nucleus of strain. We then describe models including sources of finite size and compare our numerical solution for strike-slip and dip-slip faults with the analytic solution of Okada [1992]. Our formulation allows us to represent sources of arbitrary orientation in the half-space. To illustrate this capability, we consider a case of a buried thrust fault.

First we consider the case of a dilatation source. A point source of dilatation is an approximation representing isometric magmatic intrusions subject to a pressure boundary condition [Mogi, 1958]. The surface displacement (at $x_3 = 0$) due to a source of dilatation at depth y_3 in a semi-infinite solid with Poisson's ratio ν is [Mindlin and Cheng, 1950a,b]

$$\begin{aligned} u_1 &= + \frac{1 + \nu}{\pi} \frac{x_1}{r^3} \\ u_2 &= + \frac{1 + \nu}{\pi} \frac{x_2}{r^3} \\ u_3 &= - \frac{1 + \nu}{\pi} \frac{y_3}{r^3} \end{aligned} \quad (6.46)$$

where $r = (x_1^2 + x_2^2 + y_3^2)^{1/2}$ is the distance from the source centered at the origin and an observation point at the surface. The dilatation source of eq. (6.46) can be represented by the

A. Surface displacement for a buried dilatation source



B. Numerical error

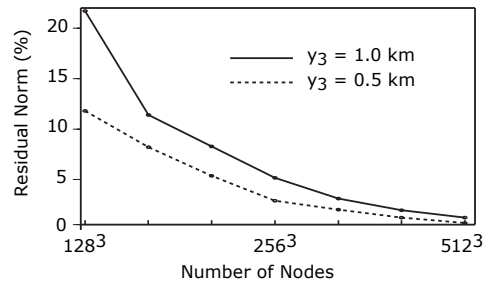


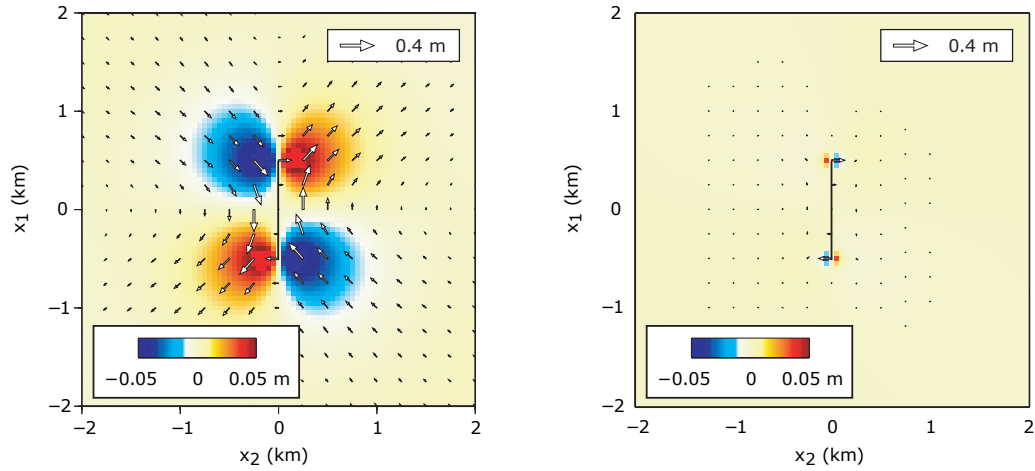
Figure 6.4: A) Map view of surface displacement due to a dilatation source centered at $y_1 = y_2 = 0$ and buried at a depth of $y_3 = 0.5$ km. Horizontal and vertical components of displacement are represented by the vectors and the color, respectively. Uplift is taken to be positive. B) The norm of the residuals between the numerical solution and the formulation of Mindlin and Cheng [1950b] as a function of the number of nodes in the 3-D grid for a uniform isotropic sampling of $\Delta x_i = 0.05$ km. The error is normalized by the norm of the analytic solution. The dashed and solid-line profiles correspond to a dilatation source at depth of $y_3 = 0.5$ and $y_3 = 1.0$ km, respectively. The numerical error decreases as the boundaries of the computational domain increases and the non-desired effect of periodicity decreases.

eigenstrain $\epsilon_{ij}^i = \delta_{ij}$, a moment density $m_{ij} = 3\kappa \delta_{ij}$ and an equivalent body force $f_i = -m_{ij,j}$ in the notation of Barbot et al. [2009a], Barbot and Fialko [submitted, 2009a], Barbot et al. [2009b], where κ is the bulk modulus. Our numerical solution for the surface displacement is shown in Fig. 6.4a for a point source at depth $y_3 = 0.5$ km. In Fig. 6.4b, we show the numerical error as a function of the number of nodes in our three-dimensional grid. We normalize the sum of the square of the residuals between the semi-analytic and the analytic solution (6.46) by the norm of the analytic signal. In these calculations we assume a Poisson's solid ($\lambda = \mu$ and $\nu = 1/4$), ignore the density contrast at the surface ($\Gamma = 0$) and use a uniform sampling size of $\Delta x_i = 0.05$ km. A simulation using 512^3 nodes takes about 30 seconds on a four-CPU shared-memory computer. The error decays to less than 1% for large computational grids where the effect of periodicity is smaller. Calculations with different values of Poisson's ratio gave rise to similar residuals.

We now consider the case of finite faults. We model finite faults with a distribution of internal forces and surface traction [Barbot et al., 2009a]. Figure 6.5a (left panel) shows the surface displacements due to a vertical left-lateral strike-slip fault with a 1 m slip. The right panel shows the residuals between our numerical solution and the analytic formulation of Okada [1992]. The residuals at the tip of the fault are due to our tapering of slip at the edges of the fault. We taper slip at the fault tips to mitigate a possible Gibbs phenomenon [Barbot et al., 2008a]; also tapered slip distribution is more physically reasonable than constant slip [e.g., Fialko, 2004c]. Figure 6.5b shows the surface displacements associated with a vertical dip-slip fault with a 1 m slip on a plane extending from the surface to a depth of 1 km. Models of dip-slip faults intersecting the surface require both equivalent body forces and equivalent surface traction to represent the slip discontinuity. The residuals with the solution of Okada [1992] are localized near the fault and arise from the displacement discontinuity, which cannot be accurately represented by a continuous field down to a scale of numerical discretization. For both the strike-slip and dip-slip faults, the residuals immediately away from the fault trace fall below 5% of the expected signal.

Finally, we use the derived semi-analytic Green function to compute the displacement field due to a thrust fault. Fig. 6.6a shows the displacement field at the surface due to a buried thrust fault 10 km long and 10 km wide in the down-dip direction. The top of the fault is buried at a depth of 5 km. The residuals with the analytic solution of Okada [1992] are shown in Fig. 6.6b (notice the change of scale). Overall, residuals are about 2% of the expected signal. The biggest residuals are located near the top of the fault and are due to slip tapering in our models. We investigate the effect of sampling and size of the computational domain on the accuracy of the numerical solution. Figure 6.6c shows the norm of the residuals as a function of the number of nodes in the computational grid for two different sampling sizes. For small grids, the error is greater for small sampling size. Figure 6.6c shows that the error corresponding to a grid with linear dimension of 12.8 km is comparable to the error arising from using a grid with the same linear dimension but doubled number of nodes. We conclude that a primary source of error

A. Strike-slip fault surface displacement and residuals with the solution of Okada (1992)



B. Vertical dip-slip fault and residuals with analytic solution

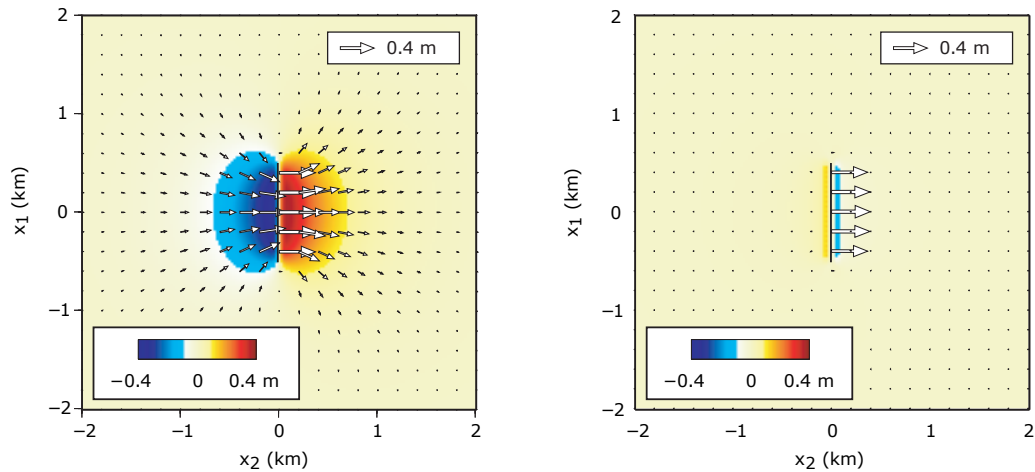
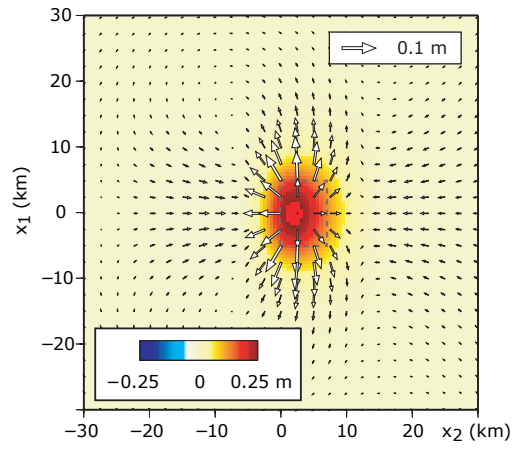
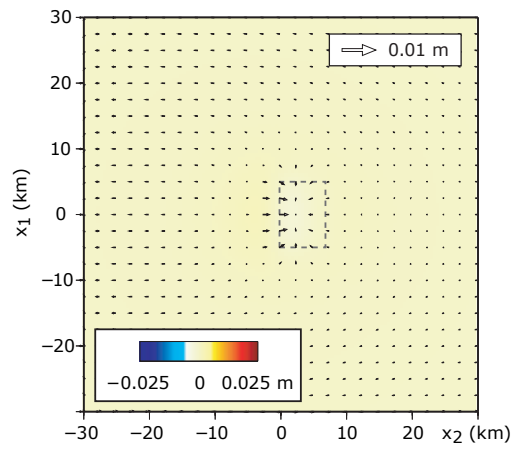


Figure 6.5: A) Map view of surface displacement due a vertical, 1 km long, strike-slip fault extending from the surface to a depth of 1 km with a 1 m slip (left) and residuals with the analytic solution of Okada [1992] (right). B) Surface displacements due to a 1 m slip on vertical dip-slip fault with same dimensions as in A). The fault trace is indicated by a solid black line. A dip-slip fault intersecting the surface is modeled with both internal body forces and surface traction. Residuals in A) are due to the tapering of the fault tip; residuals in B) come from the problem of sampling a displacement field that is not single-valued at the fault.

A. Surface displacement for a thrust fault



B. Residuals with the solution of Okada (1992)



C. Numerical error

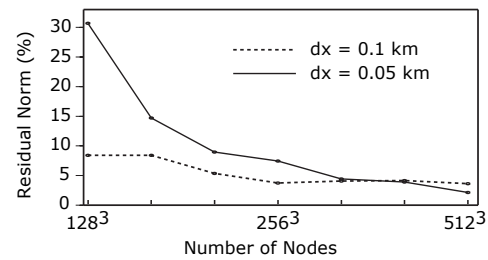


Figure 6.6: A) Map view of surface displacement due a 45° -dip, 10 km long, 10 km wide (in down-dip direction) thrust fault buried at a depth of 5 km (dashed rectangle). B) Residuals with the analytic solution of Okada [1992]. C) The norm of the residuals as a function of the number of nodes in the 3-D grid.

in this case comes from the distance to the periodic boundary. For larger computational grids, residuals associated with a smaller sampling become smaller, illustrating the tradeoff between the requirement of large computational domains and small discretization. We performed additional tests for a buried dip-slip fault, varying the dip angle from 0 to 90° and the fault length between 10 and 30 km, all other parameters being otherwise the same. We found similar good agreement between numerical and analytic solutions as the example shown in Fig. 6.6.

Figures 6.4, 6.5 and 6.6 illustrate simple point- and finite sources of deformation. Complex geometries can be readily accounted for in our method using a superposition of such elementary sources [Barbot et al., 2009a,b]. We conclude that the proposed Fourier-domain semi-analytic Green function approach is sufficiently accurate and flexible to allow realistic simulations of crustal deformation due to earthquake and volcano-related phenomena.

6.5 Conclusions

Building on the classic work of Steketee [1958a], we derived the analytic Fourier-domain solution for displacements due to an arbitrary distribution of tangential and normal loads at the surface of a semi-infinite solid. Our formulation generalizes the so-called Boussinesq's and Cerruti's problems by accounting for the effect of buoyancy at the surface due to a large density contrast between the lithosphere and the atmosphere. The buoyancy boundary condition is an approximation to the full effect of gravity where self-gravitation and internal density variations are ignored. The full Fourier-domain solution with surface buoyancy is given by eq. (6.29). We note that the solution (6.29) can be found using the Galerkin as well as the Boussinesq-Papkovich-Neuber vector potentials (see Appendix 6.7). We also derived a space-domain Green function for deformation of an elastic half space due to the application of normal loads at the surface of the half space with a buoyancy boundary condition (see Appendix 6.6). We use a perturbation approach, assuming that the effect of gravity is a small contribution to the elastic deformation, to approximate a solution for the elastic Green function. The accuracy of our solution is validated by a good agreement between the Fourier- and space-domain solutions to the generalized Boussinesq's problem.

Numerous problems of elastic deformation due to internal forces and surface traction come about from static models of faulting and from time-dependent models of postseismic relaxation [e.g., Barbot et al., 2009b, Barbot and Fialko, submitted, 2009a]. The displacement or velocity can theoretically be obtained by the convolution in the space domain between the elastic Green function and the body force, however this is not always practical because the internal forces can be distributed over a larger domain and the convolution operation scales as N^2 , where N is the number of nodes in the simulation. We derived an efficient way to evaluate the three-dimensional deformation in a half space due to the presence of an arbitrary distribution of internal forces and surface traction. Our method consists in (1) obtaining the displacement

field in a periodic full space due to the same internal forces and (2) adding a homogeneous solution to satisfy the prescribed boundary conditions, including the buoyancy effect. The periodic solution can be readily obtained in the Fourier domain and the auxiliary analytic homogeneous solution is given by eq. (6.29). The two-step method is computationally efficient and easily parallelized to deal with large computational grids. The semi-analytic solution compares well to analytic solutions for the displacement field due to strike-slip and dip-slip faults of arbitrary orientation and point-sources of dilatation, with a typical maximum error of 5% for the explored range of model sizes. Our Fourier-domain solution can be efficiently used to model elasto-static deformation [Barbot et al., 2009b], as well as quasi-static deformation such as that due to the most common postseismic mechanisms (viscoelastic relaxation, poroelastic rebound and fault creep). Applications of the proposed Green function to models of time-dependent postseismic deformation are considered elsewhere [Barbot and Fialko, submitted, 2009a].

Acknowledgement

A numerical code used in this paper is available at <http://sylvain.barbot.free.fr/crust/>. This Chapter, in full, has been submitted for publication of the material as it may appear in Geophysical Journal International. Barbot, Sylvain; Fialko, Y.. The dissertation author was the primary investigator and author of this paper.

6.6 Space-domain analytic Green function with buoyancy boundary condition

In this appendix, we derive an analytic solution for the elastic Green function for the case of a concentrated normal load applied at the surface of a semi-infinite elastic body. Our solution extends the classic solution to the so-called Boussinesq problem [Love, 1927, Nemat-Nasser and Hori, 1999] to a generalized boundary condition where surface normal displacement is counteracted by a buoyancy force. We use the analytic solution derived in this Appendix to validate the Fourier domain solution presented in Section 6.2. We first introduce the Boussinesq-Papkovich-Neuber vector potential, then use this potential to solve for the elastic Green function with buoyancy boundary condition. Our solution (eq. 6.73) is obtained using the perturbation method where we assume that the buoyancy effect is a small contribution to the elastic deformation.

6.6.1 The Boussinesq-Papkovitch-Neuber potential

The Boussinesq-Papkovitch-Neuber representation [Mindlin, 1936b] can be obtained by applying the Helmholtz decomposition to the solution to Navier's equation (6.4) as follows

$$u_i = \phi_{,i} + \epsilon_{ijk} A_{j,k} \quad \text{with} \quad A_{j,j} = 0 \quad (6.47)$$

where ϕ and A_i are scalar and vector fields, respectively, and ϵ_{ijk} is the Levi-Civita symbol. In the absence of body forces and taking

$$\alpha = \frac{\lambda + \mu}{\lambda + 2\mu} = \frac{1}{2(1 - \nu)} \quad (6.48)$$

the conservation of momentum gives rise to

$$[\phi_{,i} + (1 - \alpha)\epsilon_{ijk} A_{j,k}]_{,jj} = 0 \quad (6.49)$$

Defining the harmonic vector potential

$$B_i = \frac{1}{1 - \alpha} \phi_{,i} + \epsilon_{ijk} A_{j,k} \quad (6.50)$$

and its divergence

$$B_{j,j} = \frac{1}{1 - \alpha} \phi_{,jj} \quad (6.51)$$

one obtains, without loss of generality,

$$\phi = \frac{1 - \alpha}{2} (x_k B_k + B_0) \quad (6.52)$$

where we have used the vector identity $(x_k B_k)_{,jj} = 2 B_{j,j}$ and defined B_0 as a harmonic scalar.

From the definition of B_i , we have

$$\epsilon_{ijk} A_{j,k} = B_i - \frac{1}{1 - \alpha} \phi_{,i} \quad (6.53)$$

and one obtains the following representation

$$u_i = B_i - \frac{\alpha}{2} [x_k B_k + B_0]_{,i} \quad (6.54)$$

This is the Papkovitch-Neuber elastic potential, which represents the solution to Navier's equation in the absence of body force in terms of a harmonic vector B_i and a harmonic scalar B_0 . Without loss of generality, one has the following results

$$\begin{aligned} u_{j,j} &= (1 - \alpha) B_{j,j} \\ \frac{\sigma_{ij}}{\mu} &= (2\alpha - 1) \delta_{ij} B_{k,k} + B_{i,j} + B_{j,i} \\ &\quad - \alpha (x_k B_k + B_0)_{,ij} \end{aligned} \quad (6.55)$$

The advantage of the Papkovitch-Neuber potential is that it may allow one to attain an analytic solution to the Navier's equation in an easier way by manipulating harmonic vector and scalar potentials.

6.6.2 The Boussinesq problem with buoyancy surface boundary condition in the space domain

We look for an analytic expression for the Green function representing the displacement field experienced in the elastic half space Ω due to the application of a unit normal concentrated load $\mathbf{p} = \delta(\mathbf{x}) \hat{\mathbf{e}}_3$ at the origin, including the effect of buoyancy at the surface. The boundary condition at the surface $\partial\Omega$, recast in terms of stress components, is

$$\begin{aligned}\sigma_{13} &= 0 \\ \sigma_{23} &= 0 \\ \sigma_{33} &= -\delta(x_1)\delta(x_2) + \Delta\rho g u_3\end{aligned}\tag{6.56}$$

where $\delta(x)$ is the Dirac delta function. We consider the case where the first two components of the Papkovitch potential vanish, $B_1 = B_2 = 0$. The stress components become

$$\begin{aligned}\frac{\sigma_{13}}{\mu} &= (1 - \alpha) B_{3,1} - \alpha (x_3 B_{3,13} + B_{0,13}) \\ \frac{\sigma_{23}}{\mu} &= (1 - \alpha) B_{3,2} - \alpha (x_3 B_{3,23} + B_{0,23}) \\ \frac{\sigma_{33}}{\mu} &= B_{3,3} - \alpha (x_3 B_{3,33} + B_{0,33})\end{aligned}\tag{6.57}$$

The displacement field is

$$\begin{aligned}u_1 &= -\frac{\alpha}{2} (x_3 B_{3,1} + B_{0,1}) \\ u_2 &= -\frac{\alpha}{2} (x_3 B_{3,2} + B_{0,2}) \\ u_3 &= \left(1 - \frac{\alpha}{2}\right) B_3 - \frac{\alpha}{2} (x_3 B_{3,3} + B_{0,3})\end{aligned}\tag{6.58}$$

At the surface $x_3 = 0$, the stress components are simply

$$\begin{aligned}\frac{\sigma_{13}}{\mu} &= (1 - \alpha) B_{3,1} - \alpha B_{0,13} \\ \frac{\sigma_{23}}{\mu} &= (1 - \alpha) B_{3,2} - \alpha B_{0,23} \\ \frac{\sigma_{33}}{\mu} &= B_{3,3} - \alpha B_{0,33}\end{aligned}\tag{6.59}$$

and the vertical displacement at the surface is

$$u_3 = \left(1 - \frac{\alpha}{2}\right) B_3 - \frac{\alpha}{2} B_{0,3}\tag{6.60}$$

Notice that the expressions $(1 - \alpha) B_{3,1} - \alpha B_{0,13}$ and $(1 - \alpha) B_{3,2} - \alpha B_{0,23}$ in eq. (6.59) are harmonic in Ω and vanish at the surface $\partial\Omega$ due to the vanishing shear stress boundary condition (6.56) on $\partial\Omega$. A harmonic field that vanishes at the domain boundary is zero identically in the whole domain and one obtains the relation

$$(1 - \alpha) B_3 - \alpha B_{0,3} = 0 \quad \text{in } \Omega.\tag{6.61}$$

Using Green's third identity and the Betti's method of integration [Love, 1927, Chapter 10], the elastic response to load and gravity at the surface $\partial\Omega$ can be written

$$\frac{\sigma_{33}}{\mu} - 2\alpha\Gamma u_3 = \alpha (B_{3,3} - \Gamma B_3) = -\frac{1}{2\pi\mu} \frac{x_3}{r^3} \quad (6.62)$$

where $r = (x_k x_k)^{1/2}$ is the distance from the point source (see Figure 6.1) and we have used the wavelength

$$\Gamma = \frac{\Delta\rho g}{2\mu\alpha} \quad (6.63)$$

The component B_3 of the Papkovitch potential satisfies the inhomogeneous ordinary differential equation

$$B_{3,3} - \Gamma B_3 = -\frac{1}{2\pi\mu\alpha} \frac{x_3}{r^3} \quad (6.64)$$

The homogeneous solution to eq. (6.64) is associated with the trivial solution (zero displacements) of a stress-free boundary condition. Using the method of variation of parameters, the particular solution to (6.64) is

$$B_3 = -\frac{e^{\Gamma x_3}}{2\pi\mu\alpha} \int_0^{x_3} \frac{t e^{-\Gamma t} dt}{(\rho^2 + t^2)^{3/2}} \quad (6.65)$$

where

$$\rho = (x_1^2 + x_2^2)^{1/2} \quad (6.66)$$

The definite integral in eq. (6.65) does not readily yield a closed-form expression. An approximation of the solution to (6.64) is attainable in various ways. One is to Taylor-expand the denominator in the integrand in the right-hand-side of eq. (6.65) and keep only the first two terms to obtain

$$B_3 \simeq -\frac{e^{\Gamma x_3}}{2\pi\mu\alpha} \int_0^{x_3} \frac{t e^{-\Gamma t} dt}{\rho(\rho^2 + \frac{3}{2}t^2)} \quad (6.67)$$

for which a solution can be expressed in a closed form. However, for the sake of interpretation, we are looking for an expression that can be separated into two parts, one part corresponding to the solution with no buoyancy effects ($\Gamma = 0$) and another part describing the contribution of gravity. Assuming that $\Gamma \ll 1$, we use a perturbation approach [Bender and Orszag, 1978] and write the successive approximations of B_3 as follows

$$B_{3,3}^{(n+1)} = -\frac{1}{2\pi\mu\alpha} \frac{x_3}{r^3} + \Gamma B_3^{(n)} \quad (6.68)$$

with $B_3^{(0)} = 0$, where superscript $f^{(n)}$ denotes the approximation n of function f . The first approximation is

$$B_3^{(1)} = \frac{1}{2\pi\mu\alpha} \int_0^{x_3} \frac{-t dt}{(\rho^2 + t^2)^{3/2}} = \frac{1}{2\pi\mu\alpha} \frac{1}{r} \quad (6.69)$$

which corresponds to the well-known case where buoyancy at the surface is ignored [Love, 1927, Mindlin, 1936a, Nemat-Nasser and Hori, 1999]. The second approximation is

$$\begin{aligned} B_3^{(2)} &= \frac{1}{2\pi\mu\alpha} \left[\int_0^{x_3} \frac{-t dt}{(\rho^2 + t^2)^{3/2}} + \Gamma \int_0^{x_3} \frac{dt}{(\rho^2 + t^2)^{1/2}} \right] \\ &= \frac{1}{2\pi\mu\alpha} \left[\frac{1}{r} + \Gamma \ln(x_3 + r) \right] \end{aligned} \quad (6.70)$$

and corresponds to our analytic approximation of the effect of gravity for the Boussinesq's problem; thereafter we use the approximation $B_3 \approx B_3^{(2)}$. Using eq. (6.61) we define

$$B_0^{(n)} = \frac{1 - \alpha}{\alpha} \int_0^{x_3} B_3^{(n)}(t) dt \quad (6.71)$$

and we obtain

$$B_0^{(2)} = \frac{1 - \alpha}{2\pi\mu\alpha^2} \left[\ln(x_3 + r) + \Gamma(x_3 \ln(x_3 + r) - r) \right] \quad (6.72)$$

Finally, plugging Eqs. (6.70) and (6.72) into eq. (6.58) and using the cylindrical coordinates we obtain the following approximation of the displacement field

$$\begin{aligned} u_r &= \frac{\rho}{4\pi\mu r} \left[\frac{x_3}{r^2} - \frac{1 - \alpha}{\alpha} \frac{1 - \Gamma r}{x_3 + r} - \Gamma \frac{x_3}{x_3 + r} \right] \\ u_\theta &= 0 \\ u_3 &= \frac{1}{4\pi\mu r} \left[\alpha^{-1} + \frac{x_3^2}{r^2} + \Gamma [\alpha^{-1} r \ln(x_3 + r) - x_3] \right] \end{aligned} \quad (6.73)$$

For comparison, the Green function for the Boussinesq problem, in the absence of gravity, can be found, e.g., in Love [1927], Okumura [1995], Nemat-Nasser and Hori [1999] or Soutas-Little [1999]

$$\begin{aligned} u_r &= \frac{\rho}{4\pi\mu r} \left[\frac{x_3}{r^2} - \frac{1 - \alpha}{\alpha} \frac{1}{r + x_3} \right] \\ u_\theta &= 0 \\ u_3 &= \frac{1}{4\pi\mu r} \left[\alpha^{-1} + \frac{x_3^2}{r^2} \right] \end{aligned} \quad (6.74)$$

Notice that eq. (6.73) simplifies to the classic solution (6.74) when $\Gamma = 0$, as expected.

A comparison between Fourier domain solution (eq. 6.29) and corresponding analytic solution using the space-domain Green function (eq. 6.73) is shown in Fig. 6.7. We compute the response to a point-source moment load \mathbf{m}_{23} applied at the surface $x_3 = 0$. We take into account a density contrast at the surface by setting $\Gamma = 10^{-2} \text{ m}^{-1}$. The corresponding displacement at a horizontal plane at a depth of 3 km is shown in Fig. 6.7a. The difference between the solution that includes a buoyancy effect and the one that ignores buoyancy is shown in Fig. 6.7b. The contribution of buoyancy to the total displacement field is less than 10% of the total signal. The vertical displacement contribution of buoyancy is of opposite polarity compared to the direction of vertical displacement due to the direct effect of the applied traction. The buoyancy effect is tempering the amplitude of vertical displacement and the opposite polarity of the gravity contribution is an expected behavior. We evaluate the contribution of gravity using our space-domain Green function (6.73). The residuals between the Fourier-domain and the space-domain solutions are shown in Fig. 6.7c and a comparison between the Fourier and space-domain solutions along profile C-C' is shown in Fig. 6.7d. The residuals between the two fields are within a few percents of the maximum value of the gravity contribution. Note a good agreement between the Fourier-domain and space-domain solutions to the generalized Boussinesq's problem.

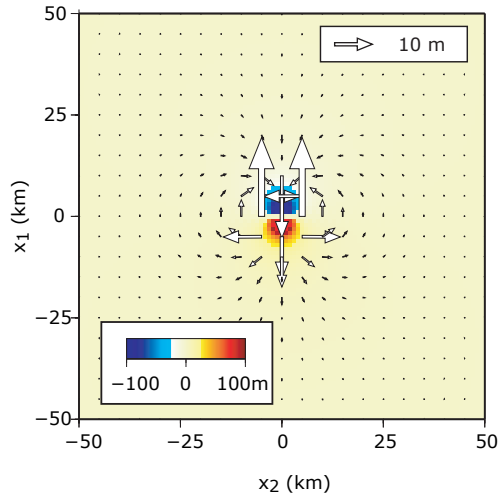
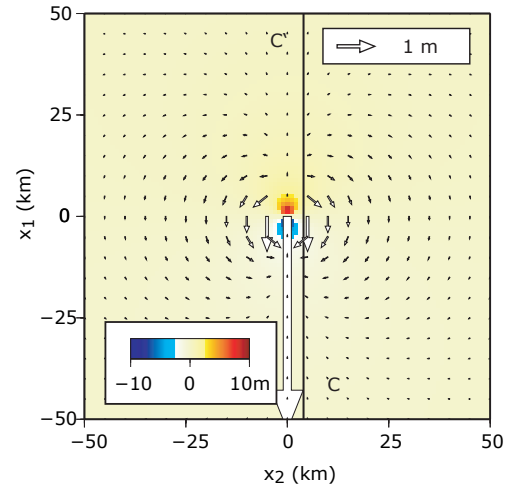
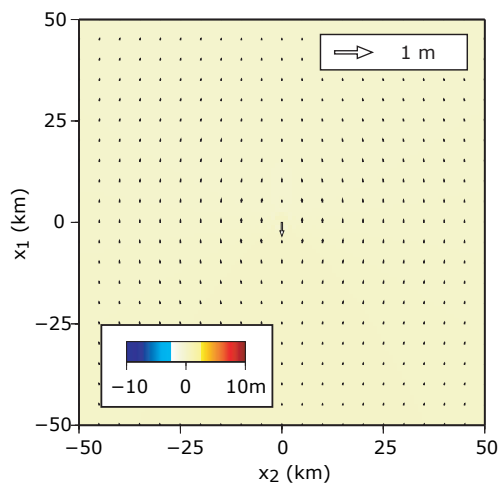
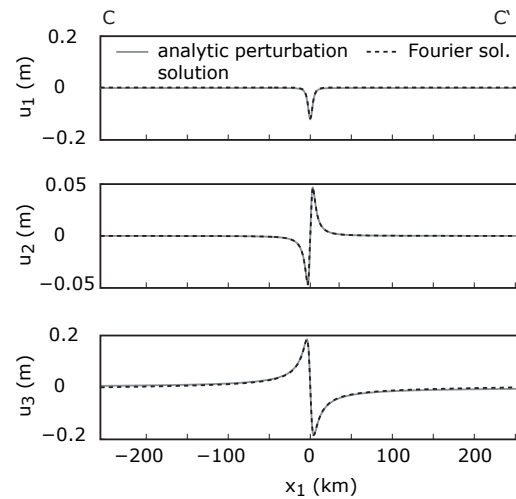
A. Full surface displacements**B. Buoyancy contribution****C. Residuals with the perturbation solution****D. Comparison with the perturbation solution**

Figure 6.7: Benchmark of the Fourier-domain solution including a buoyancy boundary condition. A) A moment \mathbf{m}_{13} is applied at the surface of the half space. B) The full surface displacement. Horizontal and vertical components of displacement are represented with arrows and colors, respectively (positive for uplift). C) The surface displacement due to the surface buoyancy, corresponding to $\Gamma = 10^{-2} \text{m}^{-1}$. Notice the reversal of the vertical displacements. D) The residuals between the Fourier-domain and the perturbation-method solutions, Eqs. (6.29) and (6.73), respectively.

Table 6.1: Commonly used two-dimensional Fourier transforms of three-dimensional functions. We denote $|\mathbf{k}| = (k_1^2 + k_2^2)^{1/2}$ and $r = (x_1^2 + x_2^2 + x_3^2)^{1/2}$.

$f(x_1, x_2, x_3)$	$\mathcal{F}[f(\mathbf{x})] = \hat{f}(k_1, k_2, x_3)$
$1/r$	$\frac{1}{ \mathbf{k} } e^{-2\pi \mathbf{k} x_3}$
$\ln(x_3 + r)$	$\frac{-1}{2\pi \mathbf{k} ^2} e^{-2\pi \mathbf{k} x_3}$
$x_3 \ln(x_3 + r) - r$	$\frac{1}{4\pi^2 \mathbf{k} ^3} e^{-2\pi \mathbf{k} x_3}$

Finally, we establish the formal relation between the perturbation solution (6.73) and the exact Fourier-domain solution (6.20), which we repeat here for convenience

$$\begin{aligned}
 \hat{u}_1(k_1, k_2, x_3) &= i\alpha\omega_1\beta B_3 [1 - \alpha^{-1} + \beta x_3] e^{-\beta x_3} \\
 \hat{u}_2(k_1, k_2, x_3) &= i\alpha\omega_2\beta B_3 [1 - \alpha^{-1} + \beta x_3] e^{-\beta x_3} \\
 \hat{u}_3(k_1, k_2, x_3) &= -\alpha\beta^2 B_3 [\alpha^{-1} + \beta x_3] e^{-\beta x_3} .
 \end{aligned} \tag{6.75}$$

Assuming small ratios of Γ/β , corresponding to a small wavelength limit, the constant

$$B_3 = \frac{-\hat{p}_3}{2\mu\alpha\beta^2(\beta + \Gamma)} \tag{6.76}$$

can be expanded in a Taylor series. Keeping the first two terms of the Taylor expansion we find

$$B_3 = \frac{-\hat{p}_3}{2\mu\alpha\beta^3} - \Gamma \frac{-\hat{p}_3}{2\mu\alpha\beta^4} + O\left(\frac{\Gamma^2}{\beta^2}\right) \tag{6.77}$$

Setting $p_3 = \delta(x_1)\delta(x_2)$, or simply $\hat{p}_3 = 1$, the first term corresponds to the classic Boussinesq's solution (6.74) and the second term gives rise to the perturbation contribution found in eq. (6.73).

To illustrate this statement, we consider the vertical component of displacement. Using the expansion (6.77) the vertical component of displacement in the Fourier domain becomes

$$\begin{aligned}
 \hat{u}_3 &= \frac{1}{2\mu\beta} [\alpha^{-1} + \beta x_3] e^{-\beta x_3} \\
 &\quad - \Gamma \frac{1}{2\mu\beta^2} [\alpha^{-1} + \beta x_3] e^{-\beta x_3}
 \end{aligned} \tag{6.78}$$

Upon inverse Fourier transforming with the pairs recalled in Table 6.6.2, we directly confirm that

$$\begin{aligned}
 u_3 &= \frac{1}{4\pi\mu r} \left[\alpha^{-1} + \frac{x_3^2}{r^2} \right] \\
 &\quad + \Gamma \frac{1}{4\pi\mu} \left[\alpha^{-1} \ln(x_3 + r) - \frac{x_3}{r} \right]
 \end{aligned} \tag{6.79}$$

is the perturbation solution (eq. 6.73). Equivalence between the remaining components of displacement can be demonstrated in a similar way.

6.7 Static deformation in a half-space due to surface traction using the Boussinesq-Papkovich-Neuber potential

In this appendix we present an alternative derivation of the Fourier domain solution for the so-called Boussinesq and Cerruti's problems. In Section 6.2 we used the Galerkin vector potential to derive the solution to the generalized problem of applied surface traction including the effect of a buoyancy restoring force at the surface of a semi-infinite elastic solid. Here, we use the Boussinesq-Papkovich-Neuber potential to derive the Fourier-domain solution to the Boussinesq and Cerruti's problems, ignoring the effect of gravity. We use this derivation to validate results of Section 6.2 in the special case where gravity is neglected (setting $\Gamma = 0$). We first derive the solution to the Boussinesq's problem and then to the Cerruti's problem.

6.7.1 The Boussinesq's problem

The Boussinesq's problem can be solved semi-analytically in the Fourier domain by making use of the Papkovitch-Neuber representation and Fourier transforming (6.54) in the horizontal direction. Using the Fourier transforms pair defined in (6.8), the transformed gradient operator becomes $\hat{\nabla} = (i\omega_1, i\omega_2, \frac{\partial}{\partial x_3})$. In Cartesian coordinates, each component of the vector potential is harmonic and it is sufficient to set $\mathbf{B} = B_3 \hat{\mathbf{e}}_3$. Hence, we have $\nabla^2 B_3 = \nabla^2 B_0 = 0$ and

$$\begin{aligned}\hat{B}_3(k_1, k_2, x_3) &= \beta b_3 e^{-\beta x_3} \\ \hat{B}_0(k_1, k_2, x_3) &= b_0 e^{-\beta x_3}\end{aligned}\tag{6.80}$$

where we have used

$$\beta = 2\pi (k_1^2 + k_2^2)^{1/2}.\tag{6.81}$$

We have discarded the positive exponentials to ensure a bounded solution in the far field. Before satisfying the surface boundary condition, we obtain the surface displacements

$$\begin{aligned}\hat{u}_1 &= -\alpha i\pi k_1 (b_0 + \beta b_3 x_3) e^{-\beta x_3} \\ \hat{u}_2 &= -\alpha i\pi k_2 (b_0 + \beta b_3 x_3) e^{-\beta x_3} \\ \hat{u}_3 &= +\beta \left[b_3 + \frac{\alpha}{2} (b_0 - b_3 + b_3 \beta x_3) \right] e^{-\beta x_3}\end{aligned}\tag{6.82}$$

At the surface, $x_3 = 0$, we have the shear stresses

$$\begin{aligned}\hat{\sigma}_{13} &= \mu i2\pi k_1 \beta [\alpha b_0 + (1 - \alpha)b_3] \\ \hat{\sigma}_{23} &= \mu i2\pi k_2 \beta [\alpha b_0 + (1 - \alpha)b_3]\end{aligned}\tag{6.83}$$

so the condition of vanishing of the shear stress at the surface is satisfied for

$$b_0 = (1 - \alpha^{-1})b_3\tag{6.84}$$

Respectively we obtain the displacement field

$$\begin{aligned}\hat{u}_1 &= -i\pi k_1 b_3 (\alpha - 1 + \alpha\beta x_3) e^{-\beta x_3} \\ \hat{u}_2 &= -i\pi k_2 b_3 (\alpha - 1 + \alpha\beta x_3) e^{-\beta x_3} \\ \hat{u}_3 &= +\frac{1}{2}\beta b_3 (1 + \alpha\beta x_3) e^{-\beta x_3}\end{aligned}\tag{6.85}$$

The surface normal stress, in the Fourier domain, is

$$\hat{\sigma}_{33} = -\mu\alpha\beta^2 b_3\tag{6.86}$$

so the Boussinesq problem is solved for

$$b_3 = -\frac{p_3}{\mu\alpha\beta^2}\tag{6.87}$$

where p_3 is the prescribed surface normal traction. Result (6.85) is the same as the one of eq. (6.20) obtained using the Galerkin biharmonic vector potential.

6.7.2 The Cerruti's problem

We start by considering the form of the solution corresponding to setting $B_2 = B_3 = 0$. The remaining non-zero harmonic scalars are thus

$$\begin{aligned}\hat{B}_0 &= b_0 e^{-\beta x_3} , \\ \hat{B}_1 &= \beta b_1 e^{-\beta x_3} .\end{aligned}\tag{6.88}$$

Making use of the Fourier transform identity,

$$\mathcal{F}[x f(x)] = \frac{i}{2\pi} \hat{f}'(k) ,\tag{6.89}$$

where the prime means differentiation with respect to the relevant wavenumber, we obtain the displacements

$$\begin{aligned}\hat{u}_1 &= \left[\left(\beta + \frac{\alpha}{2} \frac{\omega_1^2}{\beta} [1 - \beta x_3] \right) b_1 - \frac{\alpha}{2} i\omega_1 b_0 \right] e^{-\beta x_3} \\ \hat{u}_2 &= -\frac{\alpha}{2} i\omega_2 \left[i \frac{\omega_1}{\beta} (1 - \beta x_3) b_1 + b_0 \right] e^{-\beta x_3} \\ \hat{u}_3 &= -\frac{\alpha}{2} \left[i\omega_1 (-2 + \beta x_3) b_1 - \beta b_0 \right] e^{-\beta x_3}\end{aligned}\tag{6.90}$$

Using Hooke's law for a homogeneous solid, we obtain the surface shear stresses

$$\begin{aligned}\hat{\sigma}_{13} &= \mu [i\omega_1 \alpha \beta b_0 - (\beta^2 + 2\omega_1^2 \alpha) b_1] \\ \hat{\sigma}_{23} &= \mu i\omega_1 \alpha (b_0 \beta + i2\omega_1 b_1)\end{aligned}\tag{6.91}$$

The vanishing condition for σ_{23} at the surface gives

$$b_0 = -\frac{2\omega_1}{\beta} b_1\tag{6.92}$$

and the prescribed surface stress $p_1(k_1, k_2)$ gives

$$b_1 = -\frac{p_1}{\beta^2} \quad (6.93)$$

The remaining normal stress,

$$\hat{\sigma}_{33} = -(1 - \alpha)i\omega_1\beta b_1 = (1 - \alpha)\frac{i\omega_1 p_1}{\beta}, \quad (6.94)$$

is removed by applying the Boussinesq's solution (eq. 6.85) with the constant

$$b_3 = \frac{1 - \alpha}{\alpha} \frac{i\omega_1 p_1}{\mu\beta^3} \quad (6.95)$$

The solution to Cerruti's problem, arising from the application of the Papkovitch-Neuber representation, is then

$$\begin{aligned} \hat{u}_1 &= \left[\frac{b_1}{\beta} \left(\beta^2 - \frac{\alpha}{2} \omega_1^2 (1 + \beta x_3) \right) \right. \\ &\quad \left. - \frac{1}{2} i\omega_1 b_3 (\alpha - 1 + \alpha\beta x_3) \right] e^{-\beta x_3} \\ \hat{u}_2 &= \left[-\frac{\alpha b_1}{2\beta} \omega_1 \omega_2 (1 + \beta x_3) \right. \\ &\quad \left. - \frac{1}{2} i\omega_2 b_3 (\alpha - 1 + \alpha\beta x_3) \right] e^{-\beta x_3} \\ \hat{u}_3 &= \frac{\alpha\beta}{2} \left[-i\omega_1 b_1 + b_3 (\alpha^{-1} + \beta x_3) \right] e^{-\beta x_3} \end{aligned} \quad (6.96)$$

Formulation (6.96) is equivalent to eq. (6.26) obtained with the Galerkin vector potential.

Chapter 7

Towards a Unified Representation of Postseismic Mechanisms: Semi-Analytic Models of Fault Creep, Poroelastic Rebound and Power-Law Flow

Sylvain Barbot and Yuri Fialko

Abstract. We present a unified continuum mechanics representation of the mechanisms believed to be commonly involved in postseismic transients such as viscoelasticity, fault creep and poroelasticity. The time-dependent relaxation that follows an earthquake, or any other static stress perturbation, is considered in a framework of a generalized viscoelastoplastic rheology whereby some inelastic strain relaxes a physical quantity in the material. The relaxed quantity is the deviatoric stress in case of viscoelastic relaxation, the Coulomb stress in case of creep on a fault plane and the trace of the stress tensor in case of poroelastic rebound. In this framework, the instantaneous velocity field satisfies the linear inhomogeneous Navier's equation with sources parameterized as equivalent body forces and surface traction. We evaluate the velocity field using the gravitational elastostatic Green function in the Fourier domain [Barbot and Fialko, submitted, 2009b] and integrate the governing equations in the time domain using a predictor/corrector method. The accuracy of the proposed method is demonstrated by comparisons with finite element simulations of viscoelastic relaxation following strike-slip and dip-slip ruptures for linear and power-law rheologies. We also present comparisons with analytic solutions for afterslip driven by coseismic stress changes. Finally, we demonstrate that the proposed method can be used to model time-dependent poroelastic rebound by adopting a viscoelastic rheology with bulk viscosity and work hardening. The proposed method allows one to model postseismic transients that involve multiple mechanisms (afterslip, poroelastic rebound, ductile flow) with an account for the effects of gravity, non-linear rheologies and arbitrary spatial variations in inelastic properties of rocks (e.g., the effective viscosity, rate-and-state frictional parameters, poroelastic properties).

7.1 Introduction

Interpretations of the geodetic, seismologic, and geologic observations of deformation due to active faults require models that take into account complex fault geometries, spatially variable mechanical properties of the Earth’s crust and upper mantle, evolution of damage and friction, and rheology of rocks below the brittle-ductile transition [Tse and Rice, 1986, Scholz, 1988, 1998]. Studies of postseismic relaxation typically rely on models of fault afterslip [e.g., Perfettini and Avouac, 2004, 2007, Johnson et al., 2006, Freed et al., 2006, Hsu et al., 2006, Barbot et al., 2009a, Ergintav et al., 2009], viscoelastic relaxation [Pollitz et al., 2000, Freed and Bürgmann, 2004, Barbot et al., 2008b] and poroelastic rebound [Peltzer et al., 1998, Masterlark and Wang, 2002, Fialko, 2004b] to explain the observations. Existing semi-analytic models of time-dependent three-dimensional (3-D) viscoelastic deformation [Rundle, 1982, Pollitz, 1997, Smith and Sandwell, 2004, Johnson et al., 2009] are limited to linear constitutive laws. Fully numerical (e.g., finite element) methods may be sufficiently versatile to incorporate the essential physics of a ductile response [Freed and Bürgmann, 2004, Parsons, 2005, Freed, 2007, Pearse and Fialko, 2008], but often require elaborate and time-consuming discretization of a computational domain, especially for non-planar and branching faults, and assignment of spatially variable material properties to different parts of a computational mesh. Another challenge consists in simultaneous modeling of several (possibly interacting) mechanisms [Masterlark and Wang, 2002, Fialko, 2004b, Johnson et al., 2009]. For example, geodetic data from the 1992 Landers, CA earthquake were used to demonstrate the occurrence of a poroelastic rebound, a power-law viscoelastic flow in the upper mantle and afterslip on the down-dip extension of the main rupture [Peltzer et al., 1998, Freed and Bürgmann, 2004, Fialko, 2004b, Perfettini and Avouac, 2007]. Data from the 2002 Denali earthquake were also argued to be compatible with the occurrence of these three main mechanisms [e.g., Freed et al., 2006].

In this paper we introduce a computationally efficient 3-D semi-analytic technique that obviates the need for custom-built meshes but is sufficiently general to handle complex fault geometries and nonlinear rheologies. We develop a unified representation of the main mechanisms thought to participate in postseismic relaxation (see Figure 7.1). The model employs a generalized viscoelastic rheology that is compatible with linear and power-law viscous flow, poroelastic rebound and fault creep (afterslip). This framework allows one to construct fully coupled models that account for more than one mechanism of relaxation. Each mechanism contributes to some inelastic strain to relax a certain quantity in the viscoelastic body. The relaxed quantity is the deviatoric stress in case of viscoelastic relaxation, the Coulomb stress in case of fault creep and the trace of the stress tensor in the case of poroelastic rebound. The method is fast and easily parallelized to deal with large computational domains. For each above-mentioned mechanism, we present benchmarks and comparisons with analytic, semi-analytic or finite-element solutions.

This article is organized as follows. First we describe a general solution method to evalu-

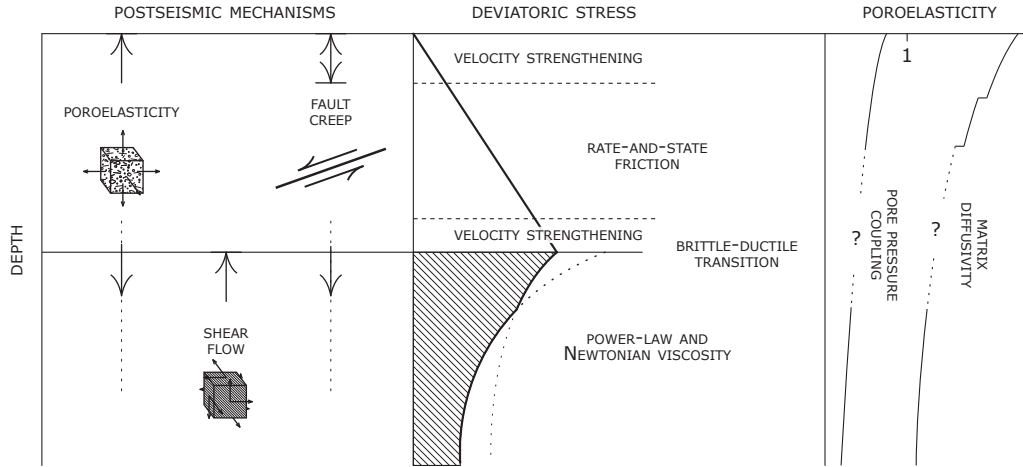


Figure 7.1: Sketch of inelastic properties of the lithosphere responsible for postseismic transients. Postseismic deformation may be due to a combination of poroelastic response, fault creep and viscous shear. The shear flow in the mantle and lower crust might be governed by a power-law viscosity for high stress and by a Newtonian viscosity at lower stress. Afterslip on fault roots is governed by a velocity-strengthening friction law. Poroelastic rebound can occur throughout the crust but likely decreases with increasing depth.

ate time series of viscoelastic relaxation. The approach is compatible with any nonlinear rheology provided the infinitesimal-strain approximation is applicable. We then consider the particular cases of three dominant mechanisms of postseismic relaxation. In Section 7.3 we consider viscoelastic deformation: We show some example calculations and benchmarks for Newtonian and power-law flow following strike-slip and dip-slip earthquakes, including the effects of gravity. In Section 7.4 we describe a viscoelastic rheology for fault creep with rate-strengthening friction. We benchmark our numerical solution against the analytic solution for a point source. In Section 7.5 and Appendix 7.7.1 we introduce the viscoelastic rheology equivalent to poroelasticity.

7.2 A general viscoelastic model

Our method of evaluating three-dimensional (3-D) time-dependent deformation due to earthquakes is based on a continuum representation of fault slip, viscous flow and change in pore fluid content. In this section, we describe the coupled equations that govern the postseismic deformation regardless of a particular relaxation mechanism and present a semi-analytic solution method to evaluate the time series of relaxation. The proposed approach can accommodate different types of relaxation mechanisms and various degrees of strain localization in a medium.

In a generalized viscoelastic body Ω , with elastic compliance tensor D_{ijkl} , the total strain-rate tensor $\dot{\epsilon}_{ij}$ may be presented as the sum of elastic (reversible) and inelastic contributions

$$\dot{\epsilon}_{ij} = \dot{\epsilon}_{ij}^e + \dot{\epsilon}_{ij}^i \quad (7.1)$$

where the dots represent time differentiation. In case of linear elasticity, the elastic strain-rate tensor can be written

$$\dot{\epsilon}_{ij}^e = D_{ijkl} \dot{\sigma}_{kl} \quad (7.2)$$

where σ_{ij} is the Cauchy stress [Malvern, 1969]. The plastic strain rate $\dot{\epsilon}_{ij}^i$, also referred to as eigenstrain rate, represents a relaxation process such as viscous flow, fault creep or poroelastic compaction. Any such source of time-dependent inelastic deformation contributes to a forcing term in strain space

$$\dot{\epsilon}_{ij}^i = \dot{\gamma} R_{ij} \quad (7.3)$$

where γ is the amplitude of inelastic strain and R_{ij} is a unitary and symmetric tensor representing the local direction of the inelastic strain-rate. The irreversible strain rate obeys a constitutive relationship or evolution law of the form

$$\dot{\gamma} = f(\sigma_{ij}, \gamma) \quad (7.4)$$

where σ_{ij} is the instantaneous Cauchy stress and γ is the cumulative amplitude of inelastic strain. The presence of parameter γ in the evolution law (7.4) represents the effects of work hardening (or softening). A particular form of operator f , which defines the material rheology, depends upon the relaxation mechanism. When no work hardening takes place the rheology $\dot{\gamma} = f(\sigma_{ij})$ is an algebraic equation. If the instantaneous inelastic strain rate depends on the history of deformation, then the rheology $\dot{\gamma} = f(\sigma_{ij}, \gamma)$ is a differential equation coupled to the equation for stress evolution. Poroelasticity, viscoelastic relaxation and fault creep can all be written in this general form.

Assuming infinitesimal strain, combining eq. (7.1), (7.2), and (7.3) and integrating, we obtain the general hereditary equation for stress evolution

$$\sigma_{ij}(t) = C_{ijkl} \epsilon_{kl}(t) - \int_0^t \dot{\gamma}(t') C_{ijkl} R_{kl}(t') dt' \quad (7.5)$$

where t' is a dummy variable of the time integration and C_{ijkl} is the elastic moduli tensor, such as $C_{ijmn} D_{klmn} = (\delta_{ik} \delta_{jl} + \delta_{il} \delta_{jk}) / 2$ [Nemat-Nasser and Hori, 1999]. One interpretation of eq. (7.5) is that in a viscoelastic material the stress is reduced by a history of inelastic relaxation. Notice that eq. (7.5) reduces to Hooke's law if no inelastic deformation occurs. The total strain ϵ_{ij} can simply be evaluated from the current displacement field

$$\begin{aligned} \epsilon_{ij}(t) &= \frac{1}{2} (\delta_{ik} \delta_{jl} + \delta_{il} \delta_{jk}) u_{k,l} \\ &= \frac{1}{2} (u_{i,j} + u_{j,i}) , \end{aligned} \quad (7.6)$$

where the latter depends on a history of deformation,

$$u_i(t) = u_i(0) + \int_0^t v_i(\tau) d\tau . \quad (7.7)$$

Similarly the rate of change of stress, $\dot{\sigma}_{ij} = C_{ijkl}\dot{\epsilon}_{kl}^e$ can be written using eq. (7.1)

$$\dot{\sigma}_{ij} = C_{ijkl}(\dot{\epsilon}_{kl} - \dot{\epsilon}_{kl}^i) \quad (7.8)$$

The inelastic contribution to the stress rate can be thought of as the instantaneous power density applied to body Ω by all internal processes, and as a forcing term in tensor space

$$\dot{m}_{ij} = C_{ijkl}\dot{\epsilon}_{kl}^i. \quad (7.9)$$

A time series of deformation at any point in Ω can be evaluated given a specific rheology (eq. 7.4). At all times, a displacement field must satisfy the condition of a vanishing surface traction

$$\int_{\partial\Omega} \sigma_{ij}(t) \hat{n}_j dA = 0 \quad (7.10)$$

The criterion (7.10) is satisfied by enforcing simultaneously a free surface boundary condition $\dot{\sigma}_{ij}\hat{n}_j = 0$ and the conservation of the rate of momentum $\dot{\sigma}_{ij,j} = 0$. Using (7.8) and (7.9) the free-surface boundary condition becomes

$$\dot{t}_i = C_{ijkl}\dot{\epsilon}_{kl}\hat{n}_j = \dot{m}_{ij}\hat{n}_j \quad (7.11)$$

where \hat{n}_i is the normal vector at the surface $\partial\Omega$. Eq. (7.11) indicates that a postseismic relaxation process contributes to some equivalent rate of surface traction \dot{t}_i if the corresponding eigenstrain-rate $\dot{\epsilon}_{ij}^i$ is non-zero at the surface $\partial\Omega$. Without loss of generality, the conservation of rate of momentum can be written

$$(C_{ijkl}\dot{\epsilon}_{kl})_{,j} + \dot{f}_i = 0 \quad (7.12)$$

which corresponds to the inhomogeneous Navier's equation in case of a homogeneous isotropic elastic solid and where we have defined the equivalent body-force rate

$$\dot{f}_i = -\dot{m}_{ij,j} \quad (7.13)$$

The mechanisms driving a post earthquake transient can be equivalently represented by the eigenstrain-rate (eq. 7.3), the power density (eq. 7.9) and the distribution of equivalent body force and surface traction rate (eqs. 7.13 and 7.11, respectively). One important aspect of the proposed generalized viscoelastic representation of postseismic mechanisms is that regardless of a particular form of the constitutive relation, including nonlinear rheologies, the instantaneous velocity field is a solution to a linear partial differential equation. The velocity field satisfies the inhomogeneous Navier's equation (7.12) with the inhomogeneous boundary condition (7.11) and the methods used to solve elasto-static problems can be also applied to nonlinear time-dependent deformation.

The instantaneous velocity field v_i can in general be obtained using the elastic Green function

$$v_i(x_i) = \int_{\Omega} G_{ij}(x_i, y_i) \dot{f}_j(y_i) dV + \int_{\partial\Omega} G_{ij}(x_i, y_i) \dot{t}_j(y_i) dA \quad (7.14)$$

Interestingly, the details of the geometry and the elastic structure of the viscoelastic body are all captured by the specific form of the elastic Green function G_{ij} . The Green function for a semi-infinite solid is given, e.g., by Love [1927] and Nemat-Nasser and Hori [1999]. The Green function accounting for the effects of gravity is given by, e.g., Pollitz [1997] for a layered spherical body and by Wang et al. [2003] for a layered half space. Because the equivalent body forces can be distributed over a large volume the convolution (7.14) can be computationally expensive. This difficulty is alleviated by using a Fourier-domain elastic Green function [Barbot et al., 2009a,b]. In this paper we describe a general method for simulation of time-dependent postseismic deformation that employs the Fourier-domain elastic Green function of Barbot and Fialko [submitted, 2009b]. The Green function of Barbot and Fialko [submitted, 2009b] correspond to a semi-infinite elastic medium with uniform elastic properties, uniform density and a gravitational restoring force at the surface of the half space. The practical efficiency of the proposed procedure is made possible by the fast Fourier-domain Green function described in the companion paper [Barbot and Fialko, submitted, 2009b], but is in general compatible with any third-party Green function.

A time series of transient deformation following a stress perturbation can be obtained as follows. From a given level of stress at time t , we evaluate the eigenstrain rate due to a particular mechanism with eq. (7.3). We evaluate the corresponding power density (7.9) and compute the associated distribution of surface traction and internal forces with eq. (7.11) and (7.13) respectively. We then solve eq. (7.12) for a velocity field. We obtain the new displacement, stress, and cumulative strain fields for time $t + dt$ by integrating the corresponding quantities in the time domain using an explicit method with a predictor/corrector scheme [Abramowitz and Stegun, 1972]. In particular, the stress-tensor field at $t + dt$ is obtained from eq. (7.5). We repeat these steps until the simulation of the viscoelastic relaxation over a specified time interval is complete.

The method is sufficiently general to deal with most mechanisms believed to be relevant to postseismic deformation such as Newtonian and non-Newtonian viscous flow, rate-strengthening fault creep and poroelasticity. One important advantage of the proposed method is an ability to handle arbitrary spatial variations in inelastic properties. Variations in inelastic properties are accounted for by changing the spatial distribution of the corresponding equivalent internal forces and surface traction. A current limitation is the assumption of uniform elastic properties. Note that variations in elastic properties (e.g., the Lamé parameters λ and G) may be readily accounted for if the respective elastic Green function is known.

7.3 Nonlinear viscoelastic flow

The lower-crust and upper-mantle rocks exhibit a ductile behavior [Nur and Mavko, 1974, Weertman and Weertman, 1975, Brace and Kohlstedt, 1980, Karato and Wu, 1993, Savage, 2000] that is often invoked to explain large-wavelength post-earthquake deformation tran-

sients [Reilinger, 1986, Pollitz et al., 2000, Johnson et al., 2009]. Geodetic [Freed and Bürgmann, 2004] and laboratory [Karato et al., 1986, Kirby and Kronenberg, 1987, Kohlstedt et al., 1995] observations indicate a stress-dependent mantle viscosity, and suggest that a power-law rheology of the form

$$\dot{\epsilon}_{ij}^i = \dot{\gamma}_0 \left(\frac{\tau}{G} \right)^{n-1} \frac{1}{G} \sigma'_{ij} \quad (7.15)$$

may be applicable to the lower crust and upper mantle, where $1 \leq n < 5$ is a power exponent, G is the shear modulus,

$$\sigma'_{ij} = \sigma_{ij} - \delta_{ij} \frac{\sigma_{kk}}{3} \quad (7.16)$$

is the deviatoric stress tensor and

$$\tau = \left(\frac{1}{2} \sigma'_{kl} \sigma'_{kl} \right)^{1/2} \quad (7.17)$$

is the norm of the deviatoric stress. The strain-rate direction is purely deviatoric

$$R_{ij} = \frac{\sigma'_{ij}}{\tau} \quad (7.18)$$

and the amplitude of strain rate is

$$\dot{\gamma} = \dot{\gamma}_0 \left(\frac{\tau}{G} \right)^n \quad (7.19)$$

where $\dot{\gamma}_0$ is a reference strain rate. Power-law creep is a thermally activated process [Karato, 2008] and $\dot{\gamma}_0$ is assumed to increase as a function of depth (Figure 7.1). For a power exponent greater than unity the effective viscosity

$$\eta = \frac{1}{\dot{\gamma}_0} G^n \tau^{1-n} \quad (7.20)$$

is lower at the initial stage of a transient deformation when stress is higher. The ductile flow is not limited by a yield surface and for a constant stress condition the effective viscosity η increases exponentially with decreasing temperature [e.g., Karato, 2008]. A time scale of the postseismic transient due to viscoelastic relaxation

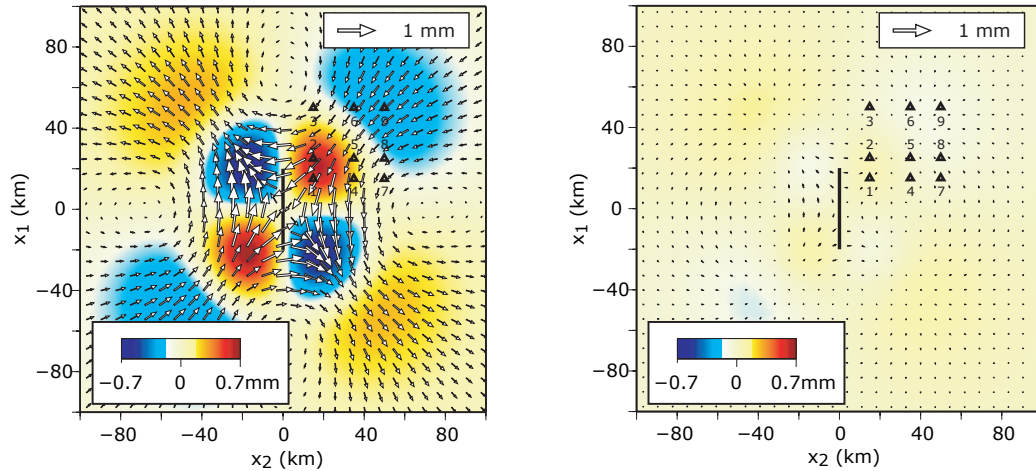
$$t_m = \frac{\eta}{G} = \frac{1}{\dot{\gamma}_0} \left(\frac{G}{\tau} \right)^{n-1} \quad (7.21)$$

is stress dependent and is shorter near the onset than at the later stages of the transient. Some ductile flow is thought to occur below the seismogenic zone (at depths greater than 15 to 50 km). The confinement of the flow below an essentially elastic plate obviates any equivalent surface traction ($\dot{t}_i = 0$) and the deformation can be represented by a distribution of internal forces only.

7.3.1 Numerical examples and benchmarks

We test our formulation of the power-law viscoelastic relaxation by considering stress perturbations due to strike-slip and dip-slip faults. In these test models, the fault slip occurs in an elastic plate that rests on a power-law viscoelastic half space. Here, we ignore the effects of

A. Strike-Slip Fault. Power-law viscosity ($n=3.5$). Displacements and residuals with finite-element calculations



B. Comparison between finite-element and Fourier-domain postseismic time series

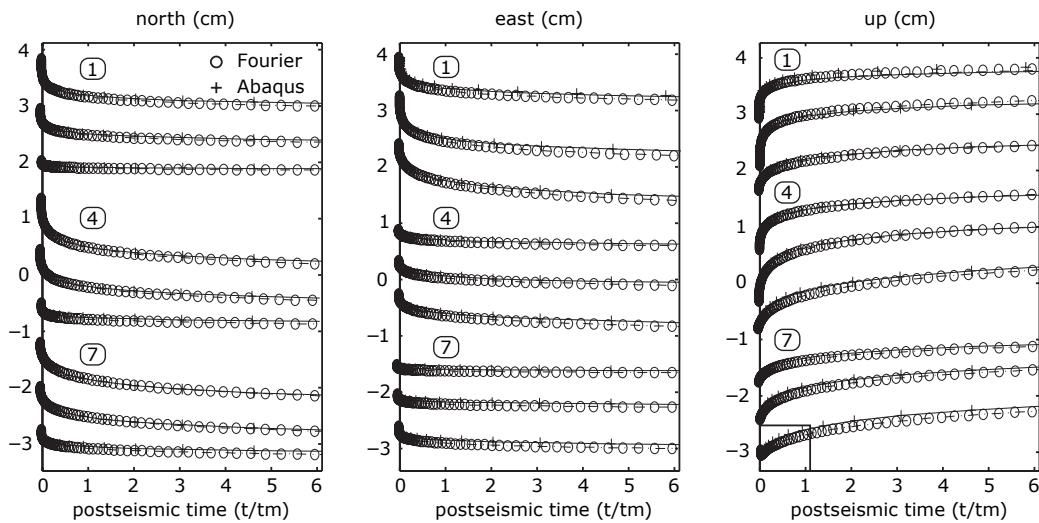
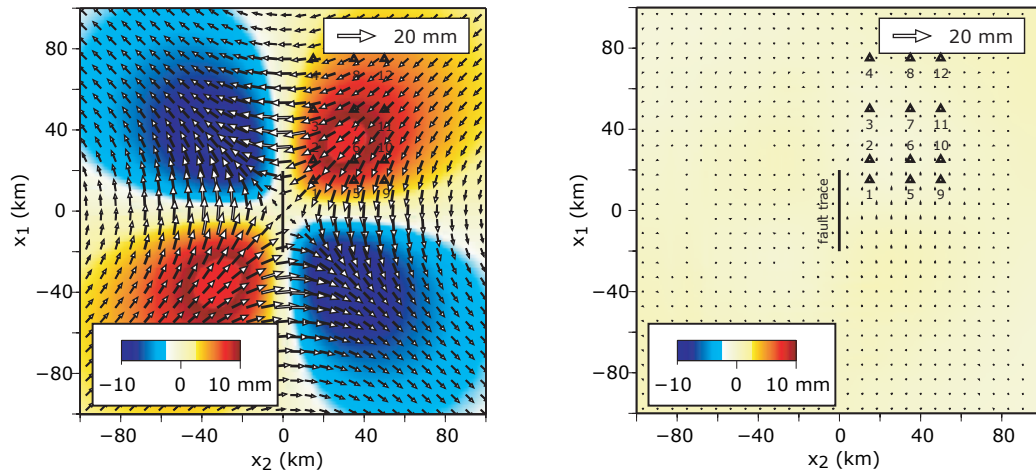


Figure 7.2: Calculated time series of surface displacements due to a stress perturbation in an elastic plate over a nonlinear viscoelastic half space. A) A map view of postseismic surface displacements at the early stage of the transient. The right panel shows the difference between our solution and finite element solution computed using Abaqus. B) Time series of surface displacements for an array of points numbered from 1 to 9 in the corresponding map. Time is scaled by $t_m = \dot{\gamma}_0^{-1} s^{1-n} L^{n-1}$.

A. Strike-Slip. Linear viscoelasticity. Surface displacements and residuals with finite-element calculations



B. Comparison between finite-element and Fourier-domain postseismic time series

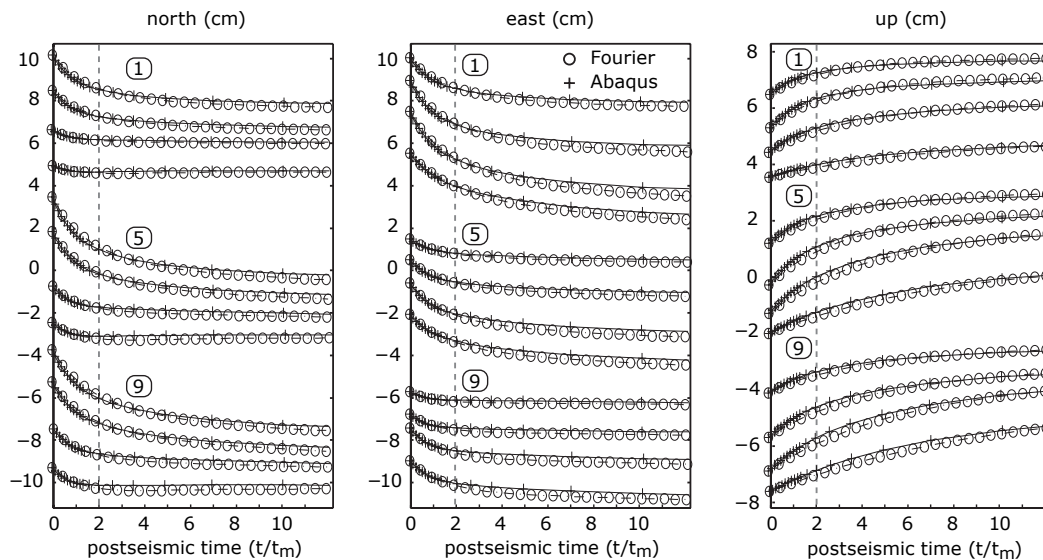


Figure 7.3: Calculated time series of surface displacements for a model shown in Figure 7.2, but for a linear viscoelastic layer (eq. (7.15) with $n = 1$). A) Left panel: A snapshot of postseismic surface displacements at time $t = 2t_m$. Right panel: difference between our solution and finite element benchmark. B) Time series of surface displacements for an array of points numbered from 1 to 9 in the corresponding map.

gravity (but see Barbot and Fialko [submitted, 2009b]). We compare the predictions of post-seismic displacement from our semi-analytic method with those computed using a finite-element approach. We use the software Abaqus to perform the finite-element calculations.

We start with the case of a strike-slip fault in an elastic brittle layer. We assume uniform and isotropic elastic properties of a Poisson’s solid (the Lamé parameters $\lambda = G$ and Poisson’s ratio $\nu = 1/4$). The brittle-ductile transition is assumed at a depth of 30 km. Below 30 km, we assume a power-law rheology with a power exponent $n = 3.5$ (see eq. 7.15). The fault slips 1 m uniformly from the surface to a depth of 10 km and is 40 km long. We perform a simulation of the viscoelastic postseismic relaxation using our generalized viscoelastic formulation. We perform the computation on a 512^3 grid with a uniform sampling of $\Delta x_i = 0.8$ km. We use an explicit method to integrate velocity and stress. We choose the adaptive time step corresponding to a tenth of the characteristic time of eq. (7.21) and march forward in time using a second-order accurate predictor/corrector method. A snapshot of the post-earthquake surface displacement at the early stage of the transient is shown in Fig. 7.2a. For the respective finite-element calculation we use a 628332-node mesh with a sampling size ranging from 0.8 km near the fault to 11.5 km in the far field. We pin the boundary of the mesh 300 km away from the fault center. A map view of the surface residuals between the simulations using our formulation and the ones using the finite element method is shown in the right panel of Fig. 7.2a. The maximum discrepancy between the two solutions is less than 10%. The simulated time series of surface displacement at the “observation” points numbered from 1 to 9 are shown in Fig. 7.2b. We choose to non-dimensionalize time using the reference time

$$t_m = \frac{1}{\dot{\gamma}_0} \left(\frac{s}{L} \right)^{1-n} \quad (7.22)$$

where $\dot{\gamma}_0$ and n are the reference strain rate and power exponent of the power law, respectively, and s/L is the strain drop on the fault. We use $s = 1$ m and $L = 10$ km. The time series exhibit the typical higher velocities near the onset of the postseismic transient with rapidly decaying velocities at later times. There is an excellent agreement between results obtained from the finite element calculations and from our method. A distinct behavior of the power-law relaxation is a change in polarity of vertical displacements at the surface of the half space. The change in polarity can be seen in the time series of vertical displacement of far-field point number 9 in Fig. 7.2b.

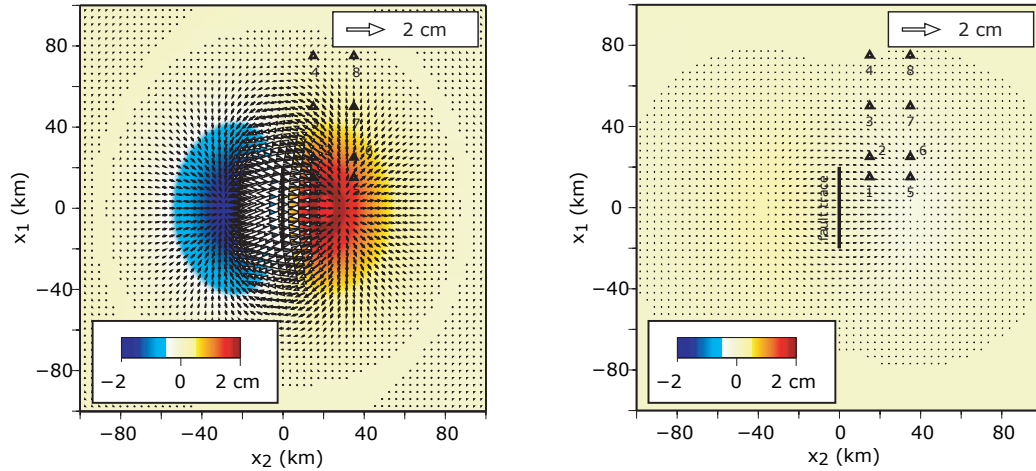
We perform a similar simulation using a Newtonian viscosity, i.e. with $n = 1$ in eq. (7.15), all other parameters being the same. A snapshot of the surface displacement due to the viscoelastic relaxation is shown in the left panel of Fig. 7.3a, corresponding to a time $t = 2t_m$ after the coseismic stress perturbation. The residuals with the finite-element forward model at this time is shown in the left panel of Fig. 7.3a. There is an excellent agreement between the finite-element and the semi-analytic results: The maximum residuals are less than 5 per cent of the expected signal. In Fig. 7.3b we compare the simulated time series of viscoelastic relaxation at points num-

bered from 1 to 12 in Fig. 7.3a. The distribution of observation points covers the near- and far fields of the fault. The finite-element and Fourier time-series differ less than 5 per cent throughout a time interval spanning 12 characteristic relaxation times. The non-Newtonian and linear viscosity models converge to the same fully relaxed solution. Before the relaxation is complete, the postseismic displacements due to a linear and a power-law rheology have the same polarity in the near field. In the far field, however, the power-law relaxation due to slip of a vertical strike-slip fault has an opposite polarity compared to the Maxwell rheology. Our simulations indicate that the far-field postseismic displacements due to a power-law mantle flow (with $n > 1$) change polarity early in the postseismic transient.

We proceed with the evaluation of postseismic relaxation due to dip-slip faulting. For simplicity, we consider the case of a vertical dip-slip fault with the same geometry as in the strike-slip models. Although the geometry is similar, changes in the slip rake lead to very different stress changes in the lithosphere. We consider first the case of a nonlinear viscoelastic upper mantle governed by the power-law rheology of eq. (7.15) with $n = 2$. A snapshot of the surface displacement early in the postseismic transient is shown in Figure 7.4a. The vertical postseismic displacement has the same polarity as the coseismic displacement. Horizontal postseismic displacements, however, are opposite to the coseismic ones. We performed the same simulation using Abaqus and the residuals are shown in the right panel of Figure 7.4a. The time series of surface displacements at points numbered from 1 to 8 in the maps are shown in Figure 7.4b. There is an excellent agreement between the semi-analytic and the finite-element results. The time series reveal two striking features. First, the initial postseismic velocities are much higher than at later times, as most visible for points 1 and 2. Second, a change in polarity occurs at far-field locations. This change is most conspicuous for point 6 in the East-West direction. A subtle change of polarity can be misleadingly interpreted as a delayed postseismic transient (e.g., the see vertical displacement of point 8).

Finally, we consider the case of a dip-slip fault in an elastic plate over a Maxwellian viscoelastic half space. The geometry of the fault and the brittle-ductile transition is the same as in previous models. The prediction from our semi-analytic model and the residuals with finite-element calculations at postseismic time $t = t_m/2$ are shown in Figure 7.5a. The time series of postseismic displacements at surface positions in the near and far field are shown in Figure 7.5b. There is an excellent agreement between the semi-analytic and the fully numerical solutions. Notice a change of polarity of far-field points 8 and 12. The overall patterns of surface displacement due to Newtonian and power-law viscosity are similar, in contrast to the case of a strike-slip fault. An overall agreement between the finite-element and the semi-analytic calculations suggests that our formulation is robust and can be used to model postseismic deformation due to nonlinear viscoelasticity.

A. Dip-Slip Fault. Powerlaw viscoelasticity ($n=2$). Displacements and residuals with finite-element calculations



B. Comparison between finite-element and Fourier-domain postseismic time series

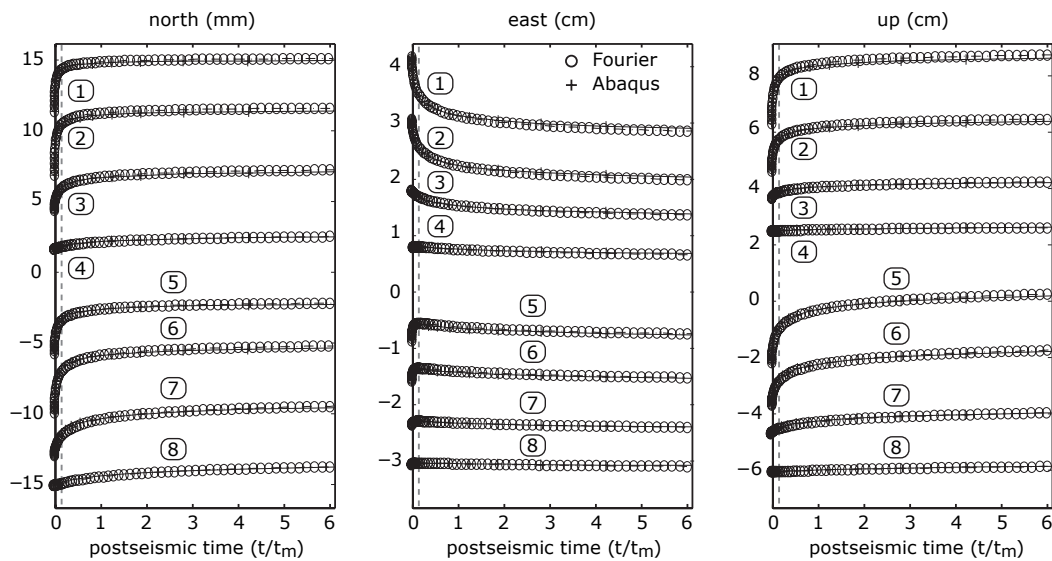
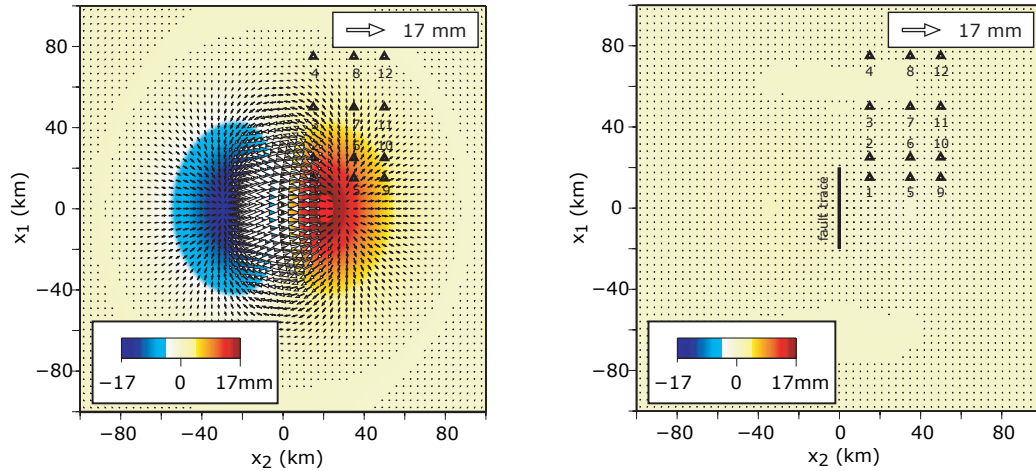


Figure 7.4: Calculated time series of surface displacements due to a vertical dip-slip fault in an elastic plate overriding a nonlinear viscoelastic half space. The model geometry is the same as in Fig. 7.2. The postseismic flow is governed by a power-law rheology with stress exponent $n = 2$. A) Left panel: A map view of postseismic surface displacements after ten months. Right panel: difference between our solution and a finite element benchmark. B) Time series of surface displacements for an array of points numbered from 1 to 8 in the corresponding map.

A. Dip-Slip Fault. Linear viscoelasticity. Surface displacements and residuals with finite-element calculations



B. Comparison between finite-element and Fourier-domain postseismic time series

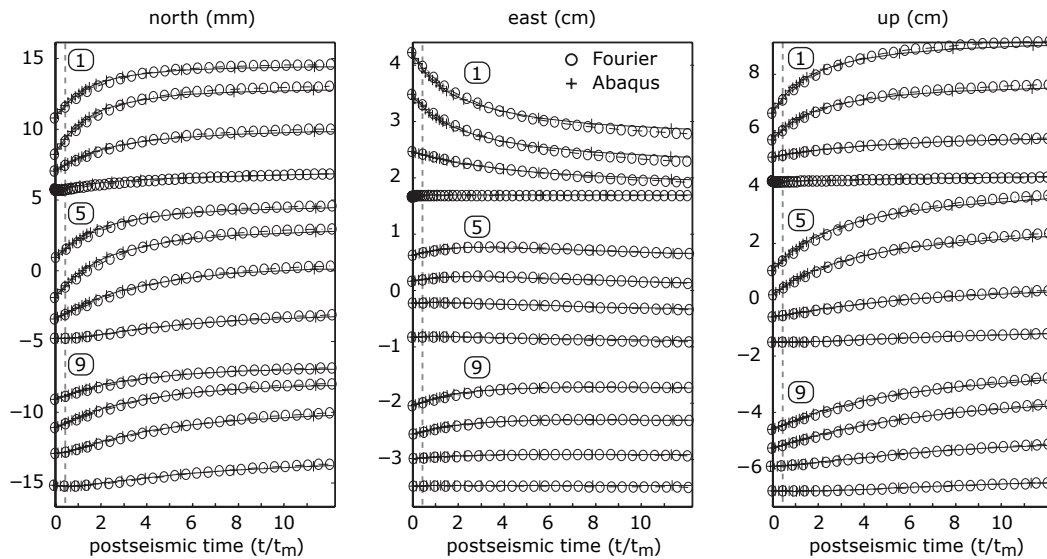


Figure 7.5: Calculated time series of surface displacement following the rupture of a vertical dip-slip fault in an elastic plate over a linear viscoelastic layer. The geometry is the same as in Fig. 7.2. The postseismic flow is governed by a linear viscoelastic rheology (eq. (7.15) with $n = 1$). A) Left panel: A snapshot of postseismic surface displacements at time $t = 0.5 t_m$. Right panel: difference between our solution and a finite element benchmark. B) Time series of surface displacements for an array of points numbered from 1 to 9 in the corresponding map.

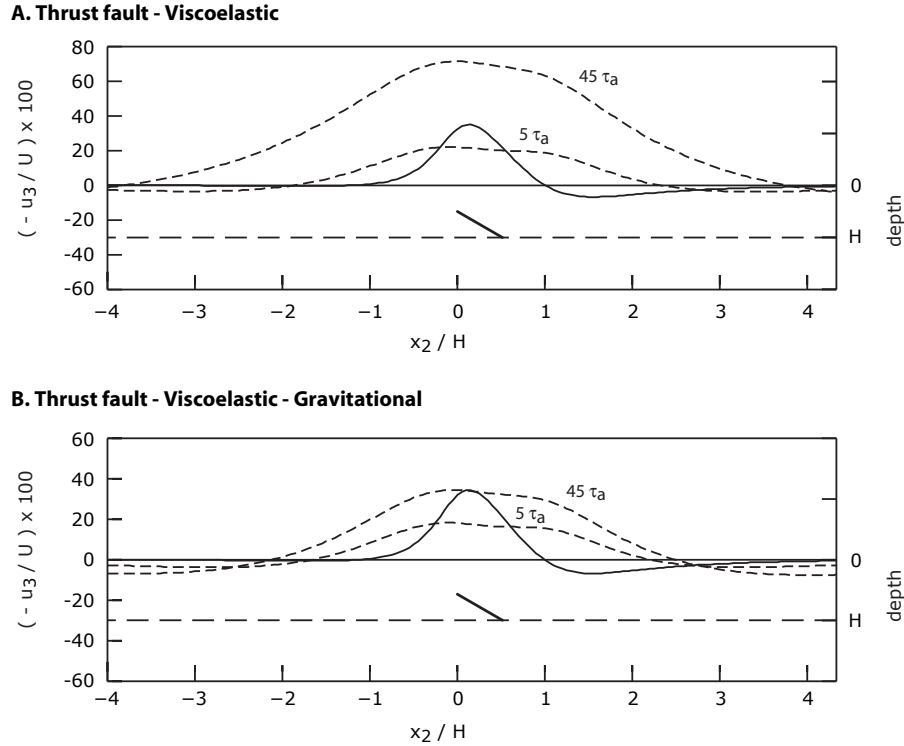


Figure 7.6: Effect of gravity on the postseismic displacement due to a thrust fault. The brittle-ductile transition occurs at depth H . The fault is $20H/3$ long in the strike direction, H wide in the dip direction and U is the magnitude of dip-slip. A) Viscoelastic relaxation but no gravitational restoring force. The surface displacement after 5 and 45 relaxation times τ_a due to a linear viscous relaxation in the half space below depth H . B) The surface displacement after 5 and 45 relaxation times when the density contrast at the surface is accounted for.

7.3.2 Effect of gravity

We include gravity in our model as the former affects surface deformation in case of viscoelastic relaxation. The principal effect of gravity is to reduce the amplitude of large-wavelength vertical deformation at late stages of viscoelastic relaxation [Pollitz et al., 2000, Freed et al., 2007]. To validate our approach, we reproduce the viscoelastic relaxation benchmarks of [Rundle, 1982, Figures 6 and 7] and [Pollitz, 1997, Figure 3]. The model includes a thrust fault in an elastic plate overlying a Newtonian viscoelastic half space with uniform elastic properties. Poisson's ratio $\nu = 1/4$ is constant in the entire half space. The brittle-ductile transition occurs at depth H . We assume a uniform density $\rho = 3300\text{kg/m}^3$ in the half space. The models of Rundle [1982] and Pollitz [1997] differs slightly in that they have an additional small density contrast at the brittle-ductile transition. The fault dips 30° , is $20H/3$ long in the strike direction and H wide in the dip direction and U is the amplitude of slip. The magnitude of the gravitational restoring

force is controlled by the wavenumber [Barbot and Fialko, submitted, 2009b]

$$\Gamma = (1 - \nu) \frac{\Delta\rho g}{G} \quad (7.23)$$

where $\Delta\rho$ is the density contrast at the surface (i.e., between rock and air) and g is the acceleration of gravity. The critical wavenumber (7.23) is associated with the dimensionless number $\Gamma H = 2.475 \cdot 10^{-2}$. Figure 7.6a shows the simulated across-fault profiles of co- and postseismic vertical displacements corresponding to the case of no gravity. The postseismic vertical displacement after 45 relaxation times, close to the full relaxation, has higher amplitude and larger wavelength than the vertical displacement after 5 relaxation times. Notice a few areas, for example between $x_2 = -4H$ and $x_2 = -2H$, that exhibit a change of polarity in the course of the postseismic transient. Such a change of polarity is an expected feature of the postseismic transient following a thrust fault, as shown Rundle [1982] and Pollitz [1997]. Our results indicate that it is also characteristic in the case of dip-slip faults, in general, for both linear and power-law rheologies (see Figures 7.4 and 7.5). The corresponding simulations which include the effect of gravity are shown in Figure 7.6b. The early postseismic displacement profile after 5 relaxation times is less affected by the gravitational restoring force. At later times, close to full relaxation, the vertical displacement is reduced by about a factor of two compared to the non-gravitational solution. The effect of buoyancy is more pronounced at later times of the postseismic transient when surface displacements have a larger wavelength. Results in Figure 7.6 compare well to the simulations of Rundle [1982] and Pollitz [1997] despite our neglect of a density contrast at the brittle-ductile transition. The deep density contrast has a much smaller effect on the patterns of surface displacements due to the smaller density contrast and the smaller wavelength of deformation at the brittle-ductile transition (due to proximity to the fault). Our calculations confirm the conclusions of Rundle [1982] and Pollitz [1997] regarding the importance of gravity for postseismic displacements during late stages of viscoelastic relaxation.

7.4 Fault creep

Fault creep, or stable sliding on a fault plane, is thought to be an important component of the earthquake cycle [e.g., Tse and Rice, 1986]. Afterslip has been widely documented following large earthquakes in various tectonic environments including subduction zones [Hsu et al., 2006] and transform faults [Bürgmann et al., 2002, Freed et al., 2006, Johnson et al., 2006, Barbot et al., 2009a]. Recent studies show that afterslip can be the dominant mechanism responsible for the postseismic transient [Freed, 2007, Barbot et al., 2008b] but it can also occur in combination with other mechanisms [Fialko, 2004a, Freed et al., 2006, Johnson et al., 2009]. Laboratory experiments and modeling of geodetic data indicate that afterslip may be governed by the rate- and state-dependent friction [Marone et al., 1991, Marone, 1998, Kohlstedt et al., 1995, Perfettini and Avouac, 2007, Barbot et al., 2009a]. In this section, we describe a continuum representation

of rate-strengthening fault creep. We use the formulation of Barbot et al. [2009a] that generalizes the classic rate-and-state friction [Dieterich, 1979, 1992] to allow for vanishing slip rates [Rice et al., 2001].

Fault creep can be viewed as a localized visco-elastoplastic deformation. The onset of sliding, or fault failure, is defined by the Coulomb yield stress [Byerlee, 1978],

$$\tau_c = \tau - \mu \sigma \quad (7.24)$$

where τ is the amplitude of shear traction in the direction of sliding, σ is the effective normal stress (positive for compression) accounting for the pore pressure contribution and μ is the coefficient of friction. A fault remains locked for strictly negative Coulomb stress $\tau_c < 0$. In this case continued loading causes deformation off of the fault [Heap et al., 2009]. When shear stress is high enough, $\tau_c = 0$, the fault fails and the subsequent slip evolution is described by a rate-strengthening friction rheology. Assuming small Coulomb stress before a stress perturbation, an assumption discussed in detail in [Barbot et al., 2009a], the slip rate is controlled by the local stress drop $\Delta\tau$ according to the constitutive law

$$\dot{s} = 2 \dot{s}_0 \sinh \frac{\Delta\tau}{a \sigma} \quad (7.25)$$

where \dot{s}_0 is a reference slip rate controlling the time scale of slip transients and $a \sigma$ is a parameter constraining the effective stress and the degree of nonlinearity in the afterslip evolution. Formulation (7.25) ignores the effect of a state variable evolution. Notice that \dot{s} is always positive, as eq. (7.25) describes the slip rate and not the slip direction.

In order to simulate fault creep in three dimensions, one needs to describe the geometry of the slip system. The change of traction t_i resolved on a fault surface S can be decomposed into normal and shear components,

$$t_i = \sigma_{ij} \hat{n}_j = t_k \hat{n}_k \hat{n}_i + \Delta\tau_i \quad (7.26)$$

where \hat{n}_i is the unit vector normal to the fault surface and $\Delta\tau_i$ is the shear component of the traction exerted on the fault such that

$$\Delta\tau = (\Delta\tau_k \Delta\tau_k)^{1/2} \quad (7.27)$$

Noting the Burger vector of the dislocation $s_i = s \hat{s}_i$, we assume that the slip-rate vector is colinear with the direction of shear traction evaluated on the fault patch,

$$\dot{s}_i = \dot{s} \Delta\hat{\tau}_i \quad (7.28)$$

and the instantaneous inelastic strain-rate direction is [e.g., Nemat-Nasser, 2004, Karato, 2008]

$$R_{ij} = \frac{1}{2} (\Delta\hat{\tau}_i \hat{n}_j + \hat{n}_i \Delta\hat{\tau}_j) \quad (7.29)$$

In the continuum representation of fault creep, the slip rate \dot{s} is associated with the inelastic strain rate

$$\dot{\gamma} = \dot{s} H_S(x_i) \quad (7.30)$$

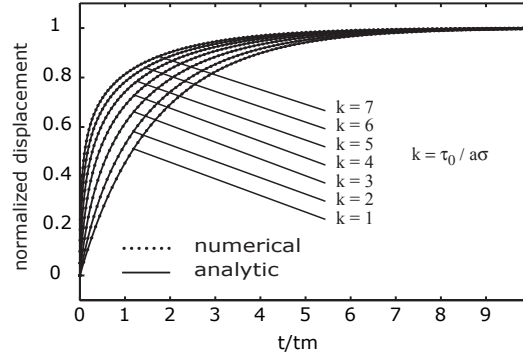


Figure 7.7: Benchmark for fault creep on an elementary fault segment (point source) governed by a rate-strengthening rheology. The Coulomb stress is perturbed homogeneously in the computational domain at time $t = 0$ with an amplitude τ_0 . The response of the fault as predicted by our numerical model and by the analytic solution to a spring-slider model are compared for various values of the initial stress perturbation.

where H_S , in dimensions of length^{-1} , is unity or zero according to whether its argument is or is not a point of the fault surface S . Fault representation using generalized functions is further discussed by Backus and Mulcahy [1976b] and Barbot et al. [2009a]. In this formulation the rake of afterslip is governed by the local stress direction and slip is constrained to occur on a predefined fault plane described by its position and orientation \hat{n}_i . Using eqs. (7.29) and (7.30) the inelastic strain rate due to fault creep can be written $\dot{\epsilon}_{ij}^i = \dot{\gamma} R_{ij}$, mathematically analogous to other deformation mechanisms, so that our solution method described in Section 7.2 also applies in case of afterslip.

7.4.1 Analytic benchmark

The response of a rate-strengthening point-source fault patch to a stress perturbation is described by Barbot et al. [2009a]. The slip impulse response to a stress drop $\Delta\tau_0$ is,

$$s(t) = \frac{\Delta\tau_0}{G^*} \left(1 - \frac{2}{k} \coth^{-1} \left(e^{t/t_0} \coth \frac{k}{2} \right) \right), \quad (7.31)$$

where G^* is the effective stiffness of the fault patch, the time scale of slip evolution is

$$t_0 = \frac{1}{2} \frac{a \sigma}{\dot{\sigma} G^*}, \quad (7.32)$$

and the degree of nonlinearity of slip evolution is controlled by the dimensionless ratio

$$k = \frac{\Delta\tau_0}{a \sigma}. \quad (7.33)$$

We compare the predictions of afterslip for a point source using our generalized viscoelastic representation and the analytic solution (7.31). We consider the case of an elementary dislocation

subjected to a stress drop $\Delta\tau_0$. We simulate the response of fault patches with frictional properties varying from $a\sigma = \Delta\tau_0/7$ to $a\sigma = \Delta\tau_0$. Figure 7.7 shows a comparison between the numerical and analytic solutions. The numerical profiles represent postseismic displacements at the surface scaled by their maximum amplitude. We perform this comparison to remove a potential numerical bias due to the Fourier-domain elastic Green function. Note an excellent agreement between analytic and numerical solutions for a wide range of stress perturbations (Figure 7.7).

7.5 Poroelastic rebound

The Earth's crust is a heterogeneous material that is composed of solid and fluid phases (e.g., porous rocks and pore fluids). The occurrence of a large earthquake alters the pore pressure in the crust. The induced stress change can create significant pore pressure gradients that may be relaxed by the movement of fluids if the host rocks are sufficiently permeable. The coupling between the pore-fluid diffusion and the effective stress introduces a time dependence into the response of the solid matrix [Biot, 1941, Rice and Cleary, 1976, Rudnicki, 1985, Wang, 2000, Coussy, 2004]. Fluids are usually assumed to be pervasive in the Earth's crust, so the poroelastic rebound is a likely physical mechanism contributing to the postseismic deformation. Peltzer et al. [1998] and Fialko [2004b] suggested that pore pressure readjustment could explain surface deformation following the 1992 Mw 7.3 Landers earthquake and Jonsson et al. [2003] documented fluid pressure changes associated with postseismic deformation due to the 2000 south Iceland earthquakes. Models of poroelastic rebound are usually limited to simulations of surface displacements at drained condition [e.g., Fialko, 2004b, Barbot et al., 2008b], which corresponds to a full relaxation. In this section we demonstrate an equivalence between the equations of poroelasticity and the generalized viscoelasticity. This will allow us to evaluate the time-dependent poroelastic rebound using the framework developed in Section 7.2.

Using a formal decomposition of the strain rate tensor (eq. 7.1), we postulate that the inelastic strain involved in a poroelastic rebound is purely isotropic,

$$\dot{\epsilon}_{ij}^i = \dot{\gamma} \frac{1}{3} \delta_{ij} , \quad (7.34)$$

i.e., the direction of relaxation in strain space is constant (cf. eq. 7.4)

$$R_{ij} = \frac{1}{3} \delta_{ij} \quad (7.35)$$

The poroelastic rebound thus can be viewed as an example of bulk viscosity. The amplitude of inelastic strain γ corresponds to the effective change in fluid content in the representative volume element (see eq. 7.55 in Appendix 7.7). In case of isotropic elastic properties, the amplitude of inelastic strain γ obeys the diffusive evolution law

$$\dot{\gamma} = D \left[(1 - \beta) \gamma - \beta \frac{\sigma}{\kappa_u} \right]_{,jj} \quad (7.36)$$

where κ_u is the undrained bulk modulus, D is the diffusivity in units of $\text{length}^2 \times \text{time}^{-1}$, $0 \leq \beta \leq 1$ is a non-dimensional parameter indicating the degree of coupling between the porous matrix and the pore space and

$$\sigma = \frac{\sigma_{kk}}{3} \quad (7.37)$$

is the isotropic stress, positive for extension. The total macroscopic stress change σ is a forcing term resulting from the coupling between matrix strain and fluid pressure. Equation (7.36) is associated with the surface boundary condition

$$\gamma = \frac{\beta}{1 - \beta \kappa_u} \sigma, \quad \text{at } x_3 = 0, t > 0 \quad (7.38)$$

Notice that eq. (7.36) is of the form $\dot{\gamma} = f(\sigma_{ij}, \gamma)$, the general evolution law of a viscoelastic process. In its simplest, isotropic form, the poroelastic deformation requires only two additional parameters, compared to linear elasticity, to describe the postseismic time-dependent deformation. The first parameter β is a non-dimensional coupling coefficient indicating what portion of the initial isotropic stress will eventually be relaxed. The second parameter is the diffusivity D which controls the timescale of the relaxation. Appendix 7.7 gives relations between β , D and other commonly used poroelastic parameters.

As fluid flow can take place in the entire crust, including near the surface, the equivalent-body-force representation of the poroelastic rebound seeks a proper distribution of internal forces and surface traction per unit time. The power density, using eqs. (7.9) and (7.34), becomes

$$\dot{m}_{ij} = \kappa_u \dot{\gamma} \delta_{ij}, \quad (7.39)$$

and we obtain the corresponding internal torque distribution per unit time

$$\dot{f}_i = -\kappa_u \dot{\gamma}_{,i}, \quad (7.40)$$

associated with the surface-traction rate

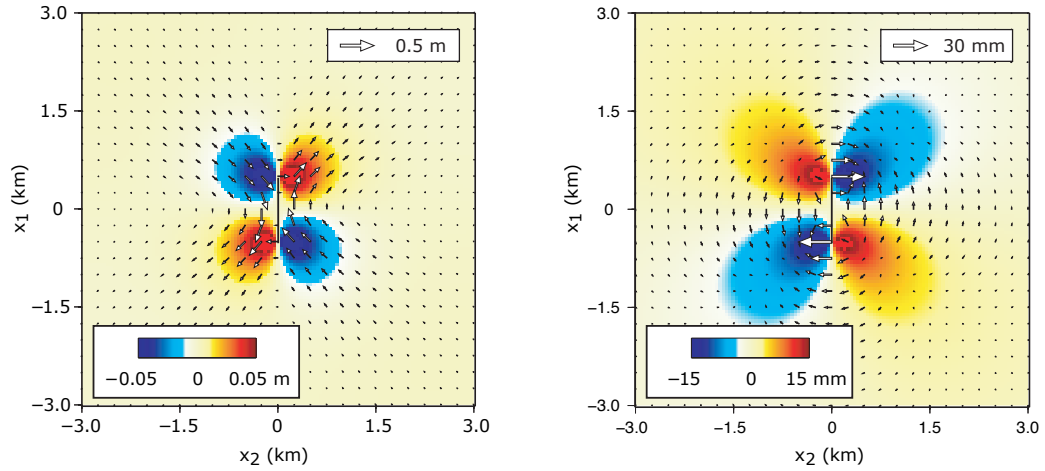
$$\dot{t}_i = -\kappa_u \dot{\gamma} \delta_{i3}, \quad \text{at } x_3 = 0. \quad (7.41)$$

The instantaneous solid matrix velocity field can be obtained using eq. (7.14) with the forcing terms and traction boundary condition of eqs. (7.40) and (7.41), respectively.

7.5.1 Methods and benchmarks

One complication of poroelastic models compared to treatment of power-law viscoelasticity, for example, is the evaluation of the evolution law. The presence of a Laplacian operator in the evolution law (7.36) makes an effective viscosity wavelength dependent. One simple way to evaluate the rate of fluid content is to use a finite-difference approximation. The finite difference method allows one to tackle heterogeneous properties and in particular to account for vertical variations in fluid diffusivity D and matrix/pore coupling β . One important limitation, however,

A. Strike-slip fault surface displacement and full poroelastic rebound (drained - undrained solutions)



B. Residuals with finite-difference and Fourier time-integration methods at full relaxation (drained condition)

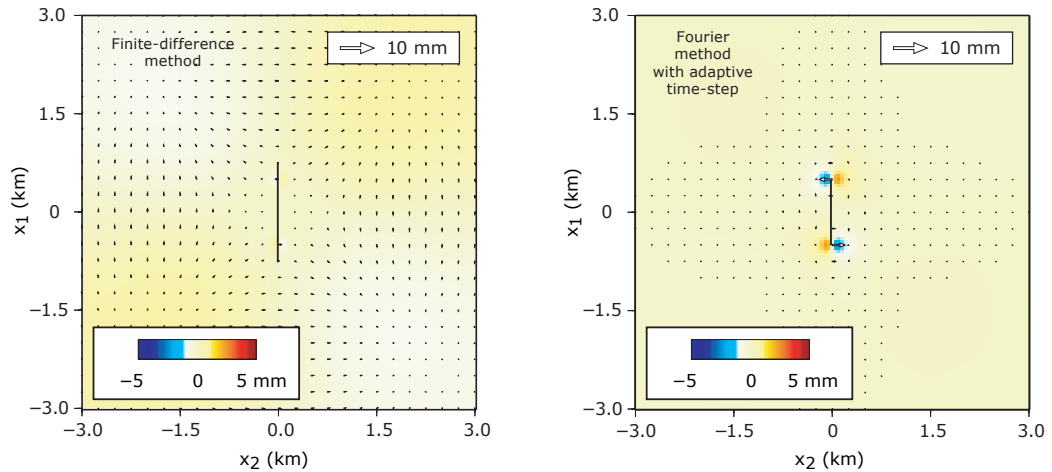


Figure 7.8: Benchmark for time series of surface displacement due to a stress perturbation in a homogeneous poroelastic half space. A strike-slip fault -with a uniform slip of 1 m along a vertical plane 1 km long extending from the surface to a depth of 1 km- changes the pressure in the surrounding rocks. A fraction β of the pressure change is relaxed by pore-fluid diffusion. The coseismic surface displacement due to the fault slip is shown in A (left panel). B) Comparison between fully time-dependent calculations and the analytic solution for the case of full relaxation (drained condition).

is the conditional stability of the finite difference integration method. The maximum time step of numerical integration is [Press et al., 1992]

$$\Delta t_{\max} = \frac{\Delta x^2}{2\tilde{D}} \quad (7.42)$$

where Δx is the grid sampling size and the product $\tilde{D} = (1 - \beta)D$ is taken to be the largest value in the computational domain. As the characteristic length scale of a problem is often a multiple of the sampling size, the finite-difference method often requires 50 to 100 computational steps to simulate a time interval of one characteristic relaxation-time. The full poroelastic rebound is approached after several characteristic times so the finite-difference method amounts to a significant computational burden. Another approach to evaluate the rate of fluid content $\dot{\gamma}$ at a time t_n is to perform the time integration in the Fourier domain. After Fourier transforming eq. (7.36) and assuming that the forcing term $\sigma(h)$ is in fact constant over a small time interval $[t_n, t_n + h]$, an approximation of the rate of fluid content is

$$\dot{\hat{\gamma}}(t_n + h) = -\tilde{D}\omega^2 e^{-\tilde{D}\omega^2 h} \left[\hat{\gamma}(t_n) - \frac{\beta}{1 - \beta} \frac{\hat{\sigma}(t_n)}{\kappa_u} \right] \quad (7.43)$$

where $\omega = 2\pi(k_1^2 + k_2^2 + k_3^2)^{1/2}$ is the radial wavenumber and the hats denote the Fourier transform of the corresponding variables. If the assumption of a constant forcing term is satisfied then eq. (7.43) is an exact solution to the fluid diffusion partial differential equation (7.36). Our quadrature method of the diffusion equation coupled to the Navier's equation is as follows: For a given time step Δt , we evaluate analytically the fluid velocity at time $t_n + \Delta t/2$ in the Fourier domain using eq. (7.43). We then integrate the change in fluid content using leapfrog in the space domain

$$\gamma(t_n + \Delta t) = \gamma(t_n) + \dot{\gamma}(t_n + \Delta t/2) \Delta t \quad (7.44)$$

Naturally, the fluid velocity is also used to evaluate the coupled elastic deformation. The Fourier method of integration is unconditionally stable and small steps are required for accuracy only to update the forcing term. We use adaptive time steps to optimize a tradeoff between accuracy and duration of the simulations: the initial time increment is a fraction of Δt_{\max} and every subsequent increments are increased by 5 per cent of the previous value. We also use a corrector-predictor approach to march forward in time. One possible disadvantage of using the proposed Fourier/leapfrog integration method is the constraint of uniform poroelastic properties. A Fourier integration method of the diffusion equation compatible with vertical variations in poroelastic properties is possible, for example using the exponential time integration method [Cox and Matthews, 2002], but it is not considered in this paper.

We test our viscoelastic formulation of the poroelastic equations with a simulation of the time-dependent poroelastic rebound following a strike-slip event. We first evaluate the full rebound using the difference between drained and undrained conditions. We then simulate the complete time series of a poroelastic rebound and compare the fully-relaxed numerical solution

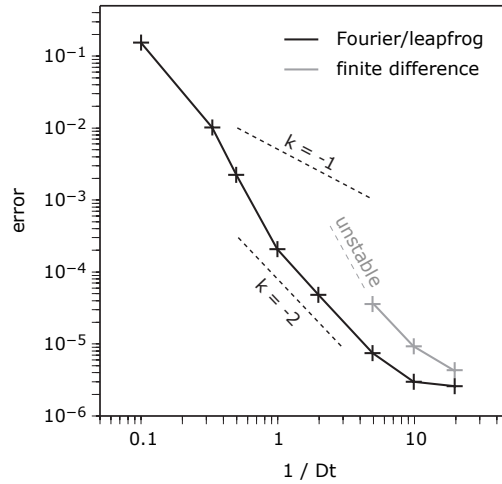


Figure 7.9: Efficiency diagram of the Fourier/leapfrog (black profile) and the finite difference (gray profile) integration schemes. The $k = -1$ and $k = -2$ slopes indicate the expected error reduction of second and third-order integration methods, respectively. The span of possible time steps is limited for the finite difference method due to a conditional stability condition.

to the static “drained-undrained” solution. The stress perturbation that is relaxed by poroelastic bulk viscosity in the crust is due to a strike-slip fault with a uniform slip of 1 m that extends from the surface to a depth of 1 km. We choose a Lamé parameter $\lambda_u = 1.5G$, where G is the shear modulus, and the coupling coefficient $\beta = 0.3$. The corresponding drained parameter is $\lambda_d = 0.85G$. We choose the diffusivity $D = 10^{-2} \text{ m}^2/\text{s}$. The characteristic length scale is the depth of the fault $W = 1 \text{ km}$ which is associated with the diffusion time scale $t_m = W^2/2D = 1.6 \text{ yr}$. Our simulation spans a time interval of $17 t_m$, presumably enough to reach full relaxation. Figure 7.8a (left panel) shows the initial displacement field at the surface due to the right-lateral strike-slip fault. The corresponding postseismic displacement after complete pore pressure readjustment is shown in the right panel of Figure 7.8a. We run two simulations; a first using the finite difference method with a constant time step of $\Delta t = \Delta t_{\text{max}}/5$ and another using the “Fourier-leapfrog” method with adaptive time steps. The residuals between the finite-difference and “drained-undrained” solutions at full rebound is shown in Fig. 7.8b (left panel). The residuals are characterized by long wavelengths which illustrates the well-known difficulty of resolving long wavelengths with a finite difference scheme for parabolic equations [Press et al., 1992]. The residuals associated with the Fourier-leapfrog method are shown in right panel of Fig. 7.8b and correspond to the last of the 130 steps required to reach full rebound. The long wavelength displacement is much better resolved.

Finally, we assess the accuracy of our proposed methods of time integration. Figure 7.9 shows the efficiency diagram for the Fourier/leapfrog and the finite difference methods. We compute the L_2 norm of the error taken at time $t = 10 t_{\text{max}}$ for various constant time-step

sizes. The error is the norm of the difference between a given solution and a reference one which was obtained with an extremely small time step. Figure 7.9 shows a cumulative error that reduces approximately quadratically with the step size for both methods. This large accuracy improvement with step size reduction indicates that the Fourier/leapfrog and the finite difference methods, when associated with a predictor-corrector approach, is third-order convergent. For a given reduced time step, the Fourier/leapfrog solutions are always about an order of magnitude more accurate than the finite difference counter part. The efficiency diagram 7.9 shows a range of possible time steps for the Fourier/leapfrog method covering about three orders of magnitude. The better accuracy of the Fourier/leapfrog method of integration along with the possibility of including adaptive time steps and a predictor/corrector scheme makes it much preferable over the finite-difference method in problems for which both schemes are applicable.

7.6 Conclusions

We introduced a unified representation of the main mechanisms believed to be involved in postseismic transients. We showed that fault creep, pore fluid diffusion and viscous flow can all be formalized within a framework of a generalized viscoelastic rheology whereby some inelastic strain relaxes a physical quantity in the lithosphere. Afterslip relaxes the Coulomb stress on a fault plane while viscoelastic flow acts to reduce the deviatoric stress in the substrate below the brittle-ductile transition. A poroelastic rebound is governed by a bulk viscous rheology with work hardening and its effect is to reduce the pressure in the solid. The proposed unified representation allows us to employ the same solution method to model postseismic relaxation involving such diverse mechanisms, including nonlinear rheologies and coupling between different mechanisms.

Our approach to model postseismic relaxation is to identify the power density that represents the effect of all driving mechanisms. The power density is associated with a distribution of internal forces and surface traction and the instantaneous velocity field is solution to the inhomogeneous Navier's equation. The technique can handle nonlinear rheologies because in this framework the instantaneous velocity satisfies a linear partial differential equation and all the strategies to solve elastostatic problems are directly applicable. We solve for a velocity field semi-analytically using the Fourier-domain Green function described in the companion paper [Barbot and Fialko, submitted, 2009b]. In general other Green functions (e.g., derived for different boundary conditions, geometry or material elastic properties) can be used in conjunction with our method. The Green function of Barbot and Fialko [submitted, 2009b] corresponds to a uniform elastic half space with a buoyancy boundary condition at the surface.

We applied the method to model nonlinear viscoelastic relaxation, stress-driven afterslip, and poroelastic rebound. We compared our simulations to results of finite element calculations for the cases of a Newtonian viscosity and a power-law rheology (with a stress power exponent of $n = 3.5$ and $n = 2$ for strike-slip and dip-slip faults, respectively). For all scenarios considered we

find an excellent agreement between our semi-analytic solutions and the fully numerical results. We show that if the ductile flow is governed by a power-law rheology the transient deformation exhibits higher rates of deformation near the onset of the postseismic period. The onset of the power-law viscoelastic relaxation following slip on a strike-slip fault is also characterized by a change of polarity of vertical displacements in the far field. The effect of gravity can be substantial at late stages of viscoelastic relaxation because of large wavelength vertical displacements. We also showed a good agreement between our semi-analytic models of stress-driven fault creep and analytic solutions. Finally, we described the effect of pore fluid diffusion in a representative volume element in terms of an effective bulk viscous rheology whereby pressure is relaxed by changes in volumetric inelastic strain. We showed the equivalence between our bulk viscosity formulation and the classic theory of poroelasticity. In the bulk viscosity formulation of poroelasticity the inelastic strain corresponds to an effective change in pore fluid content and obeys an inhomogeneous parabolic differential equation. We propose two solution methods to evaluate the instantaneous strain rate due to pore pressure diffusion. We successfully benchmarked our time-dependent simulations of poroelastic rebound against fully-relaxed solutions.

Our unified representation of postseismic mechanisms allows the simulation of sophisticated models of postseismic relaxation that incorporate realistic aspects of faulting including complex fault geometry, localization of deformation, gravitational effects and realistic variations of inelastic properties. Our semi-analytic approach simplifies the treatment of nonlinear rheologies such as power-law creep and rate-strengthening friction and enables the joint occurrence of multiple mechanisms in a self-consistent manner.

Acknowledgments

We thank Robert C. Viesca for stimulating discussions about the theory of poroelasticity. The numerical codes used in this paper are available at <http://sylvain.barbot.free.fr/crust/>. This Chapter, in full, has been submitted for publication of the material as it may appear in *Geophysical Journal International*. Barbot, Sylvain; Fialko, Y.. The dissertation author was the primary investigator and author of this paper.

7.7 Continuum Theory of Poroelastic Compaction

In this appendix, we show that the poroelastic rebound problem, which consists in describing the pore fluid diffusion and the coupled elastic deformation following an initial stress or strain perturbation, can be written as a generalized viscoelastic relaxation whereby some inelastic strain accumulates to relax a physical quantity in the material. In a poroelastic composite, the relaxed quantity is the isotropic stress as opposed to, for example, the deviatoric stress in a Newtonian viscoelastic body. In this framework, poroelasticity is an example of macroscopic

bulk viscosity. The appendix is organized as follows. First, we present the basic equations of linear poroelasticity [Bredehoeft, 1967, Rice and Cleary, 1976, Rudnicki, 1985, Kumpel, 1991] and how they come about from constitutive relations and conservation laws. Next, we show that the constitutive and governing equations of poroelasticity can be written using two end-member representations. The classic formulation uses the pore pressure as dynamic variable and the elastic moduli for drained condition as model parameters. Our alternate approach uses the perturbation of fluid density in the pore volume as dynamic variable and the elastic moduli for the undrained condition to parameterize the pore fluid flow and the associated elastic deformation. The latter approach is convenient to model initial-condition problems where the pore fluid flow is driven by a sudden stress perturbation of the ambient crust. The proposed formulation is compatible with a general viscoelastic behavior of the crust and allows the modeling of the complete time series of a poroelastic rebound.

7.7.1 The Classic Theory of Poroelasticity

The coupled partial differential equations governing the diffusion of pore pressure and the solid matrix compaction can be obtained from two constitutive relations and two conservation laws. The constitutive equations are the stress-strain relationship, an equivalent to Hooke's law augmented with an additional dynamic variable, and the linearized equation of state for the fluid density. The conservation laws are the conservation of mass for the fluid and the conservation of momentum for the solid-fluid composite. In the sequel we will adopt the nomenclature of Kumpel [1991] and Wang [2000].

In a poroelastic composite, a linearized equation of state relates the relative change in fluid content [Wang, 2000]

$$\zeta = \frac{m_f - m_{f_0}}{\rho_0}, \quad (7.45)$$

where $m_f - m_{f_0}$ denotes the increment of fluid mass per unit rock volume and ρ_0 is a reference density of the pore fluid, to the given pore pressure and confining stress as follows [Biot, 1941, Rice and Cleary, 1976, Kumpel, 1991]

$$\zeta = \frac{\alpha}{\kappa_d} \left(p/B + \frac{\sigma_{kk}}{3} \right) \quad (7.46)$$

where B is the Skempton coefficient, κ_d is the bulk modulus of the composite for drained condition and α is the dimensionless coefficient of effective stress. The pore pressure p is positive for compression and the confining stress in the solid matrix $\sigma = \sigma_{kk}/3$ is positive for extension. The stress-strain relation for the composite material is described by the generalized Hooke's law which is extended for poroelastic composite materials

$$\sigma_{ij} = 2G \frac{\nu_d}{1 - 2\nu_d} \epsilon_{kk} \delta_{ij} + 2G \epsilon_{ij} - \alpha p \delta_{ij} \quad (7.47)$$

where G is the shear modulus, ν_d is the Poisson's ratio for drained condition and the $\epsilon_{ij} = (u_{i,j} + u_{j,i})/2$ are the macroscopic strain components. In particular, summing diagonal terms in

eq. (7.47), one has

$$\sigma = \kappa_d \epsilon_{kk} - \alpha p \quad (7.48)$$

For vanishing pore pressure ($p = 0$), one obtains a form of Hooke's law where the drained elastic moduli appear as model parameters.

The fluid diffusion law is obtained from the conservation of mass, $\dot{m}_f + \rho_0 q_{k,k} = 0$, with a Darcy flow law $q_i = -x p_{,i}$ for the flux q_i , giving rise to

$$\frac{\partial}{\partial t} \left(\frac{m_f - m_{f_0}}{\rho_0} \right) = x p_{,kk} \quad (7.49)$$

where x is the Darcy conductivity in units of $\text{length}^3 \times \text{time} \times \text{mass}^{-1}$. The Darcy conductivity, also referred to as the mobility, is the ratio of the rock permeability to the fluid viscosity $x = k/\mu_f$. (The permeability has the units $k \sim \text{length}^2$ and the pore fluid viscosity $\mu_f \sim \text{mass} \times \text{length}^{-1} \times \text{time}^{-1}$.) Some more complicated expressions of the pore fluid flow can include the effect of water head [e.g., Bredehoeft, 1967] and/or anisotropic diffusivity [Singh et al., 2007]. Combination of constitutive relations (7.46) and (7.47) with the flow law (7.49) together with the conservation of momentum equation $\sigma_{ij,j} = 0$ gives rise to a set of coupled governing equations that describes the evolution of the macroscopic displacement u_i and the pore pressure p of an isotropic and homogeneous porous medium. The coupled governing equations are [e.g., Kumpel, 1991]

$$G \left(\frac{1}{1 - 2\nu_d} u_{k,ki} + u_{i,kk} \right) = \alpha p_{,i} \quad (7.50)$$

$$Q^{-1} \dot{p} = x p_{,kk} - \alpha \dot{u}_{k,k} \quad (7.51)$$

where Q^{-1} is a compressibility. The parabolic equation (7.51) is subjected to the surface boundary condition $p = 0$ at the surface of the half space. Parameters α and Q^{-1} can be expressed in terms of the Poisson's ratio for undrained conditions ν_u and the Skempton ratio B as follows

$$\alpha = \frac{3(\nu_u - \nu_d)}{(1 - 2\nu_d)(1 + \nu_u)B} \quad (7.52)$$

and

$$Q^{-1} = \frac{3}{2} \frac{1 - 2\nu_u}{1 + \nu_u} \frac{\alpha}{GB} = \frac{\alpha}{\kappa_u B} \quad (7.53)$$

The pore pressure p appears as a forcing term in the Navier's equation (7.50) and the matrix compaction $u_{k,k}$ is a forcing term of the diffusion equation (7.51), giving rise to a fully coupled system.

7.7.2 A bulk-viscosity formulation for poroelasticity

In this section, we draw a parallel between the classic poroelastic theory and the viscoelastic formalism presented in Section 7.5 of this article. We show that the classic constitutive and governing equations of poroelasticity can be written using the effective change in fluid density in the pore volume and the elastic moduli for undrained condition to parameterize the pore

fluid flow and the associated elastic deformation. Our proposed formulation can be viewed as a macroscopic formulation, where only two additional parameters -a coupling coefficient β and a diffusivity D -, compared to linear elasticity, are required to describe the time-dependent deformation. We show how these parameters relate to the microscopic properties of the fluid-solid composite.

First, in order to simplify the poroelastic equations, we define the effective coupling coefficient

$$\beta = B \alpha \quad (7.54)$$

We choose for dynamic variable the effective change of pore fluid density

$$\gamma = B \frac{m_f - m_{f0}}{\rho_0} \quad (7.55)$$

By definition, the inelastic deformation γ is identically zero in undrained condition. The linearized equation of state for the pore fluid can now be written

$$\gamma = \frac{\beta}{\kappa_d} \left(p/B + \frac{\sigma_{kk}}{3} \right) \quad (7.56)$$

Using eq. (7.54) and the stress-strain relation (7.47) for the composite material we have in the isotropic direction

$$\frac{\sigma_{kk}}{3} = \kappa_d \epsilon_{kk} - \beta p/B \quad (7.57)$$

Combining eqs. (7.54), (7.56) and Biot's stress-strain eq. (7.48) we obtain an alternate isotropic strain-rate relation invoking our chosen dynamic variable

$$\frac{\sigma_{kk}}{3} = \frac{K_d}{1 - \beta} (\epsilon_{kk} - \gamma) \quad (7.58)$$

Setting $\gamma = 0$, there follows a relationship between drained and undrained moduli

$$\begin{aligned} \kappa_u &= \frac{1}{1 - \beta} \kappa_d \\ \lambda_u &= \frac{2G}{3} \frac{1}{1 - \beta} \left(\beta + \frac{3\nu_d}{1 - 2\nu_d} \right) \\ \nu_u &= \frac{3\nu_d + \beta(1 - 2\nu_d)}{3 - \beta(1 - 2\nu_d)} \end{aligned} \quad (7.59)$$

where κ_u , λ_u and ν_u , respectively, are the bulk modulus, the Lamé parameter and the Poisson's ratio, respectively, for undrained condition. Reciprocally, given undrained elastic moduli and an effective coupling coefficient, one has

$$\begin{aligned} \lambda_d &= (1 - \beta)\lambda_u - \beta \frac{2G}{3} \\ \nu_d &= \frac{\beta(1 + \nu_u) - 3\nu_u}{2\beta(1 + \nu_u) - 3} \end{aligned} \quad (7.60)$$

Second and third formulas in eq. (7.59) and eq. (7.60) are simply derived from the first one using well-know relations between isotropic elastic moduli [e.g., Malvern, 1969]. The isotropic stress in

the solid matrix can be written

$$\frac{\sigma_{kk}}{3} = K_u (\epsilon_{kk} - \gamma) \quad (7.61)$$

which is the counterpart of eq. (7.57) which uses the effective pore pressure instead of fluid content as dynamic variable. Alternatively, the coupling coefficient β can be retrieved from inferred values of drained and undrained moduli

$$\beta = 1 - \frac{K_d}{K_u} = 3 \frac{\nu_u - \nu_d}{(1 - 2\nu_d)(1 + \nu_u)} \quad (7.62)$$

where the effective bulk modulus in undrained (initial) condition K_u is greater than in drained condition, at full relaxation ($K_u \geq K_d$). Similarly, drained and undrained conditions are associated with effective drained ν_d and undrained ν_u Poisson's ratios, respectively, with $\nu_u \geq \nu_d$.

Combining eqs. (7.56) and (7.61) we obtain an expression for the pore pressure in terms of strain in the solid matrix and strain in the pore fluid

$$\alpha p = \kappa_u (\gamma - \beta \epsilon_{kk}) \quad (7.63)$$

Substituting eq. (7.63) into eq. (7.47) we obtain the generalized stress-strain relation [see also Segall, 1985]

$$\sigma_{ij} = \lambda_u \epsilon_{kk} \delta_{ij} + 2G \epsilon_{ij} - \kappa_u \gamma \delta_{ij} \quad (7.64)$$

where the effective stress in the poroelastic composite is parameterized with the fluid strain γ instead of Biot's formulation with the pore pressure. Notice that eq. (7.64) can be written

$$\sigma_{ij} = C_{ijkl} \left(\epsilon_{kl} - \frac{1}{3} \gamma \delta_{kl} \right) \quad (7.65)$$

with the isotropic elastic stiffness tensor

$$C_{ijkl} = \lambda_u \delta_{ij} \delta_{kl} + G (\delta_{ij} \delta_{kl} + \delta_{ik} \delta_{jl}) \quad (7.66)$$

which corresponds to our formulation for stress in a viscoelastic material with bulk viscosity and whereby the ϵ_{kl} are the components of the total strain, the inelastic strain is $\epsilon_{kl}^i = \gamma \delta_{kl}/3$ and the isotropic elastic tensor C_{ijkl} is for undrained condition. Combining eqs. (7.49), (7.61) and (7.63) the Darcy's equation for fluid diffusion becomes

$$\dot{\gamma} = D \left[(1 - \beta) \gamma - \beta \frac{\sigma}{\kappa_u} \right]_{,jj} \quad (7.67)$$

and the boundary condition $p = 0$ at the surface of the half space becomes

$$\gamma = \frac{\beta}{1 - \beta} \frac{\sigma}{\kappa_u}, \quad x_3 = 0, \quad t > 0 \quad (7.68)$$

The diffusivity D , in units of $\text{length}^2 \times \text{time}^{-1}$, a combination of the microscopic parameters, is given by

$$D = \kappa_u \frac{B x}{\alpha} = M x \quad (7.69)$$

where M is Biot's modulus, the reciprocal of a storage coefficient [Detournay and Cheng, 1993, Wang, 2000]. The parabolic equation (7.67) is compatible with the general form of a viscoelastic constitutive relation with work-hardening $\dot{\gamma} = f(\sigma_{ij}, \gamma)$. Poroelasticity is therefore an example of bulk viscosity and in this framework the coupling parameter β can be thought of as a work-hardening parameter.

Finally, using conservation of momentum with formulation (7.64) one obtains the coupled governing equations

$$\begin{aligned} G \left(\frac{1}{1 - 2\nu_u} u_{k,ki} + u_{i,kk} \right) &= \kappa_u \gamma_{,i} \\ \dot{\gamma} &= D \left[(1 - \beta) \gamma - \beta \frac{\sigma}{\kappa_u} \right]_{,jj} \end{aligned} \quad (7.70)$$

where only two additional model parameters are required to describe a poroelastic rebound compared to linear elasticity. Formulations (7.50), (7.51) and (7.70) of the governing equations of poroelasticity are equivalent. Coupled eqs. (7.50) and (7.51) make use of the pore pressure p and the drained elastic moduli to parameterize the time-dependent deformation, as suggested by Biot [1941], whereas eq. (7.70) uses the effective fluid density change γ and the undrained elastic moduli. Similarly, Segall [1985, 1989] made use of the pore-fluid mass as dynamic variable, but neglected the coupling between confining stress and fluid diffusion. His approximation of the poroelastic equations is more similar to the thermoelastic theory where heat generated by the solid strain is also neglected.

We have written a viscoelastic formulation of the linear poroelasticity theory. We have shown that poroelastic rebound is the time-dependent response of an isotropic viscoelastic material with work hardening that can be described with two inelastic parameters. One corollary is that models of a poroelastic rebound from geodetic measurements can at best constrain two macroscopic parameters (for example, our proposed parameters D and β). Inferences on microscopic parameters α , B and x can only be attained with additional *in situ* measurements.

Appendix A

Numerical models of static deformation: the semi-infinite solid elasto-static Green function

Program STATICU computes the static elastic deformation due to the presence of dislocations in a semi-infinite solid with isotropic and homogeneous elastic properties and a free-surface boundary condition. The current Fortran 90 implementation uses the homogeneous elastic Green function for a half space. The Green function is performed semi-analytically in the Fourier domain, as described in Chapter 6.

A.1 Model input

The computation is performed in a Cartesian grid (see Figure A.1). The grid is defined by the number of nodes in the three directions, sx_1 , sx_2 and sx_3 , respectively. The code is designed to deal with dimensions that are only powers of two: 128, 256 or 512, for example. The spatial extent of the grid depends on the sampling intervals, Δx_1 , Δx_2 and Δx_3 , in the x_1 , x_2 and x_3 directions, respectively. The horizontal extent of the computational grid is $\Delta x_1 \times sx_1$ and $\Delta x_2 \times sx_2$, in the x_1 and x_2 directions, respectively. In the depth direction, the computational domain extends from $-\Delta x_3 \times sx_3/2$ to $\Delta x_3 \times (sx_3 - 1)/2$, but the half space extends from 0 to $\Delta x_3 \times (sx_3 - 1)/2$, with x_3 positive down. To ensure accurate models, the rule of thumb is to have the domain at least twenty times the characteristic dimension of the source, or, to have any edge of the computational grid about ten fault lengths away from a fault tip. Another constraint, to ensure good sampling, is to allow for at least five samples per fault. These two constraints can be satisfied simultaneously by maximizing the number of nodes, at the expense of computer memory. The Green function depends on the Lamé parameters λ and G . The value of the shear modulus has no influence on the computed results and only the value of Poisson's ratio ν should be considered. To avoid numerical overflow, the shear modulus should be kept small ($G = 1$ is fine).

The program STATICU computes the static deformation due to slip on faults. Internally, the program uses superposition to evaluate a distribution of internal forces and surface traction that represents the slip model. The final deformation is evaluated by the convolution between the internal forces with the elastic Green function. The number of slip patches has little influence

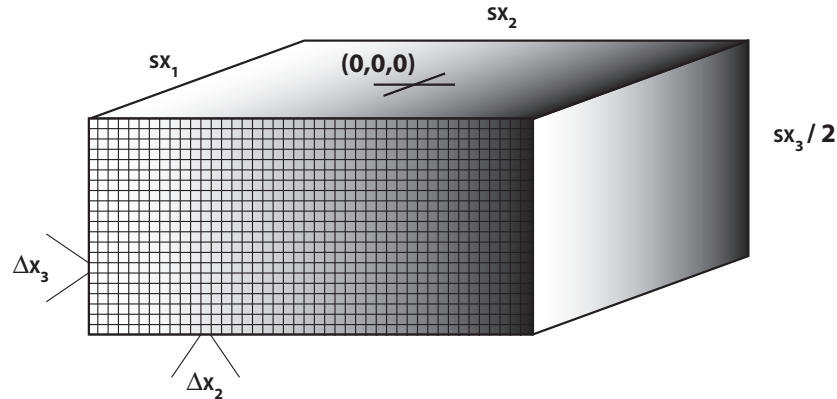


Figure A.1: The discretized half space. The origin of the reference system is at the center of the surface. The modeled half space dimension is $-\Delta x_1 \times sx_1/2$ to $\Delta x_1 \times (sx_1 - 1)/2$ in the x_1 direction, $-\Delta x_2 \times sx_2/2$ to $\Delta x_2 \times (sx_2 - 1)/2$ in the x_2 direction and 0 to $\Delta x_3 \times (sx_3 - 1)/2$ in the x_3 (depth) direction.

on the time of computation. Every slip patch is described by a geologic representation, as shown in Figure A.2. A fault segment is modeled by its length in the along-strike direction, its width in the down-dip direction, the position of the top tip (x_s , y_s , and z_s) and its strike and dip angles. By convention, an observer located at the top fault tip and oriented in the strike direction would face the fault trace and would have the fault dipping to his right for a dip angle between 0° and 90° . All quantities, without exceptions, should be given in consistent S.I. units, with lengths, slip and positions in meters (m) and with Lamé parameters in pascals (Pa). The unit of simulated displacements corresponds to the unit used for slip. The spatial dimension unit corresponds to the one used for lengths and positions. A slip model consists in an arbitrary number of slip patches. The slip distribution is smoothed to avoid stress singularities. The smoothing conserves the seismic moment. The amplitude of smoothing is controlled by a roll-off parameter going from $\beta = 0$ for no smoothing to $\beta = 0.5$ for strong smoothing. A value of $\beta = 0.2$ ensures stability of the computation.

Program STATICU automatically computes the deformation everywhere in the half space. The output can be i) a series of observation points, defined by their name (a 4-character string) and their position in the half space, ii) a horizontal-plane view of the displacement. The displacement on a horizontal plane is sampled at a prescribed depth; iii) the displacement in the entire half space for three-dimensional visualization (see Figure A.3). In the latter case, the grid is subsampled. Every output file is written in a subdirectory defined at execution time. A basic input of program STATICU is provided from the standard input or is read from a separate file and may be as follows

```
# grid size
512 512 512
# sampling and smoothing
```

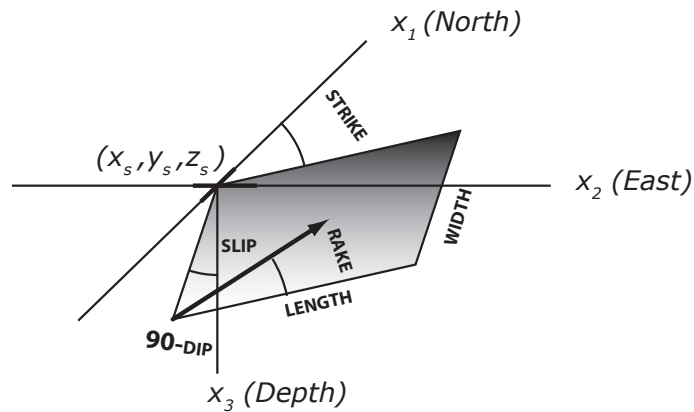


Figure A.2: Geologic model of slip on a fault. The fault is described by the position of its top tip, its length in the along-strike direction, width in the down-dip direction, its strike angle and its dip angle. The rake indicates the orientation of slip.

```

0.05 0.05 0.05 0.2
# origin shift and rotation
0 0 0
# observation depth
0
# output directory
./output1
# elastic moduli
1.0 1.0
# observation points
0
# screw/edge dislocations
1
# no slip  x1  x2  x3  length  width  strike  dip  rake
      1  1.0 -0.5 -0.0 0.5    1.0   1.0     0  45  90
# open cracks
0

```

The '#' character can be used to comment out instruction lines from the standard input. Export of sample points and map view displacement is always provided. The choice of exporting the entire grid in the VTK format for three-dimensional visualization is only provided at compilation time. Similarly, the format of the map-view export is specified at compilation time. Available formats are ASCII and binary form. The binary form is compatible with visualization in GMT, the general mapping tool application. Figure A.4 shows an example of visualizing the horizontal plane view output using the GMT program. The origin position in the input file can be used to center the computation grid at a specific position on the horizontal plane.

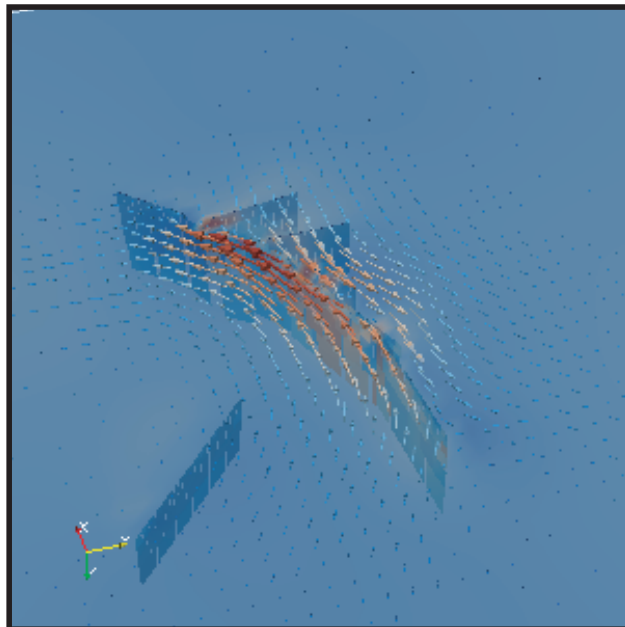


Figure A.3: Example of three-dimensional output from the program STATICU. The slip model and the associated displacement field corresponding to the 1992 Landers, CA earthquake is automatically exported in the VTK format. Here the data is visualized with the free software Paraview.

A.2 Fortran implementation

The STATICU main program uses Fortran 90 modules to perform functional operations. The entire program requires four modules. The corresponding Fortran 90 source files are:

elastic3d.f90 for stress/strain conversions, tensor operators, body-force representation of faults, coordinates manipulation and structure definition

export.f90 includes routines to sample and export data in text, binary GRD and VTK formats.

fourier.f90 for 1-D, 2-D and 3-D Fourier transforms, wavenumber calculations. This module contains interfaces to use the Cooley-Tukey FFT of Brenner (1968), the FFTW and the intel FFTs.

green.f90 for the evaluation of the elastic Green function and boundary-value problems.

The main program performs a series of actions. First the data is read from the standard input or a specified input file. Then the required memory is allocated. An excerpt of the program shows the next important operations

```
! Program 'STATICU'
```

```
! load shear dislocations
```

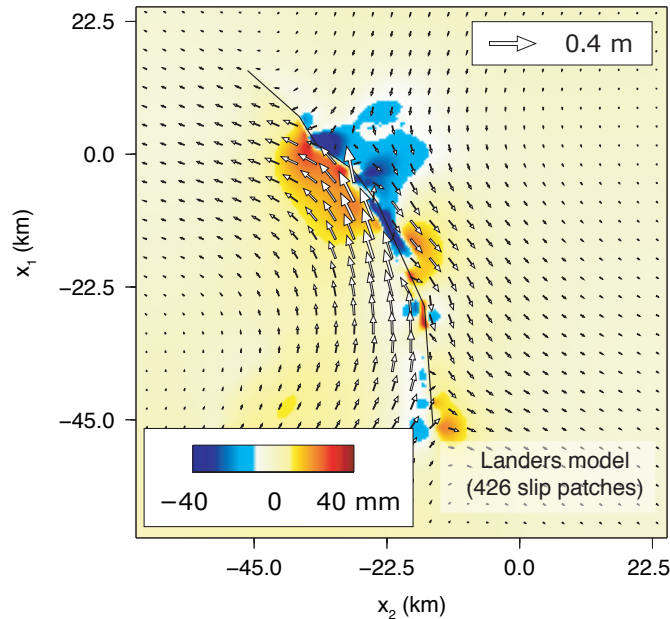


Figure A.4: Example of map-view output from the program STATICU. The surface displacement field corresponding to the 1992 Landers, CA earthquake can be automatically exported in the GRD format, allowing quick visualization with the GMT mapping tool.

```

DO i=1, ns ! number of shear faults
  ! adding sources in the space domain
  CALL source(mu,s(i)%slip,s(i)%x,s(i)%y,s(i)%z, &
    s(i)%width,s(i)%length,s(i)%strike,s(i)%dip,s(i)%rake,beta, &
    sx1,sx2,sx3,dx1,dx2,dx3,c1,c2,c3,p1,p2,p3)
END DO

! apply the 3d elastic transfert function
CALL greenfunction(c1,c2,c3,dx1,dx2,dx3,lambda,mu,p1,p2,p3,GRN_HS)

! export displacements to the GMT grd format
CALL exportgrd(c1,c2,c3,sx1,sx2,sx3/2,dx1,dx2,dx3,oz,x0,y0,wdir,0)

! export displacements at sample points
CALL exportpoints(c1,c2,c3,sx1,sx2,sx3/2,dx1,dx2,dx3, &
  opts,ptsname,0._8,wdir,.true.,x0,y0,rot)

```

The 'DO' loop adds internal body forces and surface traction to the total forcing term. After the loop is performed, the variables 'c1', 'c2' and 'c3' contain the directional components of the internal body forces. The variables 'p1', 'p2' and 'p3' contain the total surface traction. The next operation, performed by the subroutine 'greenfunction', from the module 'green', computes the three-dimensional displacement using the semi-analytic Fourier-domain Green function. The operation is performed in place: only one set of arrays are required to store the forcing terms and the resulting displacement field. After the 'greenfunction' subroutine is executed, the variables

'c1', 'c2' and 'c3' contain the three components of the displacement field. The next two operations consist in exporting the displacement field to a map-view binary file (subroutine 'exportgrd') and to individual files corresponding to sample points (subroutine 'exportpoints'). The end of the program, not shown, involves freeing memory. Note that the real Fortran 90 program can be more complicated in order to implement parallel execution, optional instructions, or additional export formats. An excerpt of 'greenfunction', the routine applying the Green function to the body-force field, is as follows

```

! Subroutine 'GreenFunction' in module 'Green'

! forward Fourier transform equivalent body-force and surface traction
CALL fft3(c1,sx1,sx2,sx3,dx1,dx2,dx3,FFT_FORWARD)
CALL fft2(t1,sx1,sx2,dx1,dx2,FFT_FORWARD)

CALL fft3(c2,sx1,sx2,sx3,dx1,dx2,dx3,FFT_FORWARD)
CALL fft2(t2,sx1,sx2,dx1,dx2,FFT_FORWARD)

CALL fft3(c3,sx1,sx2,sx3,dx1,dx2,dx3,FFT_FORWARD)
CALL fft2(t3,sx1,sx2,dx1,dx2,FFT_FORWARD)

! solve for displacement field in Fourier domain
ALLOCATE(temp1(sx1+2,sx2),temp2(sx1+2,sx2),temp3(sx1+2,sx2))
CALL elasticresponse(lambda,mu,c1,c2,c3,dx1,dx2,dx3,temp1,temp2,temp3)

! adding stress in the Fourier domain
temp1=t1-temp1
temp2=t2-temp2
temp3=t3-temp3

! add homogeneous solution to satisfy boundary condition
CALL cerruti3d(temp1,temp2,temp3,lambda,mu,c1,c2,c3,dx1,dx2,dx3)

DEALLOCATE(temp1,temp2,temp3)

! inverse Fourier-transform displacement components
CALL fft3(c1,sx1,sx2,sx3,dx1,dx2,dx3,FFT_INVERSE)
CALL fft3(c2,sx1,sx2,sx3,dx1,dx2,dx3,FFT_INVERSE)
CALL fft3(c3,sx1,sx2,sx3,dx1,dx2,dx3,FFT_INVERSE)

```

The subroutine 'greenfunction' implements the semi-analytic Green function described in Chapter 6. First, the equivalent body-force and surface traction fields are Fourier-transformed. Next, the periodic-space Green function is applied (in place) with the subroutine 'elasticresponse'. Subroutine 'elasticresponse' also evaluates the resulting traction at the surface, which becomes available in the array variables 'temp1', 'temp2' and 'temp3'. A displacement field that satisfies the homogeneous Navier's equation is evaluated and added to the current displacement field by subroutine 'cerruti3d'. The result is a displacement field that satisfies the free-surface boundary condition. The last operations consist in freeing the memory that was required to

store the surface traction and in inverse-Fourier transforming the displacement field to provide a solution in the space domain.

Appendix B

Numerical models of elastic deformation in heterogeneous media

Program STATICI simulates three-dimensional deformation in a heterogeneous elastic half space due to slip on faults of arbitrary position and orientation. Program STATICI implements the methods described in Chapter 4. The current implementation allows the elastic moduli model to be parameterized with i) a depth-dependent profile, ii) the inclusion of rectangular-parallelepiped volumes and iii) an arbitrary three-dimensional variation. The numerical strategy consists in identifying equivalent body forces and surface traction to represent the effect of variations in elastic moduli and evaluating the deformation using the homogeneous elastic Green function. The Green function corresponds to a choice of “homogenized” elastic moduli, which should be representative of the true elastic structure. The solution is obtained iteratively using the perturbation method or the successive over-relaxation method (SOR). For example, for the case of a vertically-layered elastic profile with a 30 GPa shear modulus seismogenic zone overlying a 45 GPa shear modulus half space, a choice of “homogenized” shear modulus of $\bar{G} = 30$ GPa would ensure fastest convergence and most accurate results. In principle the SOR method can be used to deal with models having arbitrary variations of elastic moduli, in particular with elastic contrasts greater than a factor of two. However, the SOR method requires defining a hyperparameter ϕ which controls the convergence of the iterative scheme. There are no sets of defined rules to choose this parameter and the convergence is therefore not systematically guaranteed. For elastic contrasts lower than a factor of two, the perturbation method should converge for a sensible choice of “homogenized” elastic moduli. For $\phi = 1$ the SOR method is equivalent to the perturbation method. Typical choices of the SOR parameter ϕ range from $\phi = 1/2$ to $\phi = 2$.

B.1 User interface

Program STATICI builds on the simpler program STATICU and both codes share similarities in their input files. In particular, the computational grid, the faults and the output products are specified the same way. The only difference in the input of program STATICI is the specification of the heterogeneous elastic structure and of the homogenized elastic moduli. The output of program STATICI is identical in form to the one of program STATICU, including output in ASCII and binary forms, for 2-D or 3-D visualization. A basic input of program STATICI may be as follows

```

# grid size
256 256 256
# sampling and smoothing (beta=0.2)
0.5 0.5 0.5 0.2
# origin shift and rotation
0 0 0
# observation depth (output surface displacements)
0
# output directory (where output files are written)
./output1
# homogenization constants (Lame's parameters) and SOR parameter
1.0 1.0 1.0
# elastic layers
3
1 0 1 1
2 10 1 1
3 10 1.1 1.1
# number of nodes of the 3D structure
0
# compliant zones
0
# observation points
0
# screw/edge dislocations
1
# index slip x1 x2 x3 length width strike dip rake
      1 1 -6 0 0      12      5      0 90 0
# open cracks
0

```

The above input corresponds to a vertically layered elastic model with a plate over a half space with a 10% increase in shear modulus in the half space. The strike-slip fault slips in the top half of the plate. The “homogenized” elastic moduli are chosen to correspond to the top plate. This choice of “homogenized” moduli ensures that the equivalent body forces representing the effect of variations of elastic moduli are located in the half space only, far from the surface. Notice that an elastic model with two layers requires three lines of specification. The first two lines define the top and bottom of the plate and the third line corresponds to the definition of the half space. The following specification

```

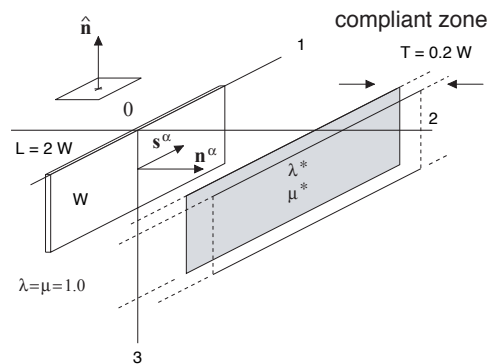
# elastic layers
2
1 0 1 1
2 10 1.1 1.1

```

would give rise to an elastic model with the Lamé parameters increasing monotonically from 1, at the surface, to 1.1 at a depth of 10 km. The deeper material would be assigned a constant shear modulus of 1.1 below 10 km. The layered modeled is described by the value of the Lamé parameters at specified depths; the intermediate values are linearly interpolated from the values

at the two nearest depths. The description of the variation of elastic properties with depth is similar to the specification of the PREM model, in seismology.

A. Conceptual model



B. Modeled elastic structure contribution

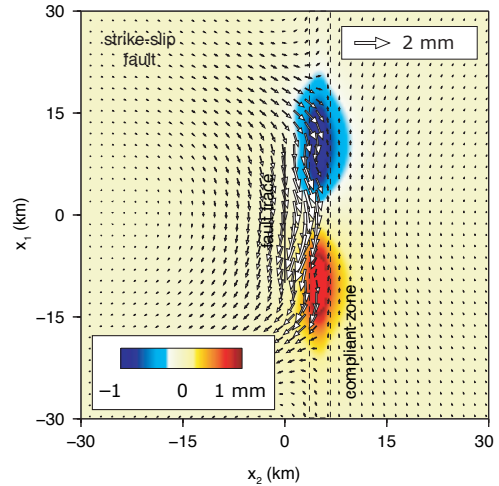


Figure B.1: Simulation of the deformation due to a strike-slip fault in a heterogeneous lithosphere. The elastic moduli are reduced around an infinitely long compliant zone in the near field of the fault. A) sketch of the geometry of the fault and the position of the compliant zone. B) Surface displacement corresponding to the elastic structure contribution showing additional strain in the vicinity of the compliant zone, compared to a model with a homogeneous lithosphere.

Another example illustrate the modeling of deformation due to a strike-slip fault nearby an infinitely long compliant zone. Figure B.1 shows the elastic structure contribution, the difference between the displacement in a heterogeneous domain with the one corresponding to a homogeneous half space. The displacement model shown in Figure B.1 can be obtained with the following input file

```
# grid size
256 256 256
# sampling and smoothing
0.3333 0.3333 0.3333 0.05
# origin shift and rotation
0 0 0
# observation depth
0
# output directory
./compliant_zone_simulation
# homogenization constant
1.0 1.0 1.0
# elastic layers
1
1 0.0 1.0 1.0
# number of nodes of the 3d elastic structure
```

```

0
# compliant zones
1
# index dlambda  dmu  x1 x2 x3 length width thickness strike dip
      1  -0.05 -0.05 -60 5  0   120   10           2    0  90
# observation points
0
# screw/edge dislocations
1
# index slip  x1 x2 x3 length width strike dip rake
      1  -1 -10  0  0   20   10     0  90   0
# open cracks
0

```

In this model, the half space is uniform except for a finite volume of reduced elastic moduli. This volume, referred to as a compliant zone, is parameterized with its variations of elastic moduli, $\Delta\lambda$ and $\Delta\mu$, its position, its linear dimension (length, width and thickness) and orientation (strike and dip angles). The geometric definition of compliant zones uses similar conventions to those for a fault, except for an additional thickness parameter that indicates the dimension of the compliant zone in the strike-perpendicular direction. The compliant zones are tapered using the roll-off parameter β that is also used to define fault slip. In the above model, the compliant has a 5% reduction in elastic moduli. Note that the definition of the compliant zone is a perturbation to the ambient elastic model, rather than a specification of the absolute value of the elastic moduli at this location.

B.2 Fortran implementation

Program STATICI is implemented in Fortran 90. The main program uses a combination of Fortran 90 modules to perform important tasks. The corresponding source files are:

heterogeneous3d.f90 for stress/strain conversions, tensor operators, body-force representation of faults, coordinate manipulation, structure definition, stress field calculation (gradients), equivalent body force calculation (divergence) and elastic structure definition

export.f90 includes routines to sample and export data in text, binary GRD and VTK formats.

fourier.f90 for 1-D, 2-D and 3-D Fourier transforms, wavenumber calculations.

green.f90 for the evaluation of the elastic Green function and boundary-value problems.

Program STATICI shares numerous routines with the Fortran 90 program STATICU. A simplified excerpt of the main program corresponding to the implementation of the perturbation solution reads as follows

```
CALL elasticstructure(lambda,mu,elasticlayer,dx3)
```

```

! adding compliant zones
DO i=1,ncz
  CALL compliantzone( &
    compzones(i)%dlambda,compzones(i)%dmu, &
    compzones(i)%x,compzones(i)%y,compzones(i)%z, &
    compzones(i)%width,compzones(i)%length,compzones(i)%thickness, &
    compzones(i)%strike,compzones(i)%dip, &
    beta,sx1,sx2,sx3/2,dx1,dx2,dx3,lambda,mu)
END DO

CALL dislocations(event,dx1,dx2,dx3,sx1,sx2,sx3,beta, &
  lambda0,mu0,lambda,mu, &
  u1,u2,u3,p1,p2,p3,sig,isMomentDensity)

! norm of the initial forces
fscaling=vectormean(u1,u2,u3,sx1,sx2,sx3/2)

! initial guess for the displacement field
CALL greenfunction(u1,u2,u3,dx1,dx2,dx3,lambda0,mu0,p1,p2,p3)

ALLOCATE(c1(sx1+2,sx2,sx3/2),c2(sx1+2,sx2,sx3/2),c3(sx1+2,sx2,sx3/2))

! variables c1,c2 and c3 contain the perturbation-method solution displacement
CALL fieldrep(c1,u1,sx1+2,sx2,sx3/2)
CALL fieldrep(c2,u2,sx1+2,sx2,sx3/2)
CALL fieldrep(c3,u3,sx1+2,sx2,sx3/2)

! 'perturbed' elastic properties (deviation from uniform)
lambda=lambda0-lambda
mu    =mu0-mu

! iteration loop
DO i=1,ITERATION_MAX

  ! instantaneous stress level
  CALL stress(lambda,mu,u1,u2,u3,dx1,dx2,dx3,sx1,sx2,sx3/2,sig)

  ! equivalent body-force & surface traction
  u1=0;u2=0;u3=0;p1=0;p2=0;p3=0
  CALL equivalentbodyforce(sig,dx1,dx2,dx3,sx1,sx2,sx3/2, &
    u1,u2,u3,p1,p2,p3)

  ! norm of the equivalent forces representing the effect of inclusions
  fnorm=vectormean(u1,u2,u3,sx1,sx2,sx3/2)

  ! solve for displacement perturbation
  CALL greenfunction(u1,u2,u3,dx1,dx2,dx3,lambda0,mu0,p1,p2,p3)

  ! update the iterative solution with the latest perturbation
  CALL fieldadd(c1,u1,sx1+2,sx2,sx3/2)

```

```

CALL fieldadd(c2,u2,sx1+2,sx2,sx3/2)
CALL fieldadd(c3,u3,sx1+2,sx2,sx3/2)

! convergence test of the perturbation method (epsilon = 1e-6)
isConvergence=fnorm/fscaling .lt. epsilon

! stop when convergence test is satisfied
IF (isConvergence) GOTO 100
END DO

100 CONTINUE

! export final solution
CALL exportgrd(c1,c2,c3,sx1,sx2,sx3/2,dx1,dx2,dx3,oz,x0,y0,wdir,0)

```

After the execution of the first 'DO' loop, the elastic moduli variables 'lambda' and 'mu' represent the modeled elastic structure. The subroutine 'dislocations' add the body forces and surface tractions to the variables 'u1', 'u2' and 'u3' for the body forces and 'p1', 'p2' and 'p3', for the tractions. The norm of the body forces is stored in the variable 'fscaling'. A displacement field is obtained after execution of the subroutine 'greenfunction', which is described in Appendix A. Next, the variables 'c1', 'c2' and 'c3' contain the three components of the final solution. The next 'DO' loop adds the higher-order terms of the perturbation solution. First, a uniform field of elastic moduli is removed to the elastic moduli model (eq. 4.16 in Chapter 4). At each iteration of the perturbation loop, the equivalent moment density (eq. 4.17) is evaluated using the subroutine 'stress' and stored in the tensor-valued array variable 'sig'. Next, a set of equivalent body force and surface traction is identified (eq. 4.19) using subroutine 'equivalentbodyforce'. The corresponding perturbation displacement field is obtained using the subroutine 'greenfunction' and is finally added to the current estimate of the solution displacement. The program execution exits the 'DO' loop if a convergence test (eq. 4.39) is satisfied. The current code in file 'statici.f90' also includes the possibility of using the successive over-relaxation method.

The module 'heterogeneous3d.f90' adds to the existing routines of STATICU module 'elastic3d.f90' the necessary routines to evaluate the current stress and to compute a set of body forces from tensor field. The equivalent moment density representing a variation in elastic moduli (eq. 4.17 in Chapter 4) is evaluated from the subroutine 'stress'. An excerpt of the Fortran 90 subroutine 'stress' is as follows

```

! subroutine 'stress' of module 'heterogeneous3d'

DO i3=1,sx3
  DO i2=1,sx2
    DO i1=1,sx1
      clambda=lambda(i1,i2,i3)
      cmu      =mu    (i1,i2,i3)

      IF (abs(cmu) .ge. epsilon .or. abs(clambda) .ge. epsilon) THEN

```

```

      ! Finite Impulse Response filter
      CALL localstrain_fir2(t,i1,i2,i3,ker1,ker2,ker3, &
                           len1,len2,len3,v1,v2,v3,sx1,sx2,sx3)
      CALL isotropicstresstrain(t,clambda,cmu)
      sig(i1,i2,i3)=t
    ELSE
      sig(i1,i2,i3)=TENSOR(0._4,0._4,0._4,0._4,0._4,0._4)
    END IF
  END DO
END DO
END DO

```

The three embedding 'DO' loops run through the three-dimensional computational grid. At each point, the deviation from the "homogenized" elastic moduli is determined and stored in the variables 'clambda' and 'cmu'. In case of no deviation, their is no equivalent moment density and the local value of the stress tensor is assigned to zero. Otherwise, the local strain is evaluated from the displacement field (variables 'v1', 'v2' and 'v3') and assigned to the tensor variable 't'. The stress (or moment density) is evaluated in place using Hooke's law with the routine 'isotropicstresstrain' and assigned to the local moment density field 'sig(i1,i2,i3)'. In the module 'heterogeneous3d.f90', the reading of the code is complicated by the possibility to compile it to run in parallel with MPI and OpenMP.

The equivalent body forces are obtained from the moment density field (eq. 4.19 in Chapter 4) using the Fortran 90 subroutine 'equivalentbodyforce' as follows

```

DO i3=1,sx3
  DO i2=1,sx2
    DO i1=1,sx1
      ! Finite Impulse Response filter
      CALL localdivergence_fir2(f1,f2,f3,i1,i2,i3, &
                               ker1,ker2,ker3,len1,len2,len3,sig,sx1,sx2,sx3)

      c1(i1,i2,i3)=c1(i1,i2,i3)-REAL(f1)
      c2(i1,i2,i3)=c2(i1,i2,i3)-REAL(f2)
      c3(i1,i2,i3)=c3(i1,i2,i3)-REAL(f3)
    END DO
  END DO
END DO

```

The first three 'DO' loops run through the computational domain. The subroutine 'localdivergence_fir2' computes the local value of the divergence of the stress tensor field 'sig'. The result is a body force whose three components are stored in the variables 'f1', 'f2' and 'f3'. The equivalent body force field is then updated with the opposite value. The reading of the code of subroutine 'equivalentbodyforce' in module 'heterogeneous3d.f90' is complicated by the possibility to compile it to run parallel with MPI or OpenMP.

Appendix C

Numerical models of time-dependent deformation

Program RELAX computes the time-dependent deformation following a stress perturbation due to the presence of a ductile substrate or a stable slipping fault. The fault creep is governed by a rate-strengthening friction and the ductile layer, by a power-law rheology. The current Fortran 90 program allows for arbitrary variations in inelastic properties but is limited to homogeneous elastic properties. The instantaneous velocity is obtained using the Green function for a half space with a free surface and a restoring force due to a density contrast between rock and air at the surface. The Green function is performed semi-analytically in the Fourier domain, as described in Chapter 6 and the simulation of the time-dependent deformation is performed using the method described in Chapter 7. The stress perturbation comes from slip on faults or magmatic unrest. The specification of the initial slip model is similar to the one in programs STATICU and STATICI.

C.1 User Interface

Similarly to programs STATICU and STATICI, the computation is performed in a Cartesian grid, which is described by the sampling size and the number of nodes in the three directions. The boundary condition at the surface includes the effect of a density contrast between rocks and air. The effect of the density contrast is specified by the parameter Γ in eq. (6.19). In program RELAX, the elastic Green function is defined by the Lamé parameters and the gravity parameter Γ . Program RELAX evaluates the time-dependent relaxation following a series of perturbations. Each perturbation is referred to as a “coseismic event”. Each event is associated with a slip model. The first event starts at time 0, in S.I. units. The time of occurrence of the following events must be prescribed. The possible inclusion of multiple events can be important in models involving nonlinear creep rheologies.

The time-dependent model shown in Figure 7.2 in Chapter 7 can be obtained from the following input to program RELAX

```
# grid size (sx1,sx2,sx3)
512 512 512
# sampling size & smoothing (dx1,dx2,dx3,beta)
0.8 0.8 0.8 0.2
```

```

# origin position and rotation
0 0 0
# observation depth
0
# output directory
./output5
# elastic parameters (lambda,mu,Gamma)
3e1 3e1 0
# integration time (t1) and time step
# (use negative integers, say '-p', to write outputs every p time steps)
1e5 -1
# number of observation planes
0
# number of observation points
12
# index name x1 x2 x3
  1 GPS1 25 10 0
  2 GPS2 25 20 0
  3 GPS3 25 30 0
  4 GPS4 25 40 0
  5 GPS5 25 50 0
  6 GPS6 25 60 0
  7 GPS7 50 10 0
  8 GPS8 50 20 0
  9 GPS9 50 30 0
 10 GP10 50 40 0
 11 GP11 50 50 0
 12 GP12 50 60 0
# number of prestress interfaces with depth
0
# number of linear viscous interfaces
0
# number of powerlaw viscous interfaces
1
# index depth gammadot0 power cohesion
  1  30 6.137788e6  3.5  0.0
# number of fault creep interface
0
# number of interseismic dislocation
0
# number of interseismic dykes
0
# number of coseismic events
1
# number of shear dislocations
1
# index slip x1 x2 x3 length width strike dip rake
  1  -1 -20 0 0  40  10  0 90  0
# number of tensile cracks
0
# number of point dilatation sources

```

0

The time series of displacement covering the interval $(0, 1e5)$, in S.I. units, will be sampled at 12 points named GPS1, GPS2, ..., GP12. Also, a series of outputs in map view will be written in subdirectory './output5'. Since the time step '-1' was chosen, the program will automatically choose a time step and the map-view output (in GRD, text and VTK formats) will be written at every computational time step. For a time step of '-3', the program would choose a computational time step automatically and write the map-view displacements to disk every three time steps. The displacement at the observation points is updated systematically, at every steps of the computation. The effect of the surface density contrast is ignored ($\Gamma = 0$). The time-dependent lithospheric deformation is controlled by a power-law rheology with stress exponent $n = 3.5$ in eq. (7.19). The brittle-ductile transition occurs at a depth of 30 m. The effect of cohesion is to modify the apparent stress (cohesion is usually set to zero). The transient deformation is due to the occurrence of a single event at time zero. The event consists in the slip of a vertical strike-slip fault.

To reproduce the results of Figure 7.7, corresponding to the transient deformation due to stable slip on a rate-strengthening friction asperities subjected to a uniform stress perturbation, one may use the following input of program RELAX

```
# grid size (sx1,sx2,sx3)
128 128 128
# sampling size & smoothing (dx1,dx2,dx3,beta)
0.05 0.05 0.05 0.2
# origin position (north,east) and rotation
0 0 0
# observation depth
0
# output directory
./output1
# elastic parameters and gravity parameter (lambda,mu,Gamma)
1 1 0
# integration time (t1)
25 -1
# number of observation planes
0
# number of observation points
1
# no name x1 x2 x3
1 GPS7 0.5 0.5 0
# number of prestress interfaces
1
# no depth s11 s12 s13 s22 s23 s33
1 0 0 7 0 0 0 0
# number of linear viscous interfaces
0
# number of powerlaw viscous interfaces
0
```

```

# number of fault creep interfaces
1
# no depth gamma0 (a-b)sigma friction cohesion
  1   0   1       1   0.6   0
# number of afterslip planes
1
# no      x1 x2 x3 length width strike dip
  1 -0.025 0 1  0.05 0.05   0 90
# number of interseismically loading faults and dykes
0
0
# number of coseismic events
1
# number of shear dislocations
1
# index slip      x1 x2      x3 length  width strike dip rake
  1   0 -1.0 0 1.1  1 0.5      0 90   0
# number of tensile cracks
0
# number of point dilatation sources
0

```

The transient deformation is due to slip on a rate-strengthening friction asperity. The rate-strengthening friction properties are uniform in the lithosphere with $\dot{\gamma}_0 = 1 \text{ s}^{-1}$ and $(a - b)\sigma = 0.6 \text{ Pa}$. Afterslip occurs on a vertical plane and is confined in a rectangular area 0.05 m long and 0.05 m wide. The occurrence of afterslip is due to a uniform stress perturbation of $\sigma_{12} = 7 \text{ Pa}$. Notice that the input of program RELAX requires the definition of a slip model. In order to model afterslip due to a uniform stress, the slip model consists in one fault with no associated slip.

To reproduce the results of Figure 7.6, showing the effect of a surface density contrast of the partterns of viscoelastic relaxation following slip on a thrust fault, one may use the following input to program RELAX

```

# grid size (sx1,sx2,sx3)
512 512 512
# sampling size & smoothing (dx1,dx2,dx3,beta)
0.05 0.05 0.05 0.2
# origin position and rotation
0 0 0
# observation depth
0
# output directory
./output1
# elastic parameters (lambda,mu) and gravity (Gamma)
1 1 2.475e-2
# integration time (t1)
45 -1
# number of observation points
0

```

```

# number of prestress interfaces
0
# number of observation planes
0
# number of linear viscous interfaces
1
# index depth gammadot0 cohesion
      1      1      1      0
# number of powerlaw viscous interfaces
0
# number of fault creep interface
0
# number of interseismic stuff
0
0
# number of coseismic events
1
# number of shear dislocations
1
# index slip  x1 x2  x3 length width strike dip rake
      1      1 -3.3 0 0.5   6.6   1      0 30 90
# number of tensile cracks
0
# number of point dilatation sources
0

```

The time-dependent deformation is due to the stress perturbation associated with 1 m slip on a thrust fault dipping 30° . The elastic moduli are $\lambda = \mu = 1$ Pa. The density contrast gives rise to a critical wavelength of $\Gamma = 2.475 \cdot 10^{-2} \text{ m}^{-1}$. The simulation covers the time interval $(0, 45 \text{ s})$. The map-view output is written at every computational step. The brittle-ductile transition occurs at a depth of 1 m. The reference strain rate is uniform in the viscous layer with $\dot{\gamma}_0 = 1 \text{ s}^{-1}$. The characteristic Maxwell time corresponding to this model is $t_m = 1/\dot{\gamma}_0 = 1 \text{ s}$. The simulation corresponds to 45 relaxation times of a linear viscoelastic relaxation.

C.2 Fortran implementation

The RELAX main program uses Fortran 90 modules to perform functional operations. The entire program requires four modules. The corresponding Fortran 90 source files are:

elastic3d.f90 for stress/strain conversions, tensor operators, body-force representation of faults, coordinates manipulation, structure definition, stress field calculation (gradients), equivalent body force calculation (divergence) and inelastic structure definition

export.f90 includes routines to sample and export data in text, binary GRD and VTK formats.

fourier.f90 for 1-D, 2-D and 3-D Fourier transforms, wavenumber calculations.

green.f90 for the evaluation of the elastic Green function and boundary-value problems including the effect of a density variation at the surface.

friction3d.f90 for the rate-strengthening friction rheology

viscoelastic3d.f90 for the power-law viscoelastic rheology

The modules `./elastic3d.f90`, `export.f90`, `fourier.f90`, `fourier.f90` and `green.f90` are mostly identical to the one used by program STATICI, except for module `green.f90` which includes the effect of the density contrast at the surface in program RELAX. Two additional modules, `friction3d.f90` and `viscoelastic3d.f90`, are used to evaluate the instantaneous strain rates due to frictional sliding or viscoelastic flow.

A simplified excerpt of program RELAX is as follows, assuming an initial displacement field (scalar-valued array variables `'u1'`, `'u2'` and `'u3'`) and initial stress perturbation (tensor-valued array variable `'sig'`) are defined,

```
t=0
DO i=1,ITERATION_MAX ! maximum number of iterations is 900
  IF (t > (interval+1e-6)) GOTO 100 ! exit when simulation is over

  ! predictor displacement at t+Dt/2 (Runge-Kutta method)
  CALL tensorfieldadd(sig,tau,sx1,sx2,sx3/2,c1=0._4,c2=-1._4)
  CALL stressupdate(u1,u2,u3,lambda,mu,dx1,dx2,dx3,sx1,sx2,sx3/2,sig)

  ! initialize large time step
  tm=1e7
  ! initialize no forcing term in tensor space
  CALL tensorfieldadd(moment,moment,sx1,sx2,sx3/2,0._4,0._4)

  ! powerlaw viscosity
  CALL viscouseigenstress(mu,nonlinearstruc,sig,sx1,sx2,sx3/2, &
    dx1,dx2,dx3,moment,MAXWELLTIME=tm)

  ! nonlinear fault creep with rate-strengthening friction
  DO k=1,np
    CALL frictioneigenstress(n(k)%x,n(k)%y,n(k)%z, &
      n(k)%width,n(k)%length,n(k)%strike,n(k)%dip,beta, &
      sig,mu,faultcreepstruc,sx1,sx2,sx3/2,dx1,dx2,dx3,moment, &
      maxwelltime=tm)
  END DO

  ! choose an integration time step
  CALL integrationstep(tm,Dt,t,oi,odt,events,e,ne)

  CALL tensorfieldadd(sig,moment,sx1,sx2,sx3/2,c1=0.0_4,c2=1._4)

  v1=0;v2=0;v3=0;t1=0;t2=0;t3=0;
  CALL equivalentbodyforce(sig,dx1,dx2,dx3,sx1,sx2,sx3/2,v1,v2,v3)
```

```

! predicted velocity
CALL greenfunctioncowling(v1,v2,v3,t1,t2,t3,dx1,dx2,dx3,lambda,mu,gam)

! v1,v2,v3 contain the predictor displacement at time t+Dt/2
CALL fieldadd(v1,u1,sx1+2,sx2,sx3/2,c1=REAL(Dt/2))
CALL fieldadd(v2,u2,sx1+2,sx2,sx3/2,c1=REAL(Dt/2))
CALL fieldadd(v3,u3,sx1+2,sx2,sx3/2,c1=REAL(Dt/2))

! corrector
CALL tensorfieldadd(sig,tau,sx1,sx2,sx3/2,c1=-REAL(Dt/2),c2=-1._4)
CALL stressupdate(v1,v2,v3,lambda,mu,dx1,dx2,dx3,sx1,sx2,sx3/2,sig)

! reinitialize moment density tensor
CALL tensorfieldadd(moment,moment,sx1,sx2,sx3/2,0._4,0._4)

! powerlaw viscosity
v1=0
CALL viscouseigenstress(mu,nonlinearstruc,sig,sx1,sx2,sx3/2, &
    dx1,dx2,dx3,moment,GAMMA=v1)

! update slip history
CALL fieldadd(gamma,v1,sx1+2,sx2,sx3/2,c2=REAL(Dt))

! nonlinear fault creep with rate-strengthening friction
! use v1 as placeholders for the afterslip planes
v1=0
DO k=1,np
    CALL frictioneigenstress(n(k)%x,n(k)%y,n(k)%z, &
        n(k)%width,n(k)%length,n(k)%strike,n(k)%dip,beta, &
        sig,mu,faultcreepstruc,sx1,sx2,sx3/2,dx1,dx2,dx3,moment,VEL=v1)
END DO

! rate of equivalent body force
v1=0;v2=0;v3=0;t1=0;t2=0;t3=0;
CALL equivalentbodyforce(moment,dx1,dx2,dx3,sx1,sx2,sx3/2,v1,v2,v3)

! instantaneous velocity at time t+Dt/2
CALL greenfunctioncowling(v1,v2,v3,t1,t2,t3,dx1,dx2,dx3,lambda,mu,gam)

! update deformation field u(t+Dt) = u(t)+Dt * v(t+Dt/2)
CALL fieldadd(u1,v1,sx1+2,sx2,sx3/2,c2=REAL(Dt))
CALL fieldadd(u2,v2,sx1+2,sx2,sx3/2,c2=REAL(Dt))
CALL fieldadd(u3,v3,sx1+2,sx2,sx3/2,c2=REAL(Dt))
CALL tensorfieldadd(tau,moment,sx1,sx2,sx3/2,c2=REAL(Dt))

! time increment
t=t+Dt

! write outputs
IF (isoutput(skip,t,i,odt,oi,events(e)%time)) THEN
    CALL exportgrd(u1,u2,u3,sx1,sx2,sx3/2,dx1,dx2,dx3,oz,x0,y0,wdir,oi)

```

```

        ! update output counter
        oi=oi+1
    END IF
END DO
100 CONTINUE

```

The time-dependent model is calculated using a second-order Runge-Kutta method. Each iteration of the first 'DO' loop corresponds to a computational time step. In the "predictor" step, the displacement at time $t + \Delta t$ is evaluated using the relation $u_i(t + \Delta/2) = u_i(t) + v_i(t)\Delta t/2$, where u_i and v_i are the displacement and velocity fields, respectively. In the "corrector" step, the instantaneous velocity is evaluated at time $t + \Delta t/2$ and the final displacement field is obtained using the relation $u_i(t + \Delta t) = u_i(t) + v_i(t + \Delta t/2)\Delta t$. After execution of the subroutine 'stressupdate', the tensor-valued variable 'sig' contains the value of the instantaneous stress (eq. 7.5). Then a large time step and the moment density (eq. 7.9) are initialized. The subroutine 'viscouseigenstress' and 'frictioneigenstress', from the modules 'viscoelastic3d.f90' and 'friction3d.f90', respectively, add the power density (eqs. 7.15 and 7.28, respectively) to the tensor-valued variable 'moment'. Next, the subroutine 'integrationstep' chooses a computation time step Δt . The time step corresponds to a recommended value from routines 'viscouseigenstress' and 'frictioneigenstress' or, if smaller, the user-specified value or, if smaller, the time to the next coseismic event. The rate of body force and surface traction are evaluated from the power density with subroutine 'equivalentbodyforce' and the instantaneous velocity is obtained using the subroutine 'greenfunctioncowling'. The latter uses the semi-analytic elastic Green function that includes the effect of the density contrast at the surface. Before the "corrector" section, the variables 'v1', 'v2' and 'v3' contain the displacement at time $t + \Delta t/2$. First in the "corrector" section, the stress corresponding to its value at time $t + \Delta t/2$ (eq. 7.5) is evaluated using subroutines 'tensorfieldadd' and 'stressupdate'. The power density is re-initialized to zero and updated with the power density due to viscoelasticity and fault creep. The corresponding rate of body force and surface traction is evaluated using subroutine 'equivalentbodyforce' and the instantaneous velocity at time $t + \Delta t/2$ is obtained with the routine 'greenfunctioncowling'. The variables 'u1', 'u2' and 'u3' are then updated to contain the cumulative displacement at time $t + \Delta t$. Before the time increment, the variable 'tau' contains the cumulatively relaxed stress, corresponding to the integral is eq. (7.5). After tracking the time progress with variable 't', the output may be written to disk. The output is written if the current time corresponds to an integer of the user-defined output time interval, or if a new coseismic event occurred. The code for the main program written in 'relax.f90' includes the above instructions but also includes the possibility to export various information (equivalent body-force field, postseismic contribution) in multiple formats (text, GRD, VTK), the effect of steadily moving faults and dykes, the treatment of linear and power-law viscosity and the inclusion of several coseismic events at different times in the simulation.

Bibliography

- M. Abramowitz and I. Stegun. *Handbook of mathematical functions with formulas, graphs and mathematical tables*. 1046 pp., U.S. Govt. Print. Off., Washington DC, 1972.
- K. Aki and P. G. Richards. *Quantitative Seismology*, volume I. W. H. Freeman and company, New York, 1980.
- Bettina P. Allmann and Peter M. Shearer. A high-frequency secondary event during the 2004 Parkfield earthquake. *Science*, 318(5854):1279–1283, November 2007.
- V. I. Alshits and H. O. K. Kirchner. Elasticity of multilayers i. basic equations and solutions. *Phil. Mag. A*, 72(6):1431–1444, 1995a.
- V. I. Alshits and H. O. K. Kirchner. Elasticity of multilayers ii. strips, coatings and sandwiches. *Phil. Mag. A*, 72(6):1445–1470, 1995b.
- N.N. Ambraseys. Some characteristic features of the North Anatolian fault zone. *Tectonophysics*, 9:143–165, 1970.
- G. Backus. Inference from inadequate and inaccurate data, i. *Proc. Nat. Ac. Sci.*, 65(1), January 1970.
- G. Backus and M. Mulcahy. Moment tensors and other phenomenological descriptions of seismic sources-i. continuous displacements. *Geophys. J. R. Astr. Soc.*, 46:341–361, 1976a.
- G. Backus and M. Mulcahy. Moment tensors and other phenomenological descriptions of seismic sources-ii. discontinuous displacements. *Geophys. J. R. Astr. Soc.*, 47:301–329, 1976b.
- W. Bakun and T. McEvelly. Recurrence models and Parkfield, California, earthquakes. *J. Geophys. Res.*, 89(B5):3051–3058, May 1984.
- W. H. Bakun and A. G. Lindh. The Parkfield, California, earthquake prediction experiment. *Science*, 229(4714):619–624, August 1985.
- W. H. Bakun, B. Aagaard, B. Dost, W. L. Ellsworth, J. L. Hardebeck, R. A. Harris, C. Ji, M. J. S. Johnston, J. Langbein, J. J. Lienkaemper, A. J. Michael, J. R. Murray, R. M. Nadeau,

- P. A. Reasenber, M. S. Reichle, E. A. Roeloffs, A. Shakal, R. W. Simpson, and F. Waldhauser. Implications for prediction and hazard assessment from the 2004 Parkfield earthquake. *Nature*, 437(7061):969–974, October 2005.
- S. Barbot and Y. Fialko. Towards a unified representation of postseismic mechanisms: Semi-analytic models of fault creep, poroelastic rebound and power-law flow. *J. Geophys. Res.*, submitted, 2009a.
- S. Barbot and Y. Fialko. Fourier-domain green function for an elastic semi-infinite solid with gravity with applications to earthquake and volcano deformation. *J. Geophys. Res.*, submitted, 2009b.
- S. Barbot, Y. Fialko, and D. Sandwell. Effect of a compliant fault zone on the inferred earthquake slip distribution. *J. Geophys. Res.*, 113(B6), June 2008a. doi: doi:10.1029/2007JB005256.
- S. Barbot, Y. Hamiel, and Y. Fialko. Space geodetic investigation of the coseismic and postseismic deformation due to the 2003 Mw 7.2 Altai earthquake: Implications for the local lithospheric rheology. *J. Geophys. Res.*, 113(B03403):B03403, 2008b. doi: 10.1029/2007JB005063. doi:10.1029/2007JB005063.
- S. Barbot, Y. Fialko, and Y. Bock. Postseismic deformation due to the Mw 6.0 2004 Parkfield earthquake: Stress-driven creep on a fault with spatially variable rate-and-state friction parameters. *J. Geophys. Res.*, 114(B07405), 2009a. doi:10.1029/2008JB005748.
- S. Barbot, Y. Fialko, and D. Sandwell. Three-dimensional models of elasto-static deformation in heterogeneous media, with applications to the Eastern California Shear Zone. *Geophys. J. Int.*, 179(1):500–520, 2009b.
- D. M. Barnett. On the screw dislocation in an inhomogeneous elastic medium: The case of continuously varying elastic moduli. *Int. J. Solids Structures*, 8:651–660, 1972.
- A. Bayasgalan, J. Jackson, and D. McKenzie. Lithosphere rheology and active tectonics in Mongolia: relations between earthquake source parameters, gravity and GPS measurements. *Geophys. J. Int.*, 163:1151–1179, 2005.
- N. B. D. Bechor and H. A. Zebker. Measuring two-dimensional movements using a single InSAR pair. *Geophys. Res. Lett.*, 33:L16311, 2006.
- Y. Ben-Zion, Z. Peng, D. Okaya, L. Seeber, J. G. Armbruster, N. Ozer, A. J. Michael, S. Baris, M. Aktar, Y. Kuwahara, and H. Ito. A shallow fault-zone structure illuminated by trapped waves in the Karadere-Duzce branch of the North Anatolian Fault, western Turkey. *Geophys. J. Int.*, 152:699–699, 2003.

- C. M. Bender and S. A. Orszag. *Advanced mathematical methods for scientists and engineers*. McGraw-Hill, New York, 1978.
- M. A. Biot. General theory of three-dimensional consolidation. *Appl. Phys.*, 12:155–164, 1941.
- W. F. Brace and D. L. Kohlstedt. Limits on lithospheric stress imposed by laboratory experiments. *J. Geophys. Res.*, 85(B11):6248–6252, 1980.
- R. Bracewell. *The Fourier Transform and its Applications*. Electrical and Computer Engineering. Tata McGraw-Hill, New York, 3 edition, 2003.
- J. D. Bredehoeft. Response of well-aquifer systems to earth tides. *J. Geophys. Res.*, 72:3075–3087, 1967.
- C. M. Brown, W. Dreyer, and W. H. Müller. The convergence of a DFT-algorithm for solution of stress-strain problems in composite mechanics. *J. Eng. Mat. Tech.*, 125:27–37, 2003.
- R. Bürgmann, S. Ergintav, P. Segall, E. H. Hearn, S. McClusky, R. E. Reilinger, H. Woith, and J. Zschau. Time-dependent distributed afterslip on and deep below the Izmit earthquake rupture. *Bull. Seism. Soc. Am.*, 92(1):126–137, 2002.
- R. Burridge and L. Knopoff. Body force equivalents for seismic dislocations. *Bull. Seism. Soc. Am.*, 54(6):1875–1888, December 1964.
- J.D. Byerlee. Friction of rock. *Pure Appl. Geophys.*, 116:615–626, 1978.
- E. Calais, M. Vergnolle, V. San'kov, Andrei Likhnev, A. Miroshnitchenko, S. Amarjargal, and J. Déverchère. GPS measurements of crustal deformation in the Baikal-Mongolia area (1994–2002): Implications for current kinematics of Asia. *J. Geophys. Res.*, 108(B10), 2003.
- Q.Z. Chen and J. Freymueller. Geodetic evidence for a near-fault compliant zone along the San Andreas fault in the San Francisco Bay area. *Bull. Seismol. Soc. Am.*, 92:656–671, 2002.
- J. S. Chester, F. M. Chester, and A. K. Kronenberg. Fracture surface energy of the Punchbowl fault, San Andreas system. *Nature*, 437:133–136, 2005.
- E. S. Cochran, M. Radiguet, P. M. Shearer, Y.-G. Li, Y. Fialko, and J. E. Vidale. Seismic Imaging of the Damage Zone Around the Calico Fault. *Eos Trans. AGU*, 87(52), 2006.
- Y. Cochran, Y-G. Li, P. Shearer, S. Barbot, Y. Fialko, and J. Vidale. Seismic and geodetic evidence for extensive, long-lived fault damage zones. *Geology*, 37(4):315–318, April 2009.
- O. Coussy. *Poromechanics*. John Wiley & Sons Ltd, Chichester, U.K., 2004.
- S. M. Cox and P. C. Matthews. Exponential time differencing for stiff systems. *J. Comp. Phys.*, 176:430–455, 2002.

- D. Cunningham. Active intracontinental transpressional mountain building in the Mongolian Altai: Defining a new class of orogen. *Earth Plan. Sc. L.*, 240(2):436–444, December 2005.
- W. D. Cunningham. Lithospheric controls on late Cenozoic construction of the Mongolian Altai. *Tectonics*, 17(6):891–902, December 1998.
- L.M. Delves and J.L. Mohamed. *Computational methods for integral equations*. 373 pp., Cambridge Univ. Press, New York, 1985.
- J.S. Deng, K. Hudnut, M. Gurnis, and E. Hauksson. Stress loading from viscous flow in the lower crust and triggering of aftershocks following the 1994 Northridge California, earthquake. *Geophys. Res. Lett.*, 26:3209–3212, 1999.
- E. Detournay and A. H.-D. Cheng. Fundamentals of poroelasticity. In J. A. Hudson, editor, *Comprehensive Rock Engineering: Principles, Practice and Projects*, volume 2, pages 113–171. Pergamon Press, Oxford, UK, 1993.
- J. Dieterich. A constitutive law for rate of earthquake production and its application to earthquake clustering. *J. Geophys. Res.*, 99(B2):2601–2618, February 1994.
- J. Dieterich and D. E. Smith. Rate-state modeling of stress relaxation in geometrically complex fault systems. *Eos Trans. AGU*, 88(52), *Fall Meet. Suppl.*, pages abstract S13B–1308, 2007.
- J. H. Dieterich. Modeling of rock friction 1. experimental results and constitutive equations. *J. Geophys. Res.*, 84(B5):2161–2168, 1979.
- J. H. Dieterich. Nucleation and triggering of earthquake slip: effect of periodic stresses. *Tectonophysics*, 144(1-3):127–139, 1987.
- J. H. Dieterich. Earthquake nucleation on faults with rate- and state-dependent strength. *Tectonophysics*, 211:115–134, 1992.
- R. K. Dokka and C. J. Travis. Late cenozoic strike-slip faulting in the Mojave Desert, California. *Tectonics*, 9(2):311–340, February 1990a.
- R. K. Dokka and C. J. Travis. Role of the Eastern California Shear Zone in accommodation Pacific-North American plate motion. *Geophys. Res. Lett.*, 17(9):1323–1226, August 1990b.
- D. Dong, P. Fang, Y. Bock, F. Webb, L. Prawirodirdjo, S. Kedar, and P. Jamason. Spatiotemporal filtering using principal component analysis and Karhunen-Loeve expansion approaches for regional GPS network analysis. *J. Geophys. Res.*, 111(B03405), 2006. doi:doi:10.1029/2005JB003806.
- O Dor, Y Ben-Zion, and J Rockwell, T. K. Brune. Pulverized rocks in the Mojave section of the San Andreas Fault Zone. *Earth Planet. Sci. Lett.*, 245:642–654, 2006.

- Y. Du, P. Segall, and H. Gao. Dislocations in inhomogeneous media via a moduli perturbation approach: General formulation and two-dimensional solutions. *J. Geophys. Res.*, 99(B7):13767–13779, June 1994.
- Y. Du, P. Segall, and H. Gao. Quasi-static dislocations in three-dimensional inhomogeneous media. *Geophys. Res. L.*, 24(18):2347–2350, September 1997.
- G. Ekström, A. M. Dziewoński, N. N. Maternovskaya, and M. Nettles. Global seismicity of 2003: centroid moment-tensor solutions for 1087 earthquakes. *Phys. Earth Plan. Int.*, 148(2-4):327–251, February 2005.
- C. Elachi. *Spaceborne Radar Remote Sensing: Applications and Techniques*. IEEE Press, 1987.
- S. Ergintav, S. McClusky, E. Hearn, R. Reilinger, R. Cakmak, T. Herring, H. Ozener, O. Lenk, and E. Tari. Seven years of postseismic deformation following the 1999, M=7.4 and M=7.2, Izmit-Düzce, Turkey earthquake sequence. *J. Geophys. Res.*, 114(B07403), 2009.
- J. D. Eshelby. The determination of the elastic field of an ellipsoidal inclusion, and related problems. *Proc. R. Soc. Lond. A*, 241(1226):376–396, 1957.
- B. Evans and D. L. Kohlstedt. Rheology of rocks. In T. J. Ahrens, editor, *Handbook of physical constants. Part 3 - Rock physics and phase relations*, pages 148–165. Am. Geophys. Union, Washington, DC, 1995.
- H. Farid and E. P. Simoncelli. Differentiation of discrete multidimensional signals. *IEEE Trans. Im. Proc.*, 13(4):496–508, April 2004.
- Y. Fialko. Probing the mechanical properties of seismically active crust with space geodesy: Study of the co-seismic deformation due to the 1992 M_w 7.3 Landers (Southern California) earthquake. *J. Geophys. Res.*, 109:B03307, 10.1029/2003JB002756, 2004a.
- Y. Fialko. Evidence of fluid-filled upper crust from observations of post-seismic deformation due to the 1992 M_w 7.3 Landers earthquake. *J. Geophys. Res.*, 109:B08401, 10.1029/2004JB002985, 2004b.
- Y. Fialko. Interseismic strain accumulation and the earthquake potential on the southern San Andreas fault system. *Nature*, 441:968–971, 2006.
- Y. Fialko. Fracture and Frictional Mechanics - Theory. In G. Schubert, editor, *Treatise on Geophysics, Vol. 4*, pages 83–106. Elsevier Ltd., Oxford, 2007.
- Y. Fialko. Temperature fields generated by the elastodynamic propagation of shear cracks in the earth. *J. Geophys. Res.*, 109:B01303, 10.1029/2003JB002497, 2004c.

- Y. Fialko, Y. Khazan, and M. Simons. Deformation due to a pressurized horizontal circular crack in an elastic half-space, with applications to volcano geodesy. *Geophys. J. Int.*, 146:181–190, 2001a.
- Y. Fialko, M. Simons, and D. Agnew. The complete (3-D) surface displacement field in the epicentral area of the 1999 M_w 7.1 Hector Mine earthquake, southern California, from space geodetic observations. *Geophys. Res. Lett.*, 28:3063–3066, 2001b.
- Y. Fialko, D. Sandwell, D. Agnew, M. Simons, P. Shearer, and B. Minster. Deformation on nearby faults induced by the 1999 Hector Mine earthquake. *Science*, 297:1858–1862, 2002.
- Y. Fialko, D. Sandwell, M. Simons, and P. Rosen. Three-dimensional deformation caused by the Bam, Iran, earthquake and the origin of shallow slip deficit. *Nature*, 435:295–299, May 2005.
- A. M. Freed. Afterslip (and only afterslip) following the 2004 Parkfield, California, earthquake. *Geophys. Res. Lett.*, 34, May 2007.
- A. M. Freed and R. Bürgmann. Evidence of power-law flow in the Mojave desert mantle. *Nature*, 430:548–551, 2004.
- A. M. Freed, R. Bürgmann, E. Calais, J. Freymueller, and S. Hreinsdottir. Implications of deformation following the 2002 Denali, Alaska, earthquake for postseismic relaxation processes and lithospheric rheology. *J. Geophys. Res.*, 111:B01401, doi:10.1029/2005JB003894, 2006.
- A. M. Freed, R. Bürgmann, and T. Herring. Far-reaching transient motions after Mojave earthquakes require broad mantle flow beneath a strong crust. *Geophys. Res. Lett.*, 34(19), 2007.
- M. Frigo and S. G. Johnson. FFTW: An adaptative software architecture for the FFT. In *ICASSP conference proceedings*, volume 3, pages 1381–1384, 1998.
- C. W. Gable, R. J. O’Connell, and B. J. Travis. Convection in three dimensions with surface plates: Generation of toroidal flow. *J. Geophys. Res.*, 96(B5):8391–8405, May 1991.
- F. Garofalo. *Fundamentals of Creep and Creep-rupture in Metals*. MacMillan, New York, N. Y., 1975.
- P. Gasperini, G. D. Forno, and E. Boschi. Linear or non-linear rheology in the Earth’s mantle: the prevalence of power-law creep in the postglacial isostatic readjustment of Laurentia. *Geophys. J. Int.*, 157:1297–1302, 2004.
- G. H. Golub and C. F. Van Loan. *Iterative Methods for Linear Systems*. Matrix Computations. Johns Hopkins U. Press, Baltimore, Md., 3rd edition, 1996.
- Y. Hamiel and Y. Fialko. Structure and mechanical properties of faults in the North Anatolian Fault system from InSAR observations of coseismic deformation due to the 1999 Izmit (Turkey) earthquake. *J. Geophys. Res.*, 112(B07412), 2007.

- Y. Hamiel, Y. Liu, V. Lyakhovsky, Y. Ben-Zion, and D. Lockner. A visco-elastic damage model with applications to stable and unstable fracturing. *Geophys. J. Int.*, 159:1155–1165, 2004.
- R. A. Harris and J. R. Arrowsmith. Introduction to the special issue on the 2004 Parkfield Earthquake and the Parkfield earthquake prediction experiment. *Bull. Seism. Soc. Am.*, 96(B4):S1–S10, September 2006.
- E. Hauksson, L.M. Jones, and K. Hutton. The 1999 M_w 7.1 Hector Mine, California, earthquake sequence: Complex conjugate strike-slip faulting. *Bull. Seism. Soc. Am.*, 92:1154–1170, 2002.
- M. J. Heap, P. Baud, P. G. Meredith, A. F. Bell, and I. G. Main. Time-dependent brittle creep in Darley Dale sandstone. *J. Geophys. Res.*, 114(B07203), 2009. doi: 10.1029/2008JB006212.
- E. H. Hearn and Y. Fialko. Can compliant fault zones be used to measure absolute stresses in the upper crust? *J. Geophys. Res.*, 114(B04403), 2009. doi: 10.1029/2008JB005901.
- E. H. Hearn, R. Bürgmann, and R. E. Reilinger. Dynamics of İzmit earthquake postseismic deformation and loading of the Düzce earthquake hypocenter. *Bull. Seism. Soc. Am.*, 92(1): 172–193, February 2002.
- E.H. Hearn and R. Bürgmann. The Effect of Elastic Layering on Inversions of GPS Data for Coseismic Slip and Resulting Stress Changes: Strike-Slip Earthquakes. *Bull. Seism. Soc. Am.*, 95(5):1637–1653, 2005.
- R. Hill. A self-consistent mechanics of composite materials. *J. Mech. Phys. Solids*, 13:213–222, August 1965. doi: 10.1016/0022-5096(65)90010-4.
- Y.-J. Hsu, M. Simons, J.-P. Avouac, J. Galetzka, K. Sieh, M. Chlieh, D. Natawidjaja, L. Prawirodirdjo, and Y. Bock. Friction afterslip following the 2005 Nias-Simeulue earthquake, Sumatra. *Science*, 312:1921–1926, June 2006.
- A. Jacobs, D. Sandwell, Y. Fialko, and L. Sichoix. The 1999 (M_w 7.1) Hector Mine, California, earthquake: near-field postseismic deformation for ERS interferometry. *Bull. Seism. Soc. Am.*, 92(4):1433–1442, May 2002.
- I. A. Johanson, E. J. Fielding, F. Rolandone, and R. Bürgmann. Coseismic and postseismic slip of the 2004 Parkfield earthquake from space-geodetic data. *Bull. Seism. Soc. Am.*, 96(4B): S269–S282, September 2006.
- K. J. Johnson, R. Burgmann, and K. Larson. Frictional properties on the San Andreas fault near Parkfield, California, inferred from models of afterslip following the 2004 earthquake. *Bull. Seism. Soc. Am.*, 96(4B):S321S338, September 2006.
- K. M. Johnson, R. Bürgmann, and J. T. Freymueller. Coupled afterslip and viscoelastic flow following the 2002 Denali fault, Alaska earthquake. *Geophys. J. Int.*, 176(3):670–682, 2009.

- P. Johnston, P. Wu, and K. Lambeck. Dependence of horizontal stress magnitude on load dimension in glacial rebound models. *Geophys. J. Int.*, 132:41–60, 1998.
- L. E. Jones and D. V. Helmberger. Earthquake source parameters and fault kinematics in the Eastern California Shear Zone. *Bull. Seism. Soc. Am.*, 88(6):1337–1352, December 1998.
- S. Jonsson, P. Segall, R. Pedersen, and G. Bjornsson. Post-earthquake ground movements correlated to pore-pressure transients. *Nature*, 424:179–183, 2003.
- L.M. Kachanov. *Introduction to Continuum Damage Mechanics*. Martinus Nijhoff, Dordrecht, 1986.
- H. Kanamori and D. L. Anderson. Theoretical basis of some empirical relations in seismology. *Bull. Seism. Soc. Am.*, 65(5):1073–1095, 1975.
- S. Karato and P. Wu. Rheology of the upper mantle: a synthesis. *Science*, 260:771–778, May 1993.
- S.-I. Karato. *Deformation of Earth Materials: An Introduction to the Rheology of Solid Earth*. Cambridge Univ. Press, Cambridge, U. K., 2008.
- S.-I. Karato, M. S. Paterson, and J. D. Fitzgerald. Rheology of synthetic olivine aggregates - Influence of grain size and water. *J. Geophys. Res.*, 91:8151–8176, July 1986. doi: 10.1029/JB091iB08p08151.
- T. Kato. *Perturbation Theory for Linear Operators*. Springer-Verlag, New York, 1980.
- S. J. Kenner and P. Segall. Postseismic deformation following the 1906 San Francisco earthquake. *J. Geophys. Res.*, 105(B6):13195–13210, June 2000.
- S. H. Kirby and A. K. Kronenberg. Rheology of the lithosphere; selected topics. *Rev. Geophys.*, 25:1219–1244, 1987.
- D. L. Kohlstedt, B. Evans, and S. J. Mackwell. Strength of the lithosphere: Constraints imposed by laboratory experiments. *J. Geophys. Res.*, 100:17587–17602, 1995.
- H.-J. Kumpel. Poroelasticity: Parameters reviewed. *Geophys. J. Int.*, 105:783–799, 1991.
- J. Langbein. Noise in GPS displacement measurements from Southern California and Southern Nevada. *J. Geophys. Res.*, 113(B05405), 2008. doi: 10.1029/2007JB005247.
- J. Langbein and Y. Bock. High-rate real-time GPS network at Parkfield: Utility for detecting fault slip and seismic displacements. *Geophys. Res. Lett.*, 31(L15S20), 2004.

- J. Langbein, J. R. Murray, and H. A. Snyder. Coseismic and initial postseismic deformation from the 2004 Parkfield, California, earthquake, observed by global positioning system, electronic distance meter, creepmeters, and borehole strainmeters. *Bull. Seism. Soc. Am.*, 96(4B):S304–S320, September 2006.
- N. Lapusta, J. R. Rice, Y. BenZion, and G. Zheng. Elastodynamics analysis for slow tectonic loading with spontaneous rupture episodes on faults with rate- and state-dependent friction. *J. Geophys. Res.*, 105(B10):23765–23789, October 2000.
- T. B. Larsen, D. A. Yuen, A. V. Malevsky, and J. L. Smedsmo. Dynamics of strongly time-dependent convection with non-Newtonian temperature-dependent viscosity. *Phys. Earth Plan. Int.*, 94:75–103, 1996.
- R. A. Lebensohn. N-site modelling of a 3D viscoplastic polycrystal using the fast Fourier transform. *Acta Mater*, 49:2723–2737, 2001.
- S. Leprince, S. Barbot, F. Ayoub, and J. P. Avouac. Automatic, precise, ortho-rectification and coregistration for satellite image correlation, application to ground deformation measurement. *IEEE Trans. Geosc. Rem. Sens.*, 45(6):1529–1558, 2007.
- Y. G. Li and P. C. Leary. Fault zone trapped seismic waves. *Bull Seism. Soc. Am.*, 80:1245–1271, 1990.
- Y.G. Li, J.E. Vidale, K. Aki, C.J. Marone, and W.H.K. Lee. Fine-structure of the Landers fault zone - segmentation and the rupture process. *Science*, 265:367–370, 1994.
- Y.G. Li, K. Aki, J.E. Vidale, and M.G. Alvarez. A delineation of the Nojima fault ruptured in the M7.2 Kobe, Japan, earthquake of 1995 using fault zone trapped waves. *J. Geophys. Res.*, 103(B4):7247–7263, 1998a.
- Y.G. Li, J.E. Vidale, K. Aki, F. Xu, and T. Burdette. Evidence of shallow fault zone strengthening after the 1992 M7.5 Landers, California, earthquake. *Science*, 279:217–219, 1998b.
- Y.G. Li, K. Aki, J.E. Vidale, and F. Xu. Shallow structure of the landers fault zone from explosion-generated trapped waves. *J. Geophys. Res.*, 104:20257–20275, 1999.
- Y.G. Li, J.E. Vidale, K. Aki, and F. Xu. Depth-dependent structure of the Landers fault zone from trapped waves generated by aftershocks. *J. Geophys. Res.*, 105:6237–6254, 2000.
- M. Lisowski, J.C. Savage, and W. H. Prescott. The velocity field along the San Andreas fault in central and southern California. *J. Geophys. Res.*, 96:8369–8389, 1991.
- J. Liu, K. Sieh, and E. Hauksson. A structural interpretation of the aftershock "Cloud" of the 1992 M_w 7.3 Landers earthquake. *Bull. Seism. Soc. Am.*, 93:1333–1344, 2003.

- P. Liu, S. Custudio, and R. J. Archuleta. Kinematic inversion of the 2004 m 6.0 Parkfield earthquake including an approximation to site effects. *Bull. Seism. Soc. Am.*, 96(4B):S143S158, September 2006.
- A. E. H. Love. *A Treatise on the Mathematical Theory of Elasticity*. Cambridge University Press, Cambridge, 1927. Reprinted in 1944 by Dover Publications, New York.
- V. Lyakhovskiy, Y. Ben-Zion, and A. Agnon. Earthquake cycle, fault zones, and seismicity patterns in a rheologically layered lithosphere. *J. Geophys. Res.*, 106:4103–4120, 2001.
- L. E. Malvern. *Introduction to the mechanics of a continuum medium*. 713 pp., Prentice-Hall, Englewood Cliffs, NJ, 1969.
- I. Manighetti, G.C.P. King, Y. Gaudemer, C.H. Scholz, and C. Doubre. Slip accumulation and lateral propagation of active normal faults in Afar. *J. Geophys. Res.*, 106:13667–13696, 2001.
- C. Marone, B. C. Raleigh, and C. H. Scholz. Frictional behavior and constitutive modeling of simulated fault gouge. *J. Geophys. Res.*, 95(B5):7007–7026, May 1990.
- C. Marone, C.H. Scholz, and R. Bilham. On the mechanics of earthquake afterslip. *J. Geophys. Res.*, 96:8441–8452, 1991.
- C. Marone, J. E. Vidale, and W. Ellsworth. Fault healing inferred from the time dependent variations in source properties of repeating earthquakes. *Geophys. Res. Lett.*, 22:3095–3098, 1995.
- C. J. Marone. Laboratory-derived friction laws and their application to seismic faulting. *An. Rev. Earth Planet. Sc.*, 26:643696, 1998.
- D. Massonnet, M. Rossi, C. Carmona, F. Adragna, G. Peltzer, K. Feigl, and T. Rabaute. The displacement field of the Landers earthquake mapped by radar interferometry. *Nature*, 364 (6433):138–142, 1993.
- T. Masterlark and H. F. Wang. Transient stress-coupling between the 1992 Landers and 1999 Hector Mine, California, earthquakes. *Bull. Seism. Soc. Am.*, 92(4):1470–1486, May 2002. doi: 10.1785/0120000905.
- G. M. Mavko. Mechanics of motion on major faults. *Ann. Rev. Earth Planet. Sci.*, 9:81–111, 1981.
- J. McClellan, T. Parks, and L. Rabiner. A computer program for designing optimum FIR linear phase digital filters. *Audio and Electroacoustics, IEEE Trans.*, 21(6):506–526, December 1973.
- J. J. McGuire and P. Segall. Imaging of aseismic fault slip transients recorded by dense geodetic networks. *Geophys. J. Int.*, 155:778–788, 2003.

- B. J. Meade. Algorithms for the calculation of exact displacements, strains, and stresses for triangular dislocation elements in a uniform elastic half space. *Comp. Geosc.*, 33(8):1064–1075, August 2007.
- W. Menke. *Geophysical Data Analysis, Discrete Inverse Theory*. Elsevier, New York, 1984.
- R. Michel, J.-P. Avouac, and J. Taboury. Measuring ground displacements from SAR amplitude images: application to the Landers earthquake. *Geoph. Res. Letters*, 26(7):875–878, April 1999.
- M. M. Miller, D. J. Johnson, T. H. Dixon, and R. K. Dokka. Refined kinematics of the Eastern California shear zone from GPS observations, 1993-1998. *J. Geophys. Res.*, 106(B2):2245–2264, 2001.
- R. D. Mindlin. Force at a point in the interior of a semi-infinite solid. *J. Appl. Phys.*, 7:195–202, May 1936a.
- R. D. Mindlin. Note on the Galerkin and Papkovitch stress functions. *Bull. Am. Math. Soc.*, 42(6):373–376, 1936b. doi: 10.1090/S0002-9904-1936-06304-4.
- R. D. Mindlin and D. H. Cheng. Nuclei of strain in the semi-infinite solid. *J. Appl. Phys.*, 21:926–930, September 1950a. doi:doi:10.1063/1.1699785.
- R. D. Mindlin and D. H. Cheng. Thermoelastic stress in the semi-infinite solid. *J. Appl. Phys.*, 21:931–933, September 1950b.
- S. Miyazaki, J. J. McGuire, and P. Segall. A transient subduction zone slip episode in southwest Japan observed by the nationwide GPS array. *J. Geophys. Res.*, 108(B2), February 2003. doi: 10.1029/2001JB000456.
- K. Mogi. Relations between the eruptions of various volcanoes and the deformations of the ground surfaces around them. *Bull. Earthquake Res. Inst. Univ. Tokyo*, 36:99–134, 1958.
- L. G. J. Montesi. Controls of shear zone rheology and tectonic loading on postseismic creep. *J. Geophys. Res.*, 109(B10), October 2004.
- L. G. J. Montési and G. Hirth. Grain size evolution and the rheology of ductile shear zones: from laboratory experiments to postseismic creep. *Earth Planet. Sci. Lett.*, 211:97–110, June 2003.
- C. Morrow and D. A. Lockner. Hayward fault rocks: Porosity, density and strength measurements. *U.S. Geol. Surv. Open File Rep.*, pages 01–421, 2001.
- C. Morrow, B. Radney, and J. Byerlee. Frictional strength and the effective pressure law of montmorillonite and illite clays. In B. Evans and T.-F. Wong, editors, *Fault Mechanics and Transport Properties of Rocks*, volume 51 of *Int. Geophys. Ser.*, pages 69–88. Academic, London, 1992.

- H. Moulinec and P. Suquet. A numerical method for computing the overall response of nonlinear composites with complex microstructure. *Comp. Meth. App. Mech. Eng.*, 157:69–94, 1998.
- J. Murray and J. Langbein. Slip on the San Andreas fault at Parkfield, California, over two earthquake cycles, and the implications for seismic hazard. *Bull. Seism. Soc. Am.*, 96(4B): S283–S303, 2006.
- J. R. Murray, P. Segall, P. Cervelli and W. Prescott, and J. Svarc. Inversion of gps data for spatially variable slip-rate on the san andreas fault near Parkfield, CA. *Geophys. Res. Lett.*, 28(2):359–362, 2001.
- S. Nemat-Nasser. *Plasticity. A Treatise on Finite Deformation of Heterogeneous Inelastic Materials*. Cambridge Monographs on Mechanics. Cambridge University Press, 2004.
- S. Nemat-Nasser and M. Hori. *Micromechanics: overall properties of heterogeneous materials*. Elsevier, 2 edition, 1999.
- T.-K. Nguyen, K. Sab, and G. Bonnet. Green’s operator for a periodic medium with traction-free boundary conditions and computation of the effective properties of thin plates. *Int. J. Sol. Struct.*, 45:6518–6534, 2008. doi: 10.1016/j.ijsolstr.2008.08.015.
- A. Niazy. An exact solution for a finite, two-dimensional moving dislocation in an elastic half-space with application to the San Fernando earthquake of 1971. *Bull. Seism. Soc. Am.*, 65(6): 1797–1826, December 1975.
- E. Nissen, B. Emmerson, G. Funning, A. Mistrukov, B. Parsons, D. Robinson, E. Rogozhin, and T. Wright. Combining InSAR and seismology to study the 2003 Siberian Altai earthquakes-dextral strike-slip and anticlockwise rotations in the northern India-Eurasia collision zone. *Geophys. J. Int.*, In Press, 2007.
- A. Nur and G. Mavko. Postseismic viscoelastic rebound. *Science*, 183:204–206, 1974.
- Y. Okada. Surface deformation due to shear and tensile faults in a half-space. *Bull. Seism. Soc. Am.*, 75(4):1135–1154, August 1985.
- Y. Okada. Internal deformation due to shear and tensile faults in a half-space. *Bull. Seism. Soc. Am.*, 82:1018–1040, April 1992.
- I. A. Okumura. On the generalization of cerruti’s problem in an elastic half-space. *Proc. Japan Soc. Civ. Eng.*, (519):1, 1995.
- M. Oskin and A. Iriondo. Large-magnitude transient strain accumulation on the Blackwater fault, Eastern California shear zone. *Geology*, 32:313–316, 2004.
- R. L. Parker. *Geophysical inverse theory*. Princeton University Press, Princeton, N.J., 1994.

- T. Parsons. Tectonic stress in California modeled from GPS observations. *J. Geophys Res.*, 111 (B03407), 2005.
- J. Pearse and Y. Fialko. Post-rifting deformation in Afar, Ethiopia, following the 2005 intrusion event. *AGU Fall Meeting Abstracts*, pages B7+, December 2008.
- W. R. Peltier. Ice age geodynamics. *Ann. Rev. Earth Planet. Sci.*, 9:199–225, 1981.
- G. Peltzer, P. Rosen, F. Rogez, and K. Hudnut. Poroelastic rebound along the Landers 1992 earthquake surface rupture. *J. Geophys. Res.*, 103(B12):30131–30145, December 1998.
- G. Peltzer, F. Campé, and Geoffrey King. Evidence of nonlinear elasticity of the crust from the Mw7.6 Manyi (Tibet) earthquake. *Science*, 286:272–275, October 1999.
- H. Perfettini and J.-P. Avouac. Postseismic relaxation driven by brittle creep: a possible mechanism to reconcile geodetic measurements and the decay rate of aftershocks, application to the Chi-Chi earthquake, Taiwan. *J. Geophys. Res.*, 109(B02304), 2004.
- H. Perfettini and J.-P. Avouac. Modeling afterslip and aftershocks following the 1992 Landers earthquake. *J. Geophys. Res.*, 112(B07409), 2007.
- A. Piombo, G. Martinelli, and M. Dragoni. Post-seismic fluid flow and coulomb stress changes in a poroelastic medium. *Geophys. J. Int.*, 162:507–515, 2005.
- F. F. Pollitz. Gravitational viscoelastic postseismic relaxation on a layered spherical Earth. *J. Geophys. Res.*, 102:17921–17941, 1997.
- Fred F. Pollitz. Post-seismic relaxation theory on a laterally heterogenous viscoelastic model. *Geophys. J. Int.*, 155:55–78, 2003a.
- Fred F. Pollitz. Transient rheology of the uppermost mantle beneath the Mojave desert, California. *Earth Plan. Sc. L.*, 215(1-2):89–104, October 2003b.
- Fred F. Pollitz, G. Peltzer, and R. Bürgmann. Mobility of continental mantle: Evidence from postseismic geodetic observations following the 1992 landers earthquake. *J. Geophys. Res.*, 105 (B4):8035–8054, April 2000.
- R. W. Preisendorfer and C. D. Mobley. *Principal Component Analysis in Meteorology and Oceanography*, volume 17 of *Develop. Atmos. Sci.* Elsevier, New York, 1988.
- W. H. Press, S. A. Teukolsky, W. T. Vetterling, and B. P. Flannery. *Numerical Recipes in C: The Art of Scientific Computing*. 2nd ed., 994 pp., Cambridge Univ. Press, New York, 1992.
- H. F. Reid. *The Mechanics of the Earthquake*, volume 2 of The California Earthquake of April 18, 1906. Carnegie Institution of Washington, 1910.

- R. Reilinger. Evidence for postseismic viscoelastic relaxation following the 1959 M=7.5 Hebgen Lake, Montana, earthquake. *J. Geophys. Res.*, 91(B9):9488–9494, August 1986.
- J. R. Rice and M. P. Cleary. Some basic stress-diffusion solutions for fluid-saturated elastic porous media with compressible constituents. *Rev. Geophys.*, 14:227–241, 1976.
- J. R. Rice, N. Lapusta, and K. Ranjith. Rate and state dependent friction and the stability of sliding between elastically deformable solids. *J. Mech. Phys. Solids*, 49:1865–1898, 2001.
- J. R. Rice, C. G. Sammis, and R. Parsons. Off-fault secondary failure induced by a dynamic slip pulse. *Bull. Seism. Soc. Am.*, 95:109–134, 2005.
- D. C. Roberts and D. L. Turcotte. Earthquakes: Friction or a plastic instability? *Geophys. monogr.*, 120:97–103, 2000.
- P. A. Rosen, S. Hensley, I. R. Joughin, F. K. Li, S. N. Madsen, E. Rodriguez, and R. M. Goldstein. Synthetic aperture radar interferometry. *Proc. IEEE*, 80(3):333–382, 2000.
- J. W. Rudnicki. Effect of pore fluid diffusion on deformation and failure of rock. In Z. P. Bazant, editor, *Mechanics of Geomaterials - Rocks, Concretes, Soils*, pages 315–347. Wiley, Chichester, 1985.
- A. Ruina. Slip instability and state variable friction laws. *J. Geophys. Res.*, 88:10,359–10,370, 1983.
- J. B. Rundle. Viscoelastic-gravitational deformation by a rectangular thrust fault in a layered earth. *J. Geophys. Res.*, 87(B9):7787–7796, 1982.
- K. Rybicki. The elastic residual field of a very long strike-slip fault in the presence of a discontinuity. *Bulletin of the Seismological Society of America*, 61(1):79–92, 1971.
- K. Rybicki and K. Kasahara. A strike-slip fault in a laterally inhomogeneous medium. *Tectonophysics*, 42:127–138, 1977.
- M. J. Rymer. Near-fault measurement of postseismic slip associated with the 1989 Loma Prieta, California, earthquake. *Geophys. Res. L.*, 17(10):1789–1792, 1990.
- D. T. Sandwell. Thermomechanical evolution of oceanic fracture zones. *Journ. Geophys. Res.*, 89:11401–11413, 1984.
- D.T. Sandwell, L. Sichoix, D. Agnew, Y. Bock, and J.-B. Minster. Near real-time radar interferometry of the M_w 7.1 Hector Mine Earthquake. *Geophys. Res. Lett.*, 27:3101–3104, 2000.
- J. Sauber, W. Thatcher, S. C. Solomon, and M. Lisowski. Geodetic slip rate for the east California shear zone and the recurrence time of Mojave desert earthquakes. *Nature*, 367:264–266, January 1994.

- J. Savage and J. Svarc. Postseismic deformation associated with the 1992 $M_w=7.3$ Landers earthquake, southern California. *J. Geophys. Res.*, 102:7565–7577, 1997.
- J. C. Savage. Dislocations in seismology. In F. R. N. Nabarro, editor, *Dislocations Theory: A Treatise*. Marcel Dekker, New York, 1974.
- J. C. Savage. Equivalent strike-slip earthquakes cycles in half-space and lithosphere-asthenosphere earth models. *J. Geophys. Res.*, 95(B4):4873–4879, April 1990.
- J. C. Savage and W. H. Prescott. Asthenosphere readjustment and the earthquake cycle. *J. Geophys. Res.*, 83(B7):3369–3376, 1978.
- J. C. Savage and S.-B. Yu. Postearthquake relaxation and aftershock accumulation linearly related after the 2003 M 6.5 Chengkung, Taiwan, and the 2004 M 6.0 Parkfield, California, earthquakes. *Bull. Seism. Soc. Am.*, 97(5):1632–1645, October 2007. doi: 10.1785/0120070069.
- J. C. Savage, M. Lisowski, and W. H. Prescott. An apparent shear zone trending north-northwest across the Mojave desert into Owens Valley, Eastern California. *Geophys. Res. Let.*, 17(12):2113–2116, November 1980.
- J. C. Savage, M. Lisowski, and J. L. Svarc. Postseismic deformation following the 1989 ($M = 7.1$) Loma Prieta, California, earthquake. *J. Geophys. Res.*, 99(B7):13757–13765, July 1994.
- J. C. Savage, J. L. Svarc, and S.-B. Yu. Postseismic relaxation and aftershocks. *J. Geophys. Res.*, 112(B11), June 2007. doi: 10.1029/2006JB004584.
- J.C. Savage. Viscoelastic-coupling model for the earthquake cycle driven from below. *J. Geophys. Res.*, 105(B11):25525–25532, November 2000.
- J.C. Savage and R.O. Burford. Geodetic determination of relative plate motion in central California. *J. Geophys. Res.*, 78:832–845, 1973.
- C. H. Scholz. *The mechanics of earthquakes and faulting*. 2nd Ed., 496 pp., Cambridge Univ. Press, New York, NY, 2002.
- C. H. Scholz. Wear and gouge formation in brittle faulting. *Geology*, 15:493–495, 1987.
- C. H. Scholz. The brittle-plastic transition and the depth of seismic faulting. *Geologische Rundschau*, 77(1):319–328, 1988.
- C. H. Scholz. *The mechanics of earthquakes and faulting*. 439 pp., Cambridge Univ. Press, New York, NY, 1990.
- C. H. Scholz. Earthquakes and friction laws. *Nature*, 391:37–42, January 1998.

- P. Segall. Stress and subsidence resulting from subsurface fluid withdrawal in the epicentral region of the 1983 Coalinga earthquake. *J. Geophys. Res.*, 90(B8):6801–6816, July 1985.
- P. Segall. Earthquakes triggered by fluid extraction. *Geology*, 17:942–046, October 1989.
- P. Segall and D.D Pollard. Mechanics of discontinuous faults. *J. Geophys. Res.*, 85:4337–4350, August 1980.
- P. M. Shearer. *Introduction to seismology*. Cambridge University Press, New York, 1999.
- K. Sieh, L. Jones, E. Hauksson, K. Hudnut, D. Eberhartphillips, T. Heaton, S. Hough, K. Hutton, H. Kanamori, A. Lilje, S. Lindvall, S. F. McGill, J. Mori, C. Rubin, J. A. Spotila, J. Stock, H. K. Thio, J. Treiman, B. Wernicke, and J. Zachariassen. Near-field investigations of the Landers earthquake sequence. *Science*, 260:171–176, 1993.
- M. Simons, Y. Fialko, and L. Rivera. Coseismic deformation from the 1999 M_w 7.1 Hector Mine, California, earthquake, as inferred from InSAR and GPS observations. *Bull. Seism. Soc. Am.*, 92:1390–1402, 2002.
- Sarva J. Singh, S. Rani, and R. Kumar. Quasi-static deformation of a poroelastic half-space with anisotropic permeability by two-dimensional surface loads. *Geophys. J. Int.*, 170(3):1311–1327, June 2007.
- B Smith and D. Sandwell. A three-dimensional semianalytic viscoelastic model for time-dependent analyses of the earthquake cycle. *J. Geophys. Res.*, 109, 2004.
- R. W. Soutas-Little. *Elasticity*. Courier Dover Publications, 1999. unabridged.
- R. S. Stein and M. Lisowski. The 1979 Homestead Valley earthquake sequence, California: Control of aftershocks and postseismic deformation. *J. Geophys. Res.*, B8:6477–6490, August 1983.
- J. A. Steketee. On Volterra’s dislocations in a semi-infinite elastic medium. *Can. J. Phys.*, 36:192–205, 1958a.
- J. A. Steketee. Some geophysical applications of the elasticity theory of dislocations. *Can. J. Phys.*, 36:1168–1198, 1958b.
- W. D. Stuart and T. E. Tullis. Fault model for preseismic deformation at Parkfield, California. *J. Geophys. Res.*, 100(B12):24079–24099, December 1995.
- P. Tapponnier and P. Molnar. Active faulting and Cenozoic tectonics of the Tien Shan, Mongolia, and Baykal regions. *J. Geophys. Res.*, 84:3425–3459, July 1979.
- A. Tarantola. *Inverse Problem Theory and Methods for Model Parameter Estimation*. Soc. Ind. App. Math, Philadelphia, PA, USA, 2004. ISBN 0898715725.

- H. Tarayre and D. Massonnet. Atmospheric propagation heterogeneities revealed by ERS-1 interferometry. *Geophys. Res. Lett.*, 23:989–992, 1996.
- W. Thatcher. Nonlinear strain buildup and the earthquake cycle on the San Andreas fault. *J. Geophys. Res.*, 88(B7):5893–5902, 1983.
- W. Thatcher and J. R. Rundle. A model for the earthquake cycle in underthrust zones. *J. Geophys. Res.*, 84(B10):5540–5556, 1979.
- C. Thurber, S. Roecker, K. Roberts, M. Gold, L. Powell, and K. Rittger. Earthquake locations and three-dimensional fault zone structure along the creeping section of the San Andreas fault near Parkfield, CA: Preparing for SAFOD. *Geophys. Res. Lett.*, 30:1112, 2003.
- S. T. Tse and J. R. Rice. Crustal earthquake instability in relation to the depth variation of frictional slip properties. *J. Geophys. Res.*, 91(B9):9452–9472, 1986.
- M. C. Tsenn and N. L. Carter. Upper limits of power law creep of rocks. *Tectonophysics*, 136: 1–26, May 1987. doi: 10.1016/0040-1951(87)90332-5.
- D.L. Turcotte, W.I. Newman, and R. Shcherbakov. Micro and macroscopic models of rock fracture. *Geophys. J. Int.*, 152:718–728, 2003.
- N. Van Puymbroeck, R. Michel, R. Binet, J.-P. Avouac, and J. Taboury. Measuring earthquakes from optical satellite images. *Applied Optics*, 39(20):3486–3494, July 2000.
- J.M. Vermilye and C.H. Scholz. The process zone: A microstructural view of fault growth. *J. Geophys. Res.*, 103:12223–12237, 1998.
- J.E. Vidale and Y.G. Li. Damage to the shallow Landers fault from the nearby Hector Mine earthquake. *Nature*, 421:524–526, 2003.
- F. Waldhauser, W. L. Ellsworth, D. P. Schaff, , and A. Cole. Streaks, multiplets, and holes: High-resolution spatio-temporal behavior of Parkfield seismicity. *Geophys. Res. Lett.*, 31(L18608), 2004. doi: doi:10.1029/2004GL020649.
- H. F. Wang. *Theory of Linear Poroelasticity with Applications to Geomechanics and Hydrogeology*. Princeton University Press, 2000.
- R. Wang, F. Lorenzo-Martin, and F. Roth. PSGRN/PSCMP-a new code for calculating co- and post-seismic deformation, geoid and gravity changes based on the viscoelastic-gravitational dislocation theory. *Computers and Geosciences*, 32:527–541, 2006.
- R.J. Wang, F.L. Martin, and F. Roth. Computation of deformation induced by earthquakes in a multi-layered elastic crust - FORTRAN programs EDGRN/EDCMP. *Comp. Geosci.*, 29: 195–207, 2003.

- S. Wdowinski, Y. Bock, J. Zhang, P. Fang, and J. Genrich. Southern California permanent GPS geodetic array: Spatial filtering of daily positions for estimating coseismic and postseismic displacements induced by the 1992 Landers earthquake. *J. Geophys. Res.*, 102:18057–18070, 1997.
- J. Weertman and J. R. Weertman. *Elementary Dislocation Theory*. Macmillan, New York, 1964.
- J. Weertman and J. R. Weertman. High temperature creep of rock and mantle viscosity. *Ann. Rev. Earth Planet. Sci.*, 3:293–315, 1975. doi: 10.1146/annurev.ea.03.050175.001453.
- H. M. Westergaard. General solution of the problem of elastostatics of an n -dimensional homogeneous isotropic solid in an n -dimensional space. *Bull. Am. Math. Soc.*, 41(10):695–699, 1935. doi: 10.1090/S0002-9904-1935-06178-6.
- S. D. P. Williams, Y. Bock, P. Fang, P. Jamason, R. M. Nikolaidis, L. Prawirodirdjo, M. Miller, and D. J. Johnson. Error analysis of continuous GPS position time series. *J. Geophys. Res.*, 109(B03412), 2004. doi: 10.1029/2003JB0022741.
- B. Wilson, T. Dewers, Z. Reches, and J. Brune. Particle size and energetics of gouge from earthquake rupture zones. *Nature*, 434:749–752, 2004.
- B. F. Windley and M. B. Allen. Mongolian plateau: Evidence for a late Cenozoic mantle plume under central Asia. *Geology*, 21(4):295298, April 1993.
- D. Wolf. Viscoelastodynamics and of a stratified, compressible planet: incremental field equations and shot- and long-time asymptotes. *Geophys. J. Int.*, 104:401–417, 1991.
- X.-M. Yang, P. M. Davis, and J. H. Dieterich. Deformation from inflation of a dipping finite prolate spheroid in an elastic half-space as a model for volcanic stressing. *J. Geophys. Res.*, 93:4249–4257, 1988.
- P. Yu, S. Y. Hu, L. Q. Chen, and Q. Du. An iterative-perturbation scheme for treating inhomogeneous elasticity in phase-field models. *J. Comp. Phys.*, 208:34–50, 2005.
- H. A. Zebker and J. Villasenor. Decorrelation in interferometric radar echoes. *Geosci. Rem. Sens. Lett.*, 30(5):950–959, 1992.
- L.P. Zhu and L.A. Rivera. A note on the dynamic and static displacements from a point source in multilayered media. *Geophys. J. Int.*, 148:619–627, 2002.